Enhancing Steel Hollow Structural Sections and Braced Frame Performance through Non-Traditional Civil Engineering Materials

by

Malcolm Lee Ammons

A dissertation submitted in partial fulfillment
of the requirements for the degree of
Doctor of Philosophy
(Civil Engineering)
in the University of Michigan
2020

Doctoral Committee:

Associate Professor Jason P. McCormick, Chair
Professor Pingsha Dong
Professor Sherif El-Tawil
Assistant Professor Seymour M.J. Spence

Malcolm L. Ammons

ammonsm@umich.edu

ORCID iD: 0000-0003-2033-9936

Dedication

To my parents, Anthony Sr. and Kamlyn, my sister, Akeelah, my brother, Anthony Jr., my friends, and anyone else that has supported me and helped me to get to this point…THANK YOU.

Acknowledgements

First and foremost, I would like to thank my Lord and Savior Jesus Christ for blessing me with the opportunity and ability to pursue a doctoral degree. I would also like to express my sincere appreciation for my advisor, Dr. Jason McCormick. His work ethic, meticulousness, professionalism, and genuine concern for others are just a few of the many character traits that I admire about him. I have learned more than I could have ever imagined under his guidance and will always be grateful for the patience that he displayed and support that he provided me throughout my doctoral studies. I look forward to our future interactions as we continue to progress in our respective careers.

I would also like to thank, Professor Dong, Professor El-Tawil and Professor Spence for agreeing to serve on my dissertation committee. I have had the privilege of taking classes that they have taught, and it strengthened the great deal of admiration and respect that I already had for them. I am truly grateful for the support that they have offered, whether in the form of a letter of recommendation, serving as an employment reference, research advice or just simple conversations in passing.

The research presented in this dissertation would not have been completed without the excellent lab technicians that I have had the opportunity to work with throughout my time here. I sincerely appreciate Steve Donajkowski, Bob Fischer, Ethan Kennedy, Jan Pantolin, and Bob Spence for their guidance and assistance with laboratory testing.

I am also grateful to have had the opportunity to travel to Japan to collaborate with researchers at the Disaster Prevention Research Institute (Kyoto University) through Award No. 1713850 from the United States National Science Foundation (NSF) East Asia and Pacific Summer Institutes Fellowship in conjunction with the Japan Society for the Promotion of Science (JSPS). Special thanks to Professor Masahiro Kurata for allowing me to work with him and his research group. I am also appreciative of the assistance provided by Hironari Shimada and Giuseppe Marzano. The experimental brace tests conducted at Kyoto University could not have been completed without their help.

I would also like to thank members of the McCormick lab group for making my research experience enjoyable and for helping with laboratory testing and running simulations. Thank you, Ana, Carolyn, Christian, Dan, Kate, and Paige for your support and friendship. I have met so many great people during my time here that I would need more space to list them all. They know who they are and know that I am truly grateful for having them in my life.

Lastly, I would like to thank my family for their love and support. I cannot imagine life without them and am truly grateful for them.

Table of Contents

List of Tables

List of Figures

List of Appendices

Abstract

Steel braced frame structures are commonly used in regions of high seismicity due to their efficiency in resisting lateral forces. Braced frames derive their lateral resistance through a vertical truss system composed of braces that are expected to yield in tension and buckle in compression to dissipate energy induced by severe earthquakes. The braces undergo substantial plastic deformations to allow for surrounding members to respond elastically. However, the performance of braced frames can become severely compromised due to local buckling of the braces and damage associated with inelastic behavior. While hollow structural sections (HSS) are traditionally the preferred type of steel brace, their ability to resist lateral forces quickly degrades after local buckling initiation. This degradation can lead to premature brace fracture and a concentration of structural damage due to large story drifts. To enhance the resilience of steel braced frame systems subject to earthquake loads, non-traditional civil engineering materials are investigated for seismic void fill applications. Transverse plate to HSS column connections are also examined because the inherent void of the HSS column is ideal for the incorporation of fill materials in braced frame systems.

An experimental and robust finite element study is undertaken to investigate circular hollow section (CHS) brace performance under large cyclic loads considering a lightweight, expanding, and high-damping polyurethane foam employed in the void of the CHS. The foam fill is shown to reduce the severity and impede the onset of local buckling at the mid-length of the braces, leading to enhanced ductility and energy dissipation capacity. Moreover, the results show that braces with larger diameter-to-thickness ratios can be employed when using the foam fill, leading to an increase in design flexibility and cost savings associated with using less steel.

Building on the concept of utilizing the inherent void of HSS, the mechanical behavior of three non-traditional civil engineering materials, a polyester resin compound, carbon foam, and polycarbonate honeycomb, are systematically characterized to assess their viability for seismic void fill applications. Specifically, the materials are tested under monotonic and cyclic loads at

quasi-static loading rates and quantities such as energy dissipation capacity, secant stiffness and yield strength are obtained to quantitatively assess their performance. Data necessary for calibrating high-fidelity finite element models of these materials are generated and a better understanding of how these materials will perform under loads that a structure would be expected to experience during an earthquake is obtained. Moreover, valuable insight is gained on how to optimize the use of these materials for seismic void fill applications.

Further improvement to braced frame systems is investigated through experimental testing and complementary numerical analyses of transverse plate to rectangular hollow section (RHS) connections, which are typically preferred over longitudinal plate to RHS connections because of their greater stiffness and strength. Findings from this investigation suggest that the design equations' limits of validity can be extended, leading to greater design flexibility. The results also provide a better understanding of how connection geometry influences the connection behavior.

Ultimately, the findings from this work permit a more efficient use of steel and allow for stringent performance-based structural response demands to be met for new and existing (retrofit) braced frame structures. This research also provides a foundation for the incorporation of new materials in the design of resilient structures subject to earthquake loads.

Chapter 1 Introduction

1.1 Motivation

The development of supplemental energy dissipation devices to mitigate and control the wind and seismic response of built infrastructure has been a focus of the civil engineering community for many years (Kareem et al. 1999; Symans et al. 2008). Such devices can be broadly classified according to their energy dissipation mechanism as passive, active, or semi-active. Passive energy dissipation devices, which do not require an external power source and instead utilize the motion of the structure to function, are commonly employed to reduce the inelastic demand on the framing system of a structure subjected to earthquake excitation. Specifically, these energy dissipation devices divert seismic input energy away from the structural system, subsequently reducing damage to the framing system (Constantinou and Symans 1993). In addition, passive auxiliary devices such as tuned mass dampers (TMD) and tuned liquid dampers (TLD) have been successfully applied to structures to mitigate motion from both wind and seismic loads (Kareem et al. 1999). Active control systems employ control algorithms to send signals to force delivery devices to attenuate vibrations and provide improved structural behavior. Although these systems usually require large external power sources and are expensive to implement, they are relatively popular in Japan with nearly 70 structures designed with active or semi-active control systems since 1989 (Ikeda 2009). Semi-active control systems are extensions of passive control systems but differ in that they typically require a small external power source to alter or control the properties of the underlying passive device. Combinations of the three aforementioned control systems, or hybrid systems, are used to alleviate the disadvantages associated with the use of a single system, with the aim of achieving improved structural performance (Fisco and Adeli 2011).

Although each of the control systems mentioned above are effective at providing improved structural performance under cyclic loading scenarios, they induce architectural restraints due to space limitations and require additional detailing and installation that can complicate construction and increase associated costs. Additionally, one of the greatest impediments to widespread

implementation of active and semi-active control strategies is the unavoidable reliance on an external power source calling into question their reliability during an extreme loading event. With the development of improved structural materials and growth of burgeoning technologies that allow for efficient commercial manufacturing, the use of non-traditional civil engineering materials within the void of hollow steel sections provides a unique opportunity to seamlessly integrate supplemental energy dissipation into the design process. Specifically, lightweight, high energy dissipating materials and aluminum foams have shown promise for void fill applications in civil engineering for motion control against seismic loads (Tu and Wang 2010). In addition to providing enhanced energy dissipation, a polyurethane foam with a density of 256 kg/m^3 has shown the ability to postpone and mitigate local buckling when employed within hollow structural sections (HSS) under three and four-point bending (Wei 2017). The mitigation of local buckling further allows more slender and economical sections to be used in extreme load mitigation scenarios.

Steel concentrically braced frames are efficient at resisting lateral loads induced by wind or earthquake loading, but have exhibited susceptibility to developing weak-story behavior during severe earthquake shaking leading to a concentration of structural and/or nonstructural damage (Hines et al. 2009; Lai et al. 2010; Simpson and Mahin 2017). This weak-story behavior results from the reduced strength and stiffness in the story relative to that of other stories, which can occur due to deterioration of brace compressive strength after global buckling. The concentration of damage that occurs in the weak story places greater inelastic deformation demands on the braces, which leads to severe local buckling followed by premature brace fracture (Figure 1-1).

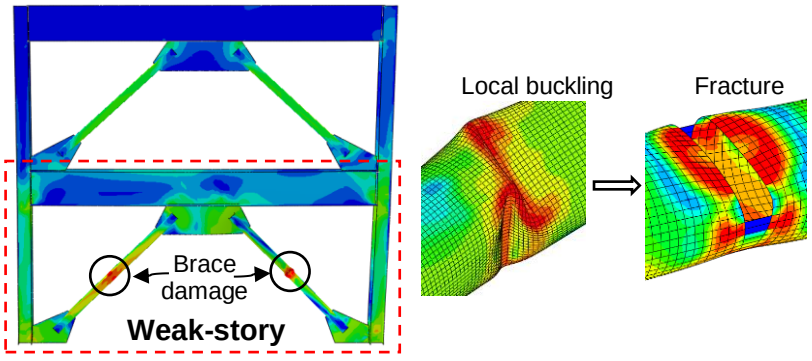

Figure 1-1 Braced frame deficiencies under seismic loads

To improve the performance of steel braced frame systems under seismic loads, the performance of different non-traditional civil engineering materials that can be used as fill in HSS braces needs to be considered under loads typically induced by earthquakes. Understanding the behavior of a variety of non-traditional materials under large cyclic loads will allow for the appropriate selection of material for fill applications in braces of steel braced frame systems. The ability of a non-traditional civil engineering fill material that is lightweight and has a high energy dissipation capacity can then be evaluated through member level studies to quantify the advantages of its use regarding both local buckling prevention and increased energy dissipation capacity. Further improvements to steel braced frames also can be considered through evaluation of transverse plate to HSS column connections.

1.2 Project Objectives

The overarching goal of this project is to improve the seismic performance of steel braced frame systems by incorporating lightweight, high energy dissipating materials in the void of HSS braces and evaluate transverse plate to HSS column connections to potentially increase their use in braced frames and other steel systems.

The goal of this project is accomplished through the following objectives:

1. Characterize the mechanical behavior of non-traditional civil engineering fill materials for use in void fill applications for steel braces in braced frame structural systems subjected to earthquake loads.

2. Characterize the behavior of filled circular hollow section (CHS) steel braces under representative seismic loading and quantify the influence that filling the braces has on overall performance.

3. Determine what CHS sizes benefit most from the inclusion of a fill material and whether the diameter-to-thickness (D/t) limits specified in the American Institute of Steel Construction (AISC) Seismic Provisions for Structural Steel Buildings (AISC 2016a) can be relaxed when considering the inclusion of fill for braced frame design.

4. Assess the adequacy of the limits of applicability for the limit state equations provided in the AISC Specification for Structural Steel Buildings (AISC 2010) and CIDECT Design Guide 3 (Packer et al. 2009) for the design of transverse plate to HSS connections in X or T configurations and determine the effectiveness of the AISC equations at predicting the strength of these connections under plate tensile load.

These objectives are accomplished through corresponding tasks summarized in Figure 1-2:

Task 1 – **Mechanical Characterization of Non-Traditional Civil Engineering Materials**: The behavior of various lightweight, high energy dissipating materials is characterized to determine those most suitable for civil engineering void fill applications. While the behavior of a lightweight polyurethane foam has shown great promise for void fill applications (Wei 2017) and is subsequently used as the fill material in Tasks 2 and 3, there are alternative materials that potentially offer greater improvements to steel brace performance when employed as infill. As such, the behavior of a polycarbonate honeycomb, pourable polyester resin compound, and a polyvinyl chloride (PVC) carbon foam are characterized under different loading rates for monotonic and cyclic loading using a uniaxial hydraulic load frame. Each material's suitability as infill for seismic applications is assessed based on its performance under cyclic and monotonic loading.

Task 2 – Experimental Assessment of Foam-Filled Brace Behavior: The behavior of foam-filled CHS steel braces is evaluated through full-scale brace member tests. To provide a baseline of CHS brace behavior, empty braces are tested and their performance is compared to that of equal size foam-filled braces. To quantify the influence of the foam fill on the performance of CHS braces under large cyclic loads, extensive analyses are performed considering the strain distribution, hysteretic behavior, energy dissipation, and post-buckling compressive resistances of the braces. To further characterize the behavior, local and global buckling mechanisms are observed throughout the loading protocol.

Task 3 – Steel Brace Finite Element Parametric Study: The experimental data from Task 2 is used to calibrate and validate high fidelity finite element models of steel braces with and without fill. These models are used in a subsequent parametric study to consider the influence of different D/t and slenderness ratios (KL/r) on foam-filled brace behavior. The models are able to accurately

simulate the interaction between the foam and steel while also capturing local and global behaviors. This extensive parametric study is undertaken to generate a more robust dataset that complements the experimental dataset with the intent of gaining a better understanding of how the foam fill influences brace performance when considering a wide range of brace geometries.

Task 4 – **Assessment of Transverse Plate to RHS Connections**: To effectively utilize non-traditional civil engineering materials for void fill applications to mitigate structural response from seismic loads in braced frame systems, it is essential to be able to employ HSS, which have an inherent void that is ideal for the incorporation of fill materials. To this end, the governing limit state and corresponding capacity of transverse plate to RHS connections are identified through experimental testing and a detailed finite element study. Specifically, strain gauge data and displacement data from an infrared optical tracking system are used to quantify the non-uniform stress distribution in welded transverse plate to HSS connections and correctly identify their limit states. Local plate yielding, shear yielding (punching) of the chord, chord face plastification and combinations thereof are considered as potential limit states. The finite element model is calibrated and validated with results from the experimental tests. A subsequent parametric study that considers parameters such as chord wall thickness, branch plate thickness, chord slenderness ratio (2γ), and nominal width ratio (β), is undertaken to explore their influence on the limit state and capacity of the connection, particularly when the latter two parameters are outside of the limits of validity specified by AISC and CIDECT.

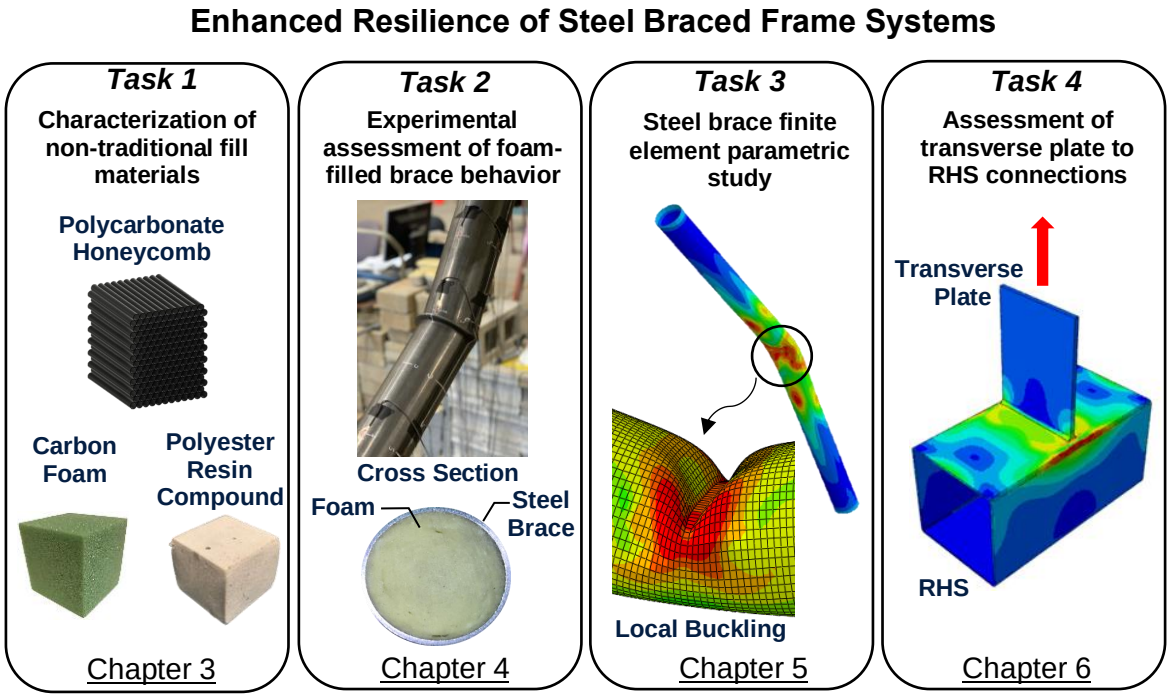

Figure 1-2 Schematic summary of research tasks

1.3 Dissertation Outline

This dissertation is organized into the following chapters:

Chapter 1: The current chapter provides the motivation behind this research and the required tasks needed to accomplish the research objectives.

Chapter 2: A brief discussion about HSS is presented, followed by an overview of studies that show the viability of non-traditional materials for civil engineering void fill applications. Past studies on HSS braces employed in the context of seismic design are also presented.

Chapter 3: This chapter presents results from material characterization tests of three lightweight, commercially produced materials and studies whether these materials are suitable for seismic void fill applications. In evaluating the potential of each material, emphasis is placed on energy dissipation capacity and performance under cyclic loads. The mechanical properties of each material are compared to each other and a previously studied polyurethane foam to determine which material is most suitable for the void fill application.

Chapter 4: This chapter presents results from twelve large-scale tests of steel CHS braces subjected to large cyclic loads. The influence of filling the braces with a lightweight polyurethane foam is examined. Furthermore, the suitability of the foam fill for retrofit applications is investigated. The experimental results are presented in the context of diameter-to-thickness ratio and slenderness ratio, as these geometric quantities have been shown to be highly influential on brace performance.

Chapter 5: A comprehensive parametric study is undertaken using experimental data from Chapter 4 to calibrate and validate a high-fidelity finite element model for empty and foam filled braces. A variety of diameter-to-thickness and slenderness ratios are examined to provide insight into their influence on brace performance. Focus is placed on assessing which section sizes benefit the most from the inclusion of the foam fill regarding ductility and energy dissipation capacity.

Chapter 6: Results from an experimental program and a companion finite element investigation of transverse plate to RHS connections under monotonic plate tension are presented. Connection capacity determined from the experimental tests and finite element study are compared to code predictions to assess how accurate the code predicted strengths are, particularly when the connections have geometric parameters that fall outside of the limits of validity.

Chapter 7: This chapter summarizes the presented research and provides conclusions based on the results of the four main content chapters. Contributions to scholarship and recommendations for future research are also provided.

Chapter 2 Literature Review

2.1 HSS Background

Hollow structural sections (HSS) are closed hollow steel sections that are commonly used as structural elements in bridges, buildings and various other built infrastructure (Figure 2-1). They typically have square (SHS), rectangular (RHS) or circular (CHS) cross sections; however, oval or elliptical hollow sections (EHS) have become increasingly popular over the past few decades due to their aesthetic appeal and differences in bending behavior about their principal axes (Chan and Gardener 2008). HSS are produced through cold forming or hot rolling with each process offering distinct advantages and disadvantages. Cold formed sections offer higher yield strengths at the corner regions but suffer from a lack of ductility in this area due to the cold forming process (Packer 1993). Hot formed or hot finished sections can be used to alleviate this shortcoming, but their availability is limited, particularly in the United States, and they are typically prohibitively expensive (Packer et al. 2010a).

(a) (b)

Figure 2-1 HSS used for a (a) retractable stadium roof (Docklands Stadium) and a (b) railway station roof (Southern Cross) in Melbourne, Australia

HSS manufactured in the United States are typically cold formed using ASTM (American Society for Testing and Materials) A500 grade steel. The preferred steel material specification stipulated

by the American Institute of Steel Construction (AISC) for round HSS, developed through consultation with fabricators based on availability, price and ease of delivery, is ASTM A500 Grade C (AISC 2016b). AISC has recently adopted a new HSS specification, ASTM A1085, with the intent of enhancing HSS performance under cyclic loads. This specification has a more stringent tolerance on wall thickness that allows for the removal of the 0.93 reduction factor on the nominal wall thickness for HSS made of ASTM A500 grade steel. This reduction is used when calculating member strength and it accounts for the fact that manufacturers tend to produce HSS with wall thicknesses closer to the lower bound of the dimensional tolerance. The more stringent tolerance on wall thickness offered by ASTM A1085 grade steel allows for the full nominal wall thickness to be used in design with HSS. Additionally, its tighter mass tolerance, minimum Charpy V-notch toughness requirement, and reduced variability in expected yield strength make it more amenable for seismic applications (AISC 2016a).

The ubiquity of HSS for structural applications is unsurprising given their many advantageous properties. HSS are excellent at resisting torsion due to the distribution of cross-sectional area about their polar axis, have a high strength-to-weight ratio, can have equal biaxial strength depending on the cross-section shape, and are visually appealing due to their smooth edges. The high strength-to-weight ratio can lead to cost savings associated with a reduction in member size and thus member weight. Equal bending strength and torsional strength for bending about multiple axes are particularly useful for column applications where columns may be subjected to flexure about both axes and accidental torsion. The excellent torsional resistance also reduces the need for lateral bracing. Furthermore, the inherent void in HSS provides a unique opportunity for filling this void with non-traditional materials that can potentially combine the advantageous properties of HSS with that of lightweight and high energy dissipating materials to enhance their overall behavior and limit local buckling.

To date, there are many authoritative resources that provide design guidance for HSS connections. Specifically, the AISC has produced Hollow Structural Section Connections Design Guide 24 (Packer et al. 2010b), which serves as a supplemental document to the AISC Steel Construction Manual (AISC 2017). While not comprehensive, the scope of this design guide includes welding considerations for HSS connections, guidance on HSS-to-HSS moment and truss connections, and guidance on simple shear connections to HSS columns. Additionally, CIDECT has disseminated

design guides that encompass a range of topics and form the basis of many modern design standards dealing with HSS (Wardenier et al. 2008; Packer et al. 2009; Kurobane et al. 2004). Both AISC and CIDECT provide guidance on the design of transverse plate to HSS connections; however, they are not consistent in regard to the equations used to predict the connection design capacity and subsequent limit states. This discrepancy, coupled with recent changes in the AISC Specification Chapter K (AISC 2016b), have provided impetus for further exploration of the behavior of this connection.

2.2 Non-Traditional Civil Engineering Materials

Non-traditional civil engineering materials such as polymer foams and honeycomb materials are typically characterized by a lightweight and high energy absorption capacity making them ideal for implementation as void fill for seismic applications. Such materials have been investigated frequently for crashworthiness and aerospace applications; however, comparatively less studies have characterized their behavior under large cyclic loads, such as those produced by earthquakes. The following sections highlight studies that have examined non-traditional civil engineering materials with emphasis placed on their beneficial properties in the context of civil infrastructure applications.

2.2.1 Foams

Polymer foams have been widely studied for crashworthiness due to their high strength and stiffness with low weight and high energy dissipation capability. A number of studies have experimentally examined axial crushing of foam filled tubes and have generally shown that the inclusion of foam fill enhances crush strength and increases energy absorption capacity (Lampinen and Jeryan 1982; Reid et al. 1986; Santosa and Wierzbicki 1998). Mirfendereski et al. (2008) created high fidelity finite element models that simulated the crushing behavior of polyurethane foam filled thin walled tubes. Additionally, Meguid et al. (2004) conducted experimental tests and finite element simulations of the crush behavior of PVC foam filled thin walled tubes. This research showed that interaction between the foam and tube enhanced energy absorption. Other studies have shown that metallic foam fill in steel tubes can increase damping levels by as much as five times that of an empty tube under representative earthquake loading (Tu and Wang 2010). More recently, Strano et al. (2015) investigated metallic foam filled tubes subjected to three-point

bending and concluded that friction at the interface between the metallic foam and tube is largely responsible for the high damping and energy absorption that were observed.

Smith et al. (2012) reviewed many applications of steel foam in the automotive, mechanical and aerospace industries, but noted that full-scale civil engineering applications had not yet been demonstrated. An experimental study by Zi et al. (2008) of a glass fiber reinforced polymer (GFRP) bridge deck filled with polyurethane foam showed increases in stiffness and strength by filling the deck voids (Figure 2-2). Steel foam sandwich panels comprised of a steel foam core sandwiched between steel sheets exhibited the potential for strength gains greater than 200% for steel sheets of the same mass (Szyniszewski et al. 2012). These studies suggest steel and metallic foams have potential for structural applications, but do not consider their ability to mitigate local buckling and provide supplemental energy dissipation under seismic and wind loads.

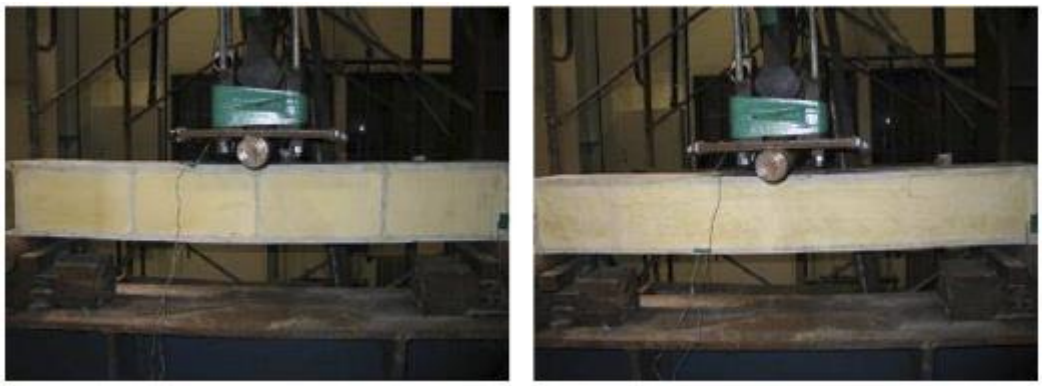

(a) (b)

Figure 2-2 GFRP bridge deck filled with polyurethane foam (a) with and (b) without webs (Zi et al. 2008)

2.2.2 Honeycomb Materials

Materials with a cellular structure have become commonplace in a range of engineering applications due to their lightweight, high strength-to-weight ratio, and energy absorption capability. Cellular materials are often characterized according to whether they have a two-dimensional geometric arrangement of prismatic cells, such as in honeycombs, or a connected network of cells in three dimensions, such as foams (Gibson 1981). The following section will focus on the former with emphasis placed on studies that characterized the mechanical behavior of honeycomb materials and highlighted their application in a variety of industries.

Many studies have examined the strength characteristics and behavior of honeycomb structures and materials through numerical and experimental means. McFarland (1963) analytically examined the crushing behavior of hexagonal cell structures under axial loading to facilitate their design for use as energy absorbers. Wierzbicki (1983) developed an equation for the crush strength of metal honeycombs as a function of cell width, cell wall thickness, and the yield stress of the material. Wu and Jiang (1997) experimentally examined aluminum honeycomb structures under quasi-static and impact loading and concluded that these structures are most effective as energy absorbers when the cell size and core height are small and the honeycomb is made from a high strength material. Similarly, Papka and Kyriakides (1994) experimentally examined the response of hexagonal metallic honeycomb to in-plane compressive loading, but also provided supplementary numerical simulations.

Research to reduce vehicle weight, thus optimizing fuel economy and lowering environmental impact, has been a common thrust in the transportation industry for many years. Driven by the need to reduce weight, while not compromising on the crashworthiness and structural integrity of vehicles in the event of collision, extensive research has been conducted on the use of thin-walled structures for energy absorption (Abramowicz 2003; Olabi et al. 2007; Qi et al. 2012; Tarlochan et al. 2013). The desire to enhance the energy absorption of thin-walled tubes under crush loads while also minimizing mass has led to studies of tubes filled with lightweight and high energy dissipating materials (Santosa and Wierzbicki 1998). Paz et al. (2014) examined square steel hollow tubes filled with a glass-fiber reinforced polyamide honeycomb structure to leverage the inherent lightweight of the honeycomb structure and energy absorption provided by the composite system. Similarly, Liu et al. (2016) examined the crashworthiness characteristics of carbon fiber reinforced plastic (CFRP) square tubes filled with aluminum honeycomb (Figure 2-3) and showed that the honeycomb was able to increase the maximum load under compression and increase absorbed energy by more than 10% when compared to empty CFRP tubes. Additionally, it was found that the combination of the tube and honeycomb fill outperformed the combined effect of the CFRP tube and honeycomb individually in regard to energy absorption, owing to interaction effects between the two materials. This finding suggests that honeycomb material used for void fill applications can provide enhanced energy dissipation and improved performance under cyclic loads.

While honeycomb structures for energy absorption have been ubiquitous in the aerospace and automotive industries, they have found comparatively less use for civil engineering applications. Davalos et al. (2001) experimentally and numerically investigated honeycomb sandwich beams to develop an analytical model for proprietary honeycomb sandwich panels that have found use for highway bridge applications. Jung and Aref (2003) examined the viability of a composite damping system composed of a polymer honeycomb and a solid viscoelastic material. This system was proposed with the intent to provide energy dissipation for infill panels subjected to in-plane shear. It was shown that the combination of both materials increased energy dissipation and shear resistance and performed better in combination as opposed to acting individually.

As can be seen from the literature, there are few studies that have examined honeycomb behavior in the context of civil infrastructure applications. Moreover, there is a lack of data that characterizes the behavior of honeycomb structures under cyclic loading. To assess the viability of honeycomb materials for void fill applications, it is critical to characterize their response under loadings that are representative of what is felt by civil infrastructure subjected to earthquakes and wind events.

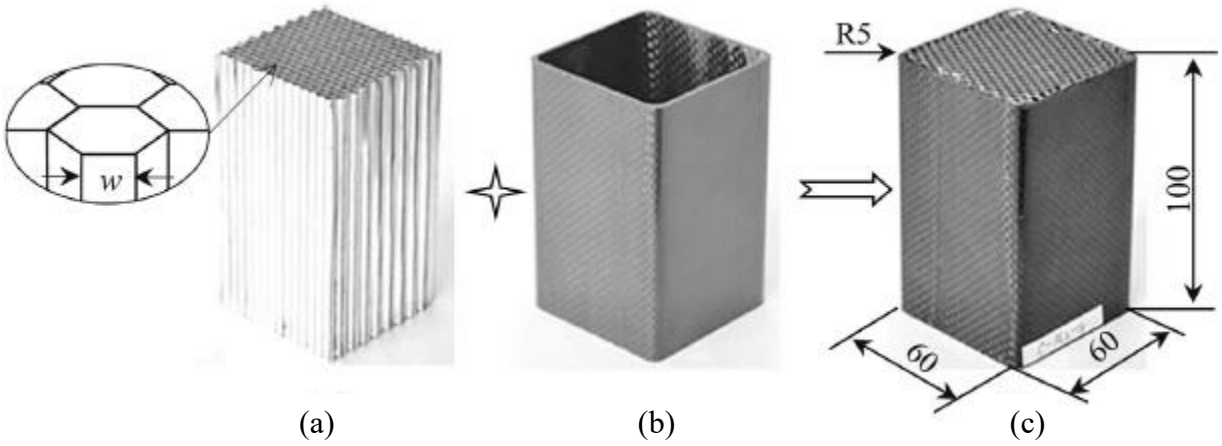

Figure 2-3 (a) Aluminum honeycomb, (b) CFRP tube and (c) CFRP tube (units: mm) filled with aluminum honeycomb (Liu et al. 2016)

2.3 HSS Brace Behavior

In the context of earthquake engineering, braced frame systems offer an efficient way to resist earthquake forces due to their high lateral strength and stiffness. They are particularly well suited for low rise structures in areas of high seismicity, but they are also employed in the core of mid to high rise structures, typically in combination with perimeter moment frames. During severe ground shaking the braces behave as "sacrificial" elements, undergoing large, inelastic deformations to prevent damage elsewhere in the structure.

2.3.1 Seismic

HSS braces are commonly employed in braced frames to dissipate seismic input energy through cycles of tension yielding and compression buckling. Numerous experimental and analytical studies have been conducted to understand the inelastic response of steel bracing members under cyclic loading. Many of these studies focused on rectangular hollow section (RHS) or square hollow section (SHS) braces (Goggins et al. 2005; Goggins et al. 2006; Haddad et al. 2010; Haddad et al. 2011; Han et al. 2007; Nip et al. 2010; Nip et al. 2013; Tremblay et al. 2003). While some studies examined a variety of cross-sectional geometries (Fell et al. 2009; Jain et al. 1980; Popov and Black 1981; Tremblay 2002), other studies solely examined circular hollow section (CHS) braces (Elchalakani et al. 2003; Kumar et al. 2015; Popov et al. 1979). Since loading protocol, material properties, and test configuration influence brace performance, it is generally difficult to establish clear conclusions regarding what factors are most influential on steel brace behavior. However, a study conducted by Tremblay (2002) that examined data from 76 tests on steel braces suggested that fracture of RHS braces is influenced by the slenderness ratio and width-to-thickness ratio of the brace, with the former being more influential. Additionally, it was noted that local buckling was less severe in more slender braces, owing to the fact that slender braces had lower compressive strains induced in the plastic hinge region due to reduced inelastic demand during brace buckling compared to that of less slender braces. Fell et al. (2009) came to similar conclusions, but also observed that RHS braces are more susceptible to local buckling induced fracture than pipe and wide flange sections because of the severe strain gradient that can develop in the corners of RHS braces.

To delay the initiation of local buckling, thus increasing the fracture life of cold formed RHS braces, Liu and Goel (1988) investigated the cyclic behavior of braces filled with concrete. They found that concrete fill is most effective on braces with larger width-thickness ratios and smaller slenderness ratios, as these are the braces that are most susceptible to early local buckling. Similarly, Goggins et al. (2006) noted that the use of concrete fill reduced the severity of local buckling and increased ductility capacity in RHS and SHS braces. The researchers also noted that more improvement was shown in less slender braces with larger width-thickness ratios. A further study on concrete fill in cold formed RHS braces by Zhao et al. (2002) found that better performance was achieved with normal weight concrete as opposed to lightweight concrete, likely resulting from the greater compressive strength of the normal weight concrete being more conducive to inhibiting local buckling. More recently, a study by Sheehan and Chan (2014) indicated that concrete fill is able to increase the number of cycles to failure in CHS braces, thus increasing energy dissipation. Figure 2-4 shows photographs that highlight the improved behavior of a concrete-filled CHS brace relative to that of an empty brace. It should be noted that CHS braces are generally recommended over RHS braces, owing to their uniformity of cross-section making them less susceptible to premature local buckling induced fracture. While these studies provide insight on the expected behavior of void-filled HSS members, the fill material used may not be optimal in seismic applications where increased seismic mass can lead to larger seismic loads. Additionally, the use of concrete fill for retrofit applications poses challenges related to the need for skilled labor, demand of strict quality control, difficulty of placement and long curing time.

Figure 2-4 Photographs of (a) local buckling and (b) fracture for an empty brace at its mid-length compared to deformation and fracture for a concrete-filled brace at its (c) mid-length and (d) end (adapted from Sheehan and Chan 2014)

2.4 Summary

The main objective of this research is to improve the performance of braced frame systems through refining the design of transverse plate to HSS column connections and incorporating lightweight, high energy dissipating materials within the void of HSS braces. The previous sections highlight the feasibility of non-traditional civil engineering materials for use in seismic void fill applications, as they have been successfully adopted for analogous applications in many other engineering domains. While non-traditional civil engineering materials show great promise for mitigating steel braced frame deficiencies through enhancement of local buckling resistance and increases in energy dissipation, ultimately leading to improved brace ductility and enhanced resilience after severe earthquakes, extensive research is necessary before the use of these materials can be realized for large-scale civil infrastructure applications. In parallel, the widespread use of HSS in different steel systems makes it critical to ensure that connections involving HSS have an accurately defined design strength. As such, the behavior of welded transverse plate to HSS connections are investigated with a focus on connections with parameters outside of the limits of validity, which few studies have considered.

.

Chapter 3 Mechanical Characterization of Non-Traditional Civil Engineering Materials

3.1 Introduction

The behavior of structures built from typical civil engineering materials such as steel, concrete, and timber is well characterized, as the majority of infrastructure around the world is built from these materials. While these structures have performed relatively well when subjected to a variety of anthropogenic and natural hazards, opportunities exist to improve their performance through the use of non-traditional civil engineering materials. Specifically, structures employing hollow structural section (HSS) members are ideal for the incorporation of non-traditional materials owing to the inherent internal void in these sections. While honeycomb materials, metal foams, and other lightweight, high-performance materials have been shown to be effective in the automotive, mechanical, and aerospace domains (Chapter 2), their implementation in large-scale civil engineering applications is scarce.

Before the use of non-traditional materials for civil engineering void fill applications can be realized, a thorough understanding of how these materials behave under loadings that are representative of what is expected to be felt by structural members during a large earthquake is necessary. To this end, a comprehensive experimental program that characterizes the mechanical behavior of three commercially produced materials is undertaken. These materials include a pourable polyester resin compound, polyvinyl chloride (PVC) carbon foam, and polycarbonate honeycomb. Each material is tested at different loading rates under monotonic and cyclic compression. A polyurethane foam has also been considered through prior studies (Wei 2017).

This chapter presents the findings from the experimental study of the three considered non-traditional civil engineering materials with an emphasis on each material's energy dissipation capacity, stiffness, sensitivity to loading rate and potential for improving the local buckling resistance of thin-walled sections. Data generated from this study is necessary for calibrating constitutive models for use in high-fidelity finite element simulations, which in conjunction with member tests can be used to determine section sizes and materials that are most effective for the

intended application. Furthermore, the results provide insight on how to best utilize these materials for optimal performance when used in an internal void fill application for seismic resistant applications.

3.2 Materials

3.2.1 Polyester Resin Compound

The first non-traditional civil engineering material considered is a pourable polyester resin compound. This compound is commercially produced by Carbon-Core Corp., which is a material manufacturer headquartered in Troy, Virginia (USA). It is specifically advertised as a compound to fill or repair a transom. A transom is the vertical section at the rear of a boat that supports the boat's engine(s). Carbon-Core also notes that the compound can be used as a general-purpose void filler and for structural applications where a high compressive strength is necessary. This particular material is selected as a potential void fill material because of its excellent compressive strength and stiffness; its pourable nature, which makes it promising for easily filling a void; and its lightweight.

Five main components make up the compound with weight percentages of each component provided by the manufacturer. The components and corresponding range of weight percentage are listed in Table 3-1 (Carbon-Core 2020). Each of these components have been used in concrete (Chen and Liu 2004; Tsivilis 2003; Marikunte et al. 1997), suggesting that the compound may exhibit similar behavior to concrete under monotonic and cyclic compression loads.

Table 3-1 Composition of the compound (Carbon-Core 2020)

Component	Percentage (%)
Styrene	25 - 29
Limestone	16 - 20
Talc	1 - 5
Fumed silica	1 - 5
Fibrous glass	1 - 5

In its initial state the fill material is a gray viscous liquid. To form the compound, a liquid catalyst of methyl ethyl ketone peroxide (MEKP) is mixed with the fill material at a designated proportion based on the material temperature and the total quantity of material required. A total of 18.9 L of

compound is used to create the specimens for mechanical testing, requiring 311 ml of the catalyst. Mixing is performed using a 127 mm wide chrome-plated steel mixing blade with a 9.5 mm shaft diameter that is connected to a high speed drill (Figure 3-1a). After thoroughly mixing for five minutes, the compound is poured into 406 mm × 210 mm × 76 mm five-sided prismatic rectangular steel molds to cure (Figure 3-1b). After 48 hours the compound is cut into cube specimens with edge lengths of 50.8 mm (Figure 3-1c). The average density of two randomly selected cut specimens is 1040 kg/m^3, which is approximately 2.3 times smaller than that of normal weight concrete (2400 kg/m^3).

(a) (b) (c)

Figure 3-1 Photographs of (a) mixing of the polyester resin compound, (b) the compound curing in a steel mold and (c) cube specimens for testing

3.2.2 PVC Carbon Foam

The PVC carbon foam is a lightweight, closed-cell foam that is manufactured by Carbon-Core, the same company that produced the polyester resin. It has a reported density of 64 kg/m^3 and compressive and tensile strengths of 1 MPa and 2.2 MPa, respectively. This material is selected as a potential void fill material due to its low friability, which is the propensity to resist fragmenting into smaller pieces when stressed. Because the ability of the foam to mitigate local buckling of the surrounding steel and provide enhanced energy dissipation is reliant on maintaining contact between the steel and fill, the low friability of the foam is critical to maximizing its effectiveness. All tested specimens have a cube geometry with an edge length of 50.8 mm and are cut from a 1.2 × 2.4 m carbon foam sheet with a 50.8 mm thickness. A photograph of a typical specimen is provided in Figure 3-2.

Figure 3-2 Typical carbon foam specimen

3.2.3 Polycarbonate Honeycomb

The final tested material is a hexagonally packed circular cell polymeric (polycarbonate) honeycomb material manufactured by Plascore Inc. (Zeeland, MI, USA). The cells of the honeycomb have a diameter of 3.2 mm and an average measured wall thickness of 0.13 mm (130 μm). The manufacturer reported density is 80.1 kg/m^3. This material is selected as a potential fill material due to its lightweight and high strength to weight ratio, making it favorable for seismic applications. Furthermore, circular cell honeycombs have been shown to be more efficient than hexagonal cell honeycombs with the same relative density owing to greater stiffness and crush strength in the in-plane directions (Lin et al. 2012). A previous investigation by Papka and Kyriakides (1998) thoroughly characterized the in-plane compressive behavior of a polycarbonate honeycomb that was manufactured by Plascore. They found that the elastic response of the honeycomb was independent of loading rate, whereas plateau stresses increased with loading rate. The honeycomb that their study considered had a cell diameter of 6.96 mm and an average wall thickness of 144 μm, both of which are larger than the honeycomb considered in this study. Furthermore, the honeycomb specimens in their study were subjected to monotonic loads as opposed to cyclic loads.

The tested specimens are fabricated from a 1.2 × 2.4 m sheet with a 50.8 mm thickness. The thickness is parallel to the out-of-plane direction, which corresponds to the axial direction of the individual tubes that make up the honeycomb (1 direction based on Figure 3-3a). To assess the sensitivity of the measured response to specimen size, three different specimen sizes are considered: 50.8 × 31.8 mm, 50.8 × 63.5 mm, and 50.8 × 95.3 mm, where the first dimension

corresponds to the specimen height (2 direction) and the second dimension corresponds to the specimen width (3 direction), as shown in Figure 3-3. The thickness of all specimens (1 direction) is 50.8 mm. As the strength and stiffness of the honeycomb are influenced by the loading direction, the honeycomb is tested in orthogonal directions. Specifically, axial compression is applied in the out-of-plane (1) and in-plane (2) directions defined by the schematic shown in Figure 3-3a. A photograph of a 50.8 × 95.3 mm specimen is shown in Figure 3-3b.

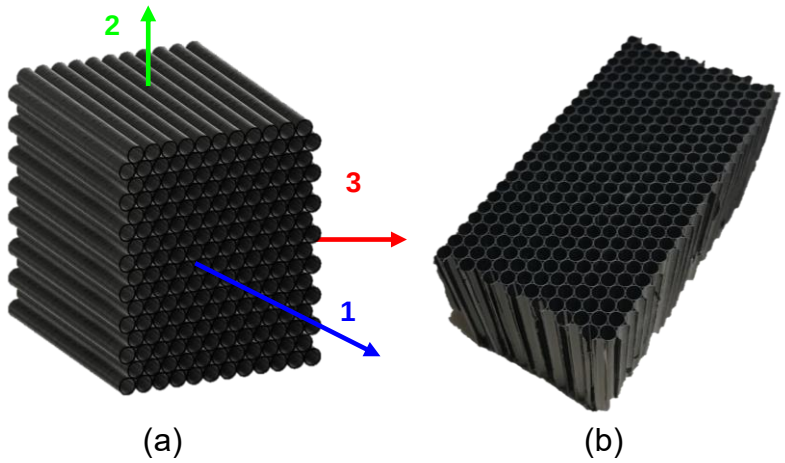

Figure 3-3 A (a) schematic defining the out-of-plane (1) and in-plane (2) loading directions for the honeycomb specimens and (b) a photograph of a typical 50.8 × 95.3 mm specimen

3.3 Test Setup and Loading Protocol

Testing for all three materials is conducted using either an 810 Material Test System (MTS) with a 100 kN force capacity (Figure 3-4a) or an Instron (Model 1336) uniaxial load frame (Figure 3-4b) with a 2200 kN force capacity. The high strength of the polyester resin compound necessitates the use of a testing apparatus with a force capacity greater than 100 kN. Specimens are centered between parallel loading platens that apply uniform compressive load to the top and bottom of the specimens while the sides remain unrestrained. The load is applied in displacement control by an actuator and force is measured using a load cell attached to the actuator. Stress is calculated as the uniaxial force measured by the load cell divided by the average measured area of the cross-section of the specimen. Strain is calculated as the distance traveled by the loading platen divided by the original height of the specimen parallel to the loading direction.

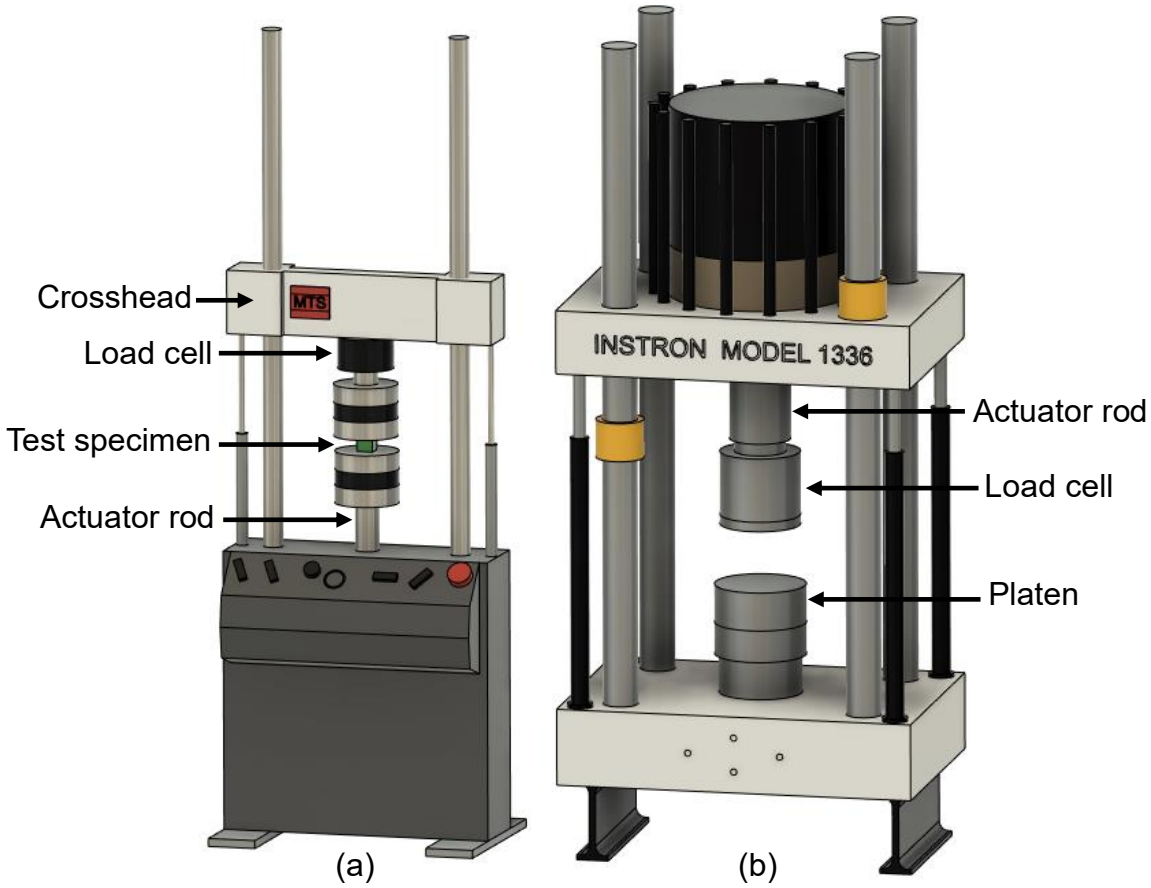

Figure 3-4 The (a) 810 MTS and (b) Instron machine (Model 1336) test setups

For the monotonic compression tests, load is applied until the platen attached to the actuator displaces to at least 70% of the original specimen height (70% strain). This level of strain ensures that material response enters into the densification regime, which is where the compressive resistance of a cellular solid begins to rapidly increase due to cell wall interactions (Li et al. 2006). The monotonic compression tests provide important material properties such as Young's modulus and yield strength, which are necessary for constitutive model calibration and for comparisons of the property variations for a given material and between different materials. For the cyclic compression tests, the loading protocol consists of a total of 12 cycles of compression – two cycles each to strains of 10%, 20%, 30%, and 40%, followed by four cycles to 50% strain (Figure 3-5). Given the cyclic nature of loadings induced by earthquake ground motions, this loading protocol is considered appropriate and represents a typical loading associated with a far field type motion.

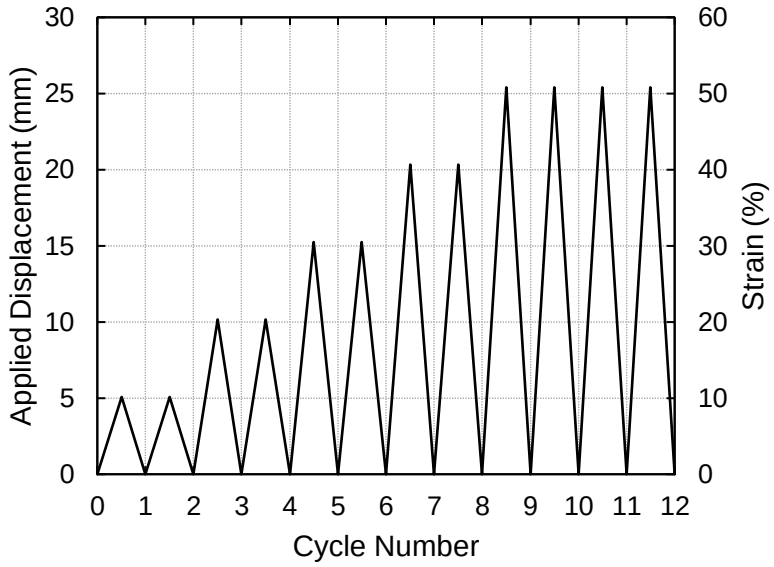

Figure 3-5 Loading protocol for cyclic compression tests

Since loading rates experienced by steel frame structures during an earthquake can vary, three different loading rates are considered: 0.25 mm/s, 2.5 mm/s, and 25.4 mm/s. These loading rates correspond to strain rates of 0.005 s^{-1}, 0.05 s^{-1}, and 0.5 s^{-1}, respectively, and are chosen because they encompass a range of strain rates that a steel frame structure can be expected to experience during an earthquake (Chang and Lee 1987). This set of tests allows for the determination of mechanical properties under different strain rates to gain a better understanding of how to optimize their use.

3.4 Results and Discussion

The results are presented separately for each material and include a discussion of their monotonic and cyclic behavior. Emphasis is placed on the cyclic load behavior, since the cyclic properties of the considered materials are critical for evaluating their potential for seismic void fill applications.

3.4.1 Polyester Resin Compound

Three specimens are tested under monotonic and cyclic compression at each loading rate for a total of 18 tests. Two duplicate specimens for each loading rate are tested to ensure that reliable mechanical properties are obtained. Figure 3-6 shows monotonic compression responses of three pourable polyester resin specimens tested at a loading rate of 0.25 mm/s. The response is characterized by three distinct regions of behavior that also have been shown to occur in metal

foams (Vendra and Rabiei 2007). The first region consists of linear behavior until approximately 3% strain with an average elastic modulus of 726 MPa (105 ksi). This elastic modulus is nearly 30 times smaller than that of concrete with a 28-day compressive strength of 21 MPa (3000 psi). The average yield strength calculated based on the 0.2% offset method is 17.9 MPa (2.60 ksi). The second region consists of a plateau where the stress remains fairly constant and extends until approximately 50% strain. During the plateau region the specimens expand perpendicular to the loading direction. The third region is characterized by densification, which consists of a steep rise in stress as the specimens begin to consolidate at approximately 50% strain. On average, the maximum stress achieved at 70% strain is approximately 121 MPa (17.5 ksi). Figure 3-7a shows the typical failure mode of a specimen after it has deformed to 70% of its initial height. The failure mode is similar to that of the specimens subjected to cyclic compression, with the damage being slightly less pronounced (Figure 3-7b).

Figure 3-8 shows the cyclic compression response of three specimens tested at a loading rate of 0.25 mm/s. The average initial elastic modulus is approximately 675 MPa (97.9 ksi), which is approximately 7% less than that of the monotonic tests. In general, the hysteresis loops at the end of the first cycle to a given strain level are much larger than those for the second cycle to the same strain level indicating substantial degradation in dissipated energy, where dissipated energy is the total area enclosed by the force-deformation curve. For example, the dissipated energy during the second cycle to 10% strain is on average 3.1 times smaller than that of the first cycle to 10% strain. However, the difference in dissipated energy gradually decreases as larger strains are reached, with the dissipated energy during the second cycle to 50% strain being on average two times smaller than that of the first cycle to 50% strain. This reduction in dissipated energy between cycles can be attributed to residual deformation that exists after the first cycle of loading. Additionally, there is a minimal reduction in maximum stress and dissipated energy from the third to fourth cycles to 50% strain compared to the first and second cycles to 50% strain. There is a 23% and 51% reduction in average maximum stress and average dissipated energy from the first to second cycle to 50% strain, respectively. The average maximum stress attained during the third cycle to 50% strain is 19.9 MPa (2.89 ksi) compared to 18.0 MPa (2.61 ksi) for the fourth cycle to 50% strain, which equates to a 9.5% reduction. Similarly, the average dissipated energy during the third and fourth cycles to 50% strain is 165 kN-mm and 138 kN-mm, respectively, which equates to a 16.4% reduction in dissipated energy. These minimal reductions in maximum stress and dissipated energy

can be attributed to the crushing failure mode shown in Figure 3-7b being fully developed at the conclusion of the second cycle to 50% strain, causing these quantities to nearly plateau during later cycles. The plateauing of the maximum stresses and dissipated energy after the first cycle to 50% strain suggests that the compound would not be effective at providing added energy dissipation or local buckling resistance under large, constant amplitude strains. The cracking pattern exhibited by the compound resembles the geometry of an hourglass and has also been shown to occur during compression tests of concrete cube specimens (Bezerra et al. 2016). Furthermore, the cracks are oriented at approximately 45° to the load direction, indicating the presence of large shear stresses.

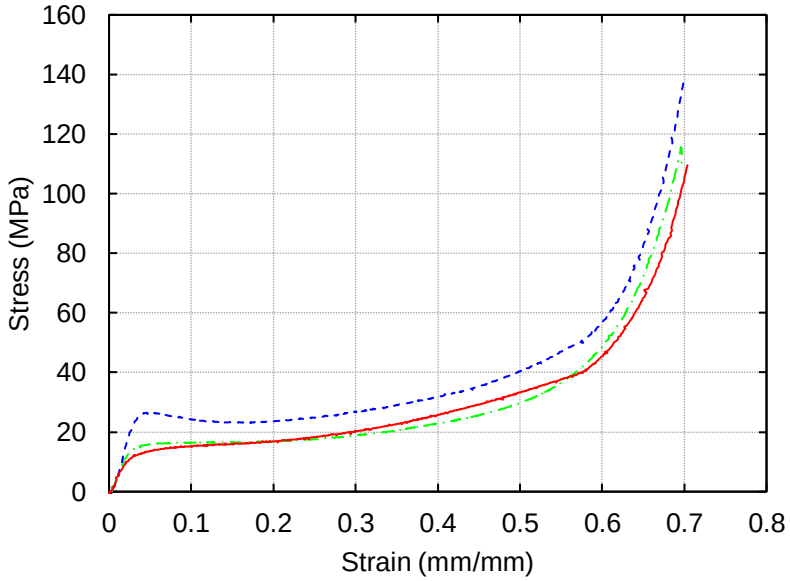

Figure 3-6 Monotonic compression response for three specimens at a loading rate of 0.25 mm/s

(a) (b)

Figure 3-7 Typical specimen failures for (a) monotonic and (b) cyclic compression

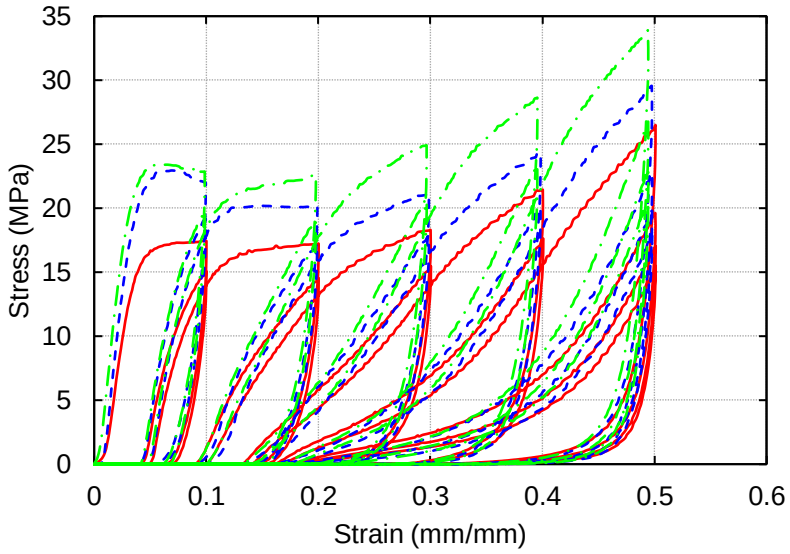

Figure 3-8 Cyclic compression response for three specimens at a load rate of 0.25 mm/s

One of the most important findings that highlights the potential effectiveness of this compound for void fill applications is its ability to recover large deformations. The ability of fill material to provide enhanced energy dissipation capacity and resistance to local buckling is largely reliant on the ability of the fill material to maintain contact with the surrounding steel. As such, the height of the specimens (parallel to the loading direction) is measured after testing using a digital caliper. For the specimens tested under cyclic compression at 0.25 mm/s, the average height immediately after testing is 40.7 mm. Given an initial nominal height of 50.8 mm and cycling to 50% strain, the specimens recover approximately 60% of the applied deformation. The ability of the compound to recover deformation suggests that it would not need to be replaced after minor to moderate

earthquakes because it could recover the deformation, allowing it to maintain contact with the surrounding steel and restrain further localized deformation of the cross-section.

Given the variability in strain rates that can be induced on a structural system when subjected to forces induced by earthquakes, it is important to quantify the mechanical behavior of each potential void fill material at different loading rates. Figure 3-9 and Figure 3-10 show the sensitivity of the mechanical properties of the compound to loading rate when subject to cyclic compression. Specifically, the average maximum stress reached during the first cycle to a particular strain level increases with an increase in loading rate with the largest difference occurring between loading rates of 2.5 mm/s and 25 mm/s (Figure 3-9). With the exception of the specimens loaded at 25 mm/s, the maximum stress is reached during the first cycle to 50% strain. The ability to exhibit increased strength with continued cycling is favorable for seismic applications as stable energy dissipation is largely reliant on the ability to resist strength degradation. The increase in strength with loading rate is not surprising considering that the composition of the compound is similar to that of concrete, which has shown increased compressive strength and stiffness as strain rate increases (Fu et al. 1991). Similarly, the average dissipated energy per cycle increases with an increase in loading rate (Figure 3-10). This increase in dissipated energy can be attributed to the increase in capacity at increasing strain levels under increasing loading rate.

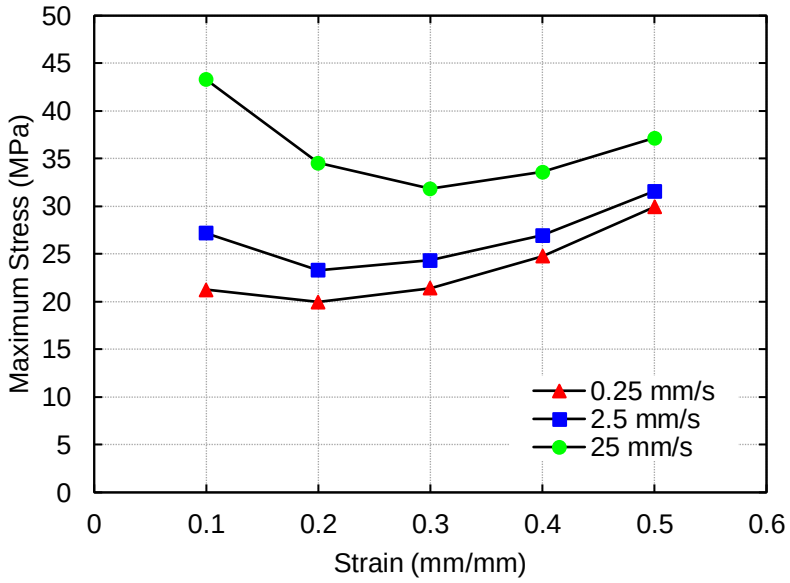

Figure 3-9 Average maximum stress under cyclic loading during the first cycle to a given strain level for three different loading rates

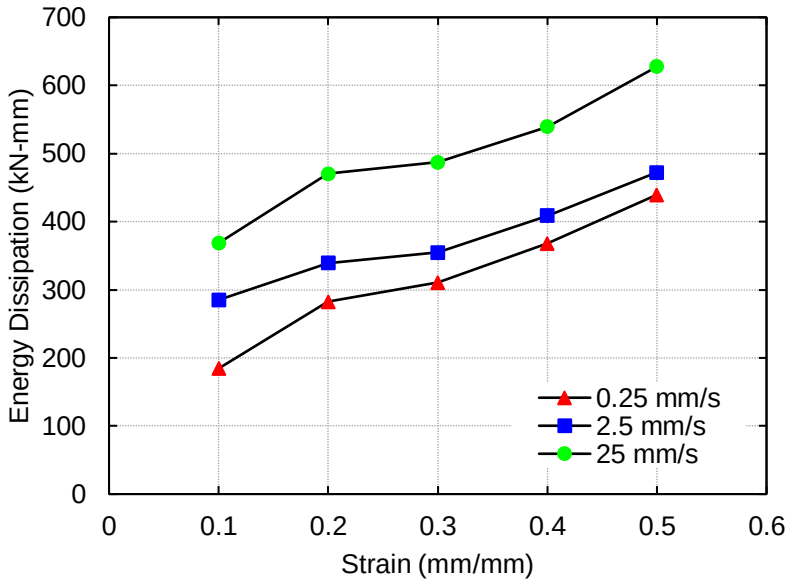

Figure 3-10 Average energy dissipation under cyclic loading during the first cycle to a given strain level for three different loading rates

3.4.2 PVC Carbon Foam

Three specimens are tested under monotonic and cyclic compression at each loading rate for a total of 18 tests. Representative stress-strain responses for monotonic and cyclic loading at the three different loading rates are shown in Figure 3-11 and Figure 3-12, respectively. The results indicate that loading rate has a negligible effect on material response and that specimen response is highly repeatable.

The behavior of the carbon foam under monotonic compression is characterized by three distinct regions: a linear-elastic region, a stress plateau with near zero stiffness, and a region with a sharp increase in stress. As seen in Figure 3-11, stress initially linearly increases until approximately 3% strain with an average elastic modulus of 33.9 MPa (4.92 ksi). A sharp stress plateau occurs soon after with an average compressive yield strength of 725 kPa (105 psi). This stress plateau is maintained until an approximate strain of 60% at which point there is a sudden rise in stress as the cells of the foam crush and begin to consolidate. The average maximum stress achieved is 1630 kPa (236 psi) at an average of 77% strain.

Referring to the specimen subjected to cyclic compression at a loading rate of 25 mm/s (Figure 3-12), the initial behavior is linear with an elastic modulus of 18.5 MPa (2.68 ksi), which is 45%

smaller than the average elastic modulus from the monotonic specimen responses shown in Figure 3-11. The peak stress achieved over the complete loading history is 679 kPa (98.5 psi) and occurs at 6% strain during the first cycle to 10% strain. In comparison, the specimen tested under monotonic compression at a rate of 25.4 mm/s achieves a stress of 772 kPa (112 psi) at the same strain level. The peak stress during the second cycle to a given strain level is on average 14.6% smaller than that of the first cycle to the same strain level suggesting that the strength of the carbon foam will degrade under constant amplitude loading leading to unstable energy dissipation. This result is further shown at the 50% strain level where the peak stress decreases from 660 kPa (95.7 psi) during the first cycle to 536 kPa (77.7 psi) during the fourth and final cycle. Stable energy dissipation is advantageous for earthquake resistant design because it protects structures from incurring damage in members that were not meant to undergo inelastic deformation. A lack of energy dissipation can have life safety implications as it can lead to a critical load-bearing element such as a column, undergoing damage and losing its load carrying capacity.

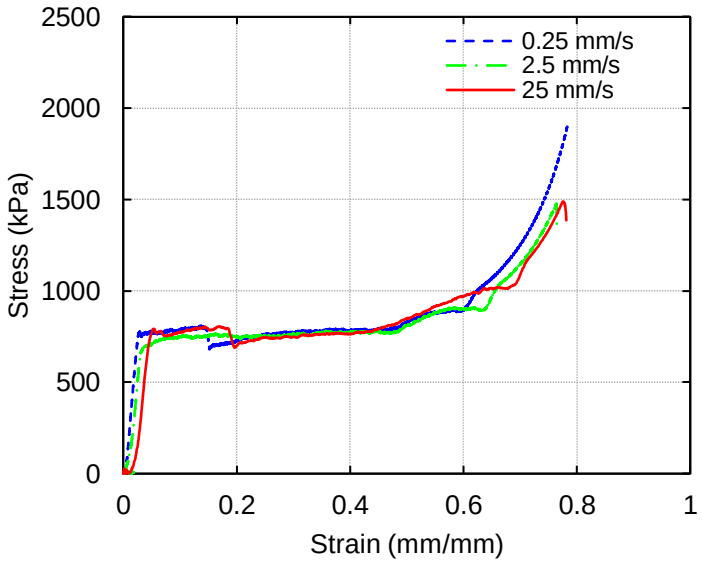

Figure 3-11 Representative monotonic stress-strain responses for PVC carbon foam specimens at three different loading rates

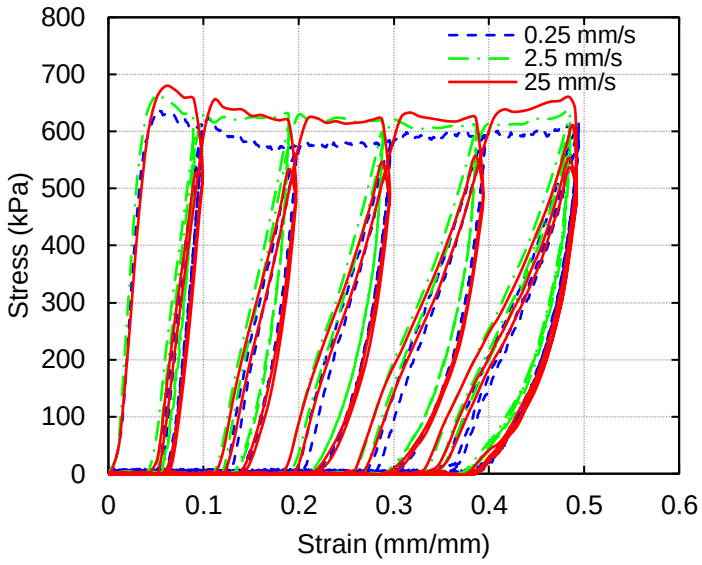

Figure 3-12 Representative cyclic stress-strain responses for PVC carbon foam specimens at three different loading rates

Figure 3-13 and Figure 3-14 show secant stiffness and hysteretic dissipated energy, respectively, as a function of cycle number for the specimen shown in Figure 3-12 that was tested under cyclic compression at a loading rate of 25.4 mm/s. Secant stiffness, which is calculated as the force corresponding to the maximum deformation in a given cycle divided by that maximum deformation, is an important quantity used to characterize non-linear structural response. For stress-strain responses that reach the same maximum deformation, the response with the larger secant stiffness will dissipate more energy than that of the response with the smaller secant stiffness. Referring to Figure 3-13, the secant stiffness peaks at 264 N/mm during the first cycle to 10% strain. After the second cycle to 10% strain, the secant stiffness drops nearly 52% from 256 N/mm to 124 N/mm indicating that the cellular structure of the carbon foam has likely collapsed during the first cycle to 20% strain (cycle 3). The secant stiffness slowly degrades before nearly plateauing around cycle number 7 (first cycle to 40% strain) at 61.6 N/mm. While the carbon foam is able to resist fragmenting into smaller pieces after undergoing continued cycling, the degradation of secant stiffness due to the foam's cellular nature suggests that it may not be optimal for void fill applications in which a large stiffness is required.

Figure 3-14 shows the hysteretic dissipated energy as a function of cycle number and indicates that the hysteresis loops from the first cycle to a given strain level are significantly larger than those from the second cycle to that same strain level. Specifically, the dissipated energy is on

average approximately 3.7 times larger for the first cycle to a given strain level compared to that of the second cycle. In general, the amount of dissipated energy increases with an increase in strain; however, the consistent degradation in dissipated energy during the excursions to 50% strain once again suggest that the foam may not be optimal for void fill scenarios in which it is subjected to constant amplitude compressive deformations.

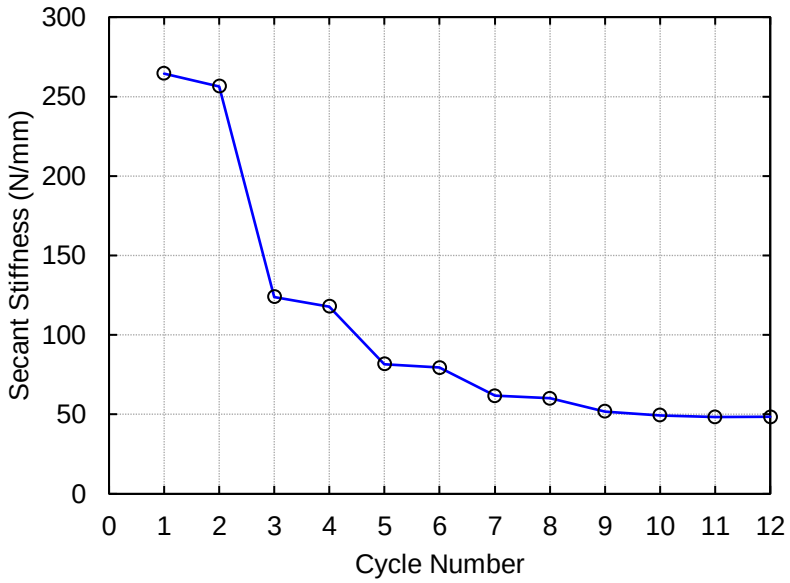

Figure 3-13 Secant stiffness of a carbon foam specimen tested under cyclic compression at a loading rate of 25.4 mm/s

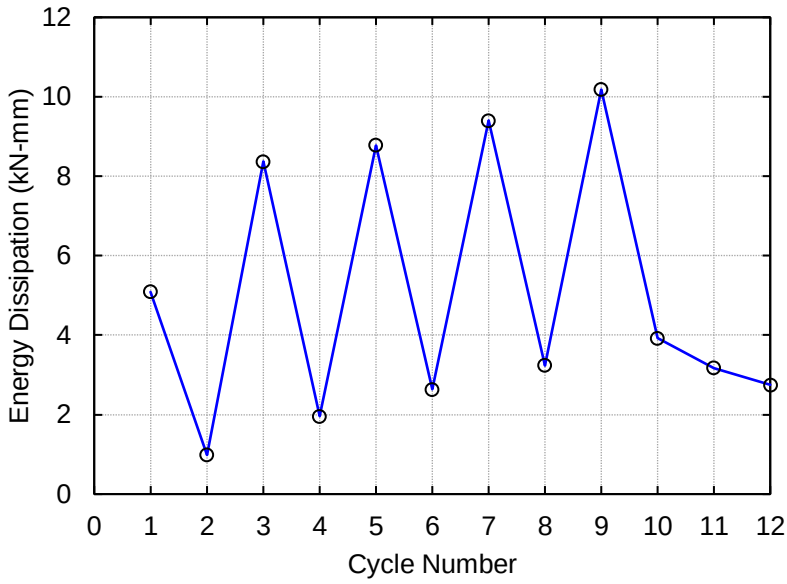

Figure 3-14 Energy dissipation for a carbon foam specimen tested under cyclic compression at a loading rate of 25.4 mm/s

Figure 3-15 shows the average maximum stress achieved during the first cycle to a given strain level for the three considered loading rates. The maximum stress decreases slightly with increasing strain up to the 40% strain level before increasing during the 50% strain level. The slight decrease in maximum stress before increasing during the first cycle to 50% strain is likely from the cellular structure of the foam being crushed before densification occurs, at which point an increase in maximum stress is observed. Overall, the maximum stress is fairly consistent for all loading rates across the different strain levels with averages of 616 kPa (89.3 psi), 636 kPa (92.2 psi), and 682 kPa (98.9 psi) under increasing loading rate, respectively. The minor increase in maximum stress with an increase in loading rate further confirms that loading rate has a negligible influence on the behavior of the carbon foam.

Figure 3-16 shows the average energy dissipation under cyclic loading during the first cycle to a given strain level for the three considered loading rates. As the strain increases from the 10% strain level to the 20% strain level, the energy dissipation increases sharply before slowly increasing during the next three strain levels. The slow increase in energy dissipation at larger strain levels is likely due to large residual deformation from earlier cycles leading to a reduction in the amount of inelastic deformation that the specimens can undergo. The minimal difference in energy dissipation per cycle for the three loading rates suggests that the energy dissipation capacity of the

carbon foam is insensitive to loading rate. This insensitivity to loading rate suggests that the carbon foam will offer the same improvement in energy dissipation capacity when used as void fill regardless of the strain rates induced in the filled structural members by earthquake ground motion.

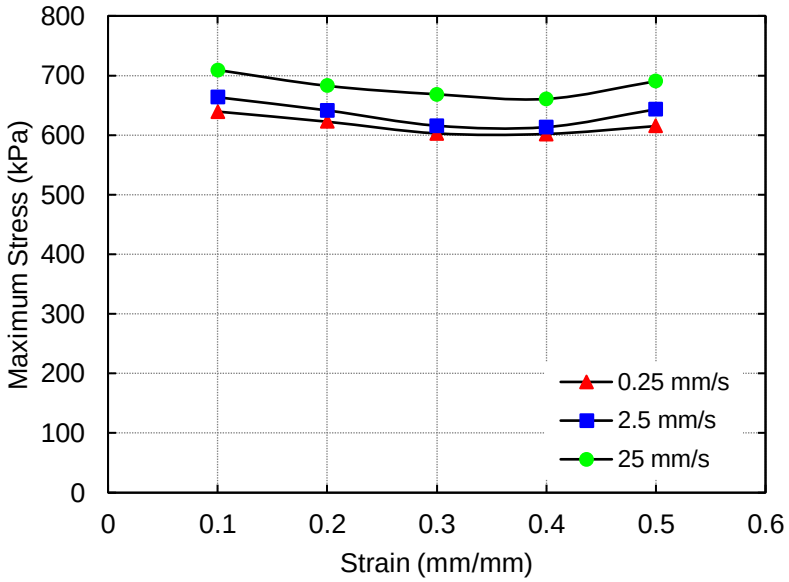

Figure 3-15 Average maximum stress under cyclic loading during the first cycle to a given strain level for three different loading rates

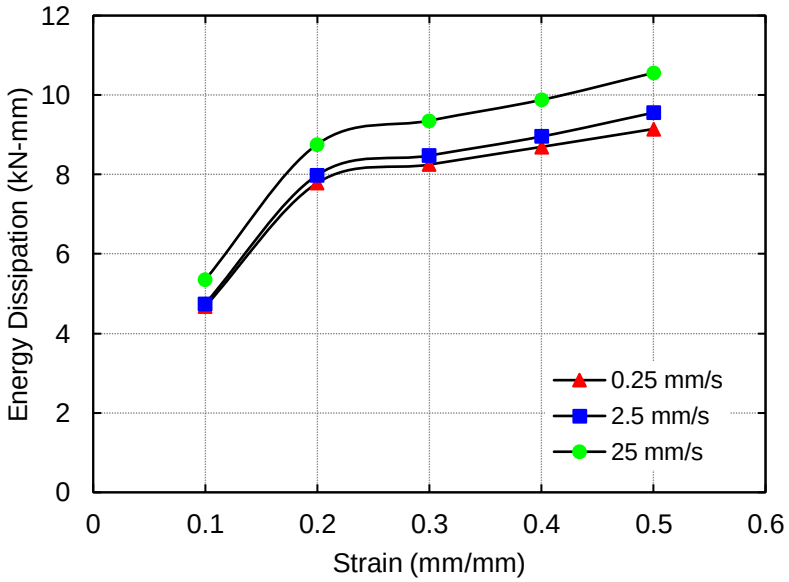

Figure 3-16 Average energy dissipation under cyclic loading during the first cycle to a given strain level for three different loading rates

3.4.3 Polycarbonate Honeycomb

Three specimens are tested at each loading rate under monotonic and cyclic compression for the in-plane and out-of-plane directions for a total of 36 polycarbonate honeycomb tests (18 monotonic and 18 cyclic). Figure 3-17 and Figure 3-18 show typical monotonic compression responses for out-of-plane and in-plane crushing of the honeycomb at a loading rate of 2.5 mm/s, respectively. As shown in Figure 3-17, the out-of-plane response is initially linear with an elastic modulus of 77.2 MPa (11.2 ksi). The out-of-plane response reaches a peak stress of 1.18 MPa (171 psi) at 2.4% strain in the elastic region before rapidly decreasing. The sudden decrease in stress after the peak results from buckling of the cell walls, with the line of buckled cells generally located in the upper half of the specimens (Figure 3-19a). After the cell walls buckle, the stress remains fairly constant until the specimen reaches nearly 75% of its original height. Following a procedure similar to Olurin et al. (2000), a plateau stress of 0.94 MPa (136 psi) is calculated by averaging the compressive stress over the nominal strain range of 10% to 60%. Eventually the folds from the buckled cell walls begin to consolidate, leading to a sharp increase in stress with little increase in strain. The typical failure mode for the out-of-plane response, shown in Figure 3-19a, is characterized by a clear line of buckled and folded cells extending through the cross-section of the specimen. When the specimens are unloaded after testing there is significant residual deformation.

A typical in-plane compression response is shown in Figure 3-18 and is similar to what was exhibited in previous experimental studies (Papka and Kyriakides 1998; D'Mello and Waas 2013). The response is initially linear with an elastic modulus of 0.74 MPa (107 psi), which is approximately 100 times smaller than that of the out-of-plane direction. This substantial difference in stiffness occurs due to the cellular arrangement of the honeycomb and its orthotropic nature leading to different collapse mechanisms when loaded in orthogonal directions. Specifically, in the out-of-plane direction the force from the loading fixture has to buckle the honeycomb cell walls, which are supported by adjacent cells, whereas in the in-plane direction deformation occurs through crushing of the cell walls (Zhang and Ashby 1992). After the elastic region, deformation localizes in rows that progressively collapse and spread to adjacent rows (Figure 3-19b). The force required to initiate collapse of an entire row of cells is larger than the force needed to sustain the collapse, resulting in stress oscillations throughout the plateau region as this process repeats. Eventually, nearly all of the cells collapse leading to a sharp increase in stress (densification).

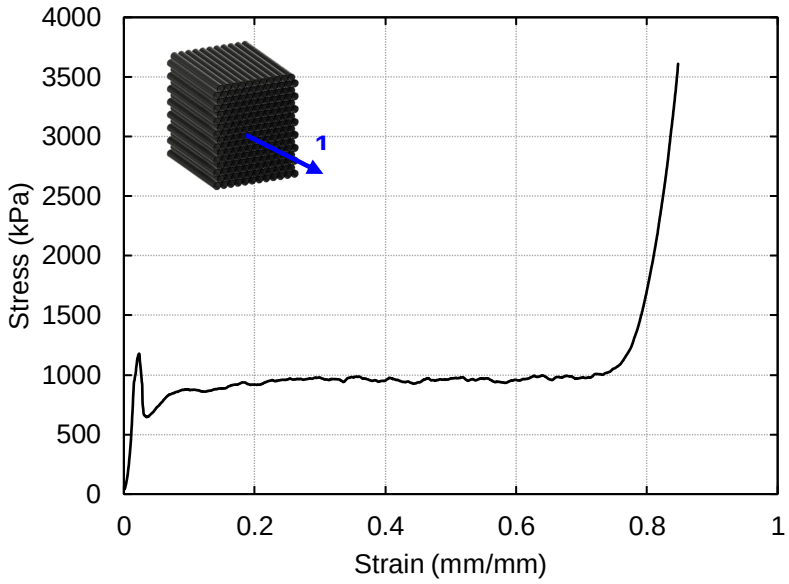

Figure 3-17 Representative out-of-plane (1 direction) monotonic compression response at 2.5 mm/s

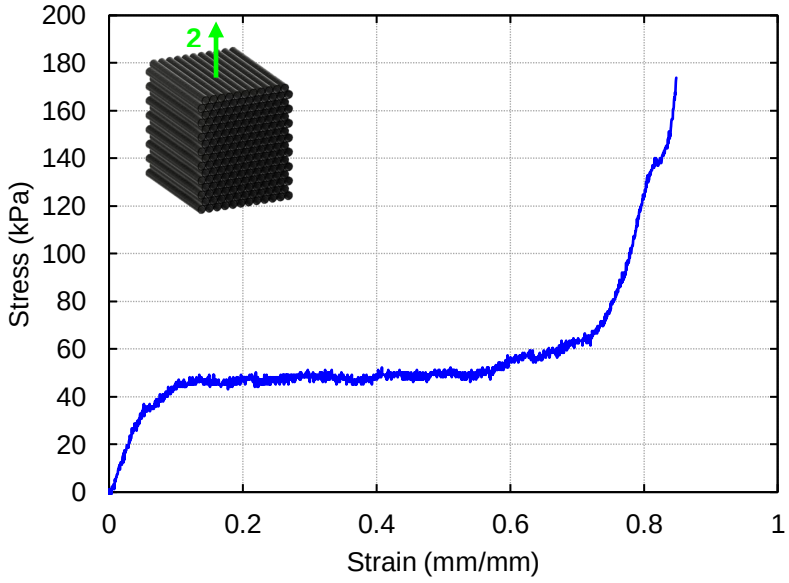

Figure 3-18 Representative in-plane (2 direction) monotonic compression response at 2.5 mm/s

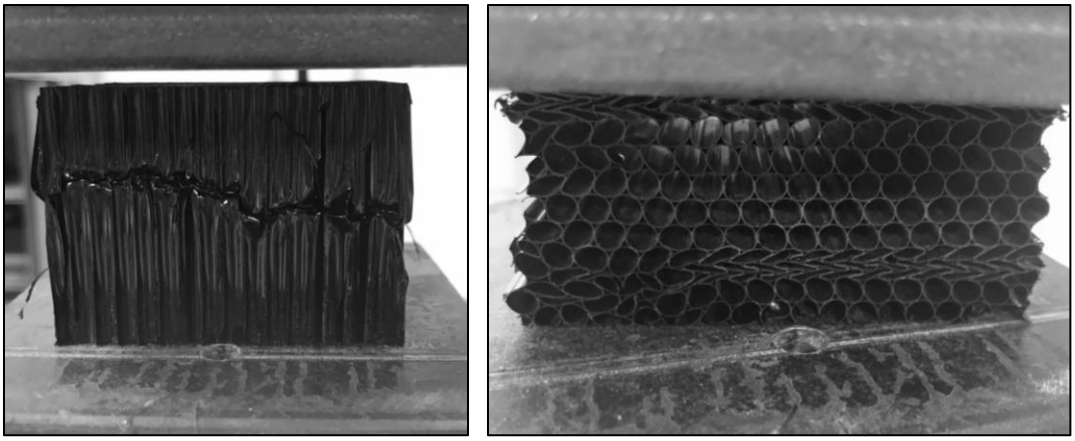

(a) (b)

Figure 3-19 Typical failure modes for the (a) out-of-plane and (b) in-plane loading directions

As the behavior of polycarbonate tends to be rate dependent (Mulliken and Boyce 2006), it is necessary to characterize how strain rate affects the response of the honeycomb under uniaxial compression. Referring to the previously mentioned study undertaken by Papka and Kyriakides (1998), it was shown that the plateau stress and the stress marking the initiation of localized deformation increases with an increase in strain rate for monotonic in-plane compression loading. Furthermore, it was noted that specimen size (i.e., width in the three direction based on Figure 3-3) has a modest effect on compressive response with larger size specimens exhibiting larger plateau stresses. Specifically, a 2 kPa (0.29 psi) difference in plateau stress was observed between specimens that differed in width by factors of two and three. Results from the current study confirm the assertions that plateau stress increases with strain rate and specimen size for monotonic in-plane compression loading (Table 3-2). In the case of out-of-plane loading, clear correlations could not be established between plateau stress and specimen size and plateau stress and strain rate (Table 3-2). The lack of clear correlations is likely due to the influence of cell geometrical imperfections on the type of folding mechanism that occurs after the initial peak load is reached (D'Mello et al. 2012).

Table 3-2 Relationship of plateau stress with specimen size and loading rate for in-plane and out-of-plane monotonic compression

Specimen Size (mm × mm)	Loading Rate (mm/s)	In-Plane Plateau Stress (kPa)	Out-of-Plane Plateau Stress (kPa)
50.8 × 31.8	0.25	48.4	979
	2.5	48.9	898
	25	53.4	1052
50.8 × 31.8	2.5	48.9	898
50.8 × 63.5		50.0	1029
50.8 × 95.3		52.5	929

Typical stress-strain responses for the honeycomb under cyclic loading are shown for the out-of-plane (Figure 3-20) and in-plane (Figure 3-21) directions at loading rates of 25 mm/s and 0.25 mm/s. Note that the oscillations in stress shown in Figure 3-21 can be attributed to the large capacity of the load cell relative to the forces that the honeycomb could resist resulting in unstable force readings. In the case of out-of-plane loading (Figure 3-20), the response at a 25 mm/s loading rate begins nearly identically to the response under monotonic compression with a linear-elastic region that has an elastic modulus of 107 MPa (15.5 ksi). The elastic region culminates in a peak stress of 1.26 MPa (183 psi). Thereafter, localized deformation occurs in the form of cell buckling, leading to a steep decrease in load. As the adjacent folds of the buckled cell walls come into contact, the stress increases until the specimen is unloaded. In general, the maximum stress and dissipated energy during the first cycle to a particular strain level are much larger than that of the second cycle to the same strain level. Specifically, the average maximum stress and dissipated energy during the first cycles to a particular strain level are 1.06 MPa (154 psi) and 16.4 kN-mm, respectively. In contrast, the second cycles to a given strain level have an average maximum stress and dissipated energy of 0.79 MPa (115 psi) and 1.84 kN-mm, respectively.

The in-plane strength of the honeycomb under cyclic loading for the specimen tested at a loading rate of 25 mm/s is substantially lower than that of the out-of-plane response, with an approximate elastic modulus and maximum stress of 590 kPa (85.6 psi) and 55 kPa (7.98 psi), respectively. Typical behavior consists of deformation being concentrated in a few weak rows of cells with the remainder of the rows of cells remaining nominally circular under repeated compressive cycling.

Furthermore, the behavior is characterized by negligible energy dissipation relative to that of the response in the out-of-plane direction. The lack of energy dissipation in the in-plane direction is revealed by the small amount of residual deformation in the specimen at the completion of the loading history. Rows of cells that were initially nominally circular before loading exhibited an ellipsoidal geometry after testing, resulting in the specimen height being only slightly shorter than in its original state. While the in-plane strength and energy dissipation capacity of the polycarbonate honeycomb used in this study are fairly low, the performance of the honeycomb can be enhanced by decreasing the diameter-to-thickness ratio of the cells or by filling the honeycomb with a lightweight foam. Mozafari et al. (2015) showed that a 208 fold increase in in-plane crushing strength can be realized by filling an aluminum honeycomb core with polyurethane foam. Similarly, D'Mello and Waas (2013) highlighted how the synergistic interaction of an elastomer and thin-wall polycarbonate honeycomb can lead to enhanced energy dissipation over short crush distances relative to that of an empty honeycomb. As such, the use of the polycarbonate honeycomb considered in this study exhibits great promise for seismic void fill applications.

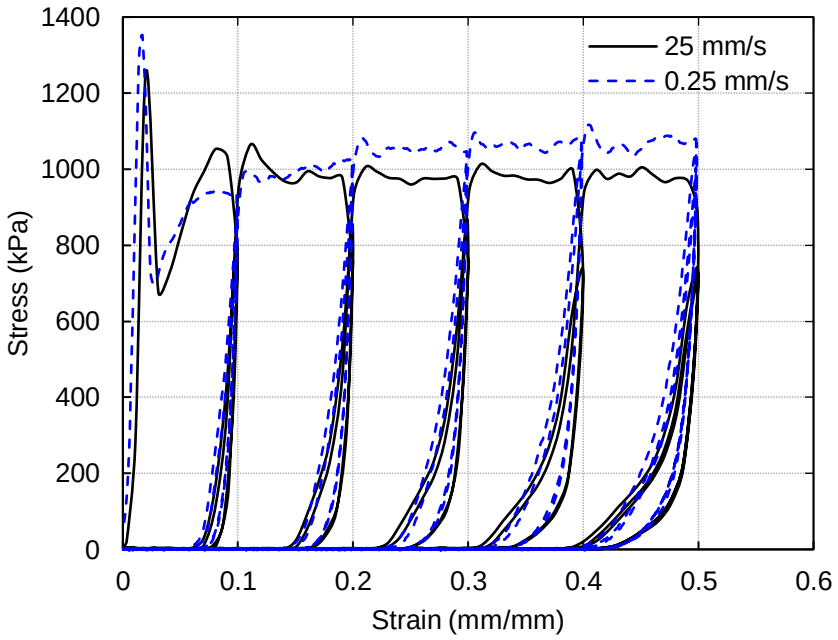

Figure 3-20 Typical stress-strain responses of the honeycomb under out-of-plane cyclic loading at 25 mm/s and 0.25 mm/s

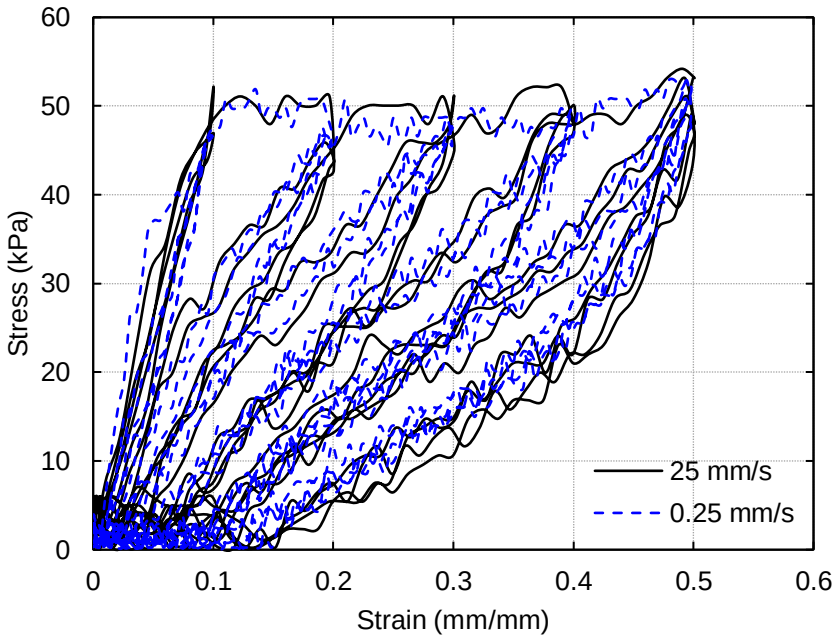

Figure 3-21 Typical stress-strain responses of the honeycomb under in-plane cyclic loading at 25 mm/s and 0.25 mm/s

Given the importance of loading rate when considering seismic applications, a comparison of important characteristic properties such as ultimate stress, cumulative dissipated energy, and initial secant stiffness is presented in Table 3-3 for the 50.8 × 63.5 mm honeycomb specimens tested under cyclic compression. Tables comparing relevant monotonic and cyclic properties at the different loading rates for all considered materials are provided in Appendix A. For the honeycomb tested under cyclic compression in the in-plane direction, the results show that increases in loading rate lead to moderate increases in ultimate stress and cumulative dissipated energy. It should be noted that the values presented in Table 3-3 are averages from the testing of three specimens at each of the considered loading rates. A trend in initial secant stiffness as loading rate increases is not evident, as the values are all quite similar. When considering the out-of-plane loading direction, it is not apparent as to how loading rate influences the characteristic properties. However, it is clear that loading in the out-of-plane direction provides superior performance regarding all three properties. On average across all three loading rates, loading in the out-of-plane direction results in values of ultimate stress, cumulative dissipated energy, and initial secant stiffness that are approximately 26, 17, and 19 times larger than those of the in-plane direction, respectively.

Table 3-3 Characteristic properties of the honeycomb (50.8 × 63.5 mm)

Loading Rate (mm/s)	In-Plane			Out-of-Plane		
	Ultimate Stress (kPa)	Cumulative Dissipated Energy (kN-mm)	Initial Secant Stiffness (N/mm)	Ultimate Stress (kPa)	Cumulative Dissipated Energy (kN-mm)	Initial Secant Stiffness (N/mm)
0.25	54.4	5.63	31.6	1390	99	608
2.5	55.1	5.80	30.9	1504	98	659
25	56.7	6.38	31.8	1352	102	523

3.5 Comparisons

An initial investigation examining a variety of potential HSS beam fill materials was undertaken by Wei (2017) to determine a material suitable for enhancing the seismic performance of beams through mitigation of local buckling and enhancement of energy dissipation capacity. A urethane rubber and three polyurethane foams of different density were considered. The material most suitable for seismic void fill applications, determined through three and four-point bending tests, was the largest density (256 kg/m^3) polyurethane foam. Its behavior was systematically characterized under monotonic and cyclic loads to obtain data necessary for creating high-fidelity finite element models of filled HSS beams under fully-reversed cyclic bending loads. Through comparison with the polyurethane foam, the materials considered in this chapter can be assessed for their suitability as potential void fill materials.

Under monotonic compression the polyurethane foam had an average yield stress of 2.62 MPa (0.38 ksi), 2.69 MPa (0.39 ksi), and 2.76 MPa (0.40 ksi) at loading rates of 0.25 mm/s, 2.5 mm/s, and 25 mm/s, respectively. Additional properties of the polyurethane foam from monotonic compression tests are provided in Appendix A (Wei 2017). While the carbon foam and polycarbonate have average crush strengths that are below 1 MPa (0.15 ksi), the polyester resin compound has an average yield strength of 17.9 MPa (2.60 ksi) at a loading rate of 0.25 mm/s. The much greater strength of the polyester resin compound compared to that of the polyurethane foam suggests that it could potentially be more effective than the polyurethane foam at mitigating local buckling. However, the polyurethane foam is approximately four times less dense than that of the polyester compound and can expand to fill a void. The expanding nature of the foam suggests that it would be more suitable than the polyester resin compound for seismic retrofit applications

and for seismic applications in general because it can result in lower inertial forces acting on a structure due to its lighter weight.

The carbon foam considered in this chapter has a lower strength than the polyurethane foam and is less dense, which most likely limits its benefits for seismic void fill applications. Furthermore, the cellular nature of the honeycomb allows it to potentially act in synergy with another material to generate enough strength to be effective at mitigating local buckling. Similarly, If the carbon foam can be produced in a greater density to provide strength commensurate with that of the polyurethane foam, it may be more suitable for seismic void fill applications.

Given the lightweight, high strength-to-weight ratio and pourable nature of the polyurethane foam, it is chosen as the fill material for the brace tests discussed in Chapter 4. However, the materials considered in this study are viable options for use in seismic void fill applications.

3.6 Conclusions

This study involves testing of three lightweight and non-traditional civil engineering materials to assess their potential for seismic void fill applications. The materials are a pourable polyester resin compound, PVC carbon foam, and a polycarbonate honeycomb. These materials can potentially be used within the inherent void of hollow structural section (HSS) braces, beams, or column members to provide enhanced structural performance under cyclic loads through added energy dissipation capacity and resistance to local buckling of the HSS. Properties such as energy dissipation capacity, secant stiffness, sensitivity to loading rate, and maximum stress are reported, as they provide valuable insight that is necessary for assessing the potential of the considered materials for seismic void fill applications.

Of the materials investigated in this study, the pourable polyester resin compound shows the most promise for seismic void fill applications owing to its many advantageous properties. For example, it is nearly 2.5 times less dense than that of normal concrete. Moreover, the compound exhibits a large energy dissipation capacity that increases with strain rate by dissipating over 600 kN-mm of energy during a single cycle of loading. It also has an ability to recover more than 50% of the deformation that it undergoes, which can limit the need for replacing the fill after minor to moderate earthquakes. During cyclic loading, the tested specimens are able to achieve stresses that

range from 20 MPa (2.90 ksi) to nearly 45 MPa (6.52 ksi), which is commensurate with that of the compressive strength of many types of concrete. As the use of concrete fill in HSS braces has been proven effective at mitigating local buckling and providing increased energy dissipation under cyclic loads (Sheehan and Chan 2014; Goggins et al. 2006), the compound's similarity in strength to concrete suggests that it will be able to do the same.

The carbon foam is shown to be insensitive to loading rate but has behavior that is characterized by severe degradation of secant stiffness after crushing of its cellular structure. The low stiffness after crushing suggests that the foam may not be effective for prolonged mitigation of local buckling, as the foam will not be able to restrain inward buckling of the surrounding steel after it is initially crushed.

While the in-plane stiffness and strength of the polycarbonate honeycomb is much lower than that of the other materials, the cellular nature of the honeycomb provides an opportunity for it to be combined with other lightweight materials to provide improved behavior for void fill applications. Additionally, if placed within the void of a rectangular hollow section brace, the honeycomb can be oriented so that it crushes in the out-of-plane direction. This orientation will allow for the greater strength and energy dissipation capacity of the honeycomb in the out-of-plane direction to be utilized.

Overall, this research generated a previously non-existent data set that characterizes the behavior of three non-traditional materials under loadings representative of what will be induced by an earthquake. The behavior of all three materials is also characterized under different loading rates so that the response of members employing these materials as fill can be understood considering strain-rate effects. Moreover, the data produced from these tests provides necessary information for creating high-fidelity finite element models that can be used to evaluate the ability of the considered materials to provide improved seismic performance at the member and system levels.

Chapter 4 Experimental Testing of Empty and Foam-Filled Braces

4.1 Introduction

Steel braced frames are commonly employed in regions of high seismicity due to their efficiency in resisting lateral loads. The performance of these braced structures is largely dependent on their ability to withstand significant inelastic deformations, which can often result in large economic losses associated with disruption of normal building functionality and repair costs. While the seismic performance of steel systems has been greatly improved through gusset plate design methods that ensure adequate ductility (Lehman et al. 2008; Roeder et al. 2011), a paradigm shift toward performance-based design and now resilience-based design has provided impetus to focus on objectives that move beyond life safety. As a result, limiting residual damage and subsequent economic losses have also become major considerations. Filling steel braces with a lightweight, high-energy dissipating foam has shown great promise for minimizing damage by providing a means to limit local buckling in the plastic hinge region leading to enhanced brace ductility and a reduction in large story drifts that can cause costly damage. The material characterization tests presented in Chapter 3 explore the use of other non-traditional materials for seismic void fill applications to limit damage to steel braced frame structures. While the three materials discussed in Chapter 3 show great potential for use in seismic void fill applications, a polyurethane foam is selected as the void fill material for the brace tests presented in this chapter because of its pourable and expanding nature that makes it amenable for new construction and seismic retrofit applications of steel braced frames. As such, the behavior of polyurethane foam-filled circular hollow section (CHS) braces is experimentally investigated to provide a quantitative understanding of their behavior under large cyclic loads typically associated with earthquake loading.

The testing program is divided between Kyoto University (KU) in Japan and the University of Michigan (UM) with the UM tests examining braces that allow for conclusions to be developed with respect to United States seismic design approaches. Overall, a total of 12 braces are tested under reversed-cyclic loading – six at KU and six at the UM. Strain, post-buckling compressive

strength, elastic stiffness, dissipated energy, maximum tensile strength and initiation of local buckling and fracture are used to evaluate the potential benefits of using foam-filled braces as compared to empty braces. Use of the foam fill for retrofit applications is also explored using two braces with different hole layouts for inserting the foam into an in-situ brace. Moreover, the experimental tests provide critical data that is necessary for calibrating and validating high-fidelity finite element models that are used to conduct an extensive parametric study to widen the parameter space and assist in developing design recommendations (Chapter 5).

4.2 Experimental Program (KU)

4.2.1 Test Specimens

The nominal brace geometric properties for the tests performed at KU are listed in Table 4-1 and include three different brace sizes. Referring to Table 4-1, the nomenclature used to identify the braces consists of two parts. The first part distinguishes between empty (E) and filled (F) braces and the second part indicates the brace outer diameter and wall thickness. An addendum to the second part of the nomenclature indicates the hole layout used to insert the foam to assess the suitability of the foam fill for retrofit applications with H1 indicating hole layout one and H2 indicating hole layout two (Figure 4-1). For example, E8932 indicates an empty brace with an outer diameter of 89.1 mm, a wall thickness of 3.2 mm and no holes along its length.

All braces are 1575 mm in length (L_B) measured from the inside of each end plate. The slenderness ratios (λ) presented in Table 4-1 are calculated using KL/r, where K is an assumed effective length factor of one based on the brace end conditions, L is the pin to pin distance in the test setup, and r is the radius of gyration. All of the braces are fabricated from Japanese STK 400 carbon steel (JIS G 3444), which has a specified minimum yield stress (F_y) of 235 MPa and a specified minimum tensile strength (F_u) of 400 MPa. The specimens are selected to ensure that the width-to-thickness ratios, or in the case of round HSS braces, diameter-to-thickness (D/t) ratios, satisfy the moderately ductile and highly ductile limits prescribed in the AISC Seismic Provisions (AISC 2016a). The limiting D/t ratios are intended to allow for seismic force resisting system members to achieve adequate ductility for their anticipated level of inelastic demand. Using $0.053\frac{E}{R_y F_y}$ and $0.062\frac{E}{R_y F_y}$, which are expressions for the limiting D/t ratios for highly ductile and moderately ductile members

stipulated in the AISC Seismic Provisions (AISC 2016a), respectively, and assuming nominal properties of the Japanese STK 400 steel, the limiting *D/t* ratios are 27.4 and 32.1, respectively. Selecting brace sections that satisfy and are above the specified *D/t* limits allow for the influence of the foam fill on brace performance to be examined with respect to CHS braces that are anticipated to have different levels of ductility.

Table 4-1 Test matrix of nominal properties (STK 400 steel braces)

Bracing member	Diameter D (mm)	Thickness t (mm)	Length L_B (mm)	Diameter-to-thickness ratio[a] D/t	Slenderness ratio[b] λ
E8932	89.1	3.2	1575	27.8	70.1
F8932	89.1	3.2	1575	27.8	70.1
E11445	114.3	4.5	1575	25.4	54.8
F11445	114.3	4.5	1575	25.4	54.8
F11435H1	114.3	3.5	1575	32.7	54.4
F11435H2	114.3	3.5	1575	32.7	54.4

[a] Calculated using nominal brace outer diameter and wall thickness
[b] λ calculated using pin to pin distance of 2131 mm

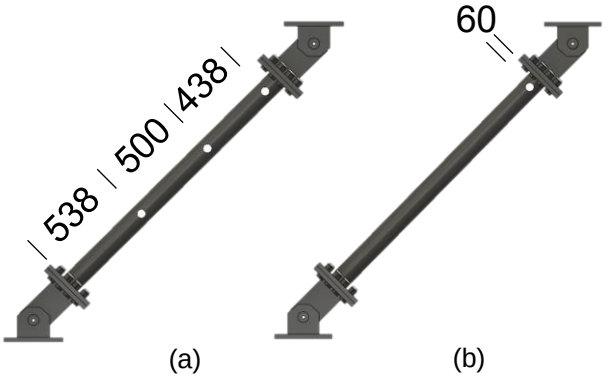

Figure 4-1 Hole layouts for foam insertion for (a) F11435H1 with three 22 mm diameter holes and (b) F11435H2 with one 16 mm diameter hole (units: mm)

4.2.2 Material Properties

4.2.2.1 Steel

Three coupons extracted from each brace size are used to determine tensile material properties, which are useful for constitutive model calibration for the finite element parametric study described in Chapter 5. A typical coupon and its corresponding dimensions are shown in Figure 4-2. Strain is calculated using the average strain readings from two strain gauges (one on the front and one on the back of the coupon) placed within the reduced width section and oriented parallel

to the loading direction. A linear variable displacement transducer (LVDT) attached between two welded studs provided strain readings to confirm the accuracy of the strain gauges. Strain is calculated by dividing the LVDT output by the distance between the welded studs (70 mm). Average values of the measured elastic modulus, yield stress determined by the 0.2% strain offset method, and measured tensile stress are listed in Table 4-2 along with ratios of measured yield stress to specified minimum yield stress and measured ultimate stress to specified minimum tensile stress.

The AISC Seismic Provisions (AISC 2016a) list R_y and R_t values for various steels, where R_y is the ratio of the expected yield stress to the specified minimum yield stress and R_t is the ratio of the expected tensile strength to the specified minimum tensile strength. The R_y and R_t values are critical for capacity-based seismic design where specific components are expected to yield while others remain elastic. If a component that is designed to yield has an unexpectedly high yield strength, it can result in other critical structural components, such as connections, being overloaded and potentially yielding or fracturing. The ratios presented in Table 4-2 are similar to R_y and R_t values, except that the expected yield stresses and expected tensile strengths are replaced by measured values. The average R_y and R_t value based on the results of the coupon tests are 1.58 and 1.1, respectively. These values are similar to those presented in the AISC Seismic Provisions (AISC 2016a) for ASTM A53 steel (R_y = 1.6 and R_t = 1.2) and ASTM A36 hot rolled bar (R_y = 1.5 and R_t = 1.2). However, the Japanese STK400 steel used in these tests differs from the ASTM A53 and A36 steels in that it has an unfavorable F_u/F_y ratio. On average, the ratio of the measured tensile strength to the measured yield stress is 1.19, whereas it is approximately 1.6 for A53 and A36 steel. The F_u/F_y ratio of 1.19 does not meet the requirements set by Eurocode 3 (EC3 2005), which states that F_u/F_y should be greater than 1.20. This requirement is in place to ensure adequate ductility, which is advantageous for seismic applications.

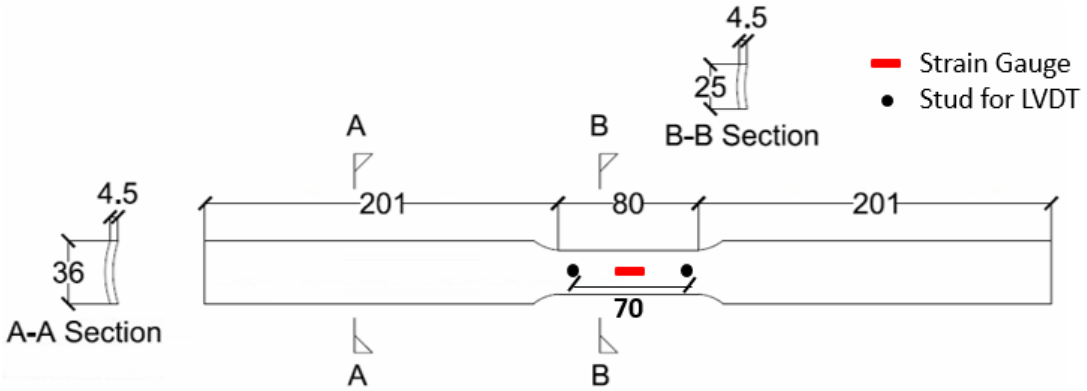

Figure 4-2 Typical tensile coupon with dimensions and instrumentation locations (units: mm)

Table 4-2 Measured material properties

Brace size (mm)	Elastic modulus (MPa)	$F_{y,\text{measured}}$ (MPa)	$F_{u,\text{measured}}$ (MPa)	$F_{y,\text{measured}}/F_y$	$F_{u,\text{measured}}/F_u$
D = 89.1; t = 3.2	186900	382	464	1.63	1.16
D = 114.3; t = 4.5	191700	344	411	1.46	1.03
D = 114.3; t = 3.5	188900	385	449	1.64	1.12

4.2.2.2 Foam

The fill material of the steel braces is a rigid, closed cell polyurethane foam manufactured by U.S. composites. The manufacturer states that the foam is commonly used for general purpose void fill applications, but also notes that it has found use for insulation and flotation applications. The density of the foam is 256 kg/m^3, which is the largest density that U.S. Composites produces for the two-part polyurethane foam. This particular density of foam is selected due to its ability to outperform lower density foams in regard to delaying local buckling, increasing cumulative energy dissipation, and slowing the degradation of secant stiffness after local buckling during three-point and four-point monotonic bending tests of small scale filled HSS beams (Wei 2017).

The foam is initially a two-part liquid that expands to form a rigid closed-cell urethane foam once thoroughly mixed and fully cured. Once the two parts are combined in equal proportions, there is approximately 45 seconds before the mixture begins to expand and harden with full expansion reached in approximately five minutes. At full expansion the foam occupies a volume roughly four times that of its initial liquid volume. The amount of expansion is temperature sensitive with higher temperatures generally leading to greater expansion. Mechanical properties of the foam have been

thoroughly characterized under monotonic and cyclic compression loads at various loading rates and can be found in Wei (2017) as mentioned in Chapter 3. Manufacturer reported properties are shown in Table 4-3 (U.S. Composites 2019).

Table 4-3 Manufacturer reported properties of the polyurethane foam fill

Parallel compressive strength (MPa)	4.0
Tensile strength (MPa)	3.1
Shear strength (MPa)	1.6
Flexural strength (MPa)	5.2

Due to the variability of the foam properties as a result of different mixing conditions (i.e., ambient temperature, mixing time, etc.), foam samples are extracted from the filled braces after testing to perform material characterization tests. The material characterization tests are useful in helping to explain differences in filled brace behavior that may arise. After testing, the braces are cut using a horizontal band saw and foam is extracted from the filled braces at different cross sections along the brace length. Both monotonic and cyclic compression tests are performed and testing is conducted using an 810 Material Test System (MTS) servo-hydraulic load frame with a 100 kN force capacity (Figure 4-3). The extracted foam is machined into cube specimens with edge lengths of 50.8 mm. Care is taken to ensure that the faces of the specimens are level in order to ensure uniform load application.

Load is applied to the foam cubes through the flanges of T-shaped steel loading platens that are inserted into hydraulic wedge grips at the top and bottom loading fixtures. The loading is applied in displacement control at a loading rate of 0.25 mm/s for the monotonic and cyclic compression tests. The specimens are centered on the loading platens while force is applied to the top surface of them and their sides remain unrestrained. Force is measured using the load cell attached to the actuator. Stress is calculated by dividing the force measured by the load cell by the average area of the cross-section of the specimen. Strain is calculated by dividing the actuator displacement by the original height of the specimen.

Figure 4-3 Mechanical behavior test setup for the polyurethane foam cubes

A total of 18 compression tests are performed (11 monotonic and 7 cyclic). The cyclic loading protocol consists of two cycles each to 10%, 20%, 30%, and 40% strain, followed by four cycles to 50% strain (Figure 4-4), which is the same cyclic protocol used in Chapter 3. Stress-strain responses for all of the specimens subjected to monotonic compression are shown in Figure 4-5 along with the corresponding brace from which they were extracted. In general, the behavior of all specimens is fairly similar, with three distinct regions of behavior displayed (linear elastic, stress plateau, and densification). The initial behavior is linear until about 5% strain. Thereafter, the foam begins to crush as the stress response remains fairly constant (stress plateau). After the cellular structure of the foam has completely collapsed at approximately 50% strain, the response begins to increase sharply with only a slight increase in strain in what is classified as the densification region. Foam specimens extracted from the same brace exhibit fairly similar stress-strain responses with substantially more scatter seen when comparing the response of specimens extracted from different braces.

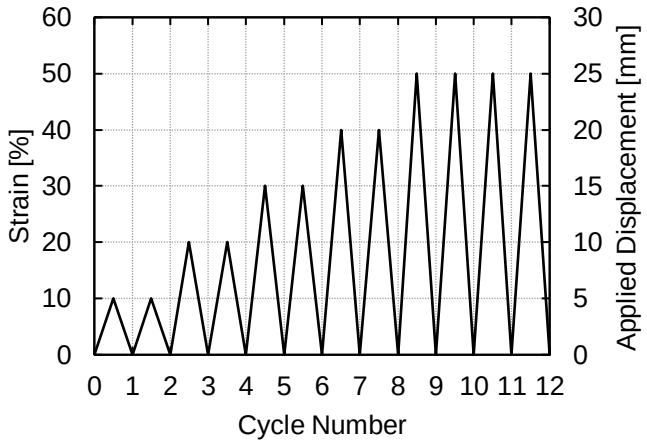

Figure 4-4 Cyclic compression loading protocol for the mechanical behavior tests of the extracted polyurethane foam

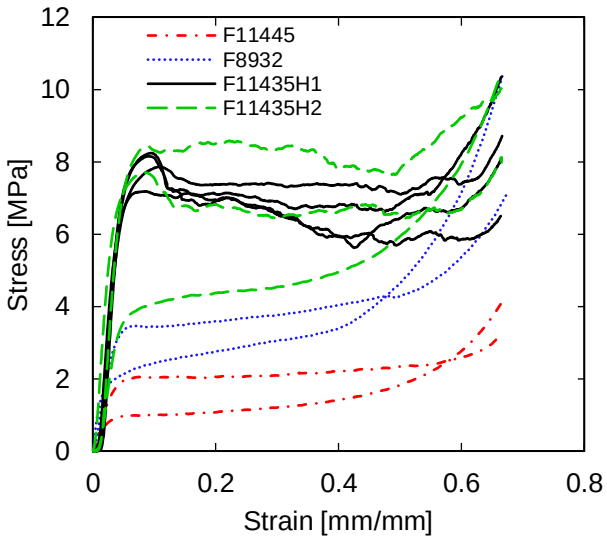

Figure 4-5 Monotonic compression stress-strain responses for the extracted polyurethane foam cubes

A summary of average values from the monotonic compression results is presented in Table 4-4. The elastic modulus of the foam ranges from 56 MPa to 228 MPa with an average of 148 MPa, indicating a large amount of variability in the stiffness of the foam. The crush strength reported in Table 4-4 is the stress at 15% strain. A strain of 15% is used to determine the crush strength of all specimens for consistency and because it generally corresponds well with a stable stress value in the plateau region. Both the crush strength and maximum stress achieved show a large amount of variability. The large scatter of the foam material properties can potentially be attributed to differences in foam expansion rate that occurred during the filling of the braces. Table 4-5 lists the

approximate amount of liquid foam used to fill a particular brace and the percentage of the brace void volume that it occupies. It is observed that the elastic modulus and crush strength of the foam correlate well with the amount of liquid foam used to fill a brace relative to its void volume. Specifically, the elastic modulus and crush strength increase with an increase in the percentage of liquid foam used relative to the void volume. This phenomenon is supported by research conducted by Linul et al. (2013), which showed that an increase in density of closed cell polyurethane foam is accompanied by an increase in yield strength and elastic modulus.

Table 4-4 Monotonic compression data summary for the extracted polyurethane foam

Bracing member	Mean			Standard Deviation		
	Elastic modulus (MPa)	Crush strength (MPa)	Maximum stress (MPa)	Elastic modulus (MPa)	Crush strength (MPa)	Maximum stress (MPa)
F8932	117	1.9	8.7	26.5	0.7	2.3
F11445	56	0.9	3.7	5.5	0.6	0.7
F11435H1	228	6.6	8.9	43.9	0.1	1.0
F11435H2	195	5.0	9.5	59.9	1.6	1.2

Table 4-5 Liquid foam volume as a percentage of brace void volume

Bracing member	Liquid foam volume (m^3)	Void volume (m^3)	Liquid foam % of void volume
F8932	2.20E-03	8.46E-03	26.0
F11445	1.80E-03	1.37E-02	13.1
F11435H1	5.10E-03	1.42E-02	35.8
F11435H2	3.70E-03	1.42E-02	26.0

Representative stress-strain responses for foam specimens subject to cyclic compression are shown in Figure 4-6 along with the corresponding brace from which they are extracted. Due to difficulty in extracting and machining foam specimens from the F8932 brace because of its small cross-sectional area, only enough specimens are prepared for monotonic testing. The results follow the same trend that is seen in the monotonic results where the specimens extracted from braces that are filled with a larger amount of foam relative to the brace void volume see the largest stresses. In general, the behavior is similar for all specimens. The first cycle to a particular strain level has a large hysteresis loop followed by a much smaller hysteresis loop during the second cycle to the

same strain level. This difference in hysteresis loop size and thus energy dissipation results from residual deformation after the first loading cycle. Maximum overall stresses range from 1.19 MPa to 8.3 MPa, once again indicating that different behavior can be achieved depending on the expansion rate of the foam.

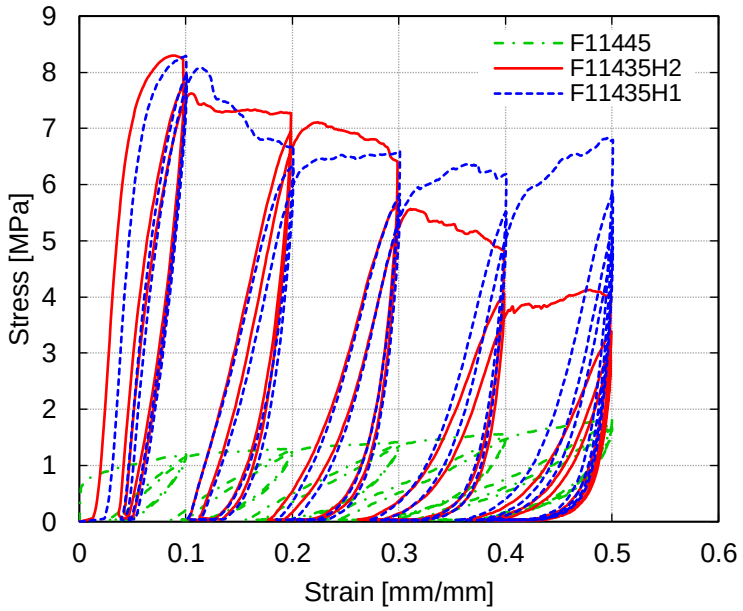

Figure 4-6 Representative cyclic compression stress-strain responses for the extracted polyurethane foam

4.2.3 Brace Fill Procedure

To isolate the influence of the foam fill on the brace behavior, foam is inserted into braces F11445 and F8932 via 24 mm diameter holes located at the center of the top endplates as shown in Figure 4-7. Similarly, to assess the viability of the foam fill for retrofit applications, braces F11435H1 and F11435H2 have the foam inserted using hole layouts along their lengths (Figure 4-1). Brace F11435H1 has three holes along its length, all of which are located out of the plane of buckling and outside of the plastic hinge region in order to limit the adverse effects that the holes may have on brace performance due to the reduction in cross-sectional area. Brace F11435H2 has one hole positioned near the top endplate and out of the plane of buckling to evaluate the influence of hole position on brace performance. Both F11435H1 and F11435H2 are oriented at 40° from the ground when the foam is poured in order to replicate retrofit conditions for a full-scale braced frame. The

foam is inserted into the braces using a funnel and occupies the void along the entire length of the brace after curing based on post-test cross-sectioning.

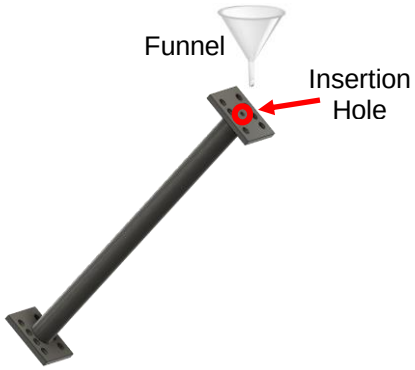

Figure 4-7 Foam insertion location for the F8932 and F11445 foam-filled braces

4.2.4 Test Setup and Loading Protocol

The test setup for all six brace tests conducted at KU is shown in Figure 4-8 and consists of a pinned steel load frame attached to a steel reaction frame. The steel braces are oriented at a 45° angle with the bottom wide flange beam of the load frame in their initial position and are connected to the frame through mechanical pin connections that allow for brace buckling about an axis perpendicular to the plane of the frame. Pin connections are used to expedite the installation and removal of the braces while limiting variation and uncertainty in brace performance that may arise from the use of gusset plate connections. 25.4 mm thick endplates that are fillet welded to ends of the braces are connected to each pin connection using eight M22 high strength bolts. A photograph of the cross section of a foam-filled brace after testing is shown in Figure 4-9.

The hydraulic jack is operated in displacement control to induce axial contraction and elongation of the braces. Load is applied quasi-statically at rates ranging from 0.05 mm/s to 0.4 mm/s. Larger loading rates are used as the loading protocol progresses to larger brace axial deformation. The lateral loading protocol is based on story drift considering a frame height of 1753 mm and a brace orientation of 45°. The loading protocol is shown in Figure 4-10 and consists of two cycles each to 0.1, 0.25, 0.5, 0.75, 1, 1.5, 2, 3, and 4% story drift until brace fracture occurs. This symmetric and stepwise increasing deformation history is intended to be representative of the deformation demand induced on braces by a far-field type earthquake. The loading protocol employed is an adapted version of the protocol used by Clark et al. (1997) and is similar to the loading history

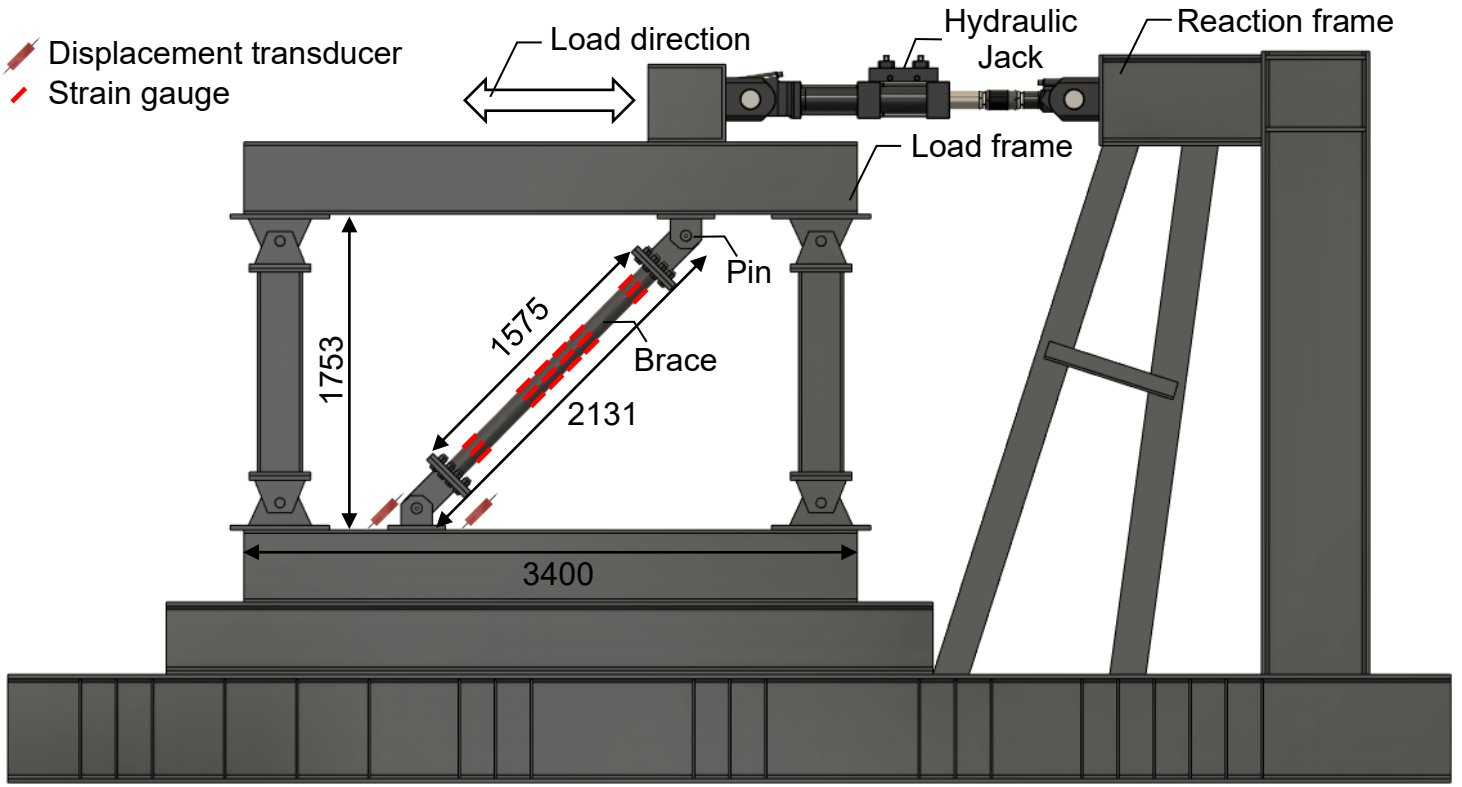

Figure 4-8 Test setup at Kyoto University (units: mm)

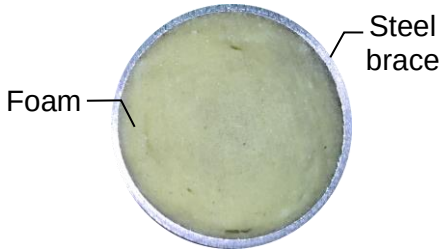

Figure 4-9 Cross section of a foam-filled brace

used by Han et al. (2007) to assess the behavior of HSS bracing members under seismic loading.

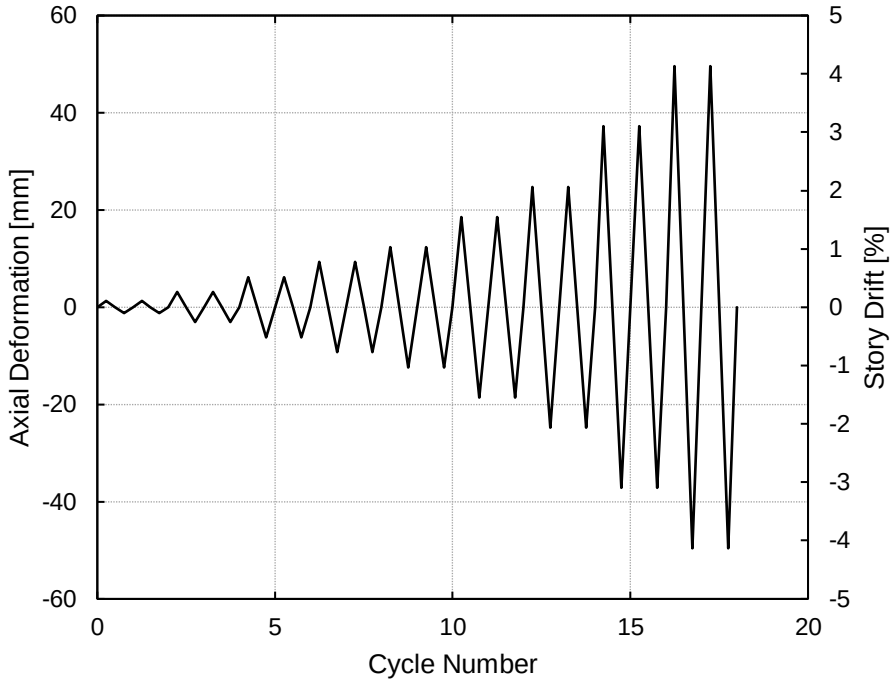

Figure 4-10 Loading protocol

4.2.5 Instrumentation

Lateral force is measured using a load cell attached to the hydraulic jack. The corresponding brace axial force is calculated using Equation 4.1:

$$P_a = \frac{P_L}{\cos\theta} \qquad \text{Equation 4.1}$$

where P_a is the axial force in the brace, P_L is the lateral force measured by the load cell, and θ is the angle that the brace makes with respect to horizontal defined by the bottom load frame beam. Brace axial deformation is calculated using the average reading from the two displacement transducers, which measure the distance between the connection pins. The displacement transducers are located on either side of the frame and are oriented parallel with the brace. Four bands of strain gauges are placed at quarter points around the circumference of the brace. The bands are spaced 125 mm apart along the brace length in the plastic hinge region. Additional strain gauges are placed 125 mm from the interior face of the brace endplates along the length of the

brace. The strain gauges are oriented parallel to the longitudinal axis of the braces. String potentiometers at quarter points along the brace length are used to measure in-plane deflection but are not shown in Figure 4-8 for clarity.

4.3 Experimental Results

4.3.1 Experimental Summary

For each of the six tested braces, axial force versus story drift hysteretic responses are provided in Appendix B. Appendix B also provides pertinent experimental quantities such as cumulative dissipated energy, maximum force in tension and compression, and maximum deformation in tension and compression. A summary of the experimental data is provided in Table 4-6.

Table 4-6 Summary of experimental data (KU)

Brace	Elastic stiffness (kN/mm)	Yield strength (kN)	Buckling strength (kN)	Maximum force (kN)		Limit state[a]	
				Tension	Compression	Local buckling	Fracture
E8932	109.3	295.4	281.3	338.2	281.3	2nd; -1.5	2nd; 3.0 (2.65)
F8932	111.1	289.1	285.4	339.9	290.0	1st; -2.0	1st; 4.0 (2.61)
E11445	194.6	437.0	433.2	505.5	439.2	2nd; -1.5	2nd; 3.0 (2.50)
F11445	197.8	440.7	415.1	504.1	459.1	1st; -2.0	1st; 4.0 (2.40)
F11435H1	158.1	383.3	355.1	433.3	375.7	2nd; -0.5	1st; 1.5 (1.24)
F11435H2	158.3	386.2	338.7	426.8	385.5	1st; -2.0	1st; 4.0 (2.07)

[a]Cycle; drift level at the initiation of local buckling (mid-length) and fracture. A negative drift level indicates compression and a positive drift level indicates tension. The number in parentheses denotes the drift percentage at fracture.

4.3.2 Hysteretic Response

Hysteretic responses of the axial force versus story drift for equal-size empty and filled braces are shown in Figure 4-11 with the instant of fracture indicated by the filled red circles. The behavior exhibited by all empty and filled braces is characterized by stable tensile capacity with significant degradation of compressive strength during each subsequent cycle of loading after global buckling. During the first few cycles of loading up to approximately 0.5% story drift, the braces behave elastically and no deformation is observable. Global buckling follows shortly after the braces yield, with the buckled shape characterized by a large mid-length deflection in the plane of the frame. Following global buckling, the braces begin to exhibit local buckling at their mid-length with the buckled shape accentuated after each subsequent compressive excursion. This local buckling

induces high strains in the plastic hinge region, which leads to small cracks during subsequent tensile excursions. The ensuing brace fracture occurs through approximately half the circumference of the brace, leading to a substantial loss of strength.

In general, the hysteretic response of the empty and equal size foam-filled braces is similar except that the foam-filled braces undergo an additional cycle of loading before fracture. The similarity in the hysteretic response of the empty and filled braces suggests that filling braces with the foam will be an amenable retrofit solution, as only minor changes in brace strength and stiffness would occur allowing for the design of the brace connections and surrounding frame members to remain the same.

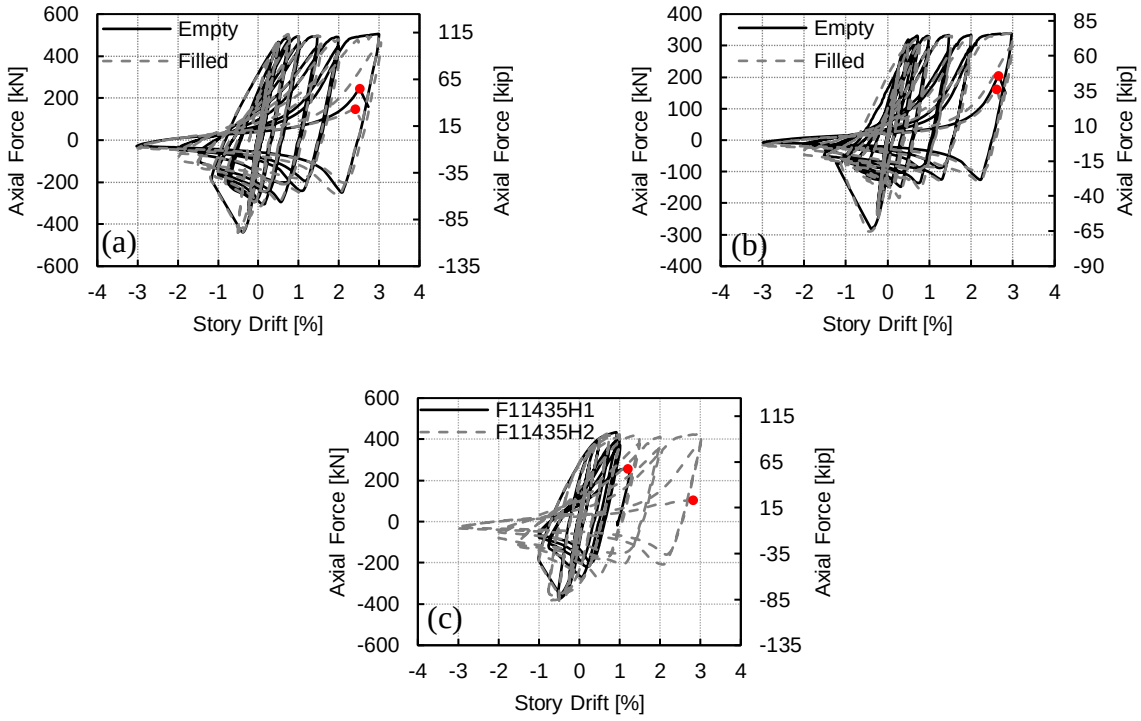

Figure 4-11 Axial force-story drift relationships for the (a) 4.5 mm wall thickness specimens, (b) 3.2 mm wall thickness specimens, and the (c) 3.5 mm wall thickness specimens with different fill techniques

4.3.3 Effect of Foam Fill on Local Buckling and Fracture

The tendency of less slender braces with a high *D/t* to undergo local buckling under large compressive stresses is a well-known phenomenon commonly seen in previous experimental investigations (Goggins et al. 2006; Liu and Goel 1988). The influence of the foam fill in regard

to its ability to reduce the severity of this local buckling and delay the accumulation of strain that precedes brace fracture is substantial. For empty braces, E8932 and E11445, local buckling initiates during the second compressive excursion to 1.5% story drift or a corresponding axial deformation of 18.6 mm. Conversely, the equivalent size filled braces, F8932 and F11445, undergo local buckling during the first compressive excursion to 2% story drift or a corresponding axial deformation of 24.8 mm. In addition to delaying the occurrence of local buckling, the foam fill also alters the local buckling mode shape from inward to outward. In doing so, the presence of the foam fill considerably reduces the severity of local buckling by limiting the inelastic deformation demand on the brace, thus leading to a delay in the occurrence of brace fracture by one cycle. Figure 4-12 displays photographs of local buckling for the empty and filled braces at the end of the cycle in which local buckling initiates. Visual observation for both sets of filled and empty braces confirms a significant reduction in the severity of local buckling for the filled braces. The empty brace with a diameter of 89.1 mm (t = 3.2 mm) has severe inward local buckling that resembles the shape of a short half sine wave (Figure 4-12a). In contrast, the equivalent size filled brace exhibits a less pronounced outward buckle with a smoother wave form (Figure 4-12b). It is interesting to note that the region where local buckling has initiated in the filled brace is shifted from its mid-length (identified by the welded stud) by approximately 104 mm. This shift can most likely be attributed to some non-homogeneity of the foam along the length of the brace. For the empty brace with a 114.3 mm (t = 4.5 mm) diameter, the local buckle severely protrudes inward (Figure 4-12c) while the buckled shape for the filled brace (Figure 4-12d) is characterized by two faint and outward protruding waves. Because the strain is dispersed over a larger length for the filled brace, the strain demand is reduced, ultimately leading to an increase in brace ductility.

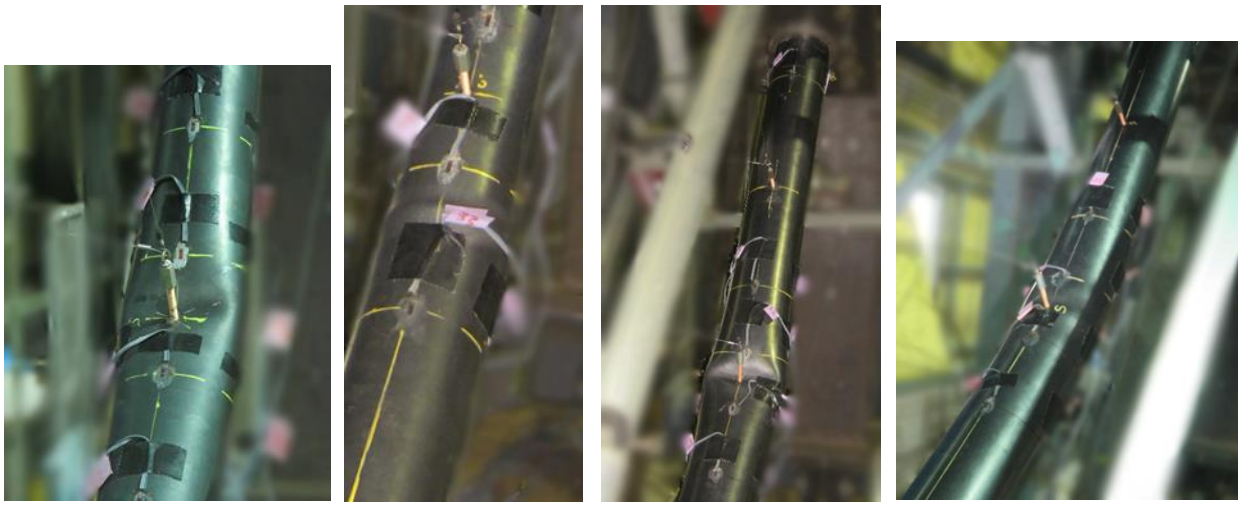

(a) (b) (c) (d)

Figure 4-12 Initiation of local buckling for the (a) E8932 brace at the end of the second compressive excursion to 1.5% story drift, (b) F8932 brace at the end of the first compressive excursion to 2% drift, (c) E11445 brace at the end of the second compressive excursion to 1.5% story drift, and (d) F11445 brace at the end of the first compressive excursion to 2% drift

4.3.4 Compressive Strength and Stiffness

The axial buckling load, elastic stiffness, maximum force, yield strength and story drift at the initiation of fracture and local buckling for each brace is reported in Table 4-6. Referring to Table 4-6, the elastic stiffness of the empty and equivalent size filled braces are within 2% of one another, while the yield strengths are within 3%. These minor differences suggest that the use of the foam fill may be amenable to current seismic design practices as the foam will not have to be directly considered other than its benefits in delaying the initiation of local buckling and providing improved ductility.

The beneficial influence of the foam fill is apparent when considering the buckling behavior of the empty and filled braces. Figure 4-13 shows normalized compression envelopes for the first loading cycle to each drift level. The abscissa represents the maximum axial deformation in the considered cycle normalized by the axial yield deformation, which is calculated using the average yield strengths and elastic moduli reported in Table 4-2. The ordinate represents the maximum compressive force attained by the brace in the considered cycle normalized by the product of the brace yield strength and gross cross-sectional area, where the yield strength is the axial force resisted by the brace when the average of all strain gauges along the brace length reaches the yield strain.

As shown in Figure 4-13, the compressive strength of the more slender braces (Figure 4-13a) degrades more rapidly than that of the less slender braces (Figure 4-13b). Specifically, the empty brace with λ = 70.1 (E8932) has a 48% reduction in normalized compressive capacity, while the empty brace with λ = 54.8 (E11445) has a 33% reduction in normalized compressive capacity with the subsequent cycle at the next drift level. The filled brace with λ = 70.1 (F8932) is able to maintain a greater compressive capacity than that of the empty brace with λ = 70.1 (E8932) until local buckling initiates during the first compressive excursion to 2% drift, when the compressive capacity of the empty and filled brace become nearly equal.

Similarly, the filled brace with λ = 70.1 (F8932) has a 37% reduction in normalized compressive capacity, while the filled brace with λ = 54.8 (F11445) has an 8% reduction in normalized compressive capacity with the subsequent cycle at the next drift level. It is also of interest to note that the foam-filled brace with λ = 54.8 had global buckling occur during the first compressive excursion to 0.75% story drift as opposed to the first compressive excursion to 0.5% story drift for the equivalent size empty brace. While the empty brace buckled at 433.2 kN, the filled brace was able to maintain 92% of its compressive capacity out to the first compressive excursion to 0.75% story drift before buckling. This delay in the occurrence of global buckling is significant in that it delays the accumulation of plastic strain responsible for local buckling, which is a precursor to brace fracture.

The ability of the foam-filled braces to maintain a larger compressive capacity than that of the equivalent size empty braces until later loading cycles is important because it provides an increase and greater stability in the energy dissipated, thus leading to improved braced frame performance. The greater reduction in compressive capacity for the empty and filled braces with λ = 70.1 compared to the braces with λ = 54.8 is attributed to their larger slenderness. Experimental data compiled and presented by Remennikov and Walpole (1998) established the tendency for braces with greater slenderness to undergo greater reductions in post-buckling compressive capacity than that of less slender braces.

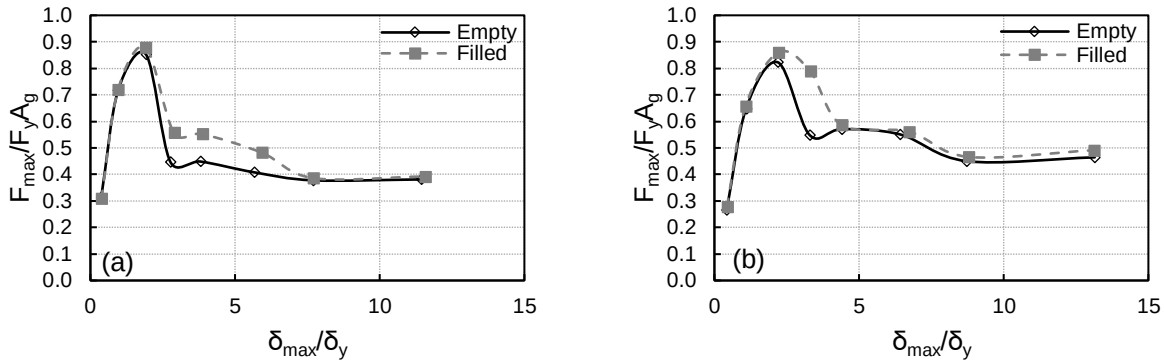

Figure 4-13 Normalized compression envelopes for the first loading cycle to each drift level for (a) braces with λ = 70.1 (D = 89.1 mm; t = 3.2 mm) and (b) braces with λ = 54.8 (D = 114.3 mm; t = 4.5 mm)

4.3.5 In-Plane Displacement

Global buckling places the braces in a half sine wave configuration with the peak displacement at the mid-length of the braces. After the onset of global buckling, the displacement of the braces at their mid-length continues to increase perpendicular to their longitudinal axis and downward within the plane of the frame as axial deformation increases. This displacement within the plane of the frame will be referred to as in-plane displacement. During severe shaking, such as what a building would undergo during a strong earthquake, out-of-plane brace buckling may impact structural partitions and cladding, possibly leading to egress difficulty and falling hazards. While the tested braces buckled within the plane of the frame (in-plane displacement), the brace displacement could have been out-of-plane had a different test configuration been used. As such, the ability to reduce mid-length displacement is crucial irrespective of the direction that the braces buckled during the experimental tests. The inclusion of foam in the voids of the tested CHS braces is able to limit the accumulation of strain in the plastic hinge region, thus leading to smaller in-plane displacement and less severe local buckling. Figure 4-14 provides in-plane displacement as a function of position along the brace length at the end of the second compressive excursion to 2% story drift. This point in the loading cycle is chosen because it is after the initiation of local buckling of all tested braces. The filled brace with a D/t of 25.4 (F11445) exhibits a 6.7% reduction in in-plane displacement (Figure 4-14a) at its mid-length compared to that of its empty counterpart, while the filled brace with a D/t of 27.8 (F8932) exhibits a 16.6% reduction in in-plane displacement (Figure 4-14b) at its mid-length compared to that of its empty counterpart. Although these reductions seem relatively insignificant, due to the formation of a plastic hinge at the brace

mid-length, the axial load sustained by the brace must decrease as the in-plane displacement increases. By reducing the in-plane displacement the filled braces can carry a larger compressive force, thus increasing the area enclosed by the hysteresis loops and subsequent energy dissipation capacity of the braces.

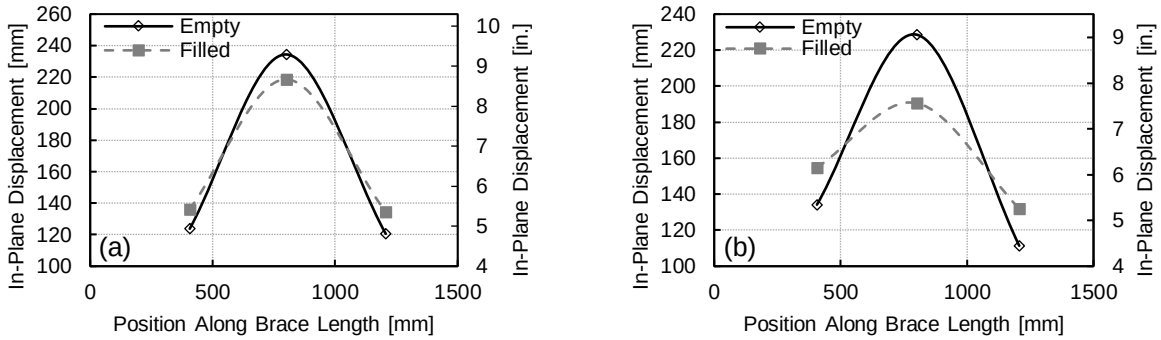

Figure 4-14 In-plane displacement at the end of the second compressive excursion to 2% story drift for: (a) braces with a *D/t* of 25.4; (b) braces with a *D*/*t* of 27.8

4.3.6 Energy Dissipation Capacity

In general, the less slender set of braces (E11445 and F11445) dissipated more energy than the more slender braces (E8932 and F8932). This trend has also been noted in previous studies (Goggins et al. 2005; Popov and Black 1981). Referring to Table 4-7, which displays the cumulative energy dissipated at the last complete cycle of loading, the tensile yield energy (product of tensile yield strength and yield displacement), and the normalized energy dissipated, the filled braces with slenderness ratios of 54.8 and 70.1 show a 23% and 24% increase in energy dissipation capacity compared to that of their equivalent size empty braces, respectively. Energy dissipation is calculated as the area enclosed by the axial force versus axial deformation hysteresis curve. The 89.1 mm diameter brace satisfies the moderately ductile limit for a brace in ordinary concentrically braced frames (OCBFs) since it has a *D/t* of 27.8, while a *D/*t of 25.4 for the 114.3 mm diameter brace satisfies the highly ductile limit for a brace used in special concentrically braced frames (SCBFs). Considering that both empty braces are expected to at least exhibit moderate levels of ductility, the large increase in energy dissipation capacity seen in the foam-filled braces suggests that there is value in using the foam fill even when the section *D/t* is low enough to achieve moderate or high levels of ductility.

Table 4-7 Energy dissipation capacity of the KU braces

Brace	Cumulative energy dissipated, ΣE (kN-mm)	Tensile yield energy, E_y (kN-mm)	Normalized energy dissipated, $\Sigma E/E_y$
E8932	47191	1464	32.2
F8932	58649	1376	42.6
E11445	89185	2308	38.6
F11445	109266	2412	45.3
F11435H1	28564	2070	13.8
F11435H2	96688	2138	45.2

4.3.7 Suitability for Retrofit

To assess the viability of foam fill as a retrofit strategy, two of the braces from the experimental test program have foam inserted through holes along the length of the brace. Both braces are oriented at an angle of 40° from the ground before inserting the foam to replicate retrofit conditions for a full-scale braced frame. The first brace that is tested, F11435H1, experiences global and local buckling occur during the second compressive excursion to 0.5% story drift. The brace buckles at 355 kN and exhibits an asymmetric buckled shape (Figure 4-15a) due to the hinge of the buckled configuration being located at the hole closest to the lower end of the brace (Figure 4-15b). The onset of local buckling initially occurs at the two holes located near the lower end and center of the brace (Figure 4-1a) and is characterized by an outward buckled shape. During subsequent compressive loading cycles, local buckling begins to concentrate at the hole near the lower end of the brace. Tearing around this hole initiates during the second tensile excursion to 1% story drift, leading to brace fracture during the first tensile excursion to 1.5% story drift.

(a) (b)

Figure 4-15 Photographs of F11435H1 showing an (a) asymmetric buckled shape and plastic hinge at the foam insertion hole near the lower portion of the brace and (b) local buckling at the same hole at the end of the second compressive excursion to 0.5% drift

From testing of brace F11435H1, it is observed that the hole size and location for foam insertion are significant factors that influence the overall brace behavior and performance. After conducting a preliminary finite element analysis and taking into consideration the relatively rapid curing rate of the foam, it is determined that a 16 mm diameter hole located 60 mm from the top endplate are a suitable size and location for F11435H2 (Figure 4-1b). Global buckling of this brace occurs during the first compressive excursion to 1% story drift at 339 kN and places the brace into a half sine wave buckled shape. Local buckling initiates around the foam insertion hole during the second compressive excursion to 0.75% story drift (Figure 4-16a), but occurs at the mid-length of the brace during the first compressive excursion to 2% story drift (Figure 4-16b). As opposed to local buckling being concentrated in one section of the brace as in the previously tested filled braces, outward local buckles are located on either side of the brace midpoint that is identified by the welded stud (Figure 4-16b). It is postulated that this is a result of non-homogeneity of the foam along the brace length. During the second compressive excursion to 2% story drift the buckled shape changes to inward as the foam crushes under increasing lateral displacement. The brace ultimately fractures approximately 150 mm from the brace midpoint during the 1st tensile excursion to 4% story drift.

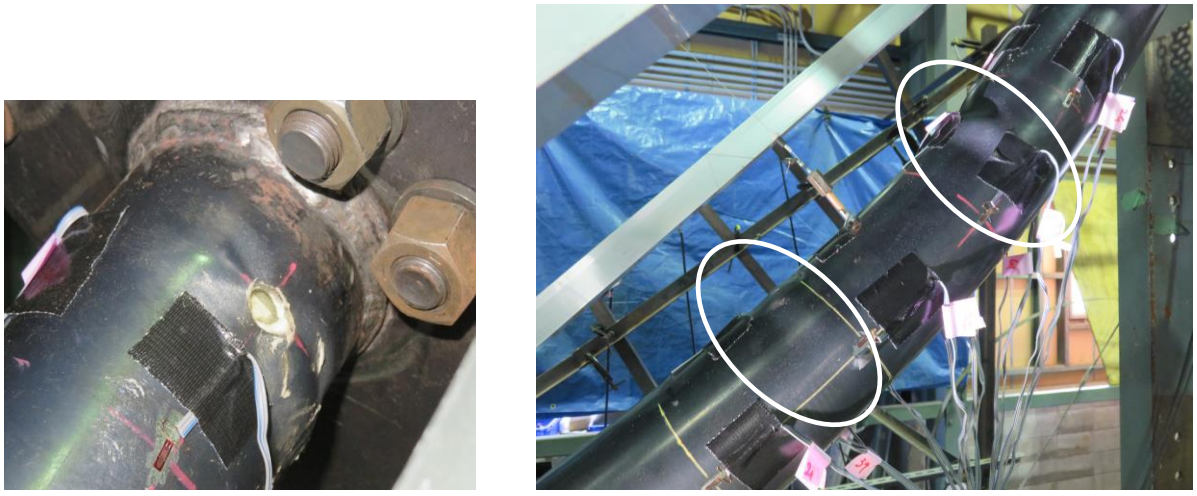

(a) (b)

Figure 4-16 Local buckling of brace F11435H2 at the (a) hole insertion location at the end of the second compressive excursion to 0.75% story drift and at the (b) mid-length at the end of the first compressive excursion to 2% story drift

In regard to energy dissipation and ductility, F11435H2 has superior performance compared to that of F11435H1. Referring to Table 4-7, the normalized energy dissipation for F11435H2 is nearly four times greater than that of F11435H1. Considering that F11435H2, with a *D/t* of 32.7,

falls well above the ductility limits stipulated for a highly ductile brace, its performance regarding energy dissipation and ductility exceeds that of the empty brace with a *D/t* of 25.4 (E11445). While more comprehensive testing needs to be performed to establish an optimal procedure for filling in-situ braces with foam, the results suggest that fill in-situ HSS braces is a viable seismic retrofit option.

4.4 Experimental Program (UM)

4.4.1 Test Specimens

The measured brace geometric properties for the tests performed at the UM are listed in Table 4-8 and include three different brace sizes. All braces are 2813 mm in length and are intentionally selected to have *D/t* greater than 27.9, which is the moderately ductile limit for round HSS members fabricated from ASTM A500 Gr. B steel (AISC 2016a). The moderately ductile limit is calculated considering an elastic modulus of 200 GPa, an R_y of 1.4, and an F_y of 290 MPa, which are nominal properties of ASTM A500 Gr. B steel. Having braces with *D/t* substantially larger than the moderately ductile limit will help provide an indication as to whether *D/t* limits can be relaxed when considering the inclusion of the foam fill. The brace nomenclature is the same as previously used for the KU tests.

Table 4-8 Test matrix of measured properties for UM braces (A500 Gr. B steel braces)

Bracing member	Diameter D (mm)	Thickness t (mm)	Length L_B (mm)	Diameter-to-thickness ratio[a] D/t	Slenderness ratio[b] λ
E1273	127.2	2.89	2813	44.0	77.3
F1273	127.0	2.86	2813	44.4	77.4
E1143	114.5	2.75	2813	41.7	86.0
F1143	114.5	2.83	2813	40.5	86.1
E1013	101.6	2.93	2813	34.7	97.4
F1013	102.0	2.92	2813	35.0	97.0

[a] Calculated using measured brace outer diameter and wall thickness
[b] λ calculated using pin to pin distance of 3398 mm

4.4.2 Material Properties

4.4.2.1 Steel

At least three tensile coupons are extracted from each brace at 90°, 180°, and 270° from the weld seam to determine pertinent mechanical properties. The coupons are tested in accordance with ASTM E8 (2016). Nominal coupon dimensions are shown in Figure 4-17 and average measured material properties are listed in Table 4-9.

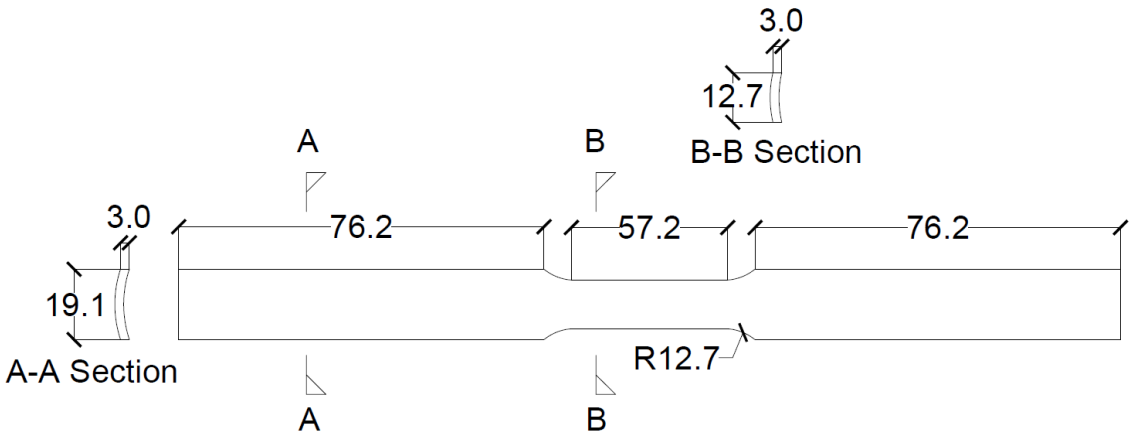

Figure 4-17 Typical tensile coupon geometry and dimensions (units: mm)

Table 4-9 Average measured properties for each UM brace

Bracing member	Elastic modulus (MPa)	F_y (MPa)	F_u (MPa)	F_u/F_y
E1273	230500	353	406	1.15
F1273	218000	358	414	1.16
E1143	198200	309	380	1.23
F1143	218400	333	407	1.22
E1013	222600	344	407	1.18
F1013	223700	345	408	1.18

4.4.2.2 Foam

To ensure optimal foam expansion, the foam is mixed in liquid quantities that allow for thorough mixing (no more than 1000 ml of each part). As such, more than one foam pour is necessary to fill the entire length of a brace. Specifically, braces F1273 and F1143 are filled with five pours each, while brace F1013 is filled with six pours. The braces are filled with foam along their entire length

using a 50.8 mm diameter hole located at the center of the top endplate. During each foam pour, a small sample is collected in an aluminum loaf pan (Figure 4-18). Cube specimens with 50.8 mm edge lengths are machined from the collected samples and tested under monotonic compression to capture any effects associated with inhomogeneity of the foam. The test setup is shown in Figure 4-3 and is the same as that used for the KU foam tests. Figure 4-19 shows stress-strain responses of three specimens tested from a single representative pour for each brace. In contrast to the foam from the KU tests, there is noticeable consistency in the foam behavior. On average, the initial elastic modulus ranges from 133 MPa to 140 MPa, the crush strength ranges from 4.3 MPa to 4.8 MPa, and the maximum stress ranges from 17.2 MPa to 18.6 MPa. The consistency in the foam behavior is likely attributable to the consistency in the mixing procedure and the laboratory temperature during the pours leading to similar foam expansion. Additionally, the foam properties are determined before the braces are tested, which eliminates the possibility of damage sustained during testing affecting the results.

Figure 4-18 Foam sample collected during a foam pour

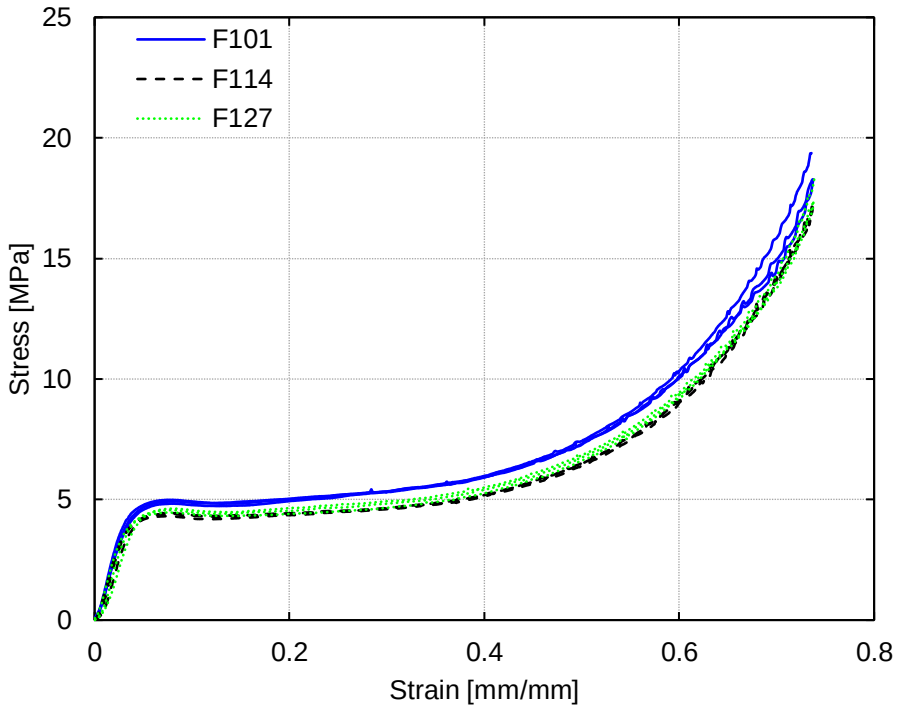

Figure 4-19 Representative monotonic compression stress-strain response of foam specimens from each filled brace (UM)

4.4.3 Test Setup and Loading Protocol

Similar to the KU test setup, the brace tests at the UM are conducted in a pinned load frame (Figure 4-20 and Figure 4-21). The braces are initially oriented at a 40.6° angle with the bottom load frame beam and have 25.4 mm thick endplates fillet welded to their ends. The endplates are bolted into mechanical pin connections using eight 15.9 mm diameter high strength bolts at each end. Lateral displacement is applied to the top of the load frame quasi-statically at 0.4 mm/s using a hydraulic actuator. The lateral force is measured using a load cell connected to the hydraulic actuator. Axial force in the brace is calculated using Equation 4.1.

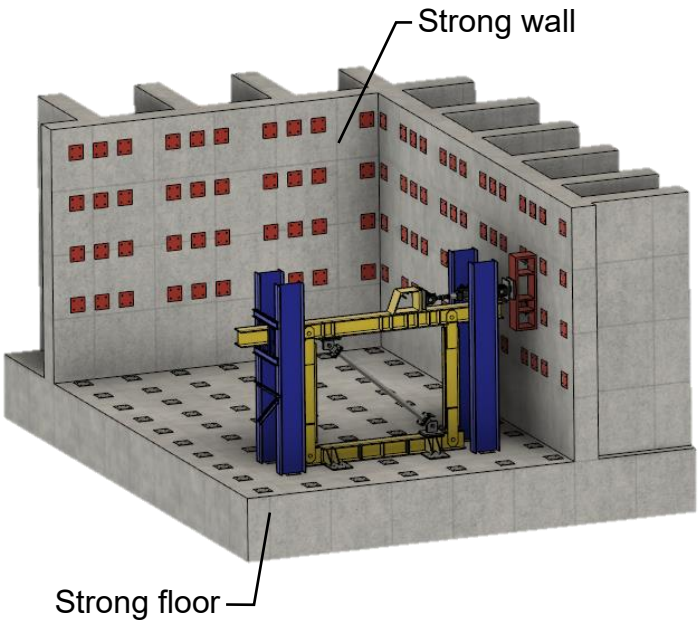

Figure 4-20 Overview of the brace test setup at UM

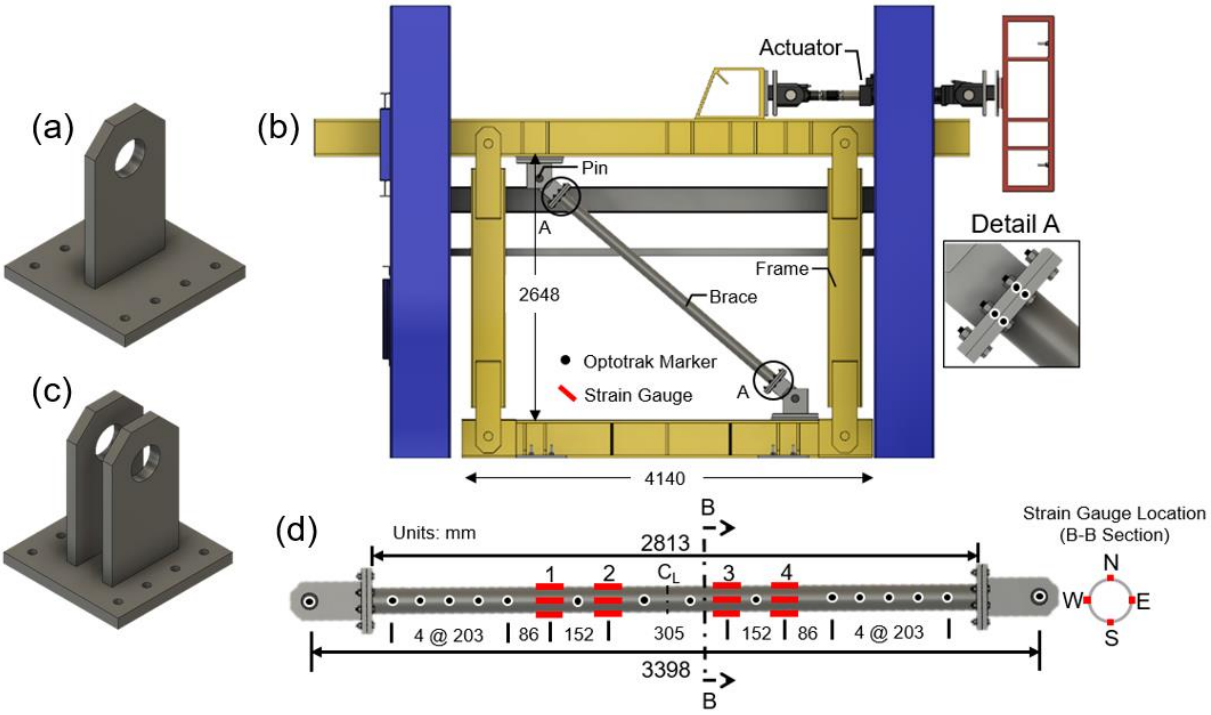

Figure 4-21 Drawing of the UM test setup including the (a) single plate pin connection, (b) load frame, (c) double plate pin connection and (d) brace instrumentation

The loading protocol is the same as that used for the KU tests and is developed in terms of story drift considering a frame height of 2648 mm and an initial brace orientation of 40.6°. The loading protocol is presented in Table 4-10 with the actuator displacements and corresponding brace axial deformation.

Table 4-10 Loading protocol (UM)

Number of cycles	Story drift (%)	Actuator displacement (mm)	Axial deformation (mm)
2	0.1	2.6	2.0
2	0.25	6.6	5.0
2	0.5	13.2	10.1
2	0.75	19.9	15.1
2	1	26.5	20.1
2	1.5	39.7	30.2
2	2	53.0	40.2
2	3	79.4	60.3
2	4	105.9	80.4

Axial deformation is measured using Northern Digital Inc.'s Optotrak Certus Motion Capture System. This system consists of light emitting diodes (markers) that are tracked in three-dimensional space by position sensors. The markers are placed along the length of the braces, on the connection plates, and on the pins (Figure 4-21b and Figure 4-21d) to capture relevant deformations. Brace axial deformation is calculated as the distance between the markers located on the pins. Strain is measured using strain gauges that are oriented parallel to the longitudinal axis of the brace and placed at quarter points of the brace circumference. The strain gauges are concentrated at the brace mid-length (plastic hinge region) where the most inelastic deformation is anticipated (Figure 4-21d).

4.5 Experimental Results

4.5.1 Experimental Summary

A detailed summary of the experimental data is provided in Appendix B along with the hysteretic response of each brace. Hysteretic responses comparing the empty and equal size filled brace behavior are shown in Figure 4-22. The red filled circles indicate the instant of fracture. A summary of the experimental data is provided in Table 4-11.

The foam fill has a negligible influence on the brace hysteretic response regarding the elastic stiffness and maximum tensile and compressive forces. However, the influence of the foam is shown in the hysteretic response by its ability to help most of the foam-filled braces undergo additional cycles of loading before fracture compared to the empty braces.

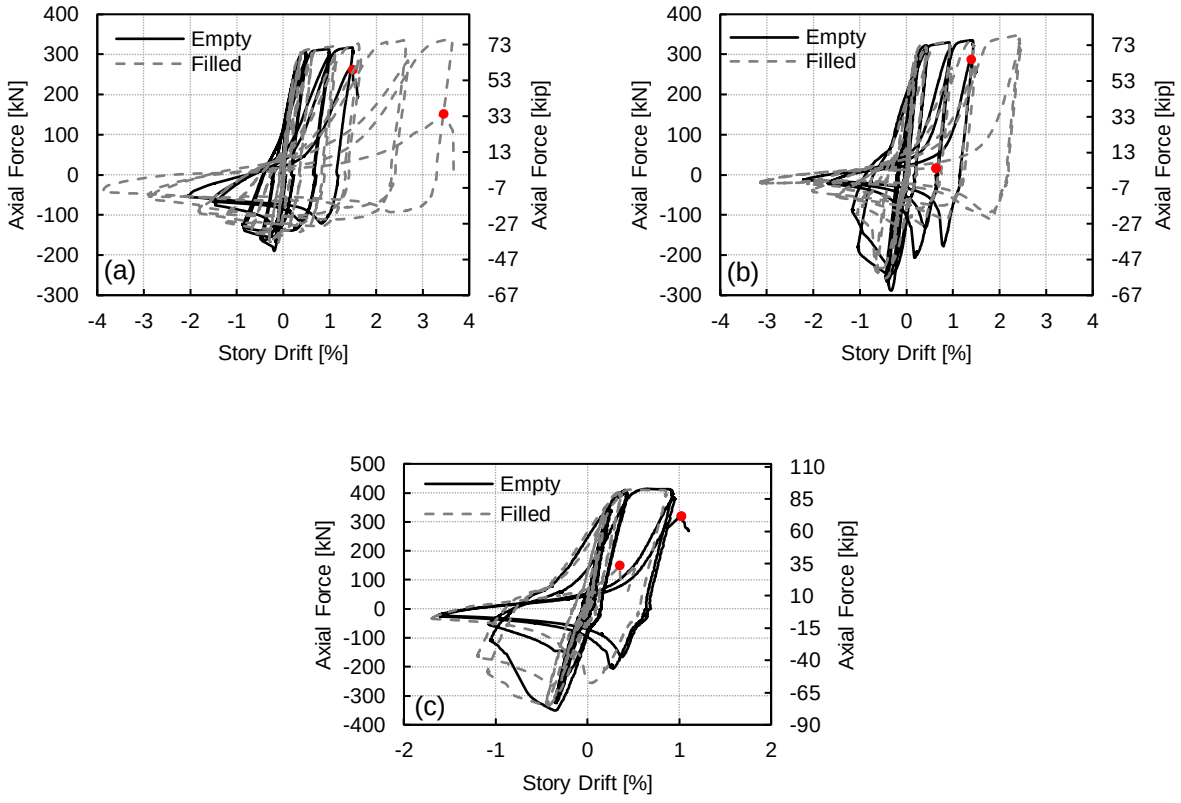

Figure 4-22 Axial force-story drift responses for the: (a) 101 mm diameter specimens; (b) 114 mm diameter specimens; and (c) 127 mm diameter specimens

Table 4-11 Summary of experimental data (UM)

Brace	Elastic stiffness (kN/mm)	Buckling mode	Maximum force (kN)		Limit State[a]	
			Tension	Compression	Local buckling	Fracture
E1273	64.8	OoP/IP	413.7	350.6	1st; -1.0	1st; 2.0 (1.10)
F1273	75.0	OoP/IP	411.3	335.4	1st; -1.0	2nd; 1.5 (0.35)
E1143	69.6	OoP/IP	335.3	288.5	2nd; -1.0	2nd; 2.0 (1.39)
F1143	74.2	OoP/IP	348.8	258.1	1st; -2.0	1st; 4.0 (0.64)
E1013	67.8	OoP	317.3	189.8	2nd; -1.0	2nd; 2.0 (1.49)
F1013	77.3	OoP	338.3	173.9	1st; -3.0	2nd; 4.0 (3.44)

[a]Cycle; drift level at the initiation of local buckling (mid-length) and fracture. A negative drift level indicates compression and a positive drift level indicates tension. The number in parentheses denotes the drift percentage at fracture.

4.5.2 E1013 and F1013

Brace E1013 (D/t = 34.7; λ = 97.4) has the smallest D/t and is the most slender of the tested braces. While it is generally agreed upon that width-to-thickness ratio and global slenderness (λ) are the two most influential parameters on brace seismic performance (AISC 2005), contradictory conclusions have been reached regarding which parameter is most influential. Fell et al. (2009) concluded that width-to-thickness ratio is the predominant factor influencing fracture ductility and that while member slenderness affects fracture ductility, it does so to a lesser extent. Tremblay (2002) noted that local buckling is more severe in less slender braces even when D/t is small, suggesting that global slenderness is the main factor affecting brace ductility. Brace E1013 (largest λ) did in fact outperform the other two empty braces with respect to ductility, fracturing during the second tensile excursion to 2% drift at a drift level of 1.49%.

For empty brace E1013, global buckling initiates during the first compressive excursion to 0.75% drift and occurs out of the plane of the frame (toward the west side as indicated by Figure 4-21d). Out-of-plane buckling is unexpected given that the mechanical pin connections (Figure 4-21a) are oriented to induce zero moment in the plane of the frame. The out-of-plane buckling is likely a result of the frame not being perfectly planar, causing the axial force induced in the brace to have a slight eccentricity. Figure 4-23 shows the brace out-of-plane displacement at the end of the first compressive excursion to 0.75% drift as a function of position. The out-of-plane displacement is measured using the Optotrak markers, where a position of 0 marks the brace centerline, negative position values indicate markers on the upper half of the brace closest to the top pin connection, and positive values indicate markers closest to the bottom pin connection. The out-of-plane

displacement peaks near the brace centerline at approximately 70.2 mm, whereas it peaks at 13 mm during the previous compressive excursion. The out-of-plane displacement increases with subsequent compressive excursions, ultimately reaching a peak of 245 mm at the end of the first compressive excursion to 2% drift (Figure 4-24a). Large out-of-plane displacement is undesirable as it can damage cladding and other building components, potentially leading to falling hazards that are detrimental to life safety and increase repair costs. Local buckling initiates during the second compressive excursion to 1% drift and is characterized by a pronounced inward buckle concentrated along a small section of the brace (Figure 4-24b). Further compressive cycling increases the severity of the buckled shape, as shown in Figure 4-24c. The brace eventually fractures soon after the initiation of local buckling with fracture occurring during the second tensile excursion to 2% drift. The fracture extends through approximately half the circumference of the brace and occurs approximately 75 mm to the left of the brace mid-length (Figure 4-24d). The force in the brace decreases immediately at the instant of fracture.

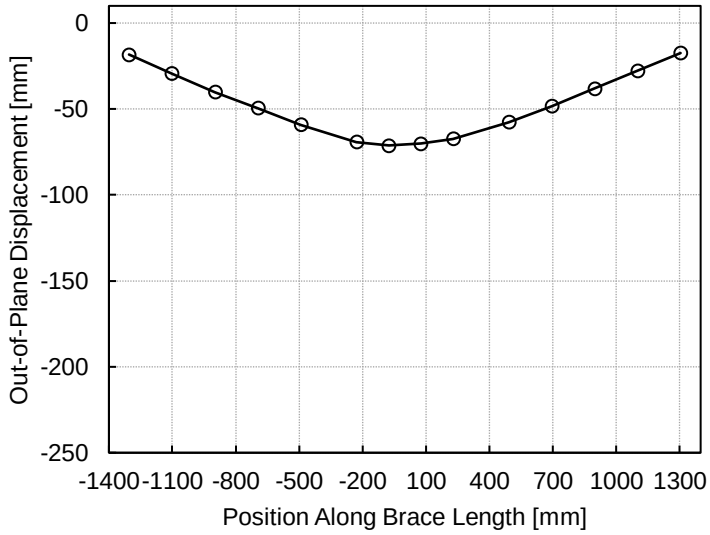

Figure 4-23 Out-of-plane displacement as a function of brace position (end of first compressive excursion to 0.75% drift) for E1013

(a)

(b)

(c)

(d)

Figure 4-24 Photographs of a) out-of-plane displacement at the end of the second compressive excursion to 2% drift, b) local buckle initiation after the second compressive excursion to 1% drift, c) severe local buckling after the first compressive excursion to 1.5% drift and d) brace fracture during the second tensile excursion to 2% drift for E1013

Filled brace F1013 (D/t = 35.0; λ = 97.0) has an initial axial elastic stiffness of 77.3 kN/mm, which is approximately 14% larger than that of empty brace E1013 (67.8 kN/mm). In tests of empty and high strength grout-filled HSS braces under reverse cyclic loading by Fell et al. (2009), the filled braces exhibited a nearly 50% greater stiffness than that of the empty braces (144 kN/mm to 213

kN/mm). The minimal difference in elastic stiffness between the empty and foam-filled brace relative to that of empty and grout-filled braces suggests that traditional seismic design practices can be followed without having to explicitly consider the presence of the foam fill. This statement is further supported by the maximum tensile and maximum compressive forces in the empty and foam-filled braces being close in value. Specifically, the empty and filled braces reach peak axial tensile forces of 317 kN and 338 kN (6.6% increase), respectively, and peak axial compression forces of 190 kN and 174 kN (8.4% decrease), respectively. The greater tensile strength of the filled brace is presumably from its larger yield strength (Table 4-9), since the foam is not expected to have any influence on tensile strength because of its low strength in tension (roughly 4 MPa). The lower compression strength of the filled brace may have resulted from larger local and global imperfections.

Global buckling of brace F1013 occurs during the first compressive excursion to 0.75% drift and is accompanied by a peak out of plane displacement of 57.3 mm, which is approximately 18% less than that of the empty brace. In this case, part of the reduction of out-of-plane displacement is attributed to the filled brace having 3 mm less axial compression than that of the empty brace during the first compressive cycle to 0.75% drift. Local buckling initiates at a drift level three times greater than that of the empty brace, occurring during the first compressive excursion to 3% drift. The local buckles occur 114 mm to the left of the brace center line toward the upper end of the brace (Figure 4-25a) and at the bottom of the brace near the interface of the brace and endplate (Figure 4-25b). The foam causes the buckles to protrude outward to form a smooth profile that resembles that of a dome. This shape contrasts with that of the empty brace, which exhibits severe inward local buckling. Further compressive cycling causes the amplitude of the local buckle at the brace mid-length to substantially increase, leading to a disc-like buckled shape at the end of the second compressive excursion to 3% drift (Figure 4-25c). The brace is able to sustain one tensile excursion to 4% drift before finally fracturing during the second tensile excursion to 4% drift (Figure 4-25d).

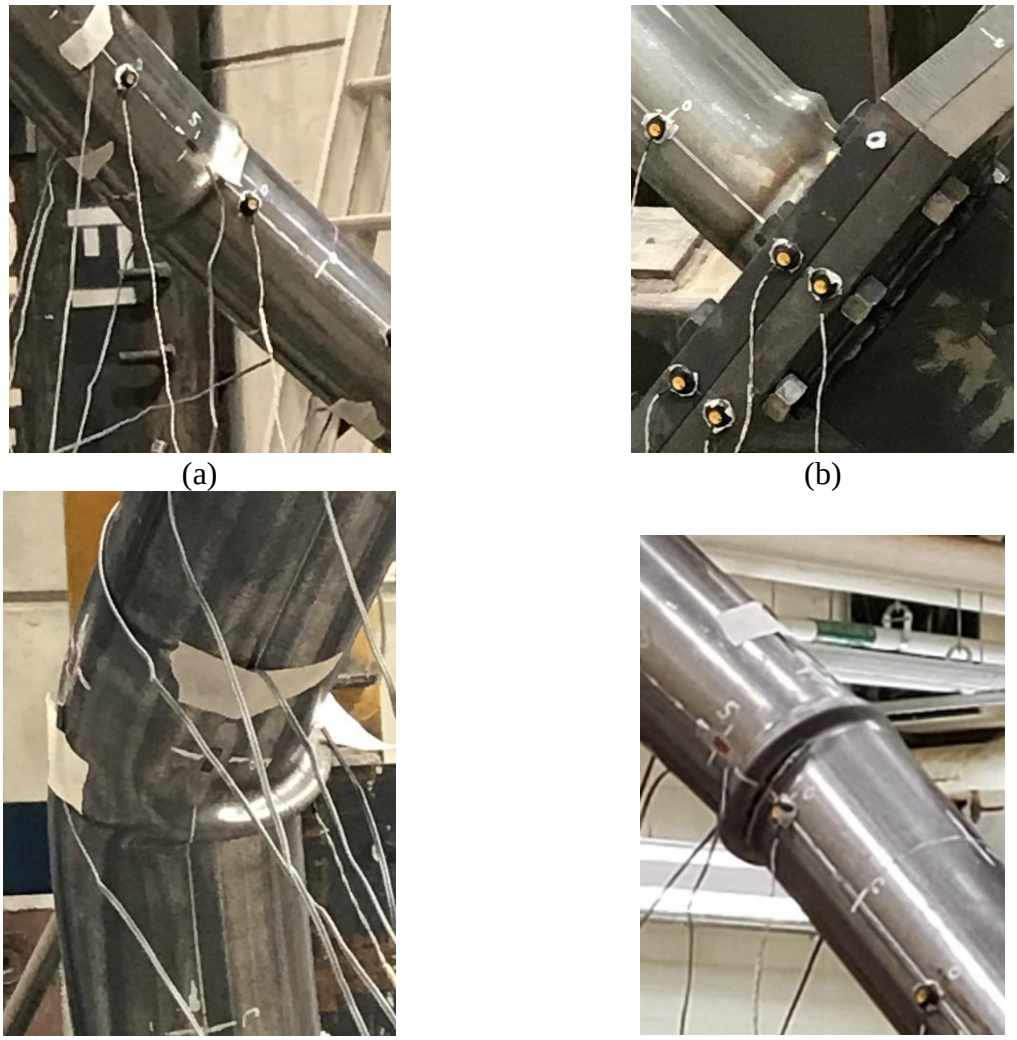

(a) (b) (c) (d)

Figure 4-25 Photographs of (a) local buckling near the brace mid-length at the end of the first compressive excursion to 3% drift, (b) local buckling near the bottom of the brace at the end of the first compressive excursion to 3% drift, (c) local buckling at the brace mid-length at the end of the second compressive excursion to 3% drift, and (d) brace fracture during the second tensile excursion to 4% drift for F1013

Regarding cumulative energy dissipated, brace F1013 dissipated 2.9 times more energy than brace E1013. As the energy dissipated per cycle of loading is fairly similar, the substantial difference in energy dissipated can be attributed to the greater ductility of the filled brace resulting from the use of the foam infill. The increased ductility of the filled brace compared to that of the empty brace can be explained by its ability to delay the accumulation of plastic strain that drives fracture at the brace mid-length. Figure 4-26 shows the strain distribution in the plastic hinge region based on the east (E) strain gauges with the horizontal axis referring to strain gauge location (Figure 4-21d) and the vertical axis referring to compressive strain. Strain readings are extracted for the empty and

filled brace during the cycle prior to the initiation of local buckling in the empty brace. Figure 4-26 shows the strain distribution during the first compressive excursion to 1% drift at a drift level of 0.67% for braces E1013 and F1013. The surface strains of the empty brace are larger than that of the filled brace at all strain gauge locations with the ratio of empty to filled brace strain reaching a peak value of 3.2 at strain gauge location two.

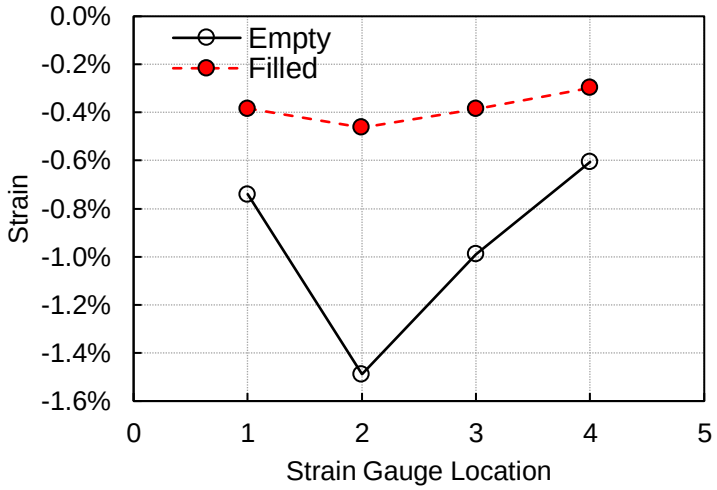

Figure 4-26 Strain distribution in the plastic hinge region for E1013 and F1013 during the first compressive excursion to 1% drift

4.5.3 E1143 and F1143

Braces E1143 and F1143 are tested using a double plate pin connection (Figure 4-21c) as opposed to a single plate pin connection (Figure 4-21a) to prevent the out-of-plane buckling and deformation of the connection plates observed in the tests of E1013 and F1013. The progression of brace behavior is similar to that of the previously described braces with tensile yielding occurring first, followed by inelastic global buckling, local buckling and then brace fracture. E1143 has an initial axial elastic stiffness of 69.6 kN/mm and globally buckles out-of-plane at 289 kN during the first compressive excursion to 0.75% drift. The buckling is accompanied by a peak out-of-plane displacement of 24.1 mm near the brace mid-length. Local buckling initiates during the second compressive excursion to 1% drift at approximately 114 mm to the left of the brace centerline (closer to the top half of the brace) and occurs on the same face as the east strain gauges (Figure 4-27a). Although local buckling initiates during the same cycle as that of E1013, the inward local buckle is more pronounced. The more prominent local buckle is expected as E1143

(D/t = 41.7; λ = 86.0) has a larger D/t and is less slender than that of E1013 (D/t = 34.7; λ = 97.4). With continued cycling, the brace begins to exhibit a combination of in and out-of-plane buckling during the first compressive excursion to 1.5% drift. Specifically, the brace moves downward within the plane of the frame while also moving out of plane toward the west. This combination of buckling modes causes the local buckle to span both the north and east faces of the brace (Figure 4-27b). Thereafter, striations form on the north face of the brace during the first tensile excursion to 2% drift (Figure 4-27c). Fracture occurs during the second tensile excursion to 2% drift near the brace mid-length and extends through a quarter of the brace circumference (Figure 4-27d).

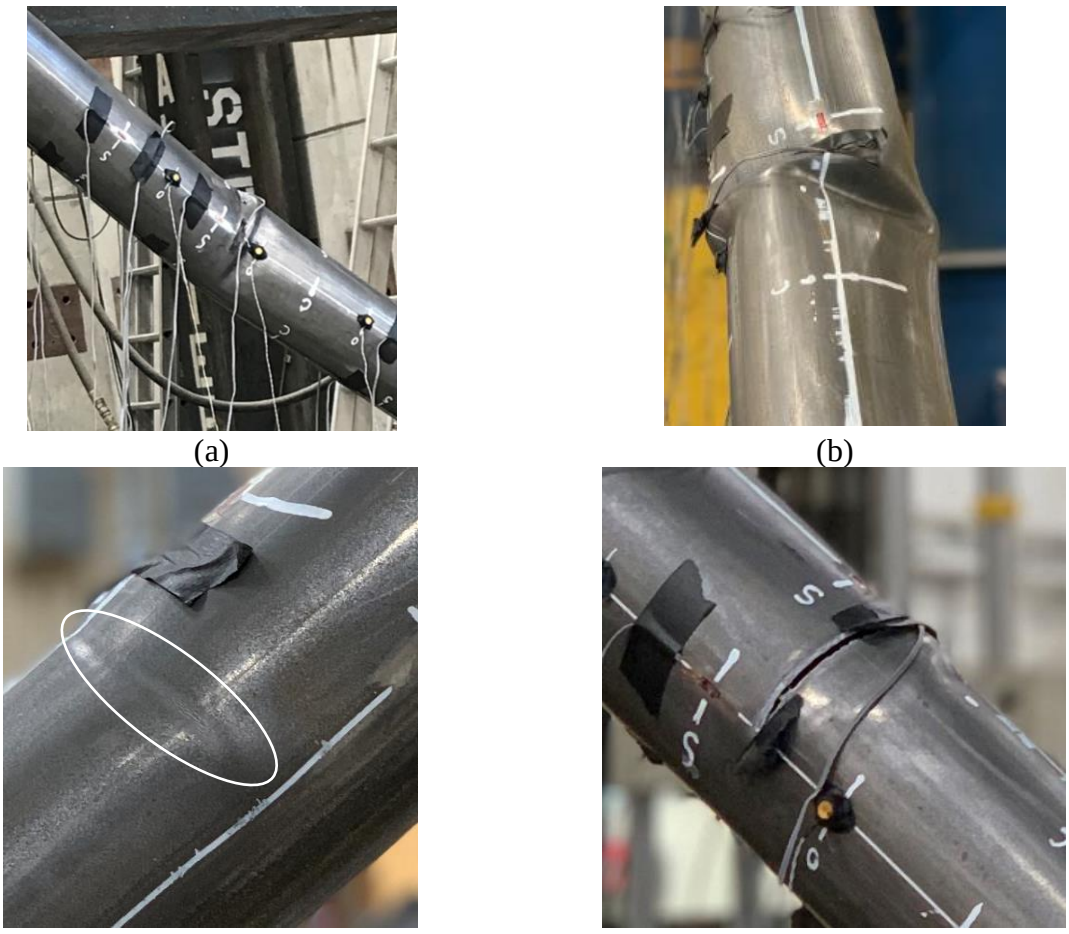

(a) (b) (c) (d)

Figure 4-27 Photographs of (a) local buckling at the end of the second compressive excursion to 1% drift, (b) local buckling at the end of the first compressive excursion to 1.5% drift, (c) striations at the end of the first tensile excursion to 2% drift, (d) and brace fracture during the second tensile excursion to 2% drift for E1143

Brace F1143 has an initial elastic stiffness of 74.2 kN/mm, which is approximately 6.6% larger than that of E1143. Maximum axial tensile and compressive forces achieved during testing are 349 kN and 258 kN, respectively, which are approximately 4% larger and 11% smaller than that of E1143, respectively. Global buckling initiates during the first compressive excursion to 0.75% drift and is accompanied by a peak out of plane displacement near the brace mid-length of approximately 43 mm. Eventually a combination of in and out-of-plane buckling occurs during the first compressive excursion to 1% drift with the buckling predominately in-plane for the remainder of the test. During the first compressive excursion to 1.5% drift, deformation that resembles a repeated half sine wave is observed at the brace mid-length. Loading during the second compressive excursion to 1.5% drift causes the wave pattern to become more pronounced (Figure 4-28a), eventually leading to the initiation of outward local buckling at approximately 121 mm to the left of the brace centerline toward the upper end of the brace during the first compressive excursion to 2% drift (Figure 4-28b). The ability of F1143 to have the onset of local buckling occur three cycles later than that of E1143 is attributed to an improved distribution of plasticity at its mid-length. The foam spreads plastic strain over a greater length, ultimately leading to a reduction of plastic strain demand and an ability to sustain additional cycles prior to fracture. With increasing cycles under compression the outward local buckled shape of F1143 is maintained, but becomes progressively more severe with the buckled shape eventually taking the form of a ring shaped disc (Figure 4-28c). The ensuing brace fracture occurs during the first tensile excursion to 4% drift (Figure 4-28d), which is double the drift level attained by E1143.

The improved behavior of foam-filled braces compared to that of empty braces is further shown in Figure 4-29, which displays the deformed shapes of E1143 at the end of the second compressive excursion to 1.5% drift and F1143 at the end of the first compressive excursion to 2% drift. E1143 is divided into two equal length straight segments while F1143 has a smooth curved profile. The ability of the foam to cause the deformed shape of F1143 to resemble a smooth curve reduces the accumulation of plastic strain at its mid-length, ultimately leading to improved ductility. Similar behavior was observed in cyclic tests of empty and concrete-filled CHS braces by Sheehan (2013), where the concrete-filled braces showed a delay in the onset of local buckling and improved ductility.

(a) (b) (c) (d)

Figure 4-28 Photographs of a (a) sine wave deformation pattern at the end of the second compressive excursion to 1.5% drift, (b) mid-length local buckling at the end of the first compressive excursion to 2% drift, (c) more severe local buckling at the end of the second compressive excursion to 2% drift and (d) brace fracture during the first tensile excursion to 4% drift for F1143

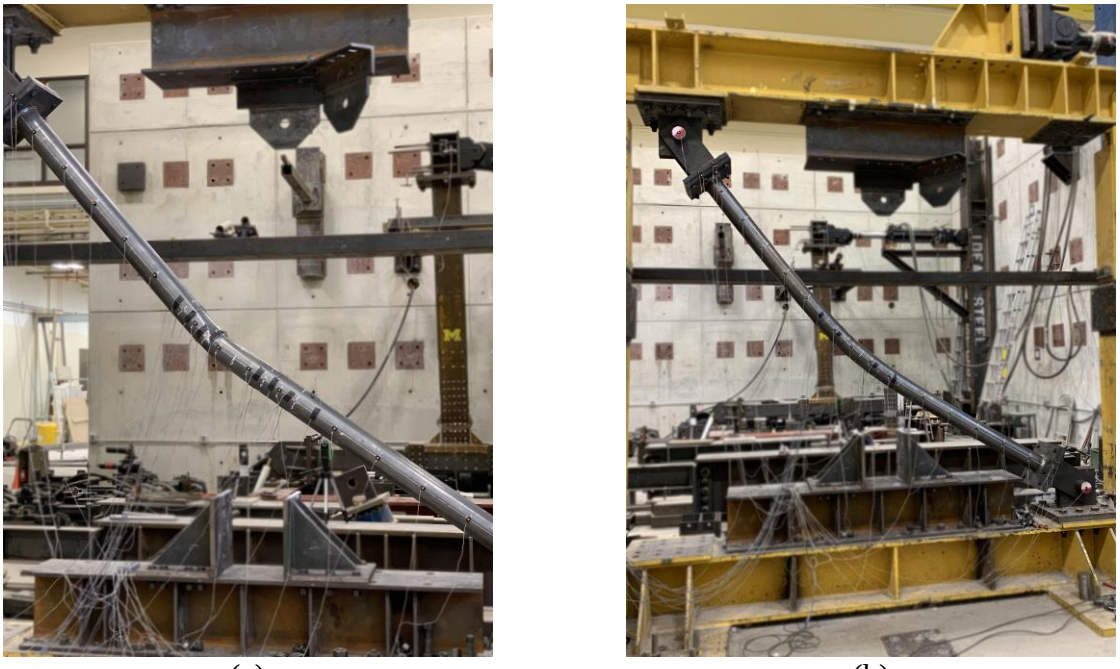

(a) (b)

Figure 4-29 Deformed shape of (a) E1143 at the end of the second compressive excursion to 1.5% drift and (b) F1143 at the end of the first compressive excursion to 2% drift

Similar to E1013 and F1013, the energy dissipated per cycle of loading for E1143 and F1143 are nearly identical with the exception of a few slightly larger values for the F1143 brace. However, the cumulative dissipated energy for the F1143 brace is 72% larger than that of the empty brace, owing to its ability to sustain more cycles of loading prior to fracture. Because greater energy dissipation occurs during cycles at larger drift levels, there is a substantial increase in cumulative energy dissipation for the filled brace even though fracture is only delayed by a few cycles.

The enhanced ductility of the F1143 brace can further be explained by the reduced strain values measured relative to those of E1143. Figure 4-30 shows the strain distribution (based on the east strain gauges) at the end of the first compressive excursion to 1% drift for braces E1143 and F1143. The filled brace has smaller strains at three of the four strain gauge locations in the plastic hinge region with a peak ratio of empty to filled brace strain of 1.38 at strain gauge location three. This reduction of strain in the plastic hinge region exemplifies the beneficial influence of the foam fill, as lower strains lead to a prolonged brace fracture life.

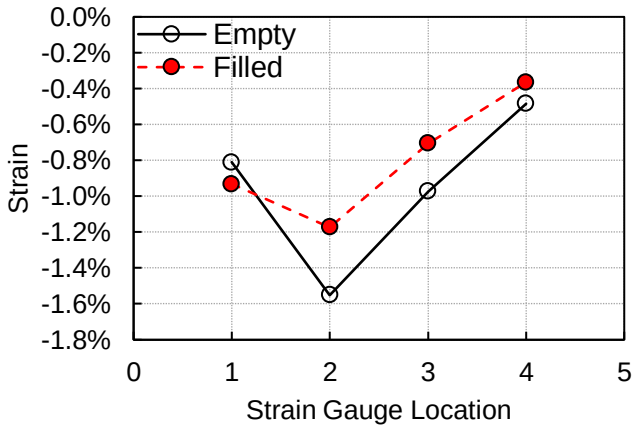

Figure 4-30 Strain distribution in the plastic hinge region for E1143 and F1143 at the end of the first compressive excursion to 1% drift

4.5.4 E1273 and F1273

Braces E1273 and F1273 are also tested using a double plate pin connection (Figure 4-21c) and both have a nominal *D/t* of 42.0, which is well above the moderately ductile limit (*D/t* = 27.9) stipulated in the current AISC Seismic Provisions (AISC 2016a). These braces are also the least slender (λ = 77.3) of the UM braces. While the filled brace has a 16% larger axial elastic stiffness than that of the empty brace, it reaches a smaller maximum compressive axial force of 335 kN.

The maximum axial tensile forces for the empty and filled braces, 414 and 411 kN, respectively, are nearly the same, reflecting the negligible influence that the foam fill has on brace behavior when under tension. For both braces, local buckling initiates during the first compressive excursion to 1% drift. The empty brace has severe inward local buckling on the north and east faces (Figure 4-31a) owing to a combination of in and out-of-plane buckling, while F1143 has outward local buckling that occurs approximately 152 mm to the left of the brace centerline toward the upper end of the brace (Figure 4-31c). Brace fracture for the filled brace (Figure 4-31d) occurs one cycle earlier than that of the empty brace (Figure 4-31b) even though the strain in the plastic hinge region at the end of the second compressive excursion to 0.75% drift (the cycle before the initiation of local buckling for both braces) is smaller than that of the empty brace at all strain gauge locations for the north, east, south and west strain gauges. Figure 4-32 presents the strain based on the east strain gauges for the empty and filled brace and shows that the strain on the surface of the filled brace is at least two times smaller than that of the empty brace at all strain gauge locations. Given the previously discussed test results, it is unlikely that use of the foam fill is detrimental to brace performance. Furthermore, while the ductility capacity of the filled brace is not improved, the empty brace only dissipates 1.2% more cumulative energy than that of the filled brace even though it sustained an additional cycle before fracture. A major finding from testing braces E1273 and F1273 is that there is a maximum *D/t* where the foam is no longer effective at improving brace ductility.

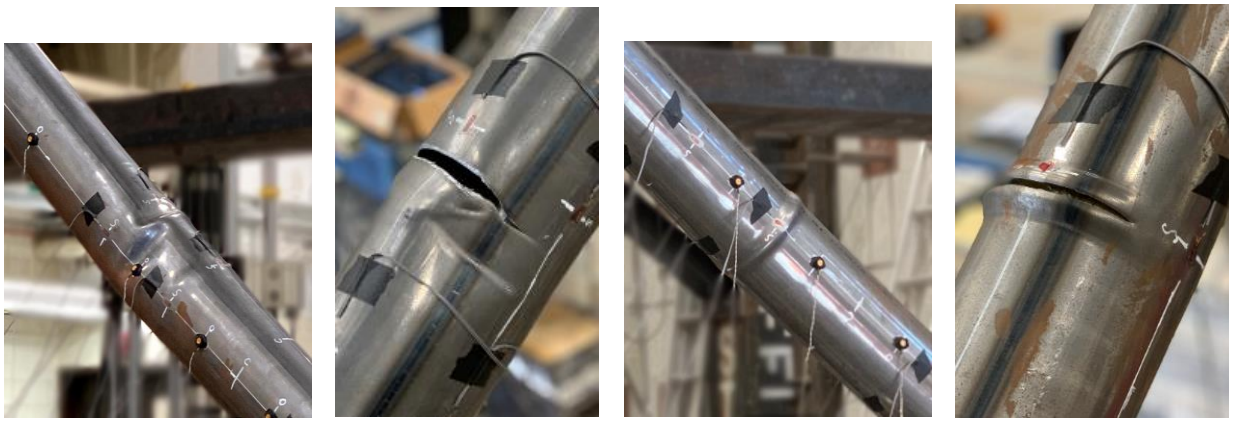

(a) (b) (c) (d)

Figure 4-31 Photographs of (a) local buckling for E1273 at the end of the first compressive excursion to 1% drift, (b) fracture for E1273 during the first tensile excursion to 2% drift, (c) local buckling for F1273 at the end of the first compressive excursion to 1% drift, and (d) fracture for F1273 during the second tensile excursion to 1.5% drift

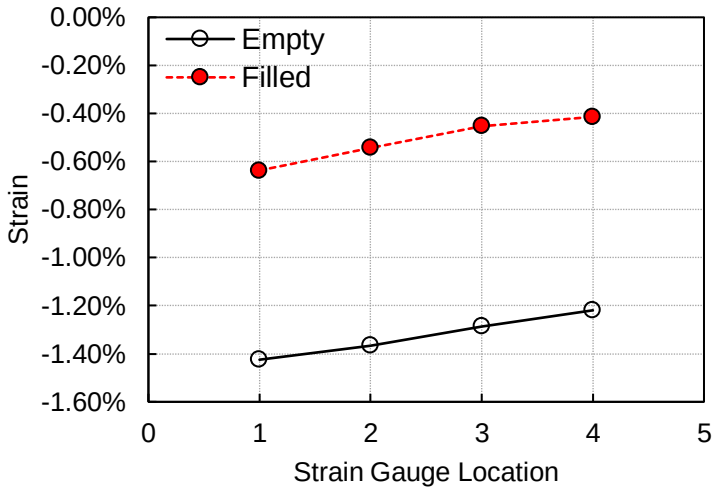

Figure 4-32 Strain distribution in the plastic hinge region for E1273 and F1273 at the end of the second compressive excursion to 0.75% drift

4.6 Conclusions

Two experimental campaigns were undertaken to investigate the ability of a lightweight, expanding polyurethane foam fill to enhance the performance of CHS braces under large cyclic loads. The first experimental investigation examined CHS braces fabricated from Japanese STK 400 steel and the second experimental investigation examined CHS braces fabricated from ASTM A500 Gr. B steel. In total, 12 braces were tested under increasing reverse-cyclic loads with D/t and λ ranging from 25.4 to 44.4 and 54.4 to 97.4, respectively. The following conclusions can be drawn from the results:

- With the exception of the braces with a D/t greater than 44.0, the foam is more effective at improving ductility in braces that have a D/t above the moderately ductile limit specified in the AISC Seismic Provisions (AISC 2016a).
- It is postulated that there is a maximum threshold of D/t where the foam no longer provides improvement to brace ductility. The finite element parametric study presented in the next chapter establishes a threshold D/t and provides valuable information regarding what section sizes benefit most from the inclusion of the foam fill.
- Compared to their empty counterparts, the onset of local buckling and fracture occurs at least one cycle later for the filled braces except for filled brace F1273, which experiences local buckling and fracture during the same cycle and one cycle earlier, respectively,

compared to its empty counterpart (E1273). The greatest improvement in ductility is shown through testing of braces E1013 and F1013. Filled brace F1013 (D/t = 35.0; λ = 97.0) experiences local buckling and fracture five and four cycles later, respectively, than its empty counterpart (E103). This increase in ductility is substantial as shown by the ability of the filled brace to sustain force during excursions to 4% drift compared to only 2% drift for the empty brace.

- The percentage increase in cumulative dissipated energy between empty and equal size foam-filled braces ranges from 22.5% to 191%, indicating that a substantial increase in energy dissipation can be achieved by filling braces with the foam.
- The differences in the elastic stiffness and maximum tension and compression values for empty and filled braces are small, suggesting that traditional seismic design practices can be adhered to without explicit consideration of the foam. The maximum differences in the elastic stiffness, maximum tension, and maximum compression values for corresponding empty and filled braces are 14.6%, 6.4%, and 11.1%, respectively.
- The hysteretic behavior of the empty and filled braces is similar; however, the local buckling modes are different with the empty braces exhibiting inward local buckling and the filled braces exhibiting outward local buckling owing to the foam's ability to restrain inward deformation within the plastic hinge region. This change in local buckling mode reduces the severity of the local buckling and minimizes the concentration of strain in the plastic hinge region, which generally leads to an increased fracture life for the filled braces.
- The use of foam fill as a retrofit option for braced frames expected to undergo large cyclic loads is viable provided that the hole size and location for foam insertion are adequately chosen to limit their influence on brace behavior. Further research that explores alternative fill techniques is necessary to establish an optimal brace filling procedure.

Chapter 5 Finite Element Modeling of Empty and Foam Filled Braces

5.1 Introduction

The current American Institute of Steel Construction (AISC) Seismic Provisions (AISC 2016a) classifies members of a seismic force resisting system as either moderately ductile or highly ductile. Each classification is based on a limiting width-to-thickness ratio that ensures adequate ductile behavior can be achieved at both the member and system levels. In the case of special concentrically braced frames (SCBFs), highly ductile members are required, since the members are anticipated to undergo substantial plastic rotations of at least 0.04 radians during a design-level earthquake. For ordinary concentrically braced frames (OCBFs), members are anticipated to undergo plastic rotations of 0.02 radians or less, causing the member limiting width-to-thickness ratio to be less stringent than those for SCBF members. Note that columns, beams, and braces of an SCBF must satisfy the highly ductile width-to-thickness limits, whereas for OCBFs, only the braces must satisfy the moderately ductile width-to-thickness limit. For round hollow structural sections (HSS), which are commonly used as bracing members, the AISC Seismic Provisions (AISC 2016a) stipulate that SCBF members shall not exceed the highly ductile width-to-thickness ratio (λ_{hd}) limit given by Equation 5.1, where E is the elastic modulus of steel, R_y is the ratio of the expected yield stress to the specified minimum yield stress, and F_y is the specified minimum yield stress. For round HSS, the width-to-thickness ratio is expressed as a diameter-to-thickness (D/t) ratio where D is the outer diameter and t is the wall thickness of the HSS.

$$\lambda_{hd} = 0.053 \frac{E}{R_y F_y} \qquad \text{Equation 5.1}$$

Similarly, OCBF bracing members shall not exceed the moderately ductile D/t limit given as λ_{md} in Equation 5.2.

$$\lambda_{md} = 0.062 \frac{E}{R_y F_y} \qquad \text{Equation 5.2}$$

In the case of round concrete-filled HSS, the highly ductile and moderately ductile *D*/*t* limits are defined by Equations 5.3 and 5.4, respectively.

$$\lambda_{hd} = 0.085 \frac{E}{R_y F_y} \quad \text{Equation 5.3}$$

$$\lambda_{md} = 0.17 \frac{E}{R_y F_y} \quad \text{Equation 5.4}$$

The *D/t* limits for round concrete-filled HSS are substantially less stringent than those of empty HSS. The limits are 60% and 174% larger for concrete-filled highly ductile and moderately ductile members, respectively, when compared to those for hollow HSS. The relaxation of the *D/t* limits for concrete-filled members stems from the ability of the concrete to impede the initiation and severity of local buckling of the surrounding steel, ultimately resulting in improved ductility. As shown in Chapter 4, filling the circular hollow section (CHS) braces with a lightweight polyurethane foam is also able to provide local buckling resistance and improve brace fracture life.

To circumvent physical limitations imposed by experimental testing and to increase the robustness of the current dataset, a comprehensive finite element study is undertaken. Data from the experimental tests is used to calibrate and validate finite element models to ensure that local and global behaviors are accurately captured. In all, 29 empty and 29 equal-size polyurethane foam filled braces are simulated. A wide variety of *D/t* and slenderness ratios (λ) are considered so that robust conclusions can be established. Overall, the main objective of this study is to quantify the efficacy of the polyurethane foam fill by establishing which section sizes benefit most from the inclusion of the polyurethane foam within the void of circular HSS braces.

5.2 Finite Element Modeling Details

Finite element (FE) models are developed using the general-purpose software suite Abaqus FEA (version 6.17). Leveraging symmetry with respect to loading, geometry and boundary conditions, one-quarter of the brace is modeled (Figure 5-1). Symmetry boundary conditions are applied to the cut planes to restrain out-of-plane displacement and restrict rotations about the axes that are

perpendicular to the respective out-of-plane directions. Axial deformation corresponding to the experimental loading history is applied to the pin reference point (Figure 5-1), which corresponds to the center of the pin shown in the University of Michigan (UM) test setup (Chapter 4). The nodes that lie on the surface of the brace end have rotation and displacement constrained to the rotation and displacement of the pin reference point using a multi-point beam constraint. This constraint creates a rigid beam between the reference point and nodes at the brace end, which replicates the interaction between the rigid pin connection and the steel brace. A global imperfection is introduced by scaling the first mode shape produced by an eigenvalue buckling analysis to produce a maximum deformation at the mid-length of the brace equal to 1.58 mm (L/1000) (Kumar and Sahoo 2018), which provides buckling loads in close agreement to the experimental results discussed in Chapter 4.

The empty and filled steel braces are modeled with four-node shell elements (S4R) with one integration point and hourglass control, while the polyurethane foam is modeled with three-dimensional eight-node continuum elements (C3D8R) with one integration point. Elements with reduced integration are used to reduce analysis time. Haddad and Shrive (2019) undertook an FE investigation of wide flange section braces under reverse cyclic loading and noted a negligible difference in behavior when considering the use of full or reduced-integration elements. Since hourglassing can be an issue when using first-order reduced-integration elements, hourglass control is employed to ensure that strain energy is generated when an element distorts. The shell elements have six degrees of freedom (three translational and three rotational degrees of freedom at each node), whereas the solid elements have three degrees of freedom (three translational degrees of freedom at each node). The use of S4R and C3D8R elements in this study is supported by their successful use by Moon et al. (2012) and Imani et al. (2015) to simulate the behavior of circular concrete-filled steel tubes under various loading scenarios.

To improve computational efficiency and accurately capture the local buckling expected at the brace mid-length, the mesh is partitioned into two distinct regions (Figure 5-1). A mesh size of 1.875t, where t is the design wall thickness of the brace (AISC 2017), is employed in the plastic hinge region based on the results of a mesh convergence study. The validity of this mesh size is further confirmed by its size being less than the critical half-wavelength of a buckled cylindrical shell, which is necessary to accurately capture local buckling deformations (Song et al. 2004). The

remainder of the brace utilizes a coarse mesh with a typical element size five times larger than that employed in the plastic hinge region. Simpson's method of integration with seven integration points through the thickness is used to calculate the cross-section behavior of the shell elements. Simpson's rule is used as opposed to Gauss quadrature because in Gauss quadrature there are no integration points on the shell surfaces, which is necessary for obtaining plastic strain data.

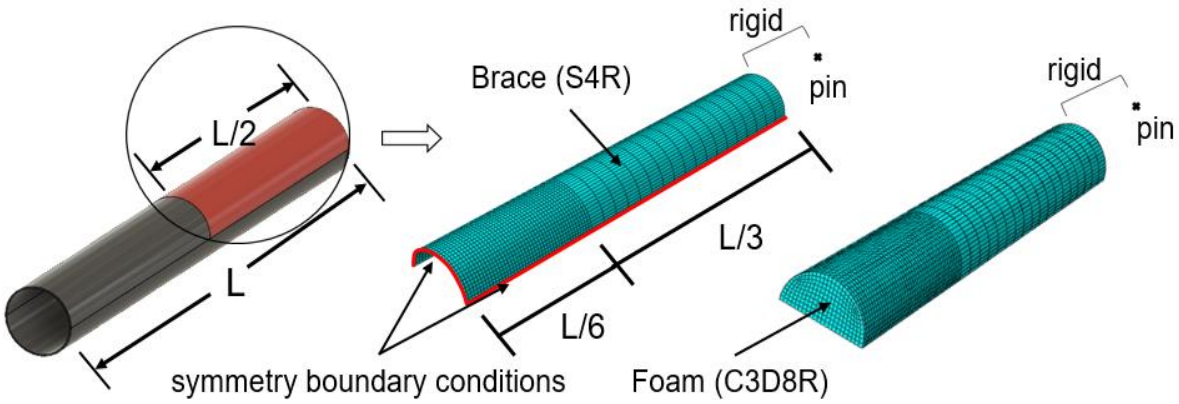

Figure 5-1 FE modeling details

The models are solved using an explicit dynamic analysis (Abaqus/Explicit) as opposed to an implicit static analysis (Abaqus/Standard). Although the tested braces were loaded quasi-statically (0.4 mm/s for the UM tests), a dynamic analysis is chosen because of its proven ability to accurately simulate complicated contact. The dynamic explicit analysis employs a central-difference scheme to integrate the equation of motions through time. One of the main differences between the implicit and explicit solver is when equilibrium is imposed. For the explicit solver, equilibrium is imposed at the beginning of a step and the solution is incrementally moved forward in time without the need for equilibrium iterations. For the static implicit analysis, a non-linear system of equations is iteratively solved at each time increment using the Newton-Raphson method. In this case, equilibrium is imposed at the end of the step and is strictly enforced so that iterations occur until an equilibrium tolerance is satisfied.

Because a dynamic solver is employed, it is important to ensure that inertial forces do not significantly influence the brace behavior. As it is sometimes impractical to simulate the brace response using a natural time scale, the loading rate is increased to up to 1 mm/s in some cases. To ensure that inertial effects are insignificant, internal energy and kinetic energy are plotted versus step time. During most of the analysis the kinetic energy should remain below 10% of the internal

energy of the system to ensure a quasi-static solution. Figure 5-2 shows plots of the kinetic energy and internal energy for an empty brace loaded at 1 mm/s (D/t = 34.5; λ = 79). The kinetic energy remains less than 0.5% of the internal energy for the duration of the analysis indicating that a quasi-static solution is obtained. For the simulation of some braces, mass scaling is also employed to reduce the analysis time. Since the stable time increment is related to material density, mass scaling is used to artificially increase material density, leading to an increase in the stable time increment and a reduction in the number of increments needed to perform the analysis. Figure 5-3 provides a comparison of axial force-deformation hysteresis responses with and without mass scaling for a brace with D/t = 34.5 and λ = 41. The response using a mass scaling factor of 30 is nearly identical to the response using no mass scaling, indicating that the analysis time can be reduced without substantially affecting brace behavior. It is also observed that physical behavior (local buckling and global buckling) and plastic strains are the same with and without the use of mass scaling.

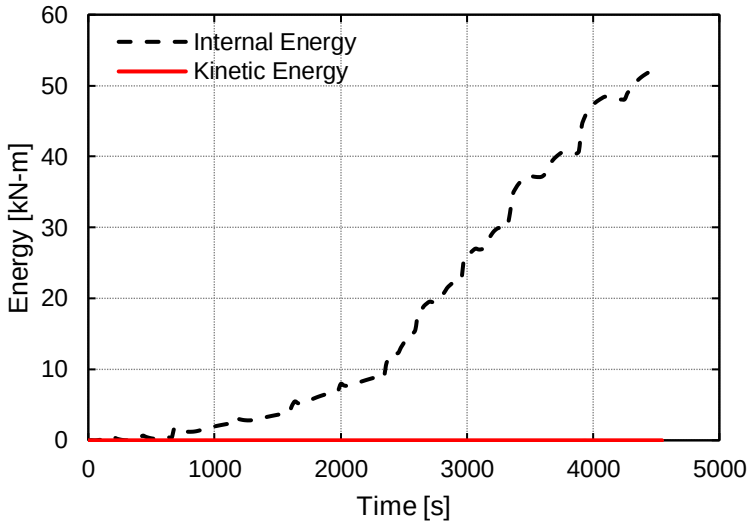

Figure 5-2 Comparison of internal and kinetic energy over the duration of a brace analysis

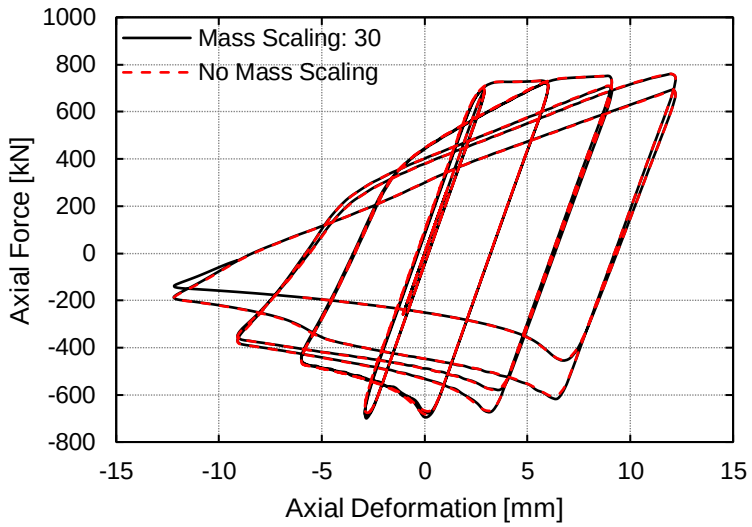

Figure 5-3 Simulated brace response with and without mass scaling

A general contact algorithm is employed to define the interaction between the foam and the steel brace. Tangential behavior is defined using a penalty friction formulation with a friction coefficient of 0.3. A friction coefficient of 0.3 denotes that the critical value at which slip occurs between the two surfaces is 30% of the normal contact pressure. Normal behavior is defined using hard contact with the allowance of separation after contact. Specifying this behavior permits an indefinite amount of contact pressure when the steel and foam are in contact and zero contact pressure when there is clearance between the two surfaces. The validity of the allowance of separation after contact has been visually confirmed by cutting the filled braces after experimental testing (Chapter 4), revealing that the foam does separate from the steel within the plastic hinge region.

5.3 Material Properties

5.3.1 Steel

A nonlinear, combined isotropic and kinematic hardening model based on the work of Lemaitre and Chaboche (1990) is employed to simulate the steel brace behavior. This model is used with a von Mises yield surface, which illustrates when yielding occurs in principal stress space and operates under the premise that yielding of a ductile metal commences when the distortional energy reaches a critical value. The plasticity model assumes that the yield behavior of metals is independent of hydrostatic pressure. The yield surface is defined by Equation 5.5, where σ_{ij} is a

stress tensor, α_{ij} is a back-stress tensor that defines the translation of the yield surface in stress space and σ_0 is the stress defining the size of the yield surface.

$$f(\sigma_{ij} - \alpha_{ij}) = \sigma_0 \quad \text{Equation 5.5}$$

For a temperature-independent problem, the rate of change of a single back-stress component is defined by Equation 5.6, where C_1 is the kinematic hardening modulus, γ_1 is the rate at which the hardening modulus decreases with increasing plastic deformation, and $\dot{\varepsilon}^{pl}$ is the equivalent plastic strain rate.

$$\dot{\alpha}_{ij} = C_1 \dot{\varepsilon}^{pl} \frac{1}{\sigma_0} (\sigma_{ij} - \alpha_{ij}) - \gamma_1 \alpha_{ij} \dot{\varepsilon}^{pl} \quad \text{Equation 5.6}$$

Integrating Equation 5.6 over a half-cycle results in Equation 5.7, where ε^{pl} is the logarithmic plastic strain and α is a back-stress.

$$\alpha = \frac{C_1}{\gamma_1} [1 - e^{-\gamma_1 \varepsilon^{pl}}] \quad \text{Equation 5.7}$$

C_1 and γ_1 are calculated using data obtained from averages of three tensile coupons that are fabricated from a dual certified steel (ASTM A500 Gr. B/C) round HSS with a nominal outer diameter of 88.9 mm and a wall thickness of 5.49 mm. The coupons are fabricated from material extracted at 90°, 180°, and 270° from the weld seam and are tested in accordance with ASTM E8 (ASTM 2016). Since the braces from the experimental programs discussed in Chapter 4 were fabricated from STK 400 and A500 Gr. B steel, respectively, the validation of the modeling approach is conducted based on material properties obtained from the experimental data of the respective material coupons. The dual certified material properties based on the aforementioned coupons are then used for the parametric study because the current specification (AISC 2016b) stipulates that ASTM500 Gr. C is the preferred material specification for round HSS.

For the coupon tests of the dual certified steel used to obtain the material properties for the parametric study, strain is calculated using extensometer readings considering a 50.8 mm gauge length, while stress is calculated by dividing the force from the load cell by the measured cross-sectional area of the coupon within the reduced width section. The data is converted to true stress and true strain using Equation 5.8 and Equation 5.9, respectively, up to the ultimate tensile strength.

$$\sigma_{True} = \sigma_{Engineering}\left(1 + \varepsilon_{Engineering}\right) \quad \text{Equation 5.8}$$

$$\varepsilon_{True} = ln(1 + \varepsilon_{Engineering}) \quad \text{Equation 5.9}$$

The conversion to true stress-true strain is only valid up to the ultimate tensile strength because of necking, at which point the strain measured by the extensometer is no longer occurring over the gauge length and is instead occurring within a localized region. The Young's modulus is calculated by fitting a regression line to the true stress-true strain data in the linear region. The yield stress is calculated using the 0.2% strain offset method. Average Young's modulus and yield stress values from the three coupon tests are reported in Table 5-1.

To calculate C_1 and γ_1, the total true strain is converted into plastic strain using Equation 5.10, where ε^{pl} is the logarithmic plastic strain, E is Young's modulus, and σ^{y}_{True} is the true yield stress.

$$\varepsilon^{pl} = ln\left(1 + \varepsilon_{Engineering}\right) - \frac{\sigma^{y}_{True}}{E} \quad \text{Equation 5.10}$$

Using the logarithmic plastic strain and true stress data, the back-stress is obtained using Equation 5.11, where σ_i is the true stress at the ith data point, α_i is the back-stress at the ith data point, and σ_0 is as previously defined.

$$\alpha_i = \sigma_i - \sigma_0 \quad \text{Equation 5.11}$$

Using the calculated back-stresses at each data point from Equation 5.11 along with the corresponding logarithmic plastic strain, the coefficients C_1 and γ_1 are determined using a nonlinear least-squares solver to best fit Equation 5.7. True stress-logarithmic plastic strain data from one of the coupon specimens is plotted in Figure 5-4 with the curve fit equation overlaid (Equation 5.12) using the C_1 and γ_1 values defined in Table 5-1. The curve corresponds well with the coupon data, confirming that the C_1 and γ_1 parameters are valid.

$$\sigma = \sigma_0 + \frac{C_1}{\gamma_1}\left[1 - e^{-\gamma_1 \varepsilon^{pl}}\right] \qquad \text{Equation 5.12}$$

Table 5-1 Parametric study material model parameters

Young's Modulus (MPa)	σ_0 (MPa)	C_1 (MPa)	γ_1	Q_∞ (MPa)	b
192500	358.5	2655	15	96.5	4

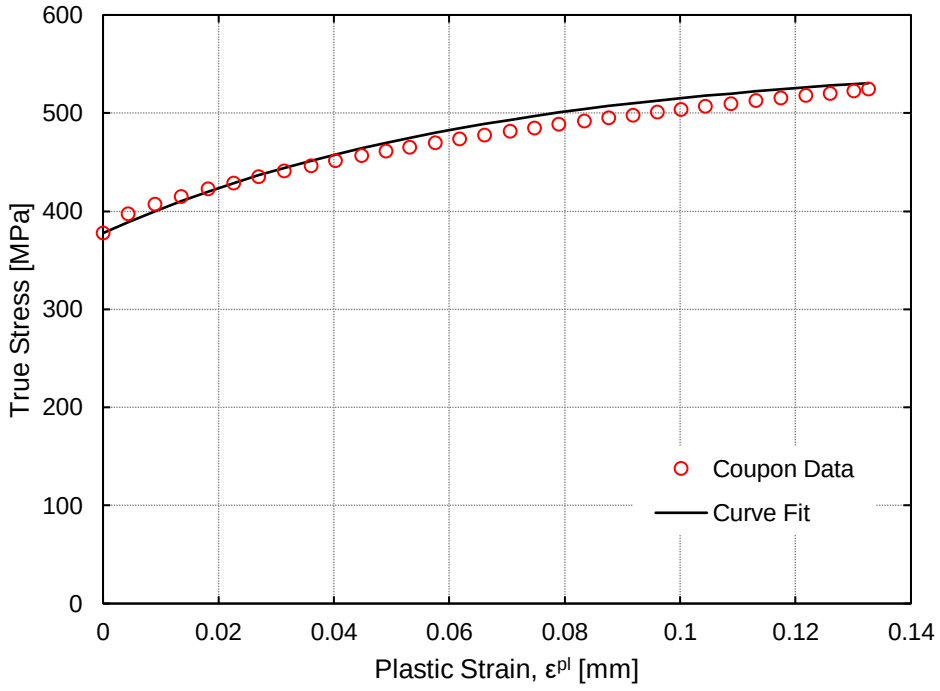

Figure 5-4 Example C_1 and γ_1 curve fitting procedure

The isotropic hardening behavior is defined by Equation 5.13, where Q_∞ is the maximum change in size of the yield surface and b is the rate at which the size of the yield surface changes.

$$\sigma = \sigma_0 + \ Q_\infty[1 - e^{-b\varepsilon^{pl}}] \qquad \text{Equation 5.13}$$

Initial values of Q_∞ and b are obtained using symmetric displacement-controlled cyclic coupon tests. The values are iteratively adjusted to ensure that the brace simulations match the experimental force-deformation hysteresis responses from the UM brace tests. A comparison of an FE and experimental force-displacement curve using the material parameters listed in Table 5-1 is provided in Figure 5-5 along with the coupon geometry and dimensions.

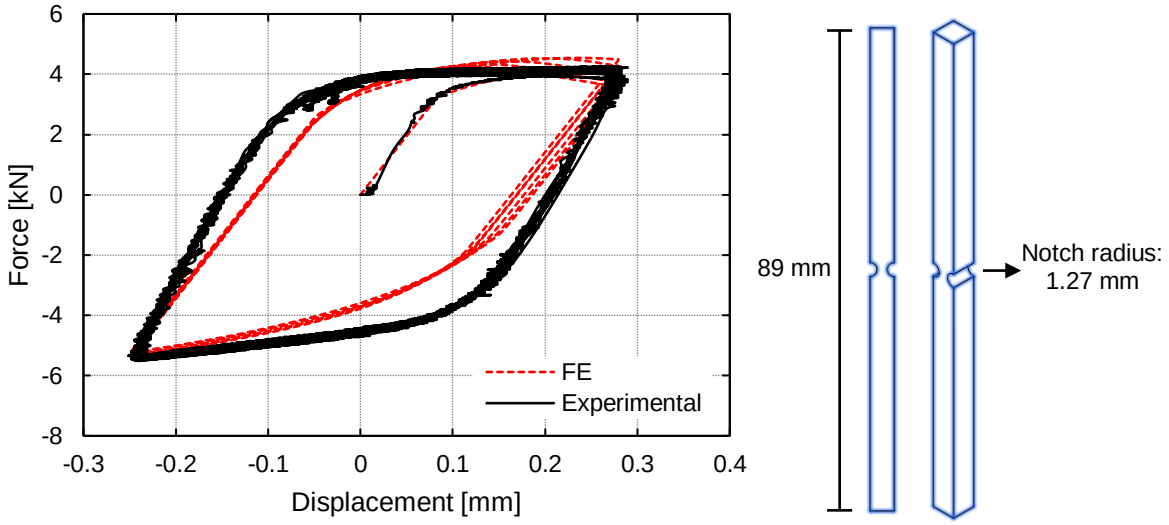

Figure 5-5 FE versus experimental cyclic coupon comparison for isotropic parameter validation

5.3.2 Foam

The crushable foam with volumetric hardening material model from the Abaqus library is employed to model the polyurethane foam fill. Although this model is suitable for monotonic loading, it has been shown to be effective at predicting the behavior of foam-filled beams under reverse cyclic loading (Wei 2017). The volumetric hardening option is selected as opposed to the isotropic hardening option because the isotropic model assumes that the foam exhibits the same behavior under hydrostatic tension and hydrostatic compression. This assumption is not suitable

for the polyurethane foam and the fill application, but it also has little consequence to modeling the foam behavior given that the foam is not stressed in hydrostatic tension. The volumetric hardening option assumes perfectly plastic behavior for hydrostatic tension loading.

Important parameters of this model are the compression yield stress ratio, *k*, which is defined as the ratio of the yield stress in uniaxial compression to the yield stress in hydrostatic compression, and the hydrostatic yield stress ratio, k_t, which is the ratio of the yield stress in hydrostatic tension to the yield stress in hydrostatic compression. The evolution of the hardening curve is defined by converting the stress-strain relationship from a monotonic compression test on a foam cube specimen into true stress and logarithmic plastic strain and then entering true yield stress values as a function of the absolute value of the plastic strain in tabular form. Appendix C provides the input used to define the evolution of the foam hardening curve. True stress and logarithmic plastic strain are calculated using Equation 5.8 and Equation 5.14, respectively.

$$\varepsilon^{pl} = -ln\left(1 - \varepsilon_{Engineering}\right) - \frac{\sigma^{y}_{True}}{E} \qquad \text{Equation 5.14}$$

Material parameters for the model are defined based on a single representative specimen from a robust set of monotonic compression tests carried out by Wei (2017). The elastic modulus and compression yield strength are 25.5 and 2.5 MPa, respectively. The Poisson's ratio is taken as 0.2, while the compression yield stress and hydrostatic yield stress ratios are taken as 1 and 0.1, respectively (Wei 2017). Stress-strain data from the experimental compression test of a polyurethane foam cube is compared with a simulation of the same test performed in Abaqus using the calibrated foam material model. The results show that good agreement is achieved between the experimental test and simulation (Figure 5-6). The deformed configuration from the simulation also matches the experimental deformations well, further supporting the validity of the material model (Figure 5-6).

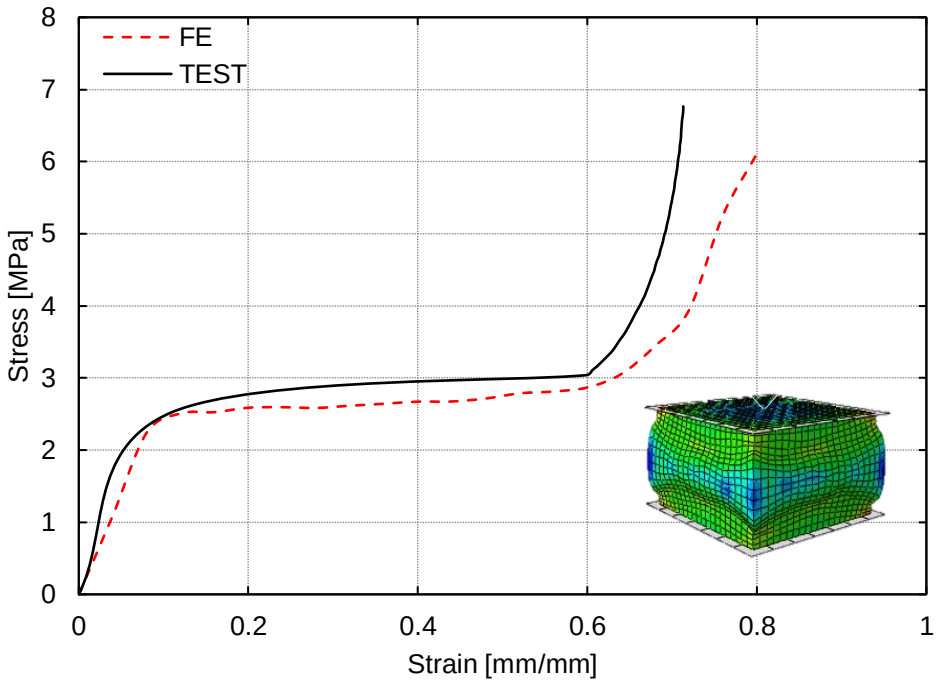

Figure 5-6 Foam material model validation

5.4 FE Validation

5.4.1 Modeling Technique

Using the preceding modeling techniques in conjunction with material properties obtained from tensile coupon tests of the Japanese STK400 steel, the FE modeling approach is validated against the Kyoto University experimental results. The material model parameters are provided in Table 5-2 based on coupon tests of the STK 400 material. A comparison of the FE and experimental hysteretic responses of the empty and foam-filled braces with a nominal outer diameter of 89.1 mm and wall thickness of 3.2 mm, referred to as brace E8932 and F8932, respectively (Chapter 4), are provided in Figure 5-7 and Figure 5-8. The simulated hysteretic responses for the empty and filled braces agree well with the corresponding experimental results. The percent error between the simulation and experimental results for the elastic stiffness, critical buckling load, and maximum tensile resistance is 10.1%, 5.1%, and 3.8%, and 11.3%, 2.5%, and 1.6%, respectively, for the empty and filled braces. This comparison demonstrates the validity of the modeling techniques regarding the ability to simulate the hysteretic response of empty and polyurethane foam-filled brace behavior under large cyclic loads. Further evidence validating the ability of the

FE modeling techniques to capture physical behavior is provided through visualization of the brace deformation. Figure 5-9 shows a comparison of the experimental mid-length deformation of brace F8932 and that resulting from the FE simulation at two different points during the loading protocol. The interaction between the foam and steel is accurately captured as shown by the outward buckled shape during the first compressive excursion to 2% drift (Figure 5-9a) and the crushing of the foam resulting in an inward buckled shape during the first compressive excursion to 3% drift (Figure 5-9b).

Table 5-2 STK 400 material model parameters

Young's Modulus (MPa)	σ_0 (MPa)	C_1 (MPa)	γ_1	Q_∞ (MPa)	b
186930	383	2830	15	42	5

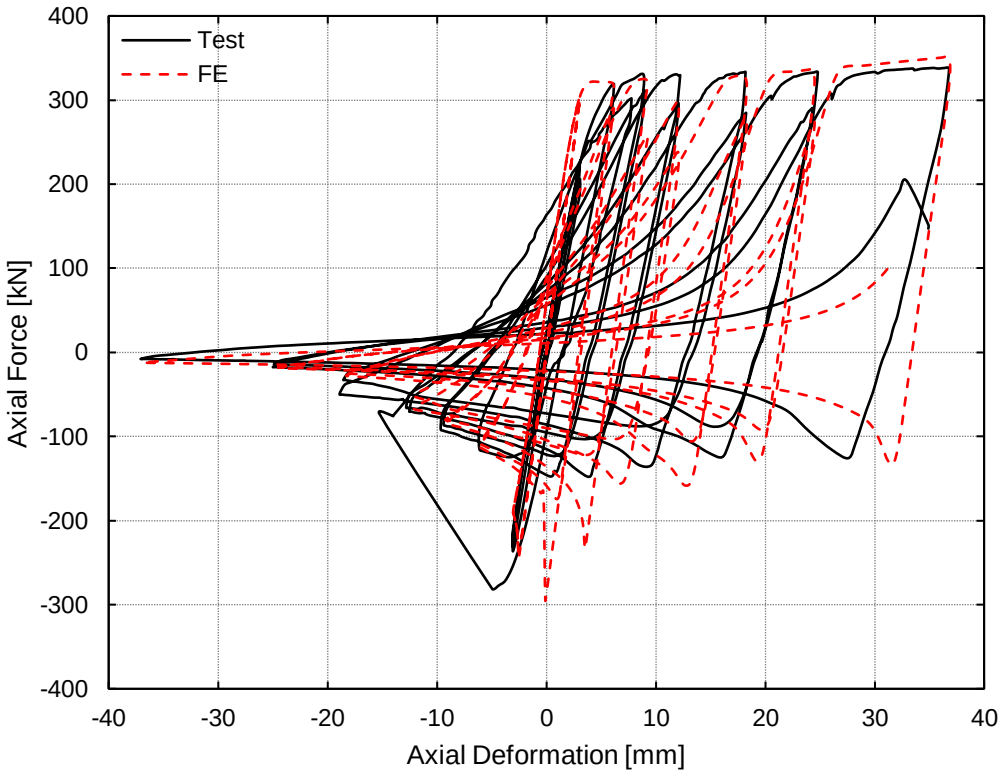

Figure 5-7 Experimental versus FE hysteretic response for empty brace E8932 (Chapter 4)

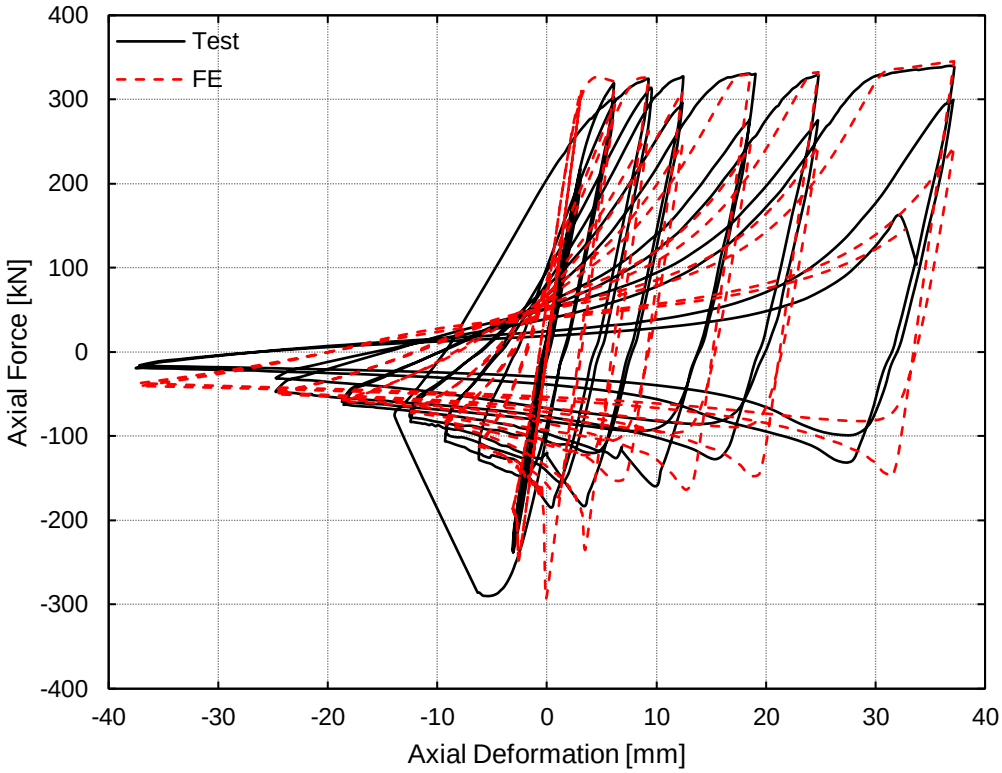

Figure 5-8 Experimental versus FE hysteretic response for filled brace F8932 (Chapter 4)

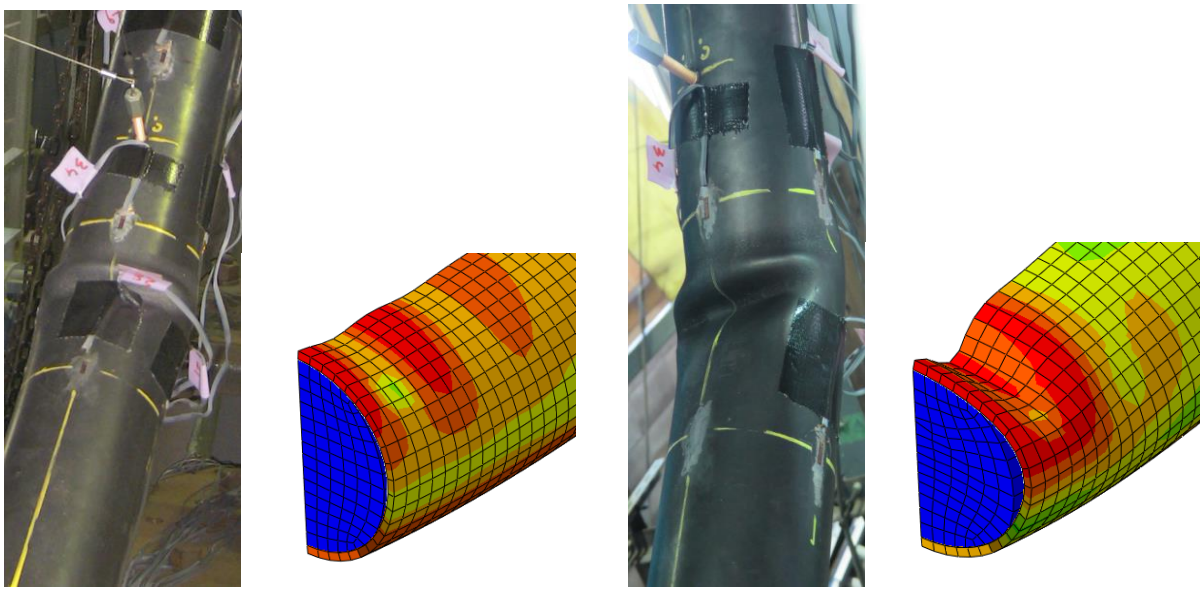

(a) (b)

Figure 5-9 Comparison of test versus FE deformation at the brace mid-length for brace F8932 during the (a) second compressive excursion to 2% drift and (b) the first compressive excursion to 3% drift

5.4.2 Material Model for A500 Gr. B/C Steel

The parametric study simulations use a material model based on A500 Gr. B/C steel. To ensure that the material model for this steel material is able to accurately simulate the brace behavior, simulations are performed using the A500 Gr. B/C material properties (Table 5-1) and compared with the UM tests. The entire brace is modeled (not one-quarter) to ensure that the material model can accurately capture the local buckling behavior exhibited by the UM tests. Since the interaction between the foam and steel using the proposed modeling methods has been shown in the previous section to be able to be accurately captured, the simulations to validate the brace behavior with the parametric study material model only consider empty braces. The simulated braces are subject to the same axial deformations that the tested UM braces underwent and the brace model is constructed using measured geometric properties. Comparisons of the experimental versus FE hysteretic responses for the empty UM braces are shown in Figure 5-10.

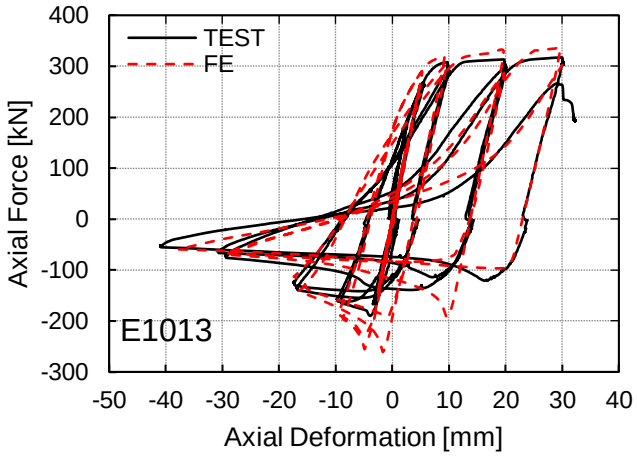

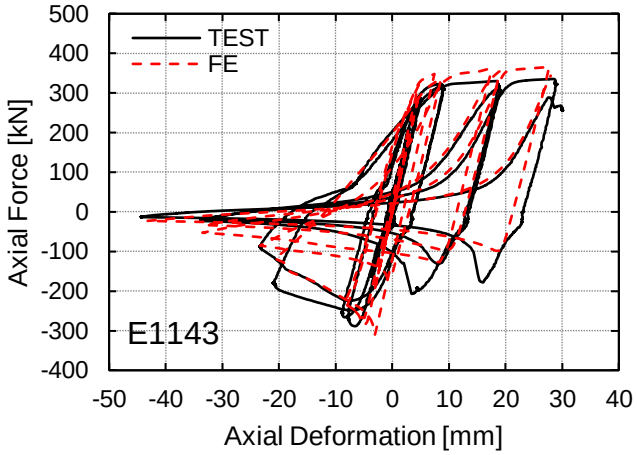

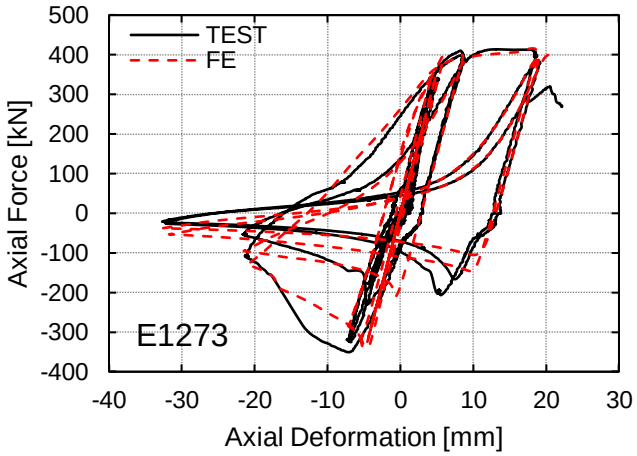

Figure 5-10 Experimental versus FE hysteretic responses of the empty UM braces (Chapter 4)

In general, the simulated responses agree well with the experimental responses for all three braces. While the ratio of FE to experimental compressive capacity is 1.37 for brace E1013, this difference is only associated with a couple of cycles and the ratios of the tensile capacity and cumulative dissipated energy are 1.06 and 1.05, respectively, indicating reasonable agreement. The difference in compressive capacity is likely due to a difference in the initial out-of-straightness used for the model compared to the actual out-of-straightness of the tested brace; nonetheless, the peak compressive strength obtained during a given cycle moves toward the experimental value as larger deformations are achieved. For brace E1143, the FE to experimental ratio for tensile capacity, compressive capacity and cumulative dissipated energy are all within 15% of unity. The differences between the simulation and experiment are likely due to the difficulty in modeling the test boundary conditions, which caused the brace to buckle in and out of the plane of the frame. The simulation of brace E1273 shows the best agreement with the ratio of FE to experimental tensile capacity, compressive capacity, elastic stiffness, and cumulative dissipated energy all being within 6% of unity. Overall, the simulations are able to accurately predict brace hysteretic response.

To further validate the material model, comparisons of when local buckling initiates are made. The simulations for braces E1013 and E1273 accurately predict the initiation of local buckling and the buckled shape, whereas the simulation for E1143 predicts the initiation of local buckling one cycle earlier than when it occurred during the test. However, as shown in Figure 5-11b, the simulation of brace E1143 is able to accurately capture the buckled shape at the brace mid-length later in the loading protocol. The local buckled shapes shown in Figure 5-11a and Figure 5-11b for E1013 and E1273, respectively, are nearly identical, further confirming the validity of the material model employed for the parametric study.

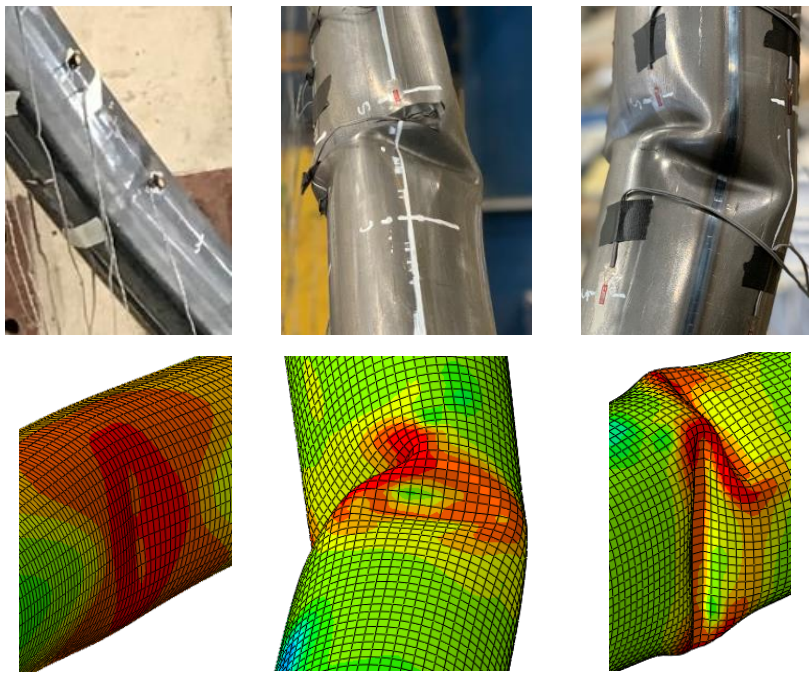

Figure 5-11 Comparison of the experimental and simulated local buckled shape for (a) brace E1013 at the end of the second compressive excursion to 2% drift, (b) brace E1143 at the end of the first compressive excursion to 1.5% drift and (c) brace E1273 at the end of the first compressive excursion to 1.5% drift

5.5 Foam Confinement

The Young's modulus and yield strength of the foam utilized in the UM brace tests are approximately 1500 and 75 times smaller, respectively, than that of the steel. Given this large discrepancy in stiffness and strength, it is of interest to determine why the foam is able to restrain inward local buckling of the steel. To assess the influence of confinement on the compressive behavior of the polyurethane foam, three confined and three unconfined experimental specimens from each brace size are created and tested under monotonic compression.

Confined and unconfined specimens for a particular brace size are created using foam from the same mixture in order to isolate the effect of the confining steel on the compressive behavior of the foam. All specimens are cut to 50.8 mm in height based on a small parametric study that considered unconfined foam specimens with heights of 38.1, 50.8 and 76.2 mm, respectively. The compressive response is similar for all specimen heights (Figure 5-12), thus the middle height of 50.8 mm is chosen for comparing confined and unconfined behavior. The unconfined specimens

are made by lining short sections (254 mm in height) of round HSS that are the diameter as the UM braces (Chapter 4) with a non-stick paper and then filling them with the foam. The same mixture of foam is then used to fill an unlined round HSS of the same size to make the confined specimens. The top and bottom surfaces of all specimens are leveled to ensure that the axial force from the loading platens is applied uniformly. Axial force is applied to the surface of the unconfined specimens via rigid steel caps (Figure 5-13). For the confined specimens, force is only applied to the surface of the confined foam using a rigid steel cylinder with the same diameter as the confined foam (Figure 5-13) so that the load is transferred directly to the foam and not the outer steel. All specimens are compressed to 75% of their original height at a loading rate of 0.25 mm/s. Measurements of the round HSS diameter, round HSS wall thickness, and foam cross-section are taken so that stress-strain curves can be generated.

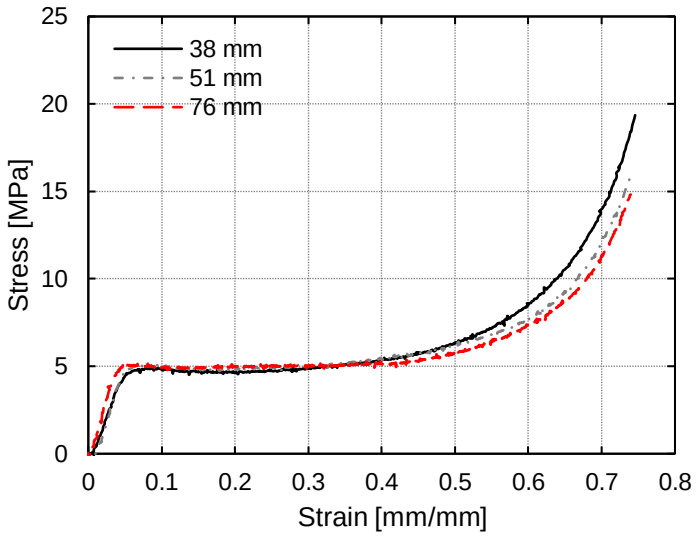

Figure 5-12 Compressive response of the unconfined foam specimens of different height

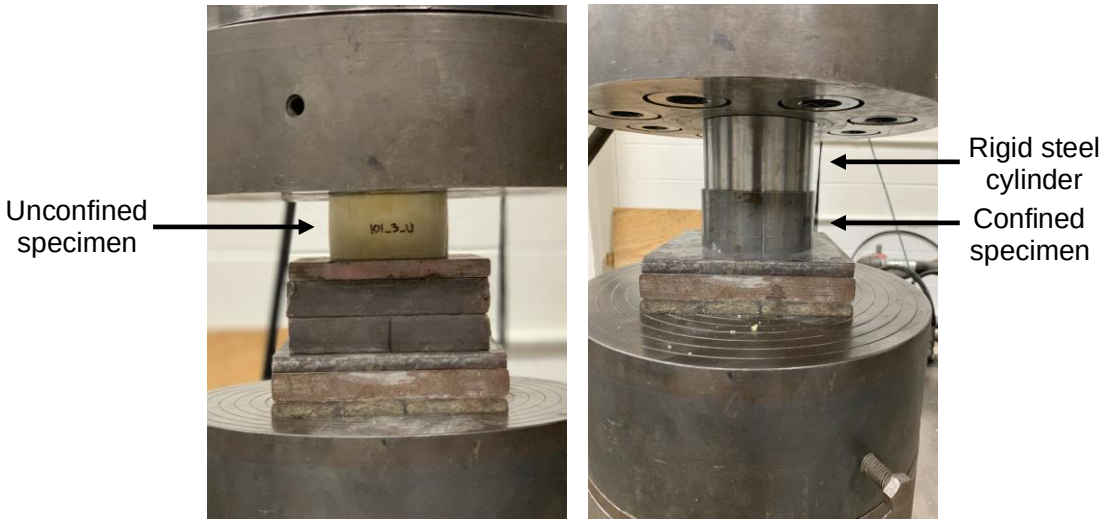

Figure 5-13 Test setup for the unconfined and confined polyurethane foam specimens

Figure 5-14 provides representative stress-strain relationships for the unconfined and confined specimens for all three brace diameters. In general, it is observed that the confined specimens have a greater Young's modulus, crush strength, and densification slope than that of the unconfined specimens. Overall, the confined and unconfined specimens show similar behavior with an elastic, plateau and densification region evident for both specimen types. The most evident distinction between the unconfined and confined behavior is the ability of the confined foam to reach much larger stresses than the unconfined foam at the same strain level, particularly in the densification region. For example, the confined specimen from the 114 mm diameter round HSS reaches a stress of approximately 50 MPa, which is 2.5 times larger than the stress achieved by the unconfined specimen. The failure modes of the two specimen types are also distinct. For the confined specimens, as larger strains are reached the bond between the foam and steel is broken and the foam crushes uniformly (Figure 5-15a). Because the transverse deformation of the foam is restrained by the steel tube, the foam is able to consolidate and achieve a larger stress at a given strain level than that of the unconfined specimens. The unconfined specimens exhibit substantial transverse deformation as axial force is applied owing to a lack of transverse restraint (Figure 5-15b). A more detailed analysis and summary of the results from all tests is presented in Appendix C.

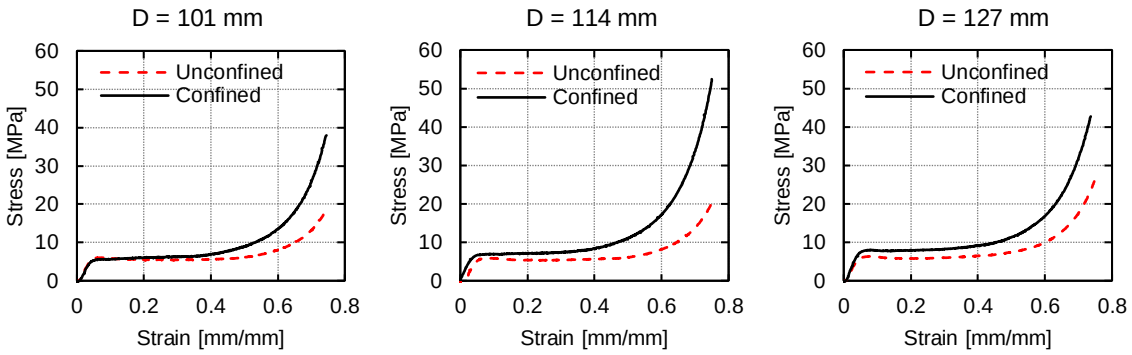

Figure 5-14 Representative monotonic compression stress-strain relationships for unconfined and confined specimens fabricated from all three brace diameters

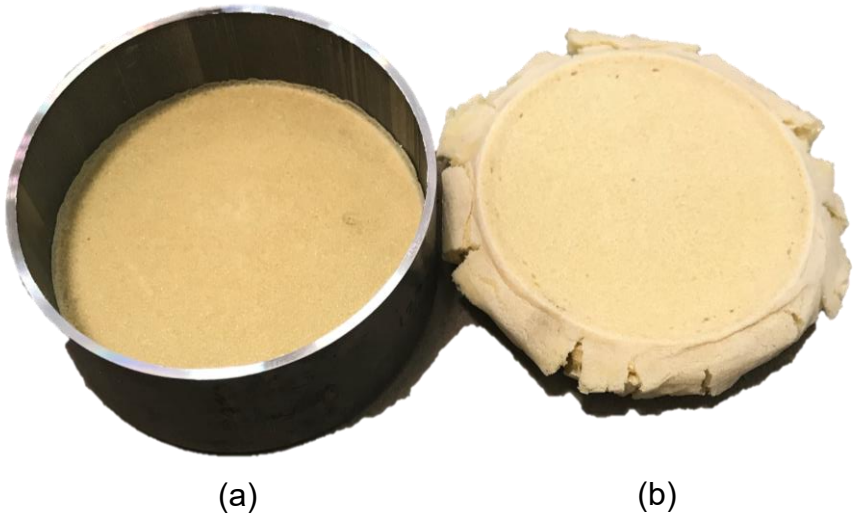

Figure 5-15 Typical failure modes for the (a) confined and (b) unconfined specimens

Using the monotonic compression response of the confined specimen from the 101 mm diameter round HSS (Figure 5-14), parameters for the Abaqus crushable foam material model (Appendix C) are calibrated and simulations are performed to assess whether the confinement of the foam influences the buckling behavior and hysteretic response of the polyurethane foam-filled braces. Figure 5-16 shows a comparison of a simulated foam cube compression test with the compression response of the tested confined foam specimen. The simulated response agrees well with the test results indicating that the model is valid. The new confined foam material model is then used to simulate the response of one of the foam-filled braces from the parametric study. The hysteretic response and the physical behavior of the brace using the two different foam models are compared to establish the influence of confining the foam.

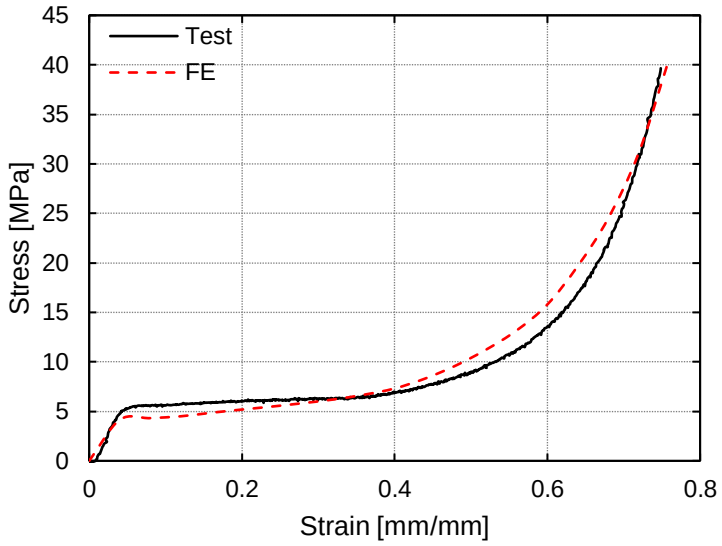

Figure 5-16 Validation of the confined foam material model

Figure 5-17 provides a comparison of the force-deformation responses using the unconfined and confined foam models for a brace from the parametric study with a D/t = 23 and λ = 41. The responses are nearly identical except that the tensile and compressive stiffness of the brace using the confined foam model is slightly larger than that of the brace using the unconfined model during the last two cycles of loading. This slight increase in stiffness with the use of the confined foam model is expected considering that the slope in the plateau region for the confined foam model is greater than that of the unconfined foam model. It is also observed that the deformation at the mid-length of the brace is similar. Figure 5-18 shows the deformed shape of the brace at the initiation of local buckling for the simulations using the two different foam models. For the brace using the unconfined model, there is inward local buckling with the largest deformation at the mid-length of the brace. For the brace simulation using the confined model, the local buckle is characterized by inward deformation with the largest deformation shifted approximately 30 mm from the brace mid-length. The similarity in the hysteretic response and local buckling behavior when employing the different foam models confirms the validity of the unconfined foam model and establishes that the effect of confinement on the foam behavior is negligible on the overall behavior of the polyurethane foam-filled braces.

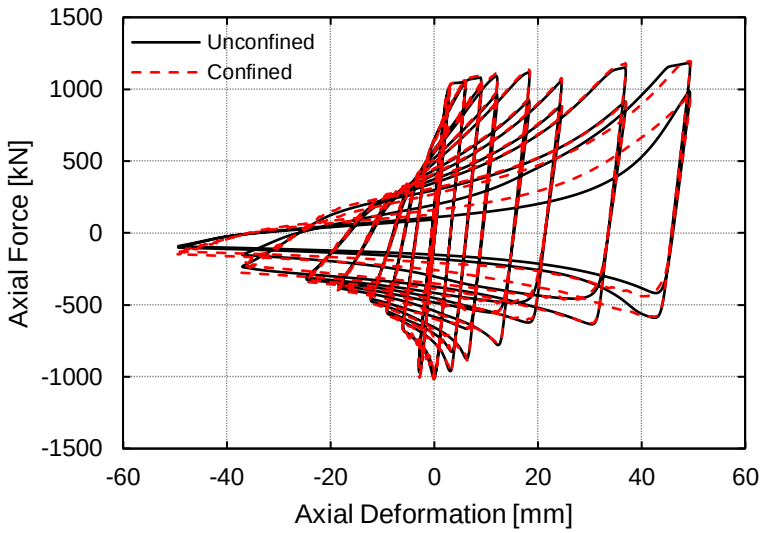

Figure 5-17 Comparison of foam-filled brace hysteretic response (D/t = 23; λ = 41) using the foam model calibrated with unconfined and confined foam data, respectively

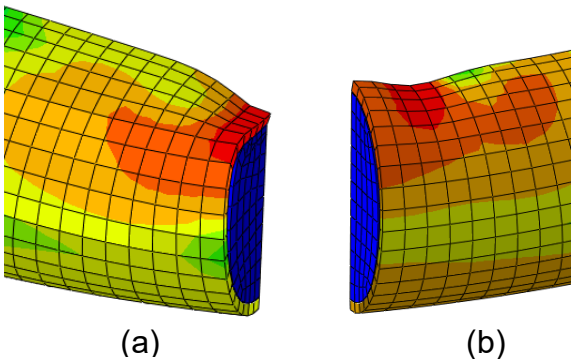

Figure 5-18 Deformed shape at the initiation of local buckling for the brace using the (a) unconfined and (b) confined foam model

5.6 FE Parametric Study

5.6.1 Parametric Study Specimens

A parametric study is undertaken that considers 29 empty braces and 29 equal size filled braces for a total of 58 simulations. The D/t and λ of the braces are shown in Figure 5-19 and a table of all section sizes is provided in Appendix C. The limiting D/t for highly (λ_{hd} = 25.7) and moderately (λ_{md} = 30.1) ductile behavior for round HSS braces fabricated from ASTM A500 Gr. C steel are

indicated by the vertical dashed lines in Figure 5-19. The red squares represent the *D/t* and λ from both experimental testing programs presented in Chapter 4. The majority of the parametric study braces have a large *D*/*t* (i.e., not highly ductile), which helps establish the effectiveness of the polyurethane foam fill and allows for determination of whether *D*/*t* limits can be relaxed when considering its inclusion. The selected brace sizes also provide a range of λ that are commonly used in seismic design so that the developed limits are relevant to design engineers (Sabelli et al. 2013). Each brace is modeled using the design wall thickness and dimensions provided in the AISC Steel Construction Manual (AISC 2017). A table of the parametric study section properties is provided in Appendix C.

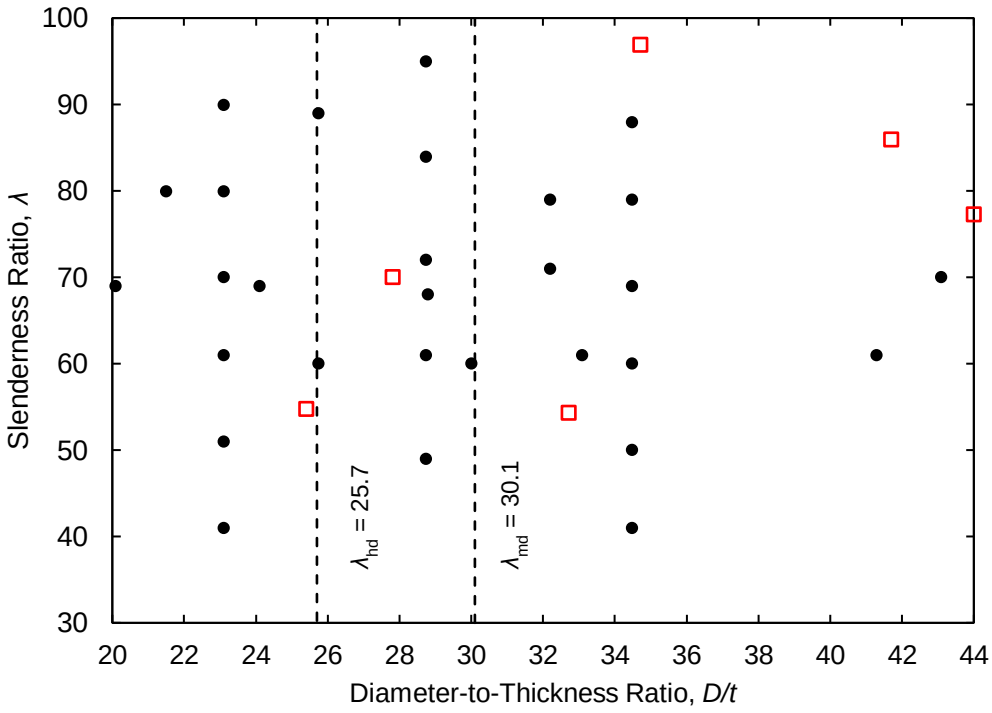

Figure 5-19 Parametric study brace sizes with respect to *D/t* and λ

5.6.2 Loading Protocol

The loading protocol used for the parametric study is the same as that used for the experimental brace tests discussed in Chapter 4 and is developed based on story drift. Figure 5-20 provides a schematic outlining how to calculate story height given an arbitrary brace length or pin to pin distance. Once the story height is defined, the necessary drift demand and subsequent brace axial

deformation can be calculated assuming an initial brace inclination angle of 45° with respect to the horizontal. The loading protocol varies because the brace length is changed to generate different λ.

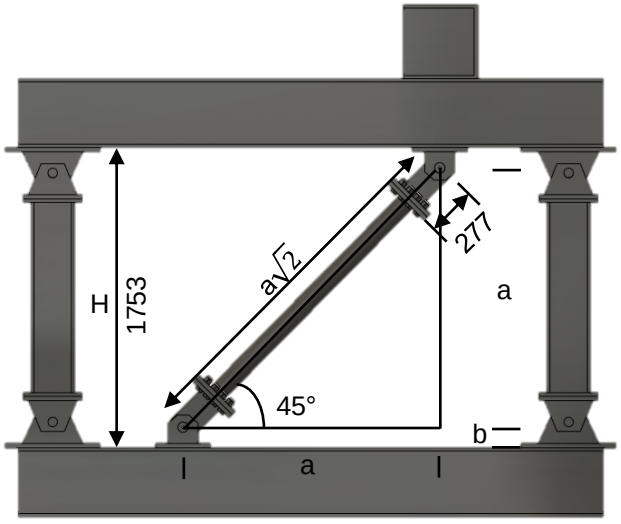

Figure 5-20 Schematic defining the development of the loading protocol

5.6.3 General Hysteretic Behavior

In general, the foam-filled braces behave similarly to their empty counterparts with respect to elastic stiffness and tensile strength. For all section sizes considered, the difference between the elastic stiffness for empty and filled braces is less than 1% with the filled braces being stiffer than the empty braces. This result is similar to the behavior observed in the experimental tests (Chapter 4), where the difference in elastic stiffness of the empty and filled braces ranged from 1.6% to 14.6%. Furthermore, the parametric study results show an average difference in tensile strength between the empty and filled braces of 1.7%. These minimal differences in stiffness and strength fulfill the intended purpose of the foam fill, which is to provide improved ductility, energy dissipation and a more stable structural response, while not altering brace strength.

Figure 5-21 and Figure 5-22 show typical axial force versus story drift responses for two sizes of empty and filled braces. The behavior of the empty and filled braces for both brace sizes are similar, but there are notable differences in compressive strength and energy dissipation, where

energy dissipation is defined as the area enclosed by the axial force-deformation curves. The filled HSS 244.5 × 6.4 (D/t = 41.3; λ = 61) brace is able to maintain nearly 60% of its compressive strength to the first compressive excursion to 1.5% drift (when local buckling initiates) compared to only 45% of the maximum compressive strength for the empty brace at the same drift level. Furthermore, the filled brace dissipates 23% more energy than the empty brace at the end of the first cycle to 1.5% drift. Similarly, the filled HSS 127 × 4.8 (D/t = 28.7; λ = 49) brace is able to maintain 44% of its compressive capacity to the second compressive excursion to 2% drift (when local buckling initiates) as opposed to 37% for the empty brace at the same drift level. This behavior leads to the filled brace providing a 26% increase in cumulative dissipated energy compared to the empty brace at the end of the second cycle to 2% drift. The aforementioned results suggest that the foam fill provides enhanced brace performance with greater benefits seen in braces with a D/t above the moderately ductile limit.

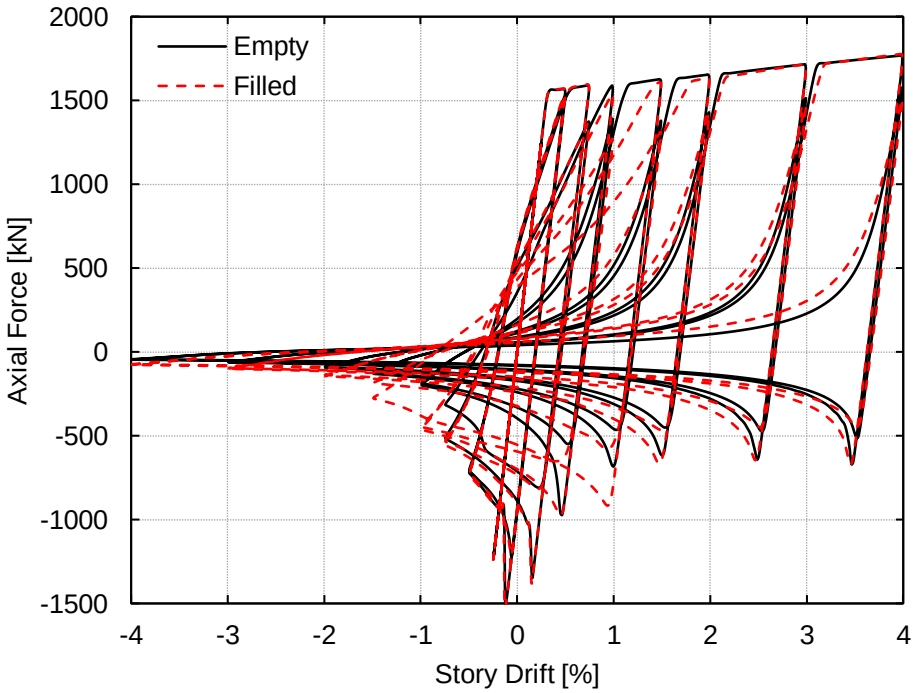

Figure 5-21 Hysteretic response for HSS 244.5 × 6.4 (D/t = 41.3; λ = 61)

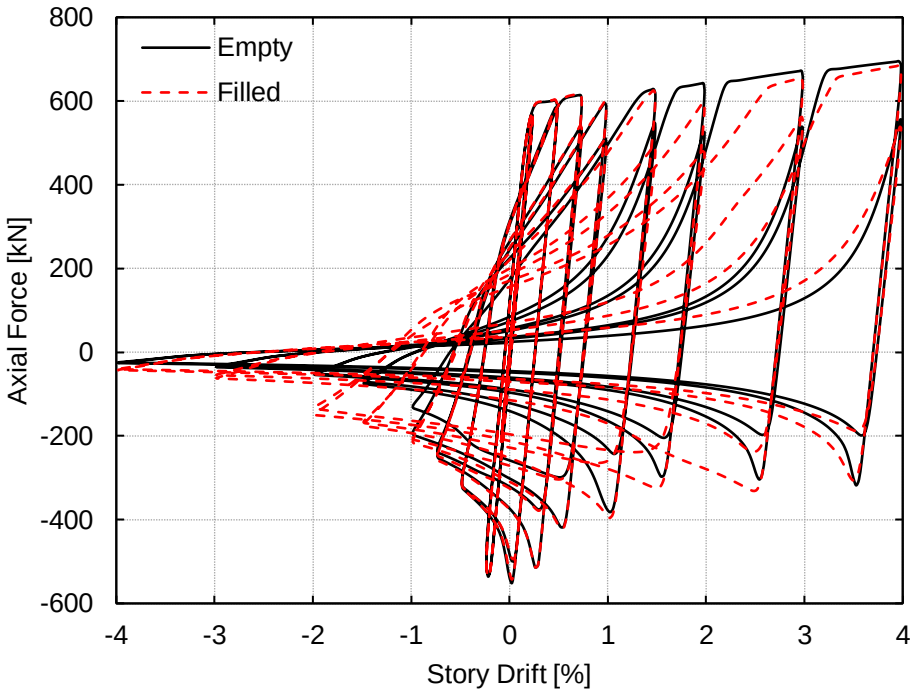

Figure 5-22 Hysteretic response for HSS 127 × 4.8 (D/t = 28.7; λ = 49)

5.6.4 Local Buckling

As shown from the experimental test program discussed in Chapter 4, use of the polyurethane foam within the void of round HSS braces under reverse cyclic loading can result in a delay in the initiation of local buckling leading to improved brace ductility. The ability of the foam to delay the initiation and mitigate the severity of local buckling is also evident from the parametric study results. Figure 5-23 shows the number of cycles to the initiation of local buckling as a function of D/t for the empty and filled braces, respectively, considering that the loading protocol applied to the braces consists of two cycles to each increasing drift level for a total of 18 cycles. The cycle in which local buckling initiates at the mid-length of the empty and filled braces is determined based on visual observation of the FE time-history animations. For the empty and filled braces the number of cycles to the initiation of local buckling decreases with an increase in D/t. Since brace fracture typically occurs soon after the initiation of local buckling, this trend suggests that braces with a larger D/t are more susceptible to premature fracture compared to braces with a smaller D/t. Additionally, Figure 5-23 generally shows that the foam-filled braces require more cycles of loading until local buckling initiates compared to that of the empty braces. The larger number of cycles required until the initiation of local buckling for the foam-filled braces suggests that they

have a larger ductility than that of the empty braces. It is also shown that braces with a *D/t* between approximately 25 and 35 benefit most from the use of the foam fill as shown by the large difference between the number of cycles to local buckling initiation for the empty and foam-filled braces that have a *D/t* within this range.

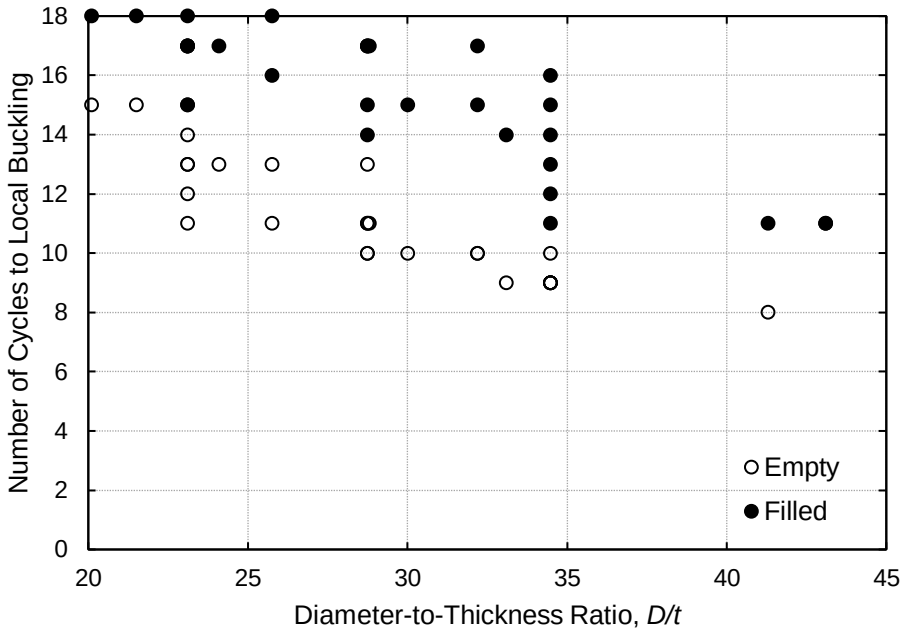

Figure 5-23 Number of cycles to local buckling initiation as a function of *D/t* for empty and foam-filled braces

It is of interest to note that the foam delays the initiation of local buckling by at least one cycle for all of the considered section sizes except for in the HSS 190.5 × 4.8 (*D/t* = 43.1; λ = 70), where local buckling initiates during the same cycle (first compressive excursion to 1.5% drift) for the empty and foam-filled braces. The empty (E1273) and foam-filled (F1273) braces with a *D/t* = 44 and λ = 77 that were tested and discussed in Chapter 4 also had local buckling initiate during the same cycle (first compressive excursion to 1% drift). Figure 5-24 shows the deformed shapes from the FE simulations for the empty (Figure 5-24a) and foam-filled (Figure 5-24b) braces at the initiation of local buckling. The empty brace has inward local buckling that resembles that of a half-sine wave, while the filled brace has outward local buckling because of the restraint provided by the foam. The buckled shapes of the similar size tested braces (E1273 and F1273) show similar local buckling behavior. Since this brace size (HSS 190.5 × 4.8) is the only one that did not

experience improvement by use of the foam fill, it is postulated that the foam will only offer improvement to brace performance regarding local buckling if the *D/t* of the brace is less than 43. Monotonic axial compression tests of circular thin-walled stub columns (*D/t* between 55 and 200) with and without concrete showed that the concrete infill had a negligible influence on the local buckling strength of the tubes (O'Shea and Bridge 1997). The negligible influence of the concrete infill was caused by the tendency of the tubes to buckle outward (whether empty or filled), rendering the concrete ineffective at providing restraint. This finding suggests that the foam fill will be ineffective in braces with a large *D/t* because of their tendency to exhibit outward local buckling. The next largest *D/t* considered in the parametric study is 41.3 (HSS 244.5 × 6.4 with a λ = 61). For this section, the filled brace experiences local buckling three cycles later than the empty brace. The ability of the foam to delay the initiation of local buckling in a section with a *D/t* that is well outside of the moderately ductile limit of 30.1 is validated through the experimental tests of the empty (E1143) and foam-filled (F1143) braces (Chapter 4), which showed the empty brace experiencing local buckling three cycles earlier than the filled brace. The experimental tests and companion FE study show that the foam fill can offer improved brace performance through delaying the initiation of local buckling for sections with a *D/t* of less than 43.

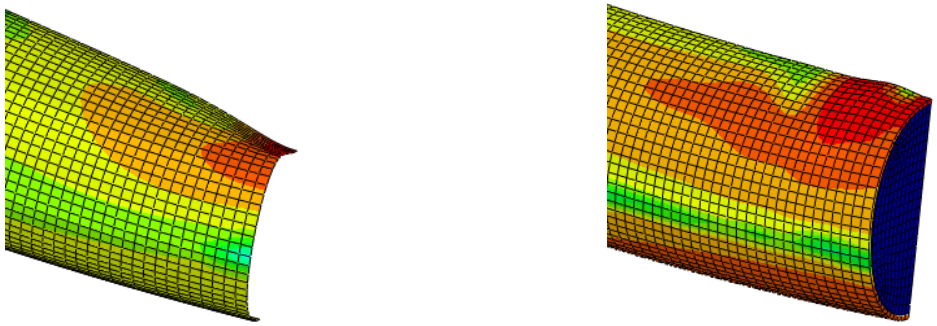

(a) (b)

Figure 5-24 Deformed shape at the initiation of local buckling for the simulated (a) empty and (b) foam-filled braces with a *D/t* = 43.1 and λ = 70

Since the behavior of braces in braced frames is also influenced by λ, it is of interest to determine how local buckling behavior is influenced by λ. Figure 5-25 shows the number of cycles to the initiation of local buckling as a function of λ for the empty and filled braces, respectively. The results suggest that the number of cycles to the initiation of local buckling increases with λ for the empty and filled braces. When comparing between the empty and filled braces, the results show that the foam fill is most effective at delaying local buckling in braces with a large λ. Since the

braces with large λ ($\lambda > 70$) have D/t values that are essentially evenly spread amongst the highly ductile, moderately ductile and no ductility (defined as neither moderately ductile or highly ductile) classifications, it is easier to isolate the influence of λ on the local buckling behavior. Braces that are either classified as moderately ductile or non-ductile and have $\lambda > 70$ show the greatest improvement regarding when local buckling initiates considering the use of the foam fill. The caveat to this improvement is that the brace must have a D/t that is less than 43, as previously demonstrated. The greater enhancement of behavior shown in members with a larger D/t when using the foam fill is not surprising given that these members have been shown to be more susceptible to local buckling. Considering all section sizes, the section size that shows the most improvement when using the foam fill regarding the delay of local buckling is the HSS 190.5 × 6.4 (D/t = 32.2; λ = 79). The filled HSS 190.5 × 6.4 brace has local buckling occur seven cycles later than that of its empty counterpart (second cycle to 1% drift compared to first cycle to 4% drift). This finding aligns with the previous discovery that the foam fill offers the greatest improvement in local buckling behavior in braces with larger D/t and larger λ. The greater improvement provided by the foam fill in braces with larger λ is likely a result of the foam being able to reduce the compressive strains in the plastic strain region by distributing them over a longer section of the brace. It is postulated that the foam is not strong enough to provide a substantial reduction in compressive strains in the plastic hinge region of less slender sections because it crushes under the larger plastic rotation that these sections must undergo to achieve the same drift level compared to a less slender brace. Since the foam is not elastic under large deformations, once it is crushed, its ability to restrain local buckling is reduced. This explains why a study by Sheehan and Chan (2014) showed that less slender concrete-filled CHS braces had a greater enhancement in performance compared to that of more slender members. The concrete is strong enough to restrain the steel as it undergoes large plastic rotation at its mid-length.

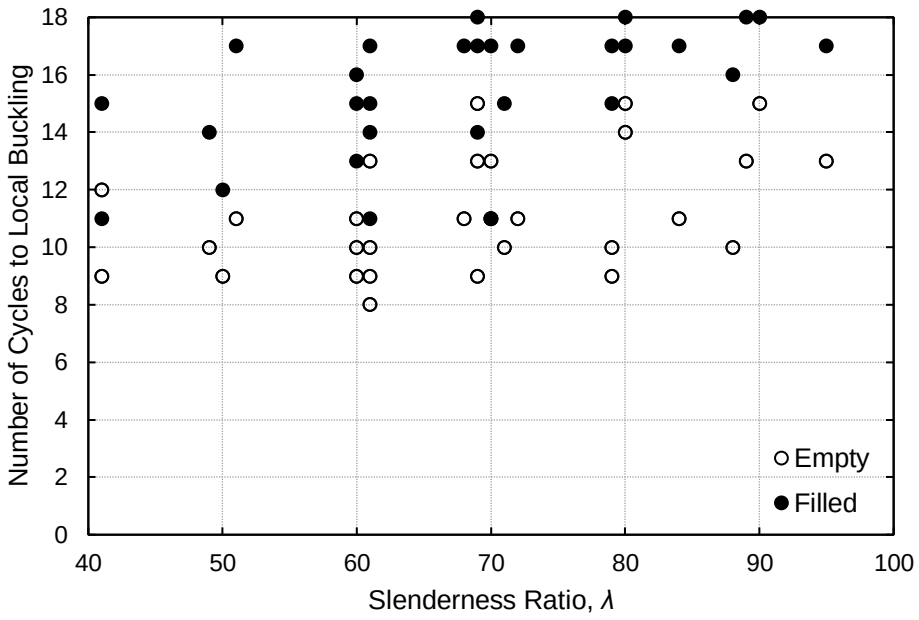

Figure 5-25 Number of cycles to local buckling initiation as a function of λ for empty and foam-filled braces

5.7 Conclusions

Data from two experimental programs (Chapter 4) is used to calibrate and validate finite element models of empty and polyurethane foam-filled CHS braces under representative seismic loads. The models can accurately simulate the interaction between the polyurethane foam fill and the steel brace. Additionally, the simulations can accurately determine when local buckling initiates as well as the buckled shape of the brace as the loading protocol progresses. The resulting models are used to conduct a parametric study to assess the influence of the foam fill on brace performance with respect to its ability to delay the initiation of local buckling and provide enhanced energy dissipation, while also providing an indication as to what section sizes benefit the most from the use of the foam within the void of CHS braces. The main conclusions from this work are as follows:

- The foam fill has a negligible influence on the elastic stiffness and tensile strength of the brace. The difference in elastic stiffness between empty and foam-filled braces is less than 1% for all of the considered sections, while the average difference in tensile strength between empty and foam-filled braces is 1.7%.

- The presence of the foam fill is able to delay the initiation of local buckling by at least one cycle for all but one of the section sizes considered. The section size that experiences no improvement in local buckling behavior with the use of the foam fill is an HSS 190.5 × 4.8 (D/t = 43.1; λ = 70). This finding establishes that the foam is only effective at delaying local buckling for braces with a D/t of less than 43.

- The maximum delay in the initiation of local buckling considering an empty and equal size filled brace (HSS 190.5 × 6.4) is seven cycles. Conservatively assuming that brace fracture occurs simultaneously with the initiation of local buckling, this seven cycle delay in when brace fracture occurs leads to the filled brace having a four times larger drift capacity than that of the empty brace (1% drift as opposed to 4% drift). This substantial increase in drift capacity can lead to cost savings associated with a decrease in residual deformation. A system-level analysis would need to be undertaken to more accurately quantify the improvement in braced frame performance that can be achieved by using foam-filled braces.

- The foam fill is most effective in braces with larger D/t and larger λ. The effectiveness of the foam for braces with a large D/t is likely a result of these sections being more susceptible to local buckling, thus having a higher ceiling for improvement. As local buckling is a precursor to brace fracture, the ability to impede the onset of local buckling is critical for prolonging the fracture life of braces.

Chapter 6 Transverse Plate to RHS Connections

6.1 Introduction

As the main focus of this research is the effective utilization of non-traditional civil engineering materials for void fill applications to mitigate structural response from seismic loads in braced frame systems, it is essential to be able to employ HSS, which have an inherent void that is ideal for the incorporation of fill materials in these systems. HSS perform well as columns, owing to their inherent torsional rigidity and efficiency in resisting compression and bending loads. While HSS come in a variety of different cross section geometries, square and rectangular hollow sections (SHS and RHS) are commonly preferred as column or truss members because their flat faces allow for easier connections relative to circular hollow sections (CHS) that require complex profiling (Packer et al. 2009). A simple means to connect other members to an RHS column is through welded branch plates. However, in the case of a branch plate welded to the face of an HSS parallel to its longitudinal axis, the inherent flexibility of the HSS face often results in excessive distortion or plastification of the connecting face. One alternative connection that has proven effective at reducing excessive deformation of the HSS face is the welded transverse branch plate to RHS (chord) connection.

The possible limit states for welded transverse branch plate to RHS connections where the transverse plate is in tension are local yielding of the plate, shear yielding of the RHS (punching shear), chord face plastification, and local yielding of the RHS sidewalls. The limit state equation for local plate yielding was derived from experimental work carried out by Rolloos (1969) on welded transverse plate to wide flange section connections in which the plate width, B_p, extended across the full width of the wide flange section. For connections to SHS and RHS the non-uniform stress distribution in the transverse branch plate that results from stiffer RHS webs near the ends of the plate led to the development of the following empirical equation:

$$b_e = 2t_w + Ct_f \qquad \text{Equation 6.1}$$

where b_e is the effective width of the connecting fillet weld, t_w is the thickness of the web of the wide flange, C is a dispersion constant that varies with plate yield stress, and t_f is the flange thickness. A modified version of Equation 6.1 for RHS sections with full width plates was published by the International Institute of Welding (1974), and was subsequently amended by Wardenier et al. (1981) to account for connections with plate widths less than the width of the RHS, differences in the RHS and plate yield stress, and differences in the RHS and plate thickness. The nominal strength equation for local plate yielding at any β (AISC 2010) became

$$R_n = \frac{10}{B/t} F_y t B_p \leq F_{yp} t_p B_p \qquad \text{Equation 6.2}$$

where F_y is the nominal yield stress of the RHS, F_{yp} is the nominal yield stress of the transverse plate, and B_p, B, t, t_p, and β are defined according to the schematic shown in Figure 6-1.

The limit state equation for shear yielding of the RHS was also developed based on the work of Wardenier et al. (1981). Specifically, a modified effective plate width equation was developed and incorporated into a general punching shear model to produce the following equation:

$$R_n = 0.6 F_y t (2t_p + 2B_{ep}) \qquad \text{Equation 6.3}$$

where $B_{ep} = \frac{10}{B/t} B_p$ is the effective plate width. This B_{ep} term can also be seen in Equation 6.2 for the limit state of local plate yielding.

While the limit state equation for chord face plastification is not included in the AISC Specification (AISC 2010), it is included in CIDECT Design Guide 3 (Packer et al. 2009) because plastification of the RHS face can theoretically govern when large compressive stresses are present in the RHS given particular β and B/t values. The limit state equation, which is based on a yield line analysis, is as follows:

$$R_n = \frac{2F_y t^2}{(1-\beta)} \left[\frac{t_p}{B} + 2\sqrt{(1-\beta)} \right] \qquad \text{Equation 6.4}$$

The limit state equation for local yielding of the RHS sidewalls is

$R_n = 2F_y t(5k + 2t_p)$ Equation 6.5

where k is the outside corner radius of the RHS. This limit state can occur when the branch plate is under tension or compression and β is approximately one. It accounts for the critical cross-section of the RHS sidewalls when the load from the branch plate is transmitted from the plate into the sidewalls.

The preceding limit state equations used to calculate the resistance of transverse plate to RHS connections under tensile axial plate load are valid for a finite range of connection geometric parameters. An older version of the CIDECT Design Guide (Packer et al. 1992) specifies that the limit state equations are valid for RHS sections with $B/t \leq 30$. This validity range represented the bounds of the test data at the time, as the validity expression was based on an experimental program undertaken by Wardenier et al. (1981) that examined transverse plate to RHS connections with chord slenderness ratios, B/t, spanning from 13.5 to 30. A more recent experimental and numerical investigation by Lu (1997) considered these connections with chord slenderness ratios ranging from 15.8 to 37.5 and β ranging from 0.18 to 0.93. Considering this new test data, CIDECT Design Guide 3 (Packer et al. 2009) specifies new limits of validity that require B/t and $H/t \leq 40$ and $\beta \geq 0.4$. The AISC Specification (AISC 2010) stipulates limits of $B/t \leq 35$ and $\beta \geq 0.25$. Given that the limits of validity are not absolute (i.e., parameters outside these limits are allowed), it is unclear whether there is a threshold that renders the limit state equations invalid concerning the ability to accurately predict connection capacity. Furthermore, the limits of validity are potentially too restrictive with respect to design flexibility leading to a need to study connection parameters outside of the current limits.

This chapter seeks to clarify the limits of validity for the design of transverse plate to RHS connections subject to monotonic plate tensile force. A secondary objective is to assess the suitability of the design equations defined in the AISC Specification (AISC 2010) for predicting the strength of these connections. To this end, an experimental program and companion numerical study are undertaken. The experimental program provides data necessary for calibrating high-fidelity finite element (FE) models and gaining a better understanding of how connection geometry influences connection behavior. The subsequent parametric FE study extends the scope of the experimental geometric parameters considered, allowing for connection behavior to be examined

outside of the limit state equations' current limits of validity. Moreover, this study has potential implications for design flexibility, as the current limits of validity can be restrictive, effectively limiting the amount of available connection geometries.

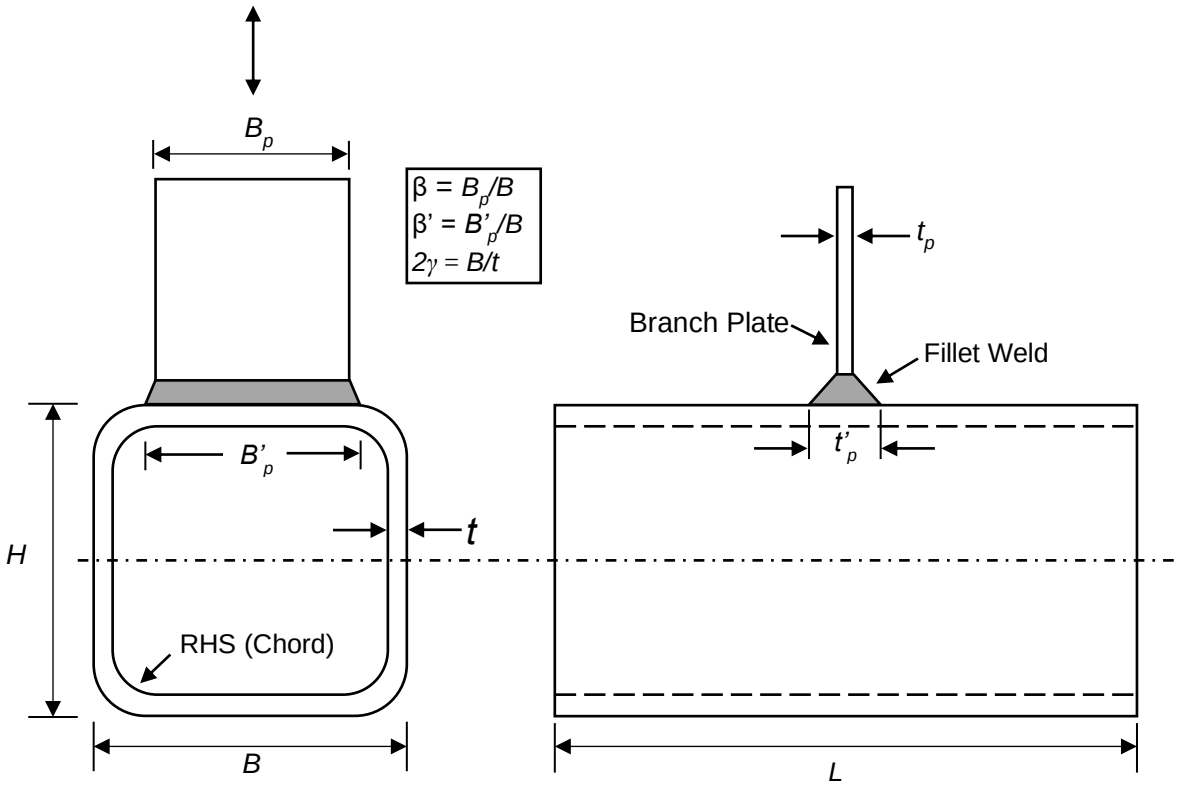

Figure 6-1 Transverse plate to RHS Connection geometric parameters

6.2 Experimental Program

6.2.1 Test Setup and Instrumentation

Testing was conducted using a 445 kN capacity uniaxial hydraulic load frame. Each of the test specimens consisted of a short RHS member ranging in length from 457 to 762 mm. For all specimens, a 12.7 mm thick end plate was welded to each of the ends of the RHS and the transverse branch plate was welded to the face of the RHS at its mid-length (Figure 6-2). Using A325 high strength bolts, the endplates of the RHS were connected to stiffened angles that were bolted to a T-slotted table to create a fixed connection. The specimens were connected to the stiffened angles using either 19.1 mm or 22.2 mm diameter bolts, whereas the stiffened angles were bolted to the T-slotted table using 15.9 mm diameter bolts. A welded double tee fixture bolted to the hydraulic

actuator loaded the branch plate in uniaxial tension via a steel cylindrical loading pin. If necessary, reinforcing plates were welded to either side of the branch plate around the pin hole to preclude bearing failure associated with the pin hole. The length of the transverse plate was carefully selected to ensure that the force transferred from the loading pin spread uniformly across the plate width before reaching the connection. The actuator was operated in displacement control at a quasi-static loading rate of 0.51 mm/min.

Tensile force applied to the branch plate was measured using a 445 kN load cell that was attached to the actuator. Deformations were captured using Northern Digital Inc.'s Optotrak Certus Motion Capture System. Optotrak markers, which are infrared light emitting diodes that are tracked in three dimensional space by position sensors, were placed along the height of the branch plate to capture any non-uniform plate deformations and to measure the deformation of the connection surface (δ) at the mid-length of the RHS. Markers located on the RHS sidewall parallel to the loading direction were used to capture any rigid body displacement of the assembly. Markers also were placed along the centerline of the connecting face of the RHS at intervals moving away from the connection to measure the deformation profile of the RHS connecting face. Strain gauges placed parallel to the loading direction and distributed across the plate width at a height of 38.1 mm from the connection surface were used to measure the non-uniform strain distribution in the branch plate (Figure 6-2). The specimens were also coated with whitewash to identify locations of yielding during testing.

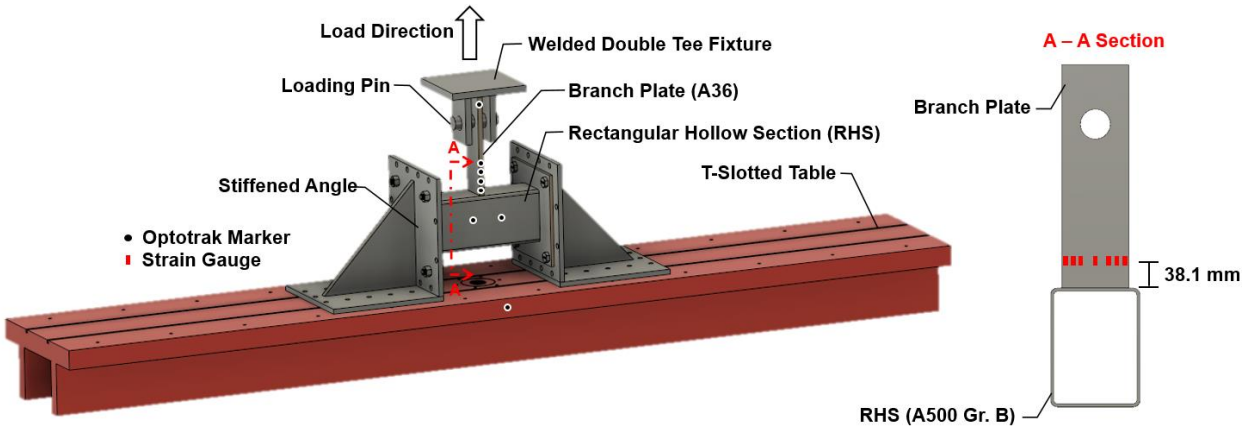

Figure 6-2 Experimental setup of the transverse plate to RHS connections

6.2.2 Test Specimens

A total of seven specimens were experimentally tested under monotonic tensile load. The connections had measured β that ranged from 0.3 to 0.81 and measured *B*/*t* that ranged from 21.9 to 42.4. Measured dimensions of the RHS, branch plate and fillet weld footprint for each specimen are provided in Table 6-1. Figure 6-1 provides a schematic showing the definition of each parameter. The naming convention used for the different specimens consists of "TP" for transverse plate, followed by the effective beta ratio, β' (e.g., 88 corresponds to β' = 0.88). Specimens in bold typeface have a geometric parameter that falls outside of the current limits of validity according to CIDECT Design Guide No. 3 (Packer et al. 2009) and the AISC Specification (*B/t* limit only) (AISC 2010). Overall, experimental testing was conducted to expand the current experimental database and provide a basis for numerical modeling to widen the scope of current design knowledge, particularly as it relates to exploring connection behavior outside of the limits of validity.

Table 6-1 Measured dimensions of test specimens

Specimen	$B \times H \times t$ (mm × mm × mm)	B/t	B_p (mm)	B'_p (mm)	β	β'	t_p (mm)	t'_p (mm)	L (mm)
TP88	152 × 203 × 5.87	26.0	115	135	0.75	0.88	18.7	46.0	457
TP84	203 × 203 × 5.82	34.9	152	171	0.75	0.84	19.0	45.7	610
TP90	253 × 103 × 5.97	**42.4**	204	229	0.81	0.90	19.3	50.8	762
TP38	253 × 103 × 5.97	**42.4**	75.9	96.8	**0.30**	0.38	12.5	38.4	762
TP50	202 × 102 × 8.86	22.8	75.9	101	**0.38**	0.50	12.5	41.7	610
TP58	205 × 305 × 9.37	21.9	102	119	0.50	0.58	12.8	36.2	610
TP75	205 × 305 × 9.37	21.9	129	154	0.63	0.75	12.5	35.3	610

6.2.3 Material Properties

The RHS members for all specimens were fabricated from ASTM A500 Gr. B steel with a specified minimum yield stress of 317 MPa and a tensile strength of 400 MPa. The branch plates were fabricated from ASTM A36 hot-rolled steel bar with a minimum yield stress of 248 MPa and a tensile strength of 400 MPa. E70 electrodes with a nominal tensile strength of 483 MPa were used for the fillet welds. Tensile coupons extracted from the flats of the RHS and from an A36 bar were tested in accordance with ASTM E8 (2016). All-weld-metal coupons were fabricated from an as-laid weld to determine the material properties of the weld material. Average measured properties are presented in Table 6-2 with all averages based on results from three coupon tests,

with the exception of the weld properties, which are based on two coupon tests. Yield stresses were determined using the 0.2% strain offset method. Note that only one set of coupon tests were performed to obtain the material properties of the transverse plates and fillet welds since the same stock material is used for all specimens.

Table 6-2 Average measured material properties

	RHS			Transverse Plate		
Specimen	Yield stress F_y (MPa)	Tensile strength F_u (MPa)	Elastic modulus E (GPa)	Yield stress F_y (MPa)	Tensile strength F_u (MPa)	Elastic modulus E (GPa)
TP88	355	443	184	318	448	192
TP84	370	462	184			
TP90	399	479	200	Fillet Weld		
TP38	399	479	200	583	633	198
TP50	381	456	184			
TP58	391	483	197			
TP75	391	483	197			

6.3 Experimental Results

The following sections present and discuss the experimental results with emphasis placed on the behavior of tested specimens that had geometric parameters that fell outside of the limits of validity stipulated by CIDECT (Packer et al. 2009) and the AISC Specification (AISC 2010).

6.3.1 General Connection Behavior

The force-deformation curves for all of the tested connections (Figure 6-3) provide a general understanding of the transverse plate connection behavior. The connection deformation was calculated as the vertical displacement of the marker at the bottom of the branch plate (closest to the connection) minus the vertical displacement of the right marker on the RHS sidewall (Figure 6-2). Displacements of both markers on the RHS sidewall were nearly identical for all tests, indicating that the RHS did not rotate during testing. Each connection initially exhibited a linear elastic region before gradually transitioning into non-linear behavior. For example, specimen TP90 had an initial elastic stiffness of 281 kN/mm, which is nearly 17 times greater than that of TP38

even though both specimens had the same *B/t* (42.4). The substantial difference in stiffness can be attributed to the β value of TP90 being nearly three times greater than that of TP38. In general, specimens with larger β values exhibited a greater initial stiffness than specimens with smaller β values, irrespective of *B/t*, owing to the plate extremities being able to better engage the stiffer RHS sidewalls.

Specimens TP84 and TP90 failed abruptly soon after reaching the non-linear range, while specimens TP38 and TP50 displayed excellent ductility with a normalized connection deformation of about 7% before the plate tensile load began to taper off due to fracture at the corner of the weld toe on the connection face. However, such large deformations are not acceptable in actual structures and the connections can be said to have suffered a serviceability related failure due to significant deformation of the RHS face. Lu et al. (1994) proposed serviceability and ultimate deformation limits of 0.01*B* and 0.03*B*, respectively, which have been commonly used to define the capacity of HSS connections that do not exhibit a clearly defined yield or peak load. The corresponding plate tensile force at the serviceability and ultimate deformation limits are designated as $F_{1\%}$ and $F_{3\%}$, respectively, and are presented in Table 6-3 along with other important experimental quantities. The specimens without $F_{3\%}$ values failed due to fracture prior to reaching a connection deformation equal to 3% of the RHS width.

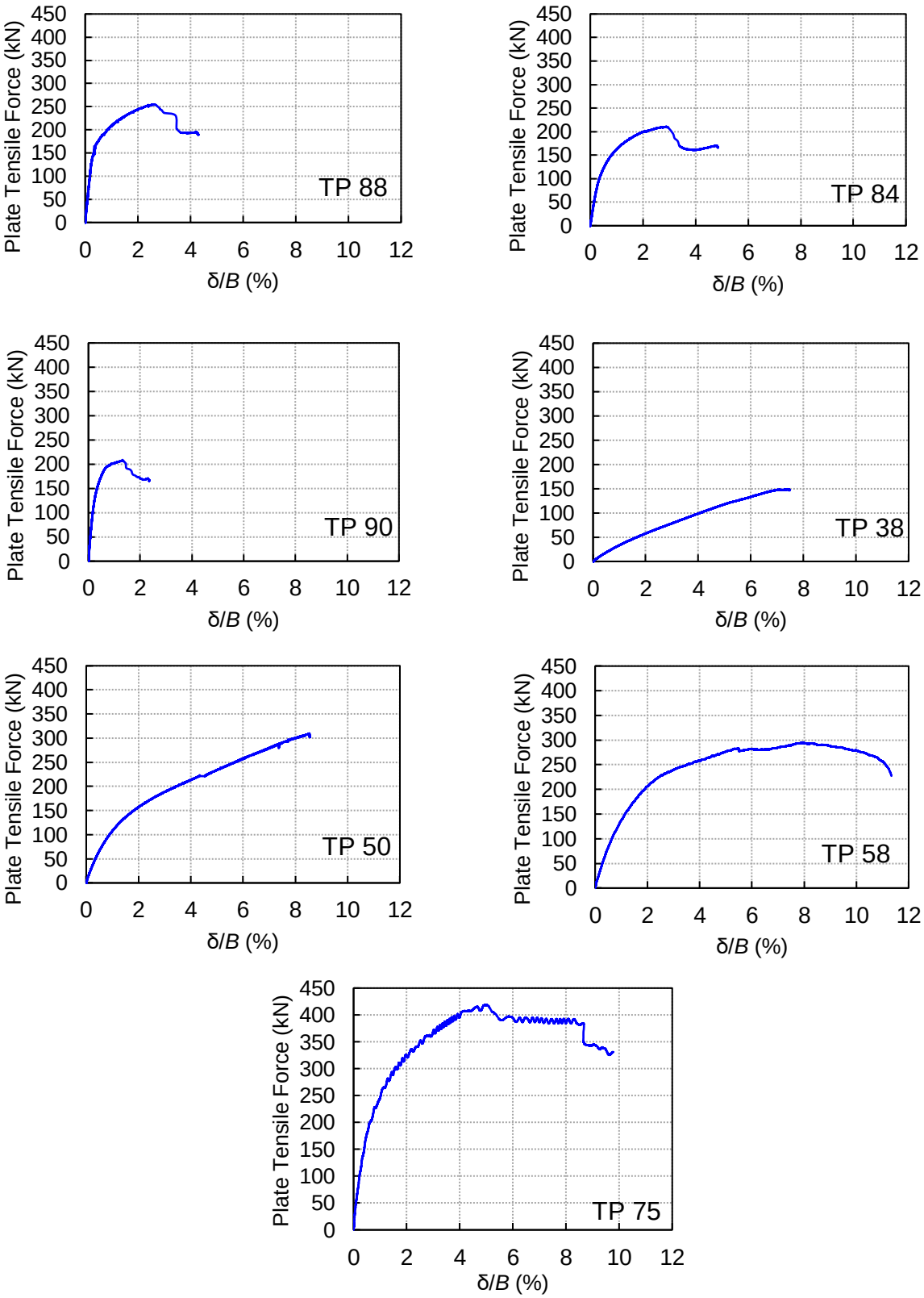

Figure 6-3 Plate tensile force versus normalized connection deformation

Table 6-3 Test results for the transverse plate to RHS connections

Specimen	*B/t*	β	Stiffness (kN/mm)	Ultimate force (kN)	Failure[1] mode	$F_{1\%}$ (kN)	$F_{3\%}$ (kN)
TP88	26.0	0.75	368	255	PS	208	--
TP84	34.9	0.75	172	210	PS	162	--
TP90	**42.4**	0.81	281	209	PS	202	--
TP38	**42.4**	**0.30**	17.0	149	CFP	33.4	78.4
TP50	22.8	**0.38**	69.3	308	CFP	108	189
TP58	21.9	0.50	83.4	294	CFP	137	240
TP75	21.9	0.63	175	419	CFP	240	371

[1]PS is punching shear and CFP is yielding of the chord face (chord face plastification)

6.3.2 Failure Modes

All of the tested specimens failed by either punching shear (PS) or yielding of the chord face (CFP). A punching shear failure is characterized by fracture in the RHS member material at the toe of the weld allowing a portion of the RHS member equal to the footprint of the weld to "punch" through the face of the RHS. Since this failure mode had been shown to occur in conjunction with chord face plastification, Davies and Packer (1982) derived an analytical equation for the connection capacity that accounted for this combined mechanism. However, its complexity prevented it from being incorporated into current limit state equations.

Chord face plastification is a failure mechanism whereby the connecting RHS face yields. The design resistance equation derived for this mechanism is based on a yield line solution and provides a conservative predictor of connection capacity as it does not account for strain hardening and membrane action, which can provide substantial capacity beyond the plastic solution. As such, this limit state is primarily in place to restrict excessive connection deformations (Davies et al. 1981).

The failure mode for specimens TP90 and TP50 are shown in Figure 6-4. TP90 failed by punching shear at a connection deformation of 1.45% of the RHS width and a plate tensile force of 202 kN. This type of sudden failure is unsurprising given that the width of the plate nearly extends to the corners of the RHS, which are inherently less ductile than the flats of the RHS due to the cold forming process (Fadden and McCormick 2014). In contrast, TP50 exhibited considerable flexibility by reaching a connection deformation of approximately 8.5% of the RHS width and a peak force of 308 kN. Chord face plastification is demonstrated by the convexity of the connection surface that peaks at the mid-length of the RHS where the branch plate is attached.

Punching shear failures were restricted to connections that had β values greater than 0.75, while chord face plastification was the failure mode for all other connections. No local plate yielding failures or yielding of the RHS sidewalls were observed largely based on the design of the branch plate.

(a) (b)

Figure 6-4 Failure of specimens (a) TP90 by punching shear (PS) and (b) TP50 by chord face plastification (CFP)

6.3.3 Strain Distribution

Graphs of plate strain distribution as a function of position along the plate width (a position of 0 delineates the plate centerline) for specimens TP38 and TP90 are given in Figure 6-5. Both specimens have the same *B*/t (42.4), but differ with respect to β. For both specimens, it is shown that larger strains are achieved near the outer edges of the plate owing to the plate extremities being able to better engage the stiffer RHS sidewalls. The strain distributions are shown at 25 kN intervals of plate force. The strain distribution for both specimens becomes increasingly non-uniform as the plate force increases since the plates do not extend the full width of the RHS. This behavior is in contrast to plates that extend the full width of the RHS, which leads to the strain (or stress) distribution becoming more uniform as the branch plate transitions out of the elastic regime and into the plastic range before plate failure (Davies and Packer 1982). Using the transverse plate material properties presented in Table 6-2, the yield strain for the transverse plates is 0.00165 or approximately 0.17%. As shown in Figure 6-5, the strains measured at the plate surface are well within the elastic range and peak at approximately 0.07% strain, even as the plate force approaches the maximum value achieved during testing. The ability of the plate to remain elastic is largely a

result of the large *B*/*t* for both specimens leading to considerable flexibility of the RHS face. The large cross-sectional area of the plate also ensures that the plate remains elastic, since the plate capacity is directly related to its cross-sectional area. While strain distributions for both specimens highlight the effective width concept, where only a small portion of the plate width is utilized to transfer the applied load at the connection, the strain distribution seen for TP90 demonstrates the significance of this concept. It is shown that the strain distribution is highly non-uniform, rendering only a smaller portion of the plate width effective as the plate force continues to increase. The strain distributions from specimens TP84, TP88, TP50 and TP75 also show an increasingly non-uniform strain distribution as plate force increases. No strain gauge data is available from specimen TP58.

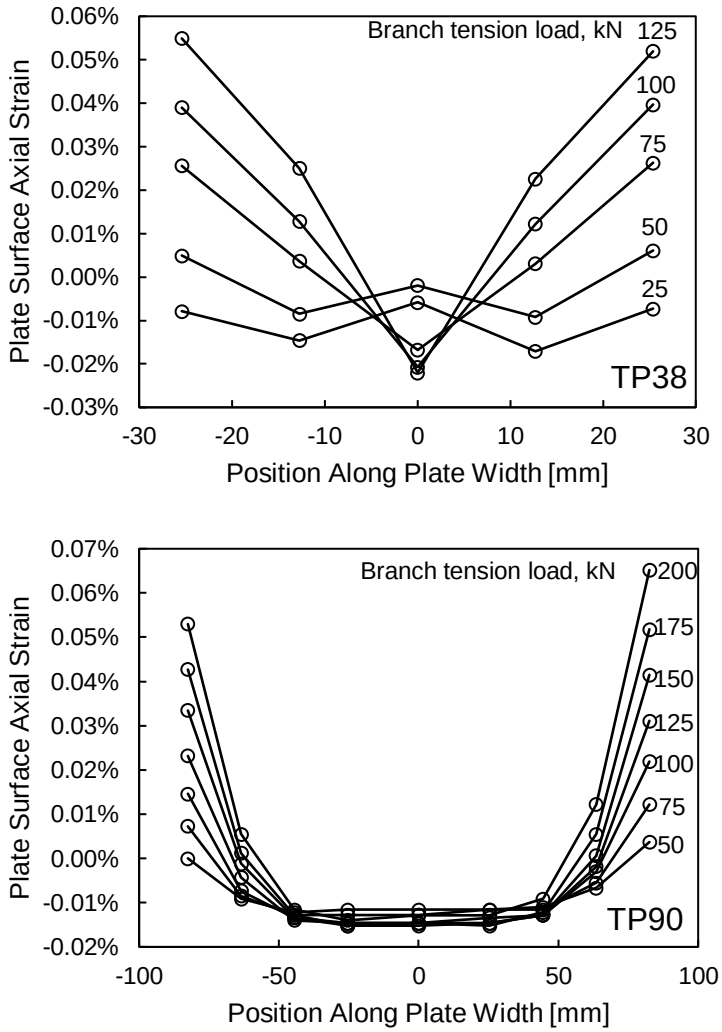

Figure 6-5 Plate strain distribution for TP38 and TP90 at different load levels

6.3.4 Code Comparisons

To assess the applicability of the current limits of validity, the connection strengths predicted by the CIDECT (Packer et al. 2009) design equations and the AISC Specification (AISC 2010) nominal strength equations are compared to those from the experimental results. As the nominal strength equations neglect the influence of the fillet weld, effective parameters (i.e., t'_p, B'_p, and β') are used to incorporate the contribution of the weld in the connection strength calculation. The effective parameters are larger than the nominal parameters because they include the geometry of the fillet weld (Figure 6-1), which increases the connection capacity predicted by the nominal strength equations. Furthermore, measured material properties (Table 6-2) are used instead of specified minimum strengths to more accurately predict the connection strength. The 2016 AISC Specification (AISC 2016b) equations are not considered in this comparison because this edition no longer explicitly includes limit state equations or limits of validity for transverse branch plate connections in Chapter K. However, these equations can be derived from equations in Chapter J or through a yield line analysis.

A comparison between the CIDECT predicted strength and the force at the serviceability deformation limit for all tests is shown in Figure 6-6a. The filled markers represent specimens that have a geometric parameter that falls outside of the limits of validity. The specimen identifier is next to the marker for clarity. In general, the CIDECT design equations are able to accurately predict the capacity based on the serviceability deformation limit as indicated by the average ratio of the CIDECT predicted strength to the measured connection force at $0.01B$ being equal to unity considering all specimens. The coefficient of variation (CoV) is 0.38, indicating a relatively large amount of scatter. The scatter would likely decrease if a wider range of connection geometries were considered. Based on the specimens with parameters outside of the limits of validity, the results suggest that the CIDECT design equations for these specimens are not always conservative, as evidenced by the markers for specimens TP50 and TP38 falling below the dashed line. However, it should be noted that the CIDECT design equations accurately predicted the failure mode of chord face plastification for specimens TP38 and TP50. Meanwhile, specimen TP90 failed by punching shear while the CIDECT design equations predicted local plate yielding as the governing failure mode. The design equations also under predicted the capacity of the connection. This under prediction of capacity is likely a result of the under prediction of the plate effective width, which

according to the local plate yielding nominal strength equation in CIDECT (Packer et al. 2009), is 0.03*B*. This effective width value is low considering that the strain distribution for TP90 (Figure 6-5) indicates large strain values over at least 0.15*B* of the plate width at its extremities.

Figure 6-6b provides a comparison between the AISC predicted nominal strength and the force at the serviceability deformation limit for all tests using the previously defined plotting convention. The average ratio of the AISC predicted nominal strength to the connection force at 0.01*B* is 1.05 for all specimens, while the coefficient of variation (CoV) is 0.40. These statistics are similar to those produced by the CIDECT equations, except the AISC equations provide an unconservative estimate of connection strength as indicated by the strength ratio being greater than one. The main difference between the AISC and CIDECT strength predictions is the discrepancy in the governing failure mode. When using the AISC equations, the predicted failure mode is local plate yielding for all specimens, whereas for the CIDECT equations chord face plastification is the predicted failure mode in all specimens except for TP88, TP84, and TP90, where local plate yielding governs. While it is concerning that the AISC equations provide an inaccurate prediction of the governing failure mode, it is postulated that using a larger sample size would lessen the frequency of inaccurate failure mode predictions. It is likely that considering a larger sample size with a wider scope of parameters would cause more accurate predictions of the governing failure mode or at the very least help in identifying which connection geometries are problematic for the strength equations to predict the failure mode.

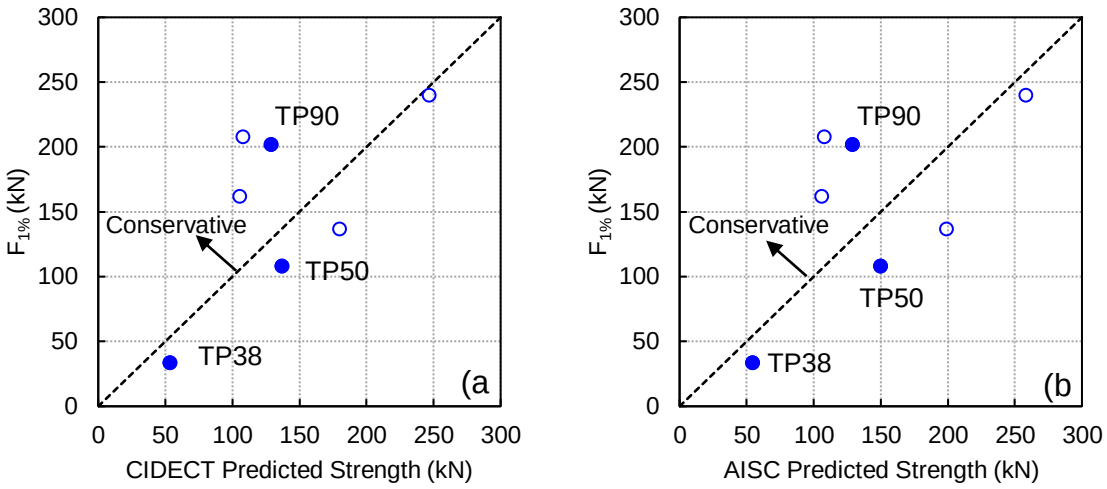

Figure 6-6 Predicted connection strength according to (a) CIDECT (Packer et al. 2009) and (b) AISC (2010)

Figure 6-7 compares the CIDECT and AISC predicted strengths with the ultimate connection force achieved during testing. As expected, both approaches provide quite conservative predictions of connection capacity, owing to the fact that they do not account for capacity increasing mechanisms such as strain hardening and membrane action.

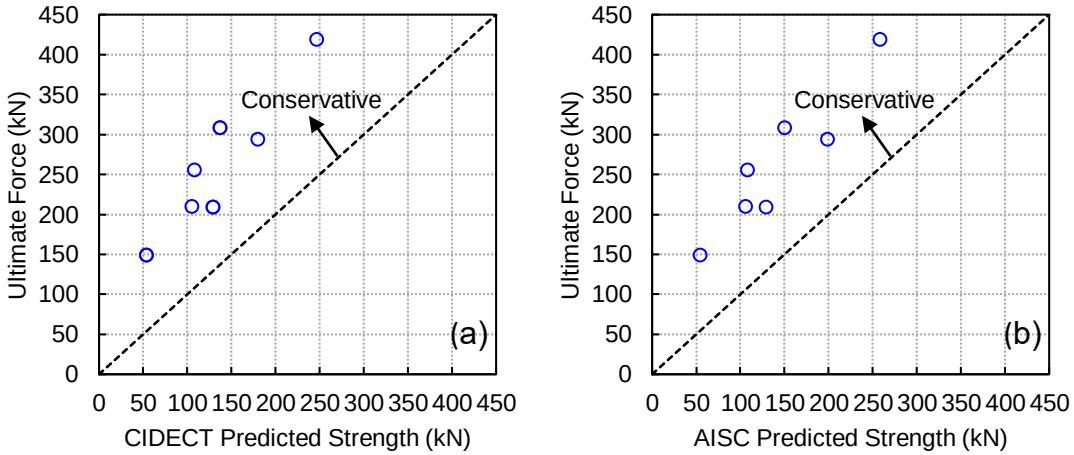

Figure 6-7 Comparison of the (a) CIDECT (Packer et al. 2009) and (b) AISC (2010) predicted strengths with the experimental ultimate connection force

6.4 Finite Element Model

The experimental results from the tested connections were used to calibrate and validate finite element models to expand the range of geometric parameters considered. Specifically, results from the experimental tests and identical FE models were compared with respect to force-deformation behavior and connection failure. The following sections highlight the numerical modeling details, which includes the model geometry, material properties, and model validation.

6.4.1 General Modeling Details

All analyses were performed using the general-purpose finite element software suite Abaqus FEA 2017 (Simulia 2017). A static nonlinear analysis using implicit time integration was used to determine the connection behavior. Specifically, nonlinear systems of equations were iteratively solved at each time increment using the Newton-Raphson method. Figure 6-8 shows the one-quarter model employed for all analyses, which leverages symmetry of the connection with respect to geometry, loading and boundary conditions to reduce computation time. Symmetry boundary conditions that restrict out of plane displacement and rotation about the axes perpendicular to the out of plane direction were applied to the nodes at the XY and YZ cut plane boundaries, respectively. As the endplates from the experimental tests were not explicitly modeled, a fixed boundary condition was applied to the nodes located on the XY plane at the end of the RHS member to constrain all degrees of freedom. An incremental displacement that places the branch plate under tension was applied to the nodes at the top face of the plate to simulate the displacement-controlled loading applied during the experimental tests. The total force in the plate was obtained by summing the forces acting on each node and multiplying that value by four to account for the one-quarter geometry. The connection deformation was taken as the vertical displacement of the node highlighted in red in Figure 6-9.

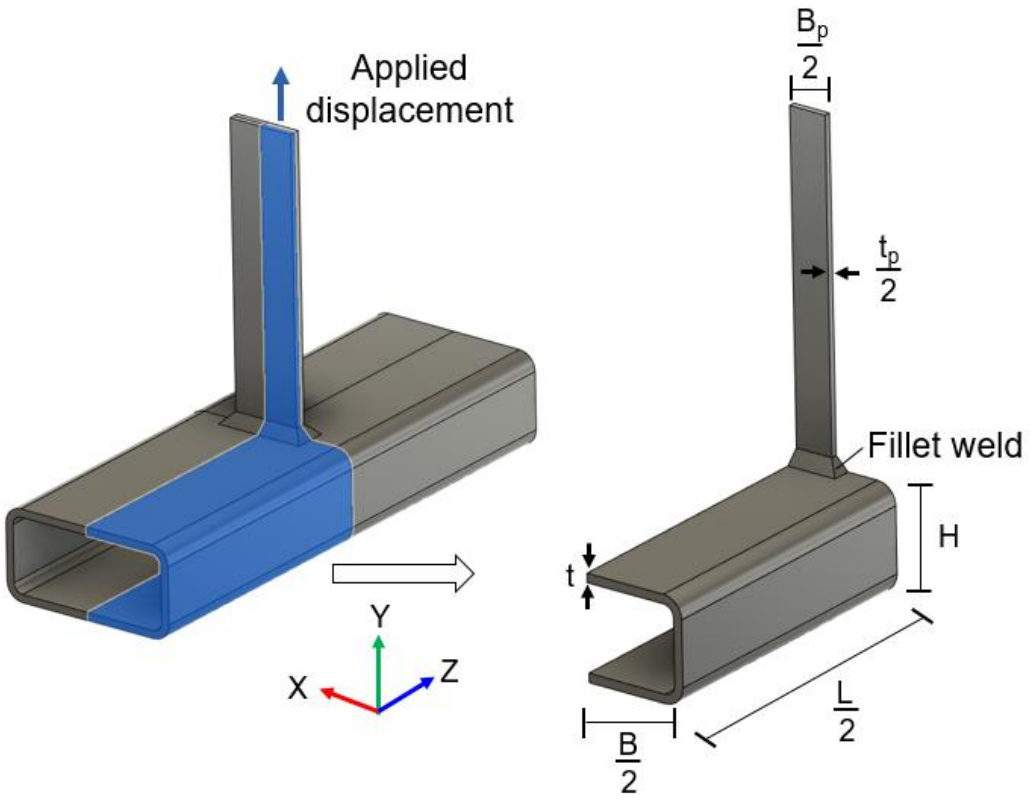

Figure 6-8 Model geometry

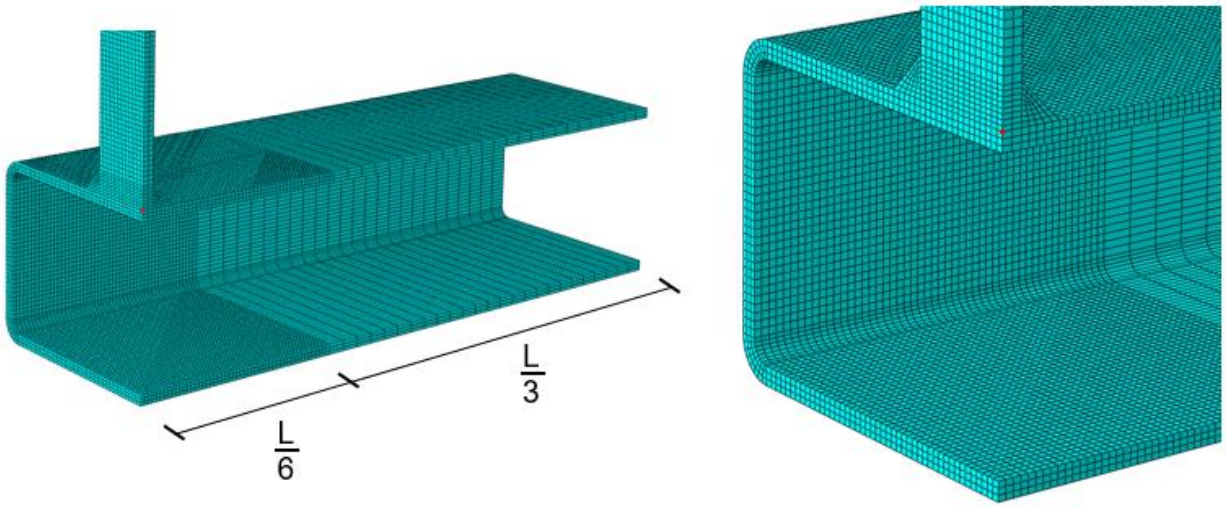

Figure 6-9 Typical mesh arrangement

A sensitivity study was conducted to determine an appropriate element type to discretize the finite element models. Two element types were considered: an eight node solid element with reduced integration and hourglass control, designated as C3D8R in Abaqus, and a 20 node solid element

with reduced integration (C3D20R). Use of C3D20R elements significantly increased the analysis time with a negligible increase in accuracy, thus C3D8R elements were employed for all regions of the model.

Similarly, a sensitivity study that considered the use of two, three and four elements to model the wall thickness of the RHS indicated that at least three elements through the thickness are necessary to accurately capture the connection behavior. The sensitivity of the force-deformation response to the number of elements used to discretize the wall thickness is provided in Figure 6-10. The ordinate is the force at a deformation of 3% of the RHS width, normalized by $F_y t^2$, and the abscissa is the number of elements through the wall thickness. For different β, the normalized force begins to converge using three elements, with only a slight increase in normalized force as B/t increases when using four elements through the chord thickness.

As shown in Figure 6-9, the mesh was partitioned into two distinct sections to improve computational efficiency and accurately capture the behavior of the connection in high stress regions. The high mesh density at the center of the connection employed elements with edge lengths of approximately 2.5 mm. Care was taken to ensure element aspect ratios of unity in this region to help alleviate the dependency of connection failure on the mesh. The remaining mesh utilized a coarser mesh with a typical element size four times larger than that employed at the central region of the connection.

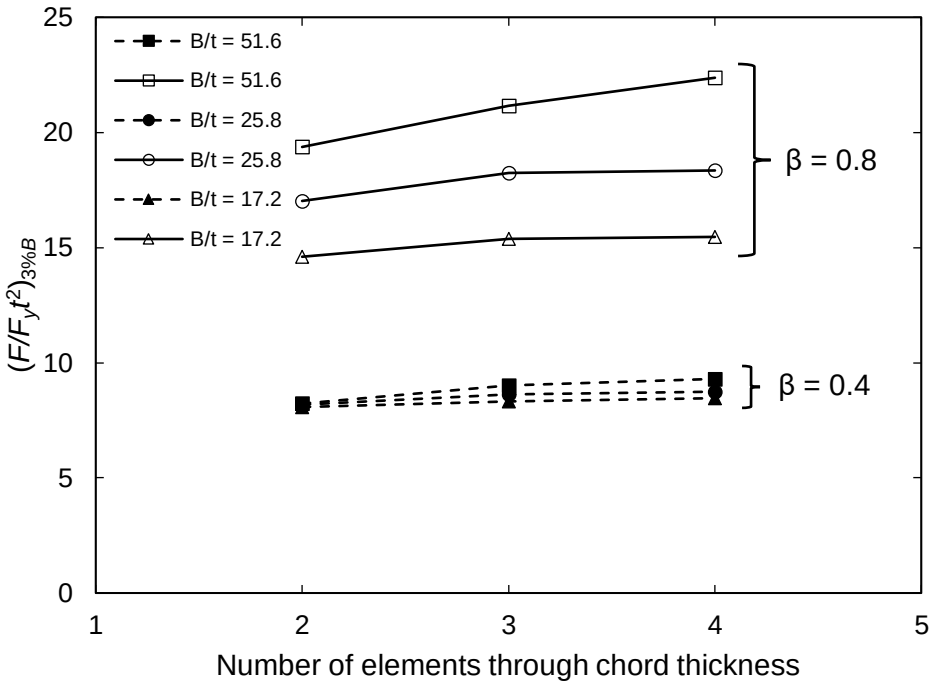

Figure 6-10 Sensitivity of force-deformation response to the number of through-thickness chord wall elements

6.4.2 Material Properties

The material properties of the corners and walls of the RHS, branch plate, and weld were defined based on the previously described tensile coupon tests in Section 6.2.3. As multiple coupons were tested for each material, a representative coupon was used to define the respective material models. Given the relative lack of ductility in the corner regions of a RHS compared to the flats due to the cold forming process, it was deemed appropriate to define separate material models for the corner material and flat material of the RHS (Fadden and McCormick 2014). Engineering stress-strain data from the coupon tests were converted to true stress-strain data using the following equations:

$$\sigma_{True} = \sigma_{Engineering}\left(1 + \varepsilon_{Engineering}\right) \quad \text{Equation 6.6}$$

$$\varepsilon_{True} = \ln\left(1 + \varepsilon_{Engineering}\right) \quad \text{Equation 6.7}$$

where σ and ε are stress and strain, respectively. The true stress-strain data was then used to define a nonlinear isotropic hardening model based on the von Mises yield criterion. Specifically,

isotropic hardening was defined in a tabular manner with stress defined as a function of plastic strain. The true stress-plastic strain data and elastic modulus for each material model are defined in Figure 6-11 and the complete material model inputs are provided in Appendix D. A Poisson's ratio of 0.3 was used for each material model.

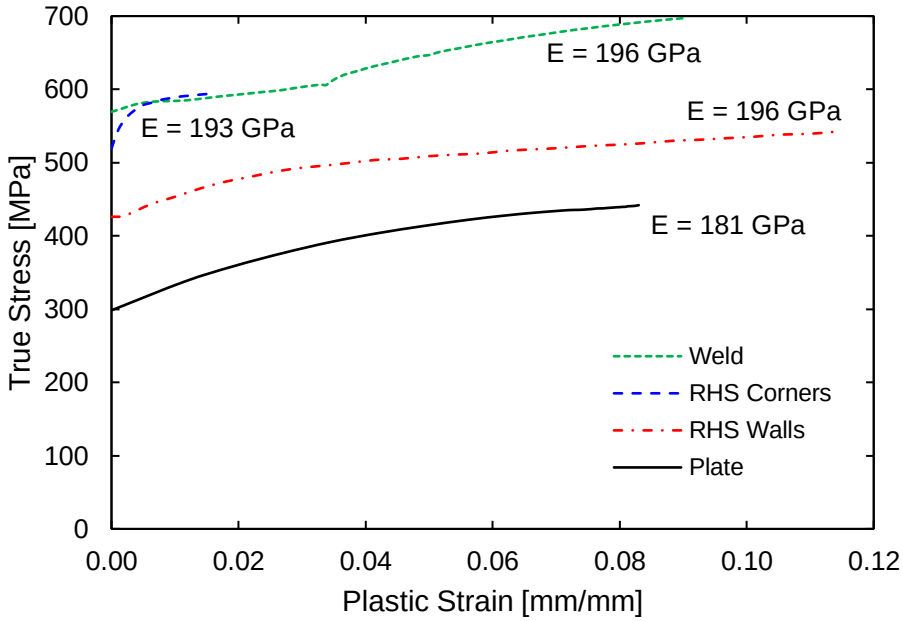

Figure 6-11 Abaqus material models

6.4.3 Fracture

A damage model was incorporated into the analyses to simulate the degradation of strength and subsequent fracture of the connection. The framework of this damage model is characterized by a two-pronged approach consisting of a damage initiation criterion and a damage evolution law. The damage initiation criterion operates under the premise that the equivalent plastic strain at the onset of damage is a function of stress triaxiality and strain rate. Analytical expressions for the equivalent plastic strain at fracture for ductile and shear failures derived by Hooputra et al. (2004) from experimental testing of aluminum were modified accordingly to produce damage initiation that agreed well with the instant of damage initiation in the experimental tests. The damage evolution law, which describes the degradation of the material stiffness, is defined by the following equation:

$$\sigma = (1 - D)\bar{\sigma} \qquad \text{Equation 6.8}$$

where D is a scalar damage variable and $\bar{\sigma}$ is the computed stress tensor without the consideration of damage. When D is equal to unity the material has zero stiffness. The damage evolution law was specified in an exponential form using an iterative procedure with the damage variable given as a function of equivalent plastic displacement to limit sensitivity to mesh size. The damage initiation and evolution parameters are provided in Table 6-4. The aforementioned damage model in conjunction with Abaqus' element removal feature provided a visual indication of fracture. It should be noted that the fracture criterion was only applied to the corners and walls of the RHS, since the welds used to connect the plate and RHS were designed to be non-critical.

Due to the softening behavior that is introduced by the use of a damage model, the implicit solver employed for the analyses experienced convergence difficulties. To overcome these difficulties, a viscous regularization scheme was introduced. This scheme is able to alleviate convergence difficulties while not compromising the results of the analysis by causing the Jacobian to remain positive-definite for small time increments. A viscosity parameter of 0.005 was used after conducting a parametric study to ensure that the accuracy of the results was not compromised by the use of this parameter. Figure 6-12 shows how the force versus connection deformation response of specimen TP50 evolves with the use of the viscosity parameter. As the viscosity parameter increases, the accuracy of the response degrades. The response using a viscosity parameter value of 0.005 is identical to the response without the use of the parameter (default value of 0) up to just before connection failure. This suggests that a value of 0.005 is low enough to accurately simulate the connection response. A viscosity parameter value of 0.005 was also used by Lapczyk and Hurtado (2007) to obtain a converged solution in an implicit analysis to determine the blunt notch strength of a fiber metal laminate.

Table 6-4 Damage model parameters

Damage Initiation		Damage Evolution	
Stress Triaxiality	Equivalent Plastic Strain	Plastic Displacement	Exponential Law Parameter
0	0.139	0.041	5
0.5	0.060		
1	0.027		
1.5	0.015		
2	0.014		

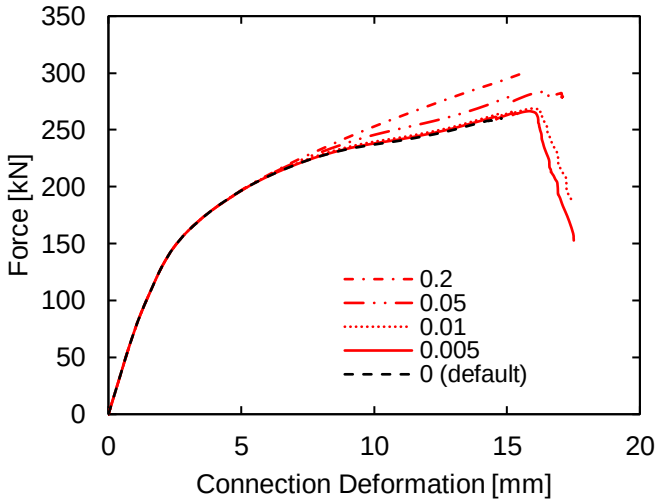

Figure 6-12 Sensitivity of the force-deformation response for specimen TP50 to the viscosity parameter

6.4.4 FE Model Validation

Using the preceding modeling techniques, numerical analyses were conducted for five of the tested connections. All models were constructed based on measured geometric dimensions. The load-deformation responses from the five experimental tests and corresponding FE models are shown in Figure 6-13. In general, the FE results agree well with the experimental data with respect to the initial stiffness, force at the serviceability (deformation of 1%B) and ultimate (deformation of 3%B) deformation limits, respectively, and the connection failure mode. A quantitative comparison of the FE and experimental results is provided in Table 6-5 which serves to further

confirm the validity of the modeling techniques employed. Table 6-5 presents the branch plate tensile force at the serviceability and ultimate deformation limits (denoted as $R_{1\%}$ and $R_{3\%}$, respectively) as well as the maximum connection force, R_{max}. The connection capacity for both the experimental and FE models is taken as R_{max} if this force is achieved prior to the connection deformation reaching the ultimate deformation limit. Otherwise, the capacity is taken as $R_{3\%}$. Yielding of the branch plate was not considered because the plate surface strains remained well within the elastic range for all tests. The ratio of the experimental to FE connection capacity, R_{ult}, has an average value of 0.92 with a coefficient of variation of approximately 0.06, suggesting that the FE models are effective at predicting the connection capacity.

The validity of the FE modeling techniques was further confirmed by the ability of the FE analyses to accurately capture connection failure. Figure 6-14 shows images of the failure modes of specimens TP84 and TP50 during testing and from corresponding FE simulations. For specimen TP84, the simulation captured the removal of the crosswall of the RHS from the connection face as shown by Figure 6-14b. Failure of specimen TP50 by chord face plastification was accurately captured by the FE simulation (Figure 6-14d), which shows the upward deformation of the connection face and damage around the weld footprint as the weld began to tear out of the connection face. The ability of the simulations to accurately predict connection failure further confirms the validity of the preceding modeling techniques.

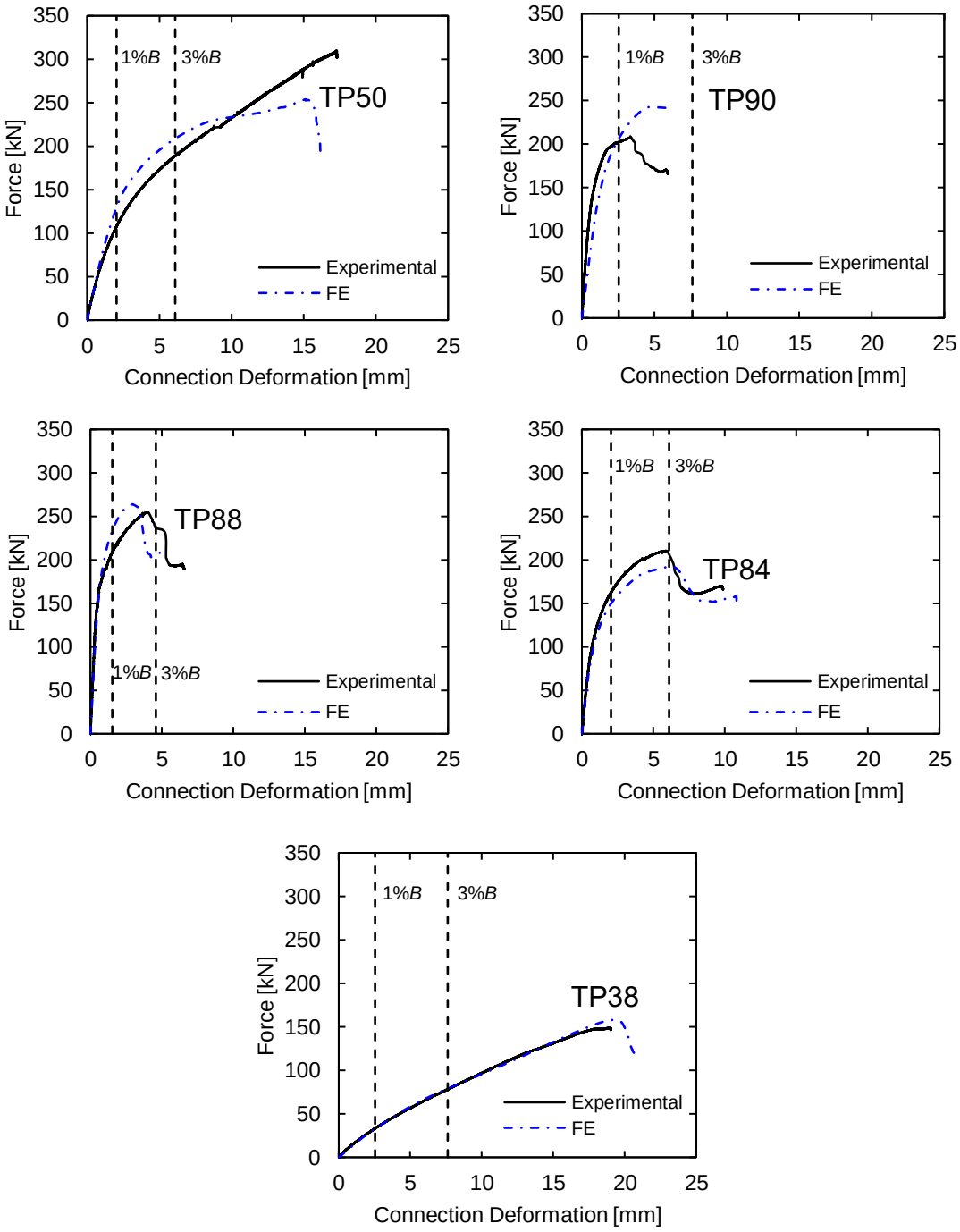

Figure 6-13 Experimental and FE load deformation curves for model validation

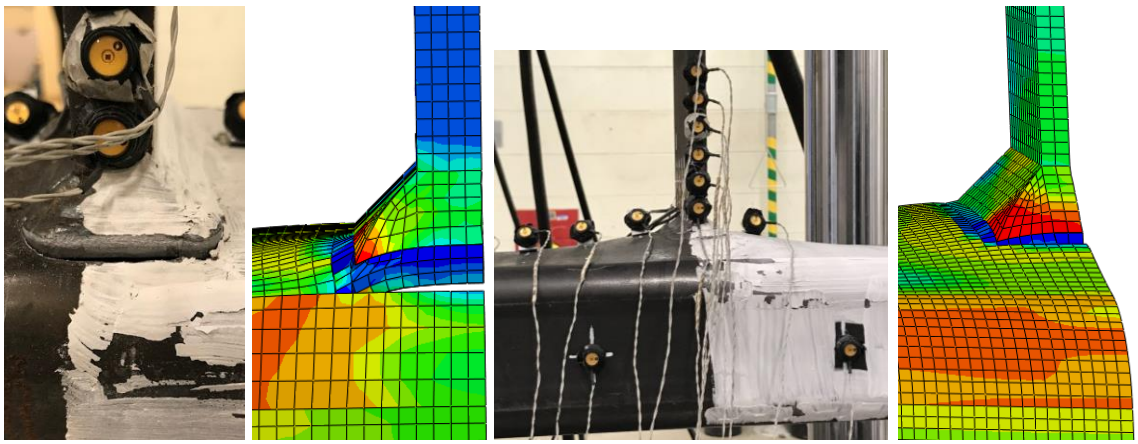

(a) (b) (c) (d)

Figure 6-14 Punching shear failure of specimen TP84 from the (a) test and (b) corresponding FE analysis as well as chord face plastification of specimen TP50 from the (c) test and (d) FE analysis

Table 6-5 FE and experimental results comparison for model validation

		Experimental [kN]			FE [kN]			Experimental/FE
Specimen	β	R_{max}	$R_{3\%}$	$R_{1\%}$	R_{max}	$R_{3\%}$	$R_{1\%}$	R_{ult}
TP38	0.3	149	78.3	33.4	158	79.0	32.7	0.99
TP90	0.8	209	--	202	247	--	206	0.85
TP50	0.375	308	189	108	254	209	130	0.90
TP88	0.75	255	--	208	264	--	242	0.97
TP84	0.75	210	--	162	193	--	149	0.92

6.5 Parametric Study

6.5.1 Parametric Study Parameters

A finite element parametric study was developed to broaden the scope of the experimental program and examine the connection behavior when the geometric parameters are outside of the limits of validity of the design equations. The study utilized the same modeling techniques as used for the validated finite element model. A total of 70 connections were modeled with 2γ ranging from 17.2 to 57.5 and β' from 0.17 to 0.97. Of the 70 connections, 37 fell outside of the limits of validity with $2\gamma > 35$, while six connections fell outside of the limits of validity with $\beta' < 0.25$. The overall parameters studied are presented in Table 6-6 based on the definitions provided in Figure 6-1. All of the HSS sections were modeled with the design wall thickness ($0.93t$), which is defined as t

according to Figure 6-1 and listed in the AISC Manual of Steel Construction (AISC 2017) as well as shown in Table 6-6. The exterior radii of the RHS corners were modeled as twice the design wall thickness. Half of the connections were modeled with a branch plate thickness of 12.7 mm while the other half had a branch plate thickness of 19.1 mm. The fillet welds were sized to carry the full capacity of the branch plate. To this end, a weld leg of 13.5 mm was used for the 19.1 mm thick branch plates and a weld leg of 8.9 mm was used for the 12.7 mm thick branch plates. These values equate to weld throat sizes of half of the plate thickness. To mitigate the influence of the fixed end boundary condition on the local deformation of the RHS face, the RHS length from the fixed boundary condition to the XY cut plane was modeled as 1.5*B* (Figure 6-8). This value was also used to determine the length of the RHS members for the experimental tests. The validity of this value is further confirmed by an FE analysis that considered different chord lengths and showed that a modeled chord length of 1.5*B* is long enough to negate any influence from end effects.

Table 6-6 Parametric study geometric parameters

RHS (mm x mm x mm)	*t* (mm)	*B*/*t*	*B* (mm)	β'
254×127×4.8	4.42	57.5	254	0.17 - 0.97
304.8×304.8×6.4	5.92	51.5	305	0.23 - 0.92
203.2×152.4×4.8	4.42	46	203	0.34 - 0.88
228.6×177.8×4.8	4.42	40.2	178	0.39 - 0.96
254×203.2×7.9	7.39	34.4	254	0.17 - 0.96
228.6×228.6×7.9	7.39	30.9	229	0.30 - 0.90
203.2×152.4×9.5	8.86	22.9	203	0.34 - 0.88
203.2×203.2×12.7	11.8	17.2	203	0.21 - 0.88

The load-deformation curve for each connection was determined using the same data extraction locations used for the FE validation models. In addition to the maximum connection force, the connection forces at the serviceability and ultimate deformation limits were extracted. Connection capacity was classified according to three limit states: RHS shear yielding (punching shear), local plate yielding, and chord face plastification. Visual observation of the FE time-history animations with von Mises contours plotted on the deformed connection in conjunction with Abaqus' element deletion feature allowed for the failure mode to be identified. The connection capacity, R_n, was defined as the maximum connection force, R_{max}, if this value was obtained before the 3%*B*

deformation level was achieved, otherwise the force corresponding to 3%B, $R_{3\%}$, governed the capacity. When local plate yielding occurred based on von Mises contours plotted on the deformed connection configurations, the connection capacity was defined as the lesser of the force at the initiation of weld failure (i.e., when the von Mises stress in the weld exceeded its tensile capacity) and the force corresponding to a deformation of 3%B. As the welds were sized to carry the full capacity of the plate, it was deemed appropriate to consider plate failure as occurring simultaneously with weld failure. For cases in which significant deformation occurred in the plate, a threshold difference of 0.18 mm between the connection deformation and plate deformation was used to define the connection capacity. This definition of connection capacity was necessary for connections in which the plate cross-sectional area was small relative to the RHS wall thickness (ratio of plate cross-sectional area to RHS wall thickness ≤ 3), which led to the entire cross section of the plate yielding before weld failure or the deformation limits were reached. As shown in Figure 6-15, this threshold was defined based on when the deformation of the plate and connection began to appreciably differ. Of the 28 connections that were classified as plate yielding failures, this phenomenon occurred three times in connections with a low B/t (17.2) and low β (β < 0.5).

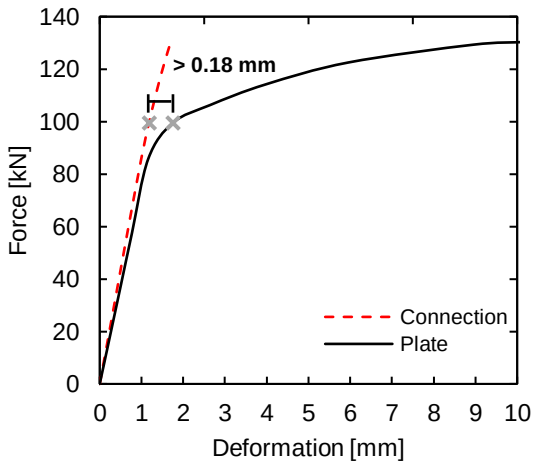

Figure 6-15 Connection capacity definition for local plate yielding

6.5.2 General Behavior

Figure 6-16 presents the normalized connection capacity (R_n/F_yt^2) as a function of β' for chord slenderness ratios (2γ) that fall outside (Figure 6-16a) and within (Figure 6-16b) the AISC Specification (AISC 2010) limits of validity for transverse T- and X- type connections under plate

axial load. It should be noted that the chord yield stress, F_y, used to normalize the connection capacity, is the yield stress obtained from coupon tests and subsequently used to define the material model for the RHS walls. Irrespective of whether the chord slenderness ratio falls within the limits of validity, the connection capacity is shown to increase with an increase in β'. This trend is likely a result of greater engagement of the stiffer RHS corners and sidewall as the plate width increases, ultimately leading to an increase in normalized connection capacity. Figure 6-17 shows the connection capacity, R_n, as a function of β' for all chord slenderness ratios. Filled markers represent connections with chord slenderness ratios outside of the limits of validity, while unfilled markers represent connections with chord slenderness ratios within the limits of validity. Referring to Figure 6-17a, there is no strong trend regarding how the chord slenderness ratio influences connection capacity for a constant β'. However, Figure 6-17b, which delineates the chord wall thickness instead of the chord slenderness ratio, more clearly indicates that connection capacity increases with an increase in chord wall thickness. This result suggests that chord wall thickness is more influential on connection capacity than chord slenderness ratio. Previous experimental studies by Davies et al. (1981), Wardenier et al. (1981), and Lu (1997) would not have shown this trend since different chord slenderness ratios were produced for their tests by changing the chord wall thickness while keeping the chord width constant. It is postulated that connection capacity increases with RHS wall thickness because it results in a larger shear area of the RHS and a greater plate effective width according to the AISC design equations.

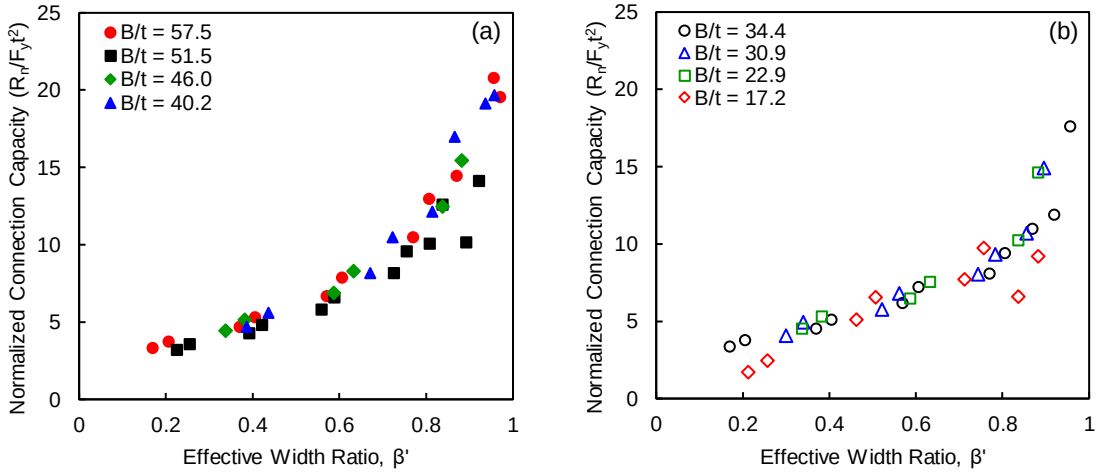

Figure 6-16 Normalized connection capacity as a function of effective width ratio, β', for (a) connections with $B/t > 35$ and (b) connections with $B/t < 35$.

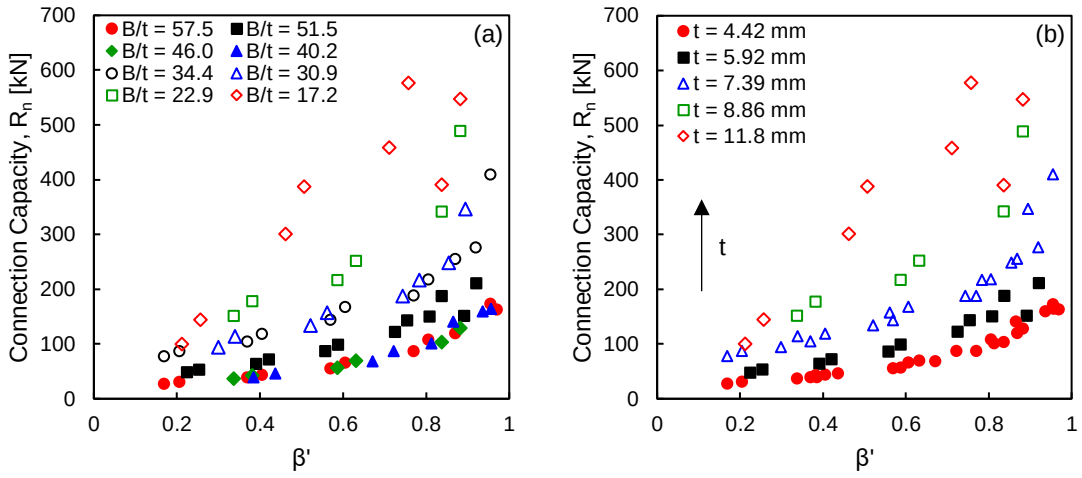

Figure 6-17 Connection capacity as a function of effective width ratio, β', delineated by (a) chord slenderness and (b) chord wall thickness

Of the 70 connection configurations simulated, 40 failed by chord face plastification, 28 failed by local yielding of the branch plate, and two connections failed by shear yielding of the RHS. For the connections that failed by chord face plastification, 30 of them had chord slenderness ratios outside of the limits of validity ($2\gamma > 35$). It was anticipated that connections with large chord slenderness ratios (i.e., those that extend outside of the limits of validity) would fail by chord face plastification, as the inherent flexibility of these connections leads to significant deformation of the RHS face. In the connections that failed by chord face plastification, after achieving the 3%*B* ultimate deformation limit, additional tensile loading of the branch plate led to punching shear failure in connections with large β' (β' > 0.8). Significant deformation of the RHS chord face is shown in Figure 6-18a, which presents the original and deformed configuration at 3%*B* with a von Mises stress contour plotted on the deformed configuration for a connection with a *B*/*t* of 51.5 and β' of 0.84. For this same connection, punching shear failure initiated at a connection deformation of 4%*B* (beyond the 3%*B* deformation limit of 9.14 mm) with a portion of the RHS face being completely removed at approximately 14.7 mm (4.8%*B*) of connection deformation (Figure 6-18b).

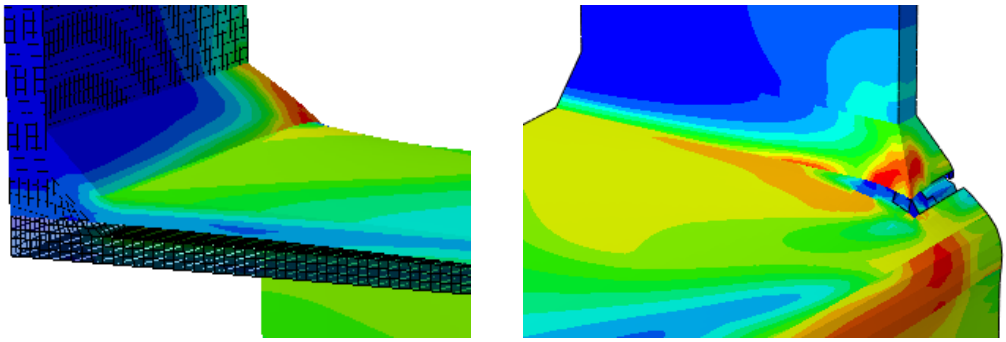

(a) (b)

Figure 6-18 Von Mises stress contours for an HSS 304.8×304.8×6.4 with B_p = 229 mm and t_p = 19.1 mm at (a) the 3%B deformation limit with the undeformed (black lines) and deformed shape and (b) punching shear failure.

Of the connections that failed by local plate yielding, 23 of them had a chord slenderness ratio below 35, suggesting that connections outside of the limits of validity according to chord slenderness ratio are not as susceptible to local plate yielding due to the greater flexibility of these connections relative to connections with a lower chord slenderness ratio. The greater flexibility of the connections with a chord slenderness ratio above 35 arises from the thinness of the RHS wall relative to its width leading to a less stiff RHS wall. The low stiffness of the wall allows for large connection deformations to occur before the plate undergoes substantial deformation, causing the connection to fail by reaching a deformation limit as a result of deformation of the chord face and not plate yielding. Furthermore, it should be noted that failure by local plate yielding occurred in connections with β' values spanning from 0.21 to 0.97 with many of the connections (~70%) having a β' greater than 0.7. Local plate yielding in connections with large β' can likely be attributed to the greater connection stiffness provided by engagement of the corners and sidewalls of the RHS leading to large stresses in the branch plates, particularly at their extremities. The connections that had significant plate deformations had low β' values (β' < 0.5) and low chord slenderness (2γ < 17.2), suggesting that the stiffness of the RHS chord was greater than that of the branch plate due to the large chord wall thickness relative to that of the RHS chord width. These connections also had branch plates with a small cross-sectional area, which lead to the plates yielding earlier than if their cross-section had been larger.

The two connections that experienced punching shear failure had chord slenderness ratios of 40.2 and 57.5 and β' values of 0.87 and 0.96, respectively. In both cases the effective plate width, B'_p,

was less than that of $B - 2t$, ensuring that punching shear failure was physically possible. Behavior of both connections was characterized by deformation of the RHS face along its width that eventually led to the branch plate causing the RHS connecting face to fracture at the toe of the weld near the corner of the connection. For the connection with a β' of 0.87, punching shear failure occurred nearly simultaneously with the connection deformation reaching 3%*B*. Figure 6-19 shows the force-deformation curve associated with this connection (Figure 6-19a) along with evidence of punching shear failure (Figure 6-19b). Davies and Packer (1982) derived an analytical solution for this combined failure mode, noting that a combined mechanism is more realistic because uniform shear yielding around the weld perimeter of the connection is unlikely.

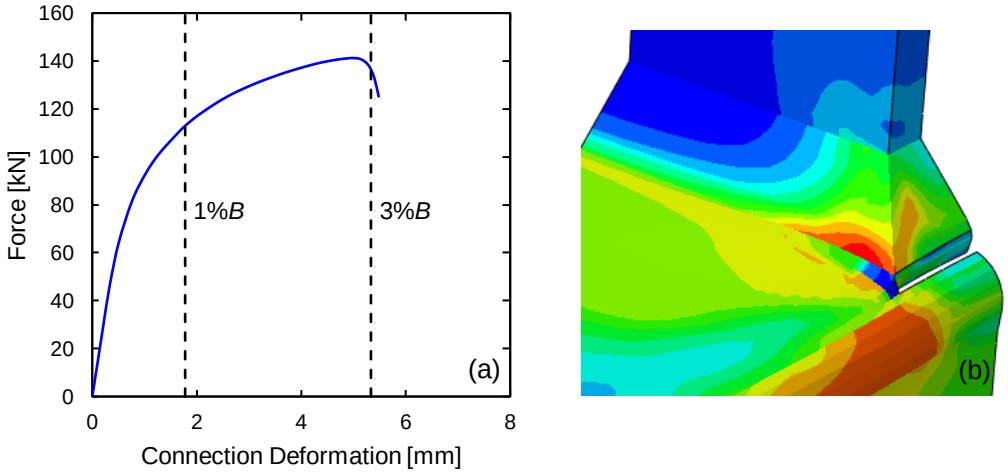

Figure 6-19 HSS 228.6×177.8×4.8 with B_p = 127 mm and t_p = 19.1 mm (a) force-deformation curve and (b) punching shear failure.

6.5.3 Code Comparisons

To determine the suitability of the design recommendations provided by the AISC Specification (AISC 2010), the connection capacity obtained from the FE results, R_n (FE), is compared to the nominal strength predicted by the AISC limit state equations, R_n (AISC 2010). It should be noted that the limit state equation used to define the predicted connection strength is based on the failure mode exhibited in the FE results and is not necessarily the governing connection capacity predicted by the minimum value of all applicable limit state equations. To make an accurate comparison between the FE and code predicted nominal strengths, effective geometric properties and actual material properties were used in calculating the connection capacity based on the limit state

equations. Figure 6-20 presents a graphical comparison of the FE and code predicted connection capacities as a function of effective width ratio, β' (Figure 6-20a), and chord width to thickness ratio, 2γ (Figure 6-20b). In general, the AISC equations do fairly well at predicting the actual connection capacity given by the FE results with most of the connection capacity ratios falling near unity. For connections with β' values greater than 0.45 the AISC design recommendations tend to under predict connection capacity, with greater conservatism displayed in some connections with large β' values (β' > 0.9). For connections with β' values below 0.45 the AISC design recommendations tend to overestimate connection capacity, with this tendency more pronounced in connections that fall outside of the limits of validity (β' < 0.25). Referring to Figure 6-20b, the AISC design equations reasonably predict connection capacity for all chord slenderness ratios with connection capacity being slightly overestimated for connections with chord slenderness ratios outside of the limits of validity (2γ > 35). Overall, for connections with 2γ > 35, the average value of the ratio of FE to code predicted connection capacity is 1.05 with a coefficient of variation of 0.33, which further supports the notion that the AISC limit state equations can predict connection capacity reasonably well for the range of geometric parameters considered herein. Similarly, for connections with 2γ < 35, the average value of the ratio of FE to code predicted connection capacity is 1.10 with a coefficient of variation of 0.24, indicating that the FE results agree reasonably well with the capacities predicted using the AISC equations.

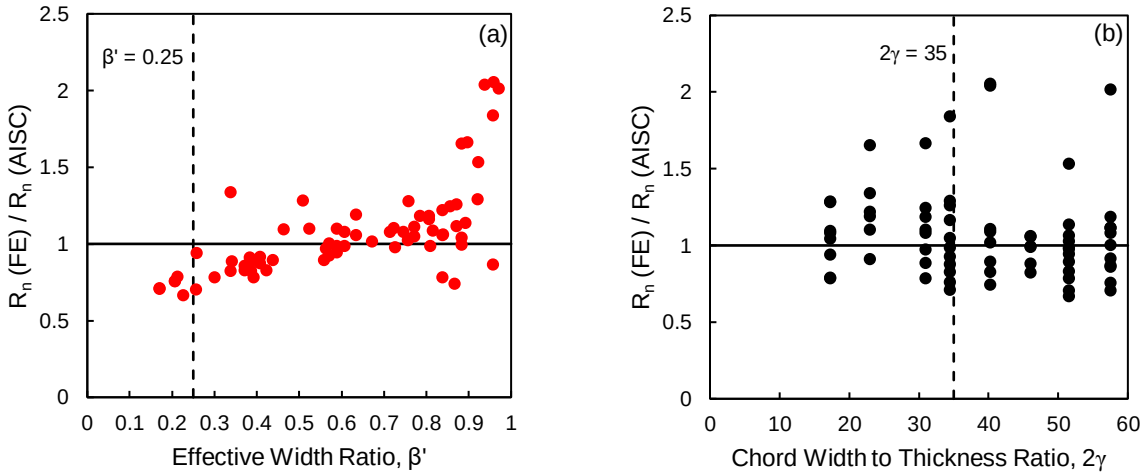

Figure 6-20 Comparison of FE results with AISC design recommendations as a function of (a) effective width ratio, β', and (b) chord slenderness ratio, 2γ.

As previously stated, the plots shown in Figure 6-20 do not necessarily compare the FE connection capacity with the connection capacity predicted by the governing limit state equation. For all 70 connection configurations considered, local plate yielding was the controlling limit state for design based on the AISC Specification equations (AISC 2010). Figure 6-21 shows the ratio of predicted connection capacity for the FE results versus the local plate yielding limit state equation as a function of effective width ratio, β' (Figure 6-21a), and chord width to thickness ratio, 2γ (Figure 6-21b). With the exception of three connections, the local plate yielding equation is noticeably conservative with a mean ratio of connection capacity of 1.36 and a coefficient of variation of 0.23. While experimental results from Wardenier et al. (1981) and the plots shown in Figure 6-21 support the notion that the local plate yielding equation provides a lower bound solution, there are cases in which the FE results are significantly under predicted by the AISC equations, which give a capacity nearly 2.5 times smaller than that of the FE results. This finding suggests that the local plate yielding equation may be too conservative, potentially leading to connection designs that are inefficient. The reason for the conservatism of the local plate yielding equation is likely because it does not explicitly account for β (Wardenier et al. 1981). If the local plate yielding equation was an explicit function of β, the effective width and thus the connection strength could potentially be larger than when β is not considered. One solution to this conservatism could be to incorporate β into the nominal strength equation and then conduct a regression analysis with an extensive FE and experimental database to generate a design equation with a better statistical fit.

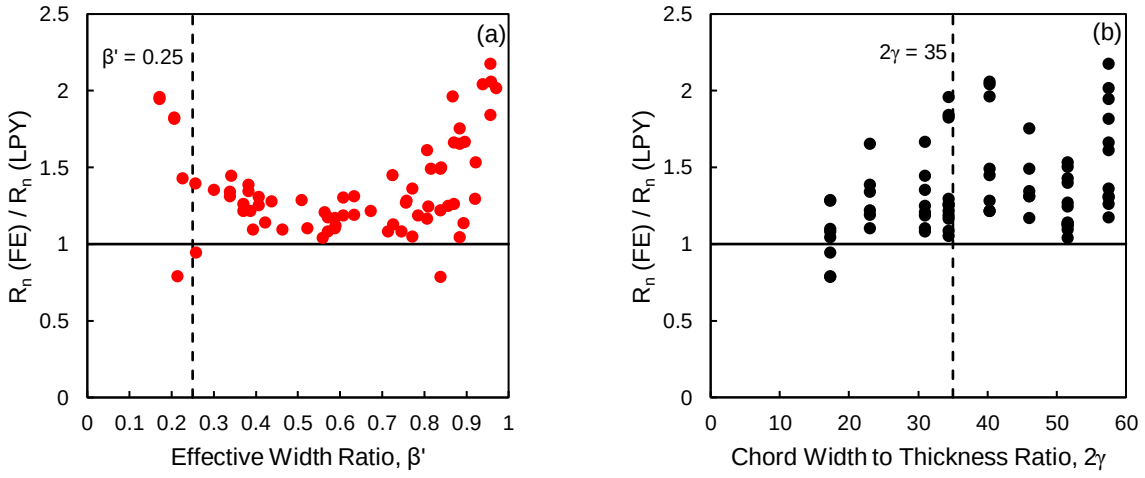

Figure 6-21 Comparison of FE results with governing local plate yielding (LPY) equation as a function of (a) effective width ratio, β', and (b) chord slenderness ratio, 2γ.

6.6 Conclusions

An experimental and FE parametric study were undertaken to widen the scope of current design knowledge on transverse plate to RHS connections under plate tensile load. Seven connection configurations were experimentally tested and the FE parametric study considered 70 connection configurations with effective width ratios and chord slenderness ratios varying from 0.17 to 0.97 and 17.2 to 57.5, respectively. The finite element models were calibrated using data from the experimental testing and included geometric and material nonlinearity in addition to a model that predicted the onset of connection fracture.

The parametric study results indicated that the limit state equations for design are able to reasonably predict connection capacity outside of the ranges of validity defined in the AISC Specification (AISC 2010). In general, the limit state equations for the observed failure mode are slightly conservative in their prediction of connection capacity. When comparing the FE results to the connection capacity predicted by the governing limit state equation of local plate yielding, the limit state equation tended to provide a significant underestimate of connection strength. As only two plate thicknesses were considered in the parametric study, this significant conservatism may not occur for connections with smaller plate thicknesses.

Chapter 7 Summary and Conclusions

7.1 Summary

Supplemental energy dissipation devices provide a means to control the wind and seismic response of built infrastructure. While many devices have been thoroughly investigated and subsequently implemented in large scale civil engineering infrastructure applications, they induce architectural constraints and can complicate construction leading to an increase in associated costs. Furthermore, many supplemental energy dissipation devices require an external power source, which can fail during an extreme loading event such as an earthquake. A more reliable means of providing energy dissipation can be realized by taking advantage of the inherent void in hollow structural section (HSS) members. The development of new materials in conjunction with more efficient manufacturing techniques has increased the variety of potential fill materials that can be used in the void of HSS to enhance performance. Specifically, a fill material can postpone and mitigate the severity of local buckling in steel members leading to improved ductility and energy dissipation as well as a more stable structural response. To this end, the main goal of this research was to improve the seismic performance of steel braced frame systems by incorporating lightweight, high energy dissipating materials in the void of HSS braces and evaluate transverse plate to HSS column connections to increase the resilience of both new and existing braced frame structures.

The mechanical characterization of three commercially produced materials (Chapter 3) is undertaken to gain a thorough understanding of how these materials behave under loadings that are representative of what is expected to be felt by structural members during an earthquake. The materials are a pourable polyester resin compound, polyvinyl chloride (PVC) carbon foam, and a polycarbonate honeycomb. Mechanical properties such as yield strength, Young's modulus, and crush stress (propagation stress) are determined through monotonic and cyclic compression tests of cube specimens cut from each material. Testing is conducted in displacement control considering three different loading rates to gain a better understanding about how to optimize the use of each material for the intended seismic void fill application. Comparison of each material

with a previously investigated polyurethane foam (Wei 2017) led to the selection of the polyurethane foam as the fill material for the brace application discussed in Chapters 4 and 5. The selection of the polyurethane foam as the fill material is based on its lightweight, high strength-to-weight ratio and pourable nature making it amenable for new construction and seismic retrofit applications of steel braced frames. However, the other materials that were investigated have the potential to improve the seismic performance of members as well.

An experimental testing program (Chapter 4) and complementary finite element (FE) study (Chapter 5) is undertaken to develop a quantitative understanding of how polyurethane foam-filled circular hollow section (CHS) braces behave under large cyclic loads that are typically associated with forces induced by an earthquake. Quantities such as compressive and tensile strength, elastic stiffness, dissipated energy, strain, and the initiation of local buckling and fracture are used to evaluate the potential benefits of using foam-filled braces compared to empty braces. An FE model is calibrated and validated against the data generated by the experimental tests. The FE model can accurately simulate the interaction of the foam and steel brace in addition to capturing the degradation of compressive strength and evolution of tensile strength with increasing brace axial deformation. A robust parametric study that considers 29 different section sizes (29 empty and 29 foam filled braces) is performed using the validated FE model. The results from the parametric study are used to determine which section sizes benefit most from the use of the foam fill and to establish a threshold D/t and λ (global slenderness) where the foam fill no longer improves brace performance.

The final phase of this research consists of an experimental and companion numerical investigation of transverse plate to HSS connections (Chapter 6). Seven connections with different geometric parameters are tested under monotonic branch plate tension. The connection parameters of some of the experimentally tested connections are intentionally chosen to fall outside of the limits of validity specified in the AISC Specification (AISC 2010) to assess whether the limits of validity are potentially too restrictive with respect to design flexibility. The companion numerical study makes use of the experimental results to calibrate and validate high-fidelity FE models. The parametric study considers a total of 70 connections with a wide range of geometric parameters above and below the limits of validity in order to broaden the scope of the experimental program and gain a better understanding of connection behavior outside of these limits.

7.2 Conclusions

- The mechanical characterization results show that all three of the considered materials are viable options for use in seismic void fill applications. The most promising material is the pourable polyester resin compound. It has a density that is nearly 2.5 times less dense than that of normal strength concrete and shows the ability to dissipate over 600 kN-mm of energy during a single cycle of compressive loading. Furthermore, its ability to recover more than 50% of the deformation it undergoes during cyclic loading suggests that it will not need to be replaced after minor to moderate earthquakes because it can recover the deformation, allowing it to maintain contact with the surrounding steel and restrain further localized deformation of the cross-section. The polyester resin compound also can reach stresses of up to 45 MPa, which bodes well for energy dissipation applications because strength and energy dissipation capacity are related.

- The properties that are most indicative of the potential of a material to improve performance under cyclic loads in void fill applications are energy dissipation capacity, elastic stiffness, cyclic compressive strength, and the ability to maintain contact with the surrounding material (i.e., through low friability or the ability to recover deformations). For retrofit applications and new construction, it is important that the fill material can be easily placed in the void with minimal potential for voids (e.g., by being pourable and/or expandable).

- Experimental testing of empty and equal size foam-filled braces under large fully reversed cyclic loads shows that the foam fill is more effective in improving ductility in braces that have a *D/t* above the moderately ductile limit specified in the AISC Seismic Provisions (AISC 2016a) compared to braces that have a *D/t* below this limit.

- In general, the experimental hysteretic response of empty and foam-filled braces is similar. The maximum difference in the elastic stiffness, maximum tension, and maximum compression values for corresponding empty and foam-filled braces is 14.6%, 6.4%, and 11.1%, respectively. The FE parametric study considering 29 different section sizes of empty and foam-filled round HSS braces confirms that the foam fill has a negligible influence on the elastic stiffness and tensile strength of the brace over a wide range of

parameters. The difference in elastic strength between empty and foam-filled braces is less than 1% for all of the considered sections, while the average difference in tensile strength between the empty and foam-filled braces is 1.7%. The negligible difference in these quantities for empty and foam-filled braces allows for easy incorporation into current capacity-based seismic design approaches.

- Experimental testing of empty and equal size foam-filled braces under large fully reversed cyclic loads shows that the foam fill can delay the initiation of local buckling leading to improved ductility. Local buckling and fracture occur at least one cycle later for the foam-filled braces compared to their empty counterparts except for the foam-filled brace with a D/t greater than 44.0 (F1273), which experiences local buckling during the same cycle as its empty counterpart (E1273) and fracture one cycle earlier than its empty counterpart. The foam-filled brace with a D/t of 35.0 (F1013) has local buckling and fracture occur five and four cycles later, respectively, than that of its empty counterpart (E1013), showing that the foam fill can lead to substantial improvement in brace ductility and energy dissipation capacity. The FE parametric study of empty and foam-filled braces shows that the foam is effective at delaying local buckling for braces with a D/t of less than 43.0. Additionally, greater improvement considering local buckling behavior is shown in braces with larger $D/$t and larger λ.

- The percentage increase in cumulative dissipated energy between tested empty and equal size foam-filled braces ranges from 22.5% to 191%, indicating that a substantial increase in energy dissipation can be achieved by filling braces with the foam.

- The use of the two part polyurethane foam-fill as a retrofit option for steel braces in braced frames expected to undergo large cyclic loads is viable provided that the hole size and location for foam insertion are adequately chosen to limit their influence on brace behavior.

- HSS to transverse plate connections that are tested under axial branch plate tension show that the strain distribution on the surface of the branch plate is highly non-uniform, confirming the need for the use of an effective width factor in calculating limit state capacities.

- An FE parametric study of HSS to transverse plate connections shows that the limit state equations for the observed failure mode are slightly conservative in their prediction of connection capacity, but overall are able to reasonably predict connection capacity outside of the ranges of validity defined in the AISC Specification (AISC 2010). However, the local plate yielding limit state equation (AISC 2010) can be highly conservative with the nominal connection capacity nearly 2.5 times smaller than that of the simulated capacity in some cases.

7.3 Recommendations for Future Research

Although the work presented in this dissertation is extensive, additional research is suggested to augment the conclusions that are developed. The recommendations for future research are as follows:

- Research on other potential void fill materials is necessary to establish a wider range of suitable materials for seismic void fill applications as well as applications in other extreme dynamic loading scenarios, such as those caused by severe wind events. In addition to comprehensive material characterization tests, life cycle cost analyses should be undertaken to holistically assess the performance of the considered materials, including how they will impact the environment and withstand corrosive environments.

- Given that this study only investigates the improvement in member performance considering a polyurethane foam as the void fill material, research that examines the use of different fill materials should be undertaken to help establish which are the most effective. Since different materials are likely to affect member performance for different loading scenarios, this research could help establish an optimal fill material for a given loading condition.

- The polyurethane foam fill considered in this dissertation is shown to be effective at providing added energy dissipation and improving ductility through mitigation of local buckling in CHS braces subject to reverse cyclic loading. While CHS are generally recommended for use as energy-dissipating steel braces (Packer et al. 2010), different section types (e.g., square or rectangular HSS) and connection configurations (gusset plates

or proprietary connections) can be considered to more accurately assess the influence of the foam fill on braced frame performance.

- The symmetric loading protocol used to evaluate the performance of the empty and foam-filled braces in this study is representative of the demands induced on steel braces in braced frames by a far-field type ground motion. Protocols that are representative of the brace demands induced by near-fault and long duration ground motions can be considered to further assess the influence of the foam fill on braced frame performance.

- Since this research involves improvement to braced frame performance through component level investigations, it is suggested that future studies take a system-level approach in order to develop more robust design recommendations.

Appendix A

This appendix contains a summary of the material characterization data presented in Chapter 3.

Table A-1 Monotonic characteristic properties of the polyester resin compound

Loading Rate (mm/s)	Elastic Modulus (MPa)	Yield Stress (kPa)
0.25	726	17900
2.5	837	26560
25	1290	38200

Table A-2 Monotonic characteristic properties of the carbon foam

Loading Rate (mm/s)	Elastic Modulus (MPa)	Yield Stress (kPa)
0.25	29	680
2.5	32	720
25	27	636

Table A-3 Monotonic characteristic properties of the polycarbonate honeycomb (50.8 × 31.8 mm)

	In-Plane		Out-of-Plane	
Loading Rate (mm/s)	Elastic Modulus (MPa)	Plateau Stress (kPa)	Elastic Modulus (MPa)	Plateau Stress (kPa)
0.25	0.64	48.4	119	979
2.5	0.59	48.9	123	898
25	0.50	53.4	114	1052

Table A-4 Monotonic characteristic properties of the polyurethane foam (Wei 2017)

Loading Rate (mm/s)	Elastic Modulus (MPa)	Yield Stress (kPa)
0.25	54.6	2620
2.5	47.7	2690
25	53.7	2760

Table A-5 Cyclic characteristic properties of the polyester resin compound

Loading Rate (mm/s)	Ultimate Stress (kPa)	Cumulative Dissipated Energy (kN-mm)	Initial Secant Stiffness (N/mm)
0.25	29940	2599	10591
2.5	31600	2804	13611
25	43290	3497	21493

Table A-6 Cyclic characteristic properties of the carbon foam

Loading Rate (mm/s)	Ultimate Stress (kPa)	Cumulative Dissipated Energy (kN-mm)	Initial Secant Stiffness (N/mm)
0.25	639	53	299
2.5	663	56	349
25	709	63	277

Table A-7 Cyclic characteristic properties of the polycarbonate honeycomb (50.8 × 63.5 mm)

	In-Plane			Out-of-Plane		
Loading Rate (mm/s)	Ultimate Stress (kPa)	Cumulative Dissipated Energy (kN-mm)	Initial Secant Stiffness (N/mm)	Ultimate Stress (kPa)	Cumulative Dissipated Energy (kN-mm)	Initial Secant Stiffness (N/mm)
0.25	54.4	5.63	31.6	1390	99	608
2.5	55.1	5.80	30.9	1504	98	659
25	56.7	6.38	31.8	1352	102	523

Appendix B

This appendix contains the measured hysteretic responses and other important data from the brace tests presented in Chapter 4. All of the reported quantities are based on axial measurements. Note that the tabular values are only for complete cycles of loading (i.e., the cycle in which fracture occurred is not included).

Table B-1 Experimental results for brace E8932 (D/t = 27.8; λ = 70.1)

Drift (%)	Cycle	Cumulative dissipated energy (kN-mm)	Max. tensile force (kN)	Max. compressive force (kN)	Max. deformation (mm)	Min. deformation (mm)
0.1	1	34.5	78.4	103.3	1.2	1.2
0.1	2	67.7	81.6	103.2	1.2	1.2
0.25	3	272	205.9	236.2	3.1	3.1
0.25	4	412	220.8	231.2	3.0	3.1
0.5	5	4297	319.0	281.3	6.2	15.3
0.5	6	6094	302.0	124.7	7.8	6.2
0.75	7	9147	329.8	147.5	8.9	9.7
0.75	8	11699	311.0	123.2	9.0	9.4
1	9	15671	330.4	148.0	12.2	12.5
1	10	18971	295.5	103.1	12.1	12.8
1.5	11	24668	333.2	134.6	18.2	18.9
1.5	12	29107	284.4	87.9	18.2	18.6
2	13	35228	332.9	124.6	24.8	25.0
2	14	39250	290.3	88.1	24.3	24.9
3	15	47191	338.2	125.7	36.8	37.1
3	16			Fracture		

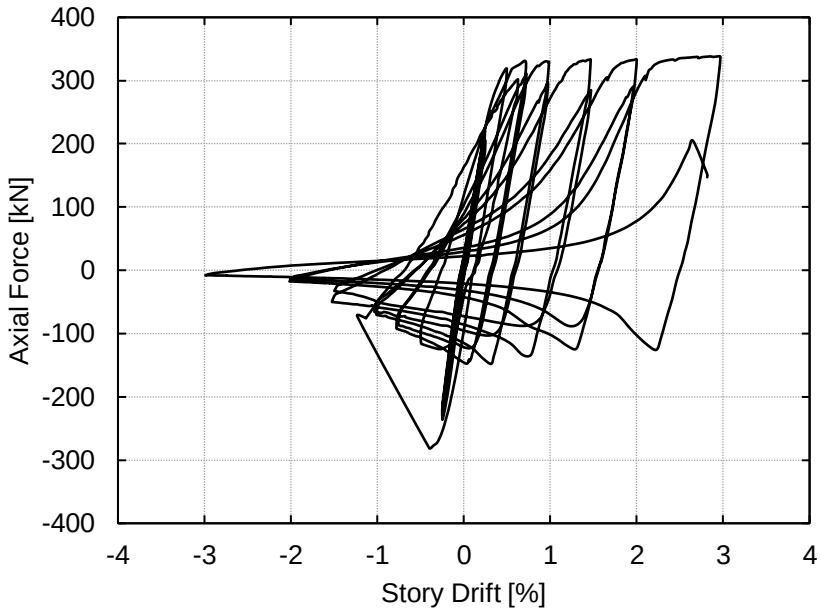

Figure B-1 Brace E8932 hysteretic response (D/t = 27.8; λ = 70.1)

Table B-2 Experimental results for brace F8932 (D/t = 27.8; λ = 70.1)

Drift (%)	Cycle	Cumulative dissipated energy (kN-mm)	Max. tensile force (kN)	Max. compressive force (kN)	Max. deformation (mm)	Min. deformation (mm)
0.1	1	30.9	84.6	101.8	1.2	1.3
0.1	2	49.9	86.9	94.3	1.2	1.2
0.25	3	219	207.3	237.6	3.1	3.1
0.25	4	333	217.3	236.3	3.1	3.1
0.5	5	4678	318.8	290.0	6.1	13.9
0.5	6	6504	302.2	147.6	6.1	6.2
0.75	7	9688	324.2	183.9	9.3	9.3
0.75	8	12581	312.5	155.0	9.6	9.2
1	9	16833	327.0	182.2	12.5	12.5
1	10	20304	295.9	119.2	12.4	12.5
1.5	11	26530	330.8	159.1	19.0	18.6
1.5	12	31150	276.0	94.0	18.5	18.7
2	13	38039	328.5	127.3	24.8	24.8
2	14	43430	274.7	85.5	24.8	24.8
3	15	52860	339.9	129.4	37.2	37.5
3	16	58649	299.6	98.0	37.1	37.2
4	17			Fracture		

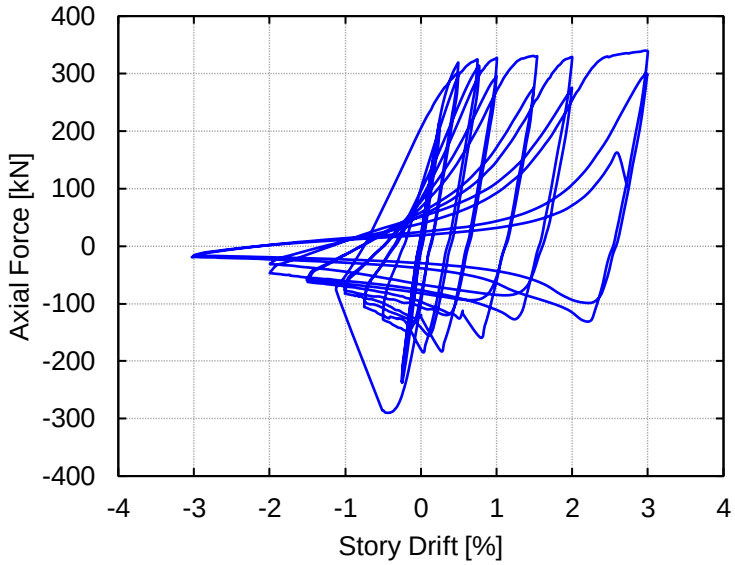

Figure B-2 Brace F8932 hysteretic response (D/t = 27.8; λ = 70.1)

Table B-3 Experimental results for brace E11445 (D/t = 25.4; λ = 54.8)

Drift (%)	Cycle	Cumulative dissipated energy (kN-mm)	Max. tensile force (kN)	Max. compressive force (kN)	Max. deformation (mm)	Min. deformation (mm)
0.1	1	41.8	120.8	142.4	1.2	1.2
0.1	2	81.7	124.5	142.1	1.2	1.2
0.25	3	325	289.5	346.2	3.1	3.1
0.25	4	506	300.9	344.1	2.9	3.1
0.5	5	7317	465.6	439.2	6.2	14.4
0.5	6	11004	466.1	257.6	6.3	8.8
0.75	7	16428	493.4	293.4	9.3	9.3
0.75	8	21824	478.6	279.5	9.7	9.4
1	9	29596	493.3	304.8	12.4	12.4
1	10	36709	466.1	246.7	12.7	12.5
1.5	11	47697	495.5	294.1	18.2	18.1
1.5	12	56186	446.9	201.4	18.1	18.2
2	13	66903	491.5	240.3	24.6	24.7
2	14	74970	446.9	193.3	24.7	24.8
3	15	89185	505.5	248.1	37.1	37.5
3	16			Fracture		

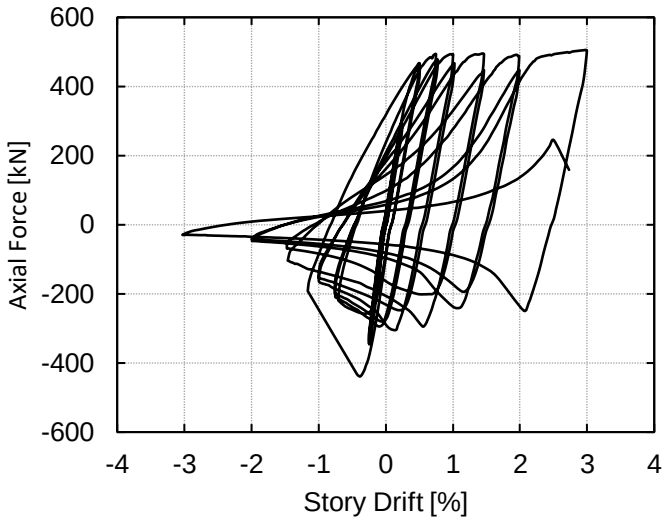

Figure B-3 Brace E11445 hysteretic response (D/t = 25.4; λ = 54.8)

Table B-4 Experimental results for brace F11445 (D/t = 25.4; λ = 54.8)

Drift (%)	Cycle	Cumulative dissipated energy (kN-mm)	Max. tensile force (kN)	Max. compressive force (kN)	Max. deformation (mm)	Min. deformation (mm)
0.1	1	39.3	110.1	148.6	1.2	1.3
0.1	2	71.9	114.7	148.3	1.2	1.3
0.25	3	312	282.1	351.0	3.0	3.1
0.25	4	471	291.7	341.8	2.9	3.1
0.5	5	2863	463.7	459.1	6.2	6.3
0.5	6	5389	471.3	438.2	6.2	6.2
0.75	7	14556	504.1	421.8	9.4	14.7
0.75	8	20706	487.6	292.8	9.6	10.2
1	9	28844	492.6	313.3	12.4	13.4
1	10	35903	460.6	244.6	12.4	12.5
1.5	11	47840	496.8	299.8	19.0	19.0
1.5	12	57741	457.6	209.6	19.3	18.6
2	13	71043	478.3	248.9	24.8	24.8
2	14	81824	418.1	182.5	25.1	24.7
3	15	97929	495.1	262.4	37.1	37.2
3	16	109266	463.3	202.7	37.8	37.2
4	17	Fracture				

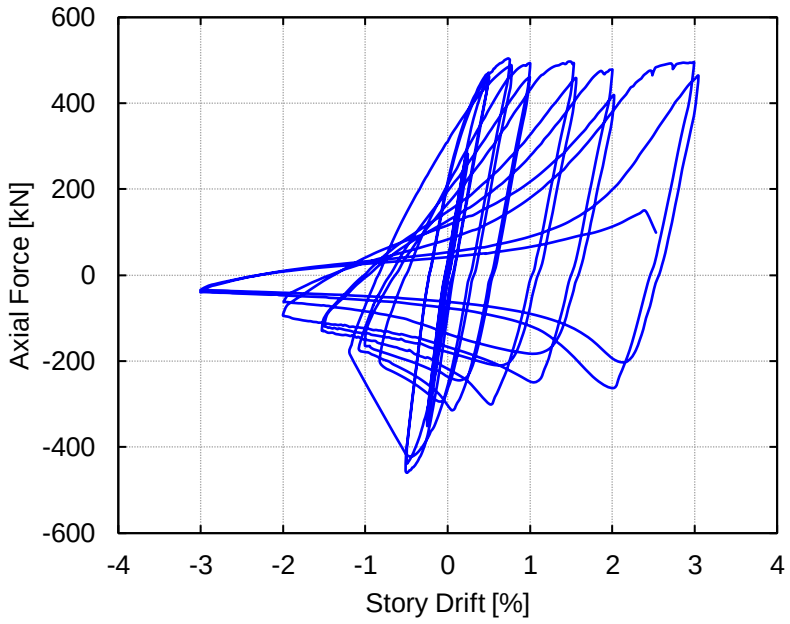

Figure B-4 Brace F11445 hysteretic response (D/t = 25.4; λ = 54.8)

Table B-5 Experimental results for brace F11435H1 (D/t = 32.7; λ = 54.4)

Drift (%)	Cycle	Cumulative dissipated energy (kN-mm)	Max. tensile force (kN)	Max. compressive force (kN)	Max. deformation (mm)	Min. deformation (mm)
0.1	1	36.7	111.9	116.8	1.2	1.2
0.1	2	68.5	121.8	113.9	1.3	1.2
0.25	3	310	262.3	287.0	3.0	3.0
0.25	4	495	281.7	284.4	3.1	3.1
0.5	5	2957	396.5	375.7	6.2	6.5
0.5	6	8440	396.3	355.1	6.2	12.4
0.75	7	14942	433.3	268.3	11.4	9.5
0.75	8	18701	366.6	193.0	9.2	9.3
1	9	23947	409.4	218.5	12.4	12.4
1	10	28564	370.5	197.0	12.5	12.4
1.5	11			Fracture		

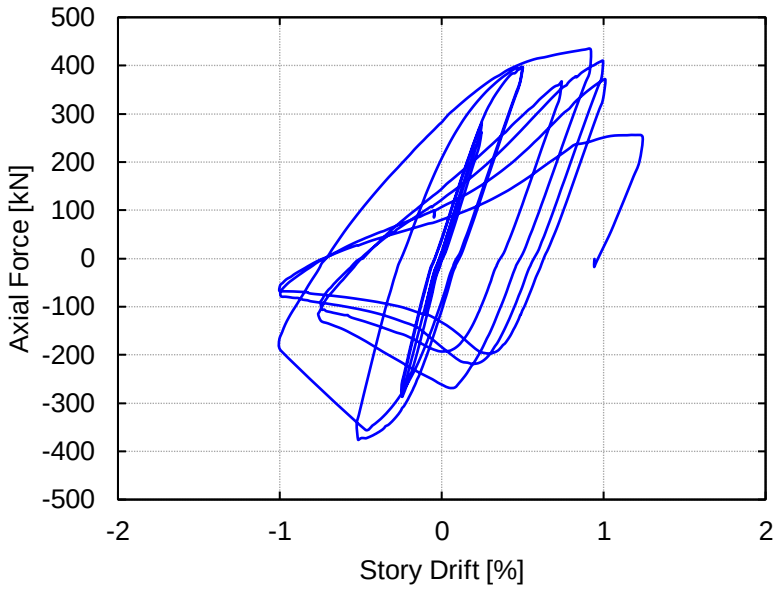

Figure B-5 Brace F11435H1 hysteretic response (D/t = 32.7; λ = 54.4)

Table B-6 Experimental results for brace F11435H2 (D/t = 32.7; λ = 54.4)

Drift (%)	Cycle	Cumulative dissipated energy (kN-mm)	Max. tensile force (kN)	Max. compressive force (kN)	Max. deformation (mm)	Min. deformation (mm)
0.1	1	37.3	98.5	120.9	1.2	1.2
0.1	2	70.3	101.2	123.6	1.2	1.2
0.25	3	302	256.6	301.5	3.1	3.1
0.25	4	481	269.9	299.9	3.0	3.2
0.5	5	2750	402.5	385.5	6.2	6.2
0.5	6	5238	404.0	374.4	6.2	6.2
0.75	7	11481	426.8	381.5	9.2	9.5
0.75	8	18099	419.5	358.0	9.4	9.5
1	9	27763	423.2	344.9	12.4	12.4
1	10	35251	412.2	278.8	12.4	12.3
1.5	11	45889	421.7	273.4	18.5	18.7
1.5	12	54429	377.9	181.7	18.5	18.8
2	13	66116	411.5	206.0	24.9	24.8
2	14	74961	355.0	154.4	24.7	24.8
3	15	88439	426.7	206.6	37.5	37.2
3	16	96688	382.5	159.7	37.1	37.2
4	17			Fracture		

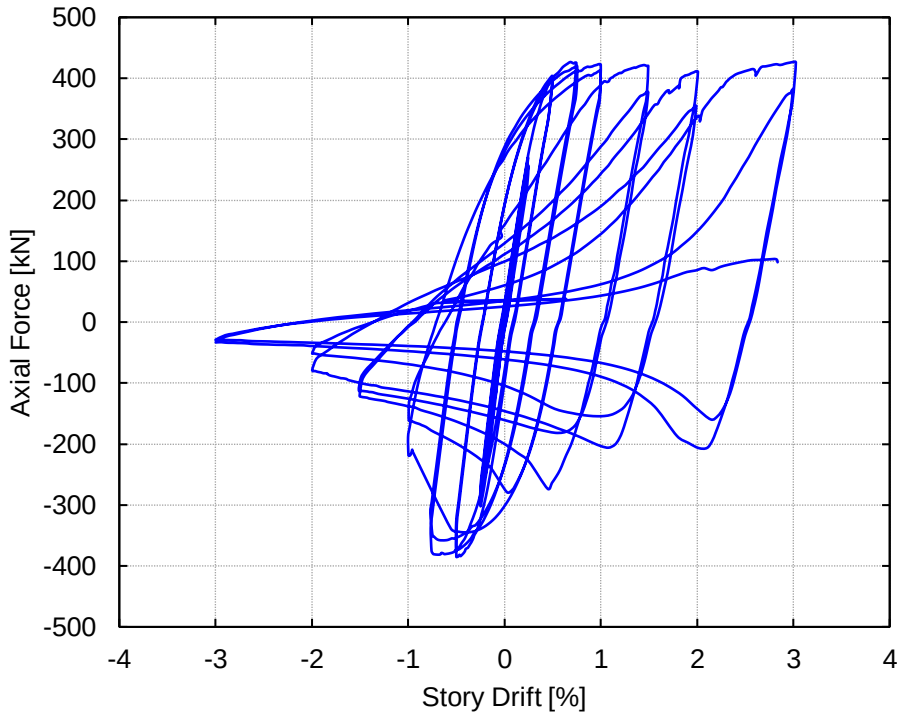

Figure B-6 Brace F11435H2 hysteretic response (D/t = 32.7; λ = 54.4)

Table B-7 Experimental results for brace E1013 (D/t = 34.7; λ = 97.4)

Drift (%)	Cycle	Cumulative dissipated energy (kN-mm)	Max. tensile force (kN)	Max. compressive force (kN)	Max. deformation (mm)	Min. deformation (mm)
0.1	1	0	47.8	17.6	0.7	0.3
0.1	2	0	46.6	17.6	0.6	0.3
0.25	3	0	90.3	72.4	0.8	1.2
0.25	4	0	88.7	73.4	0.9	1.2
0.5	5	27.7	184.4	167.6	2.6	3.2
0.5	6	75.9	178.4	167.0	2.4	3.4
0.75	7	1525	267.6	189.8	5.6	9.2
0.75	8	2860	267.5	161.9	5.5	9.8
1	9	6922	307.9	154.6	9.9	16.9
1	10	10564	292.9	141.5	10.0	17.4
1.5	11	18826	313.5	139.1	19.9	29.4
1.5	12	24493	299.6	114.2	20.2	30.8
2	13	33634	317.3	120.8	30.3	41.0
2	14			Fracture		

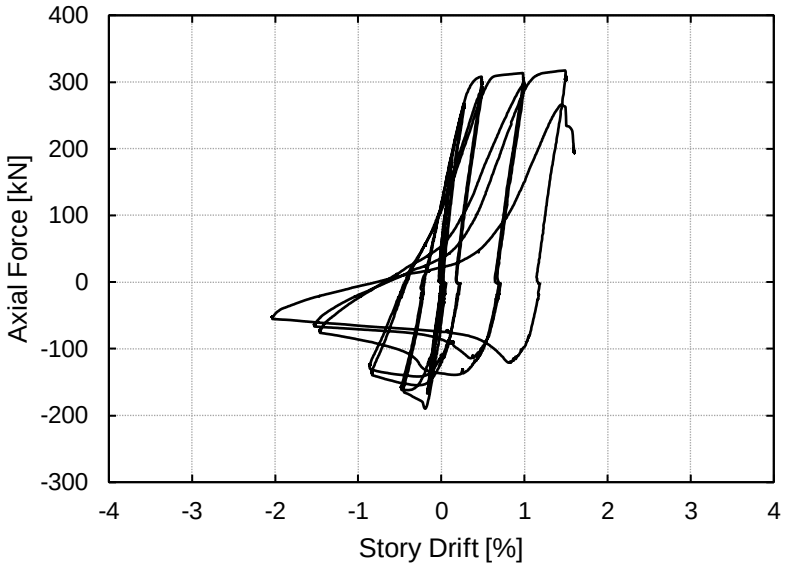

Figure B-7 Brace E1013 hysteretic response (D/t = 34.7; λ = 97.4)

Table B-8 Experimental results for brace F1013 (D/t = 35.0; λ = 97.0)

Drift (%)	Cycle	Cumulative dissipated energy (kN-mm)	Max. tensile force (kN)	Max. compressive force (kN)	Max. deformation (mm)	Min. deformation (mm)
0.1	1	1.66	40.6	17.7	0.5	0.4
0.1	2	1.35	37.9	17.8	0.5	0.5
0.25	3	7.75	107.3	48.1	1.4	0.9
0.25	4	12.6	105.4	49.0	1.3	1.0
0.5	5	164	222.5	118.5	3.8	2.5
0.5	6	251	219.3	116.6	3.8	2.5
0.75	7	1784	305.9	173.9	7.7	6.3
0.75	8	3100	297.1	163.4	7.7	6.5
1	9	7419	313.6	153.8	12.6	13.8
1	10	11156	303.4	144.3	12.8	13.9
1.5	11	20271	321.1	141.2	22.8	25.0
1.5	12	27454	298.3	121.6	23.0	25.6
2	13	39425	327.0	127.2	33.0	36.2
2	14	48934	290.4	101.9	33.7	36.7
3	15	67652	335.6	109.7	53.4	57.5
3	16	79942	285.3	79.9	54.3	58.3
4	17	97977	338.3	91.7	73.2	78.2
4	18			Fracture		

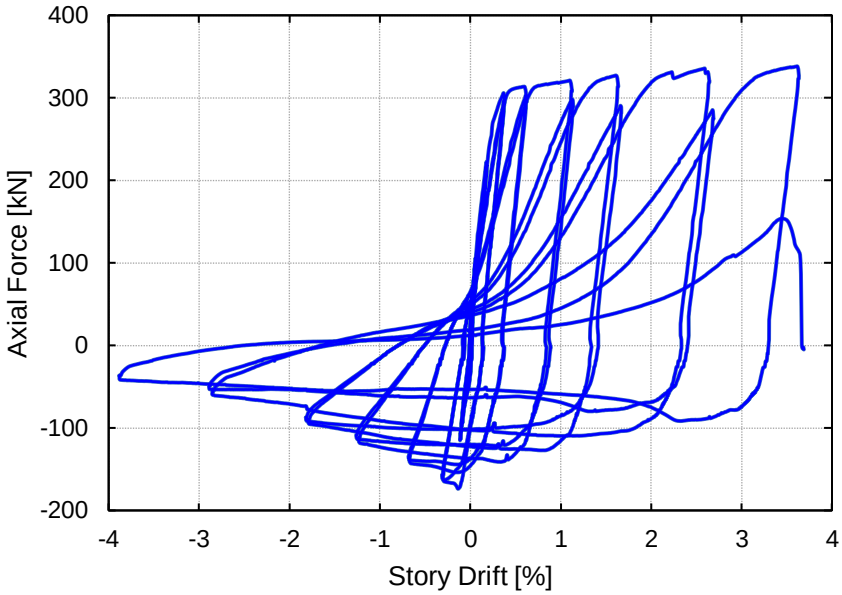

Figure B-8 Brace F1013 hysteretic response (D/t = 35.0; λ = 97.0)

Table B-9 Experimental results for brace E1143 (D/t = 41.7; λ = 86.0)

Drift (%)	Cycle	Cumulative dissipated energy (kN-mm)	Max. tensile force (kN)	Max. compressive force (kN)	Max. deformation (mm)	Min. deformation (mm)
0.1	1	0	46.7	18.0	0.5	0.7
0.1	2	0	45.6	17.9	0.4	0.7
0.25	3	0	119.4	52.2	1.6	1.6
0.25	4	0	117.2	50.9	1.4	1.6
0.5	5	107	211.2	160.0	3.0	3.9
0.5	6	183	205.7	162.6	2.9	3.9
0.75	7	1468	287.8	288.5	5.2	8.0
0.75	8	2947	288.1	265.9	4.9	9.0
1	9	10007	322.6	248.3	9.1	21.1
1	10	16904	319.9	224.3	9.2	23.5
1.5	11	25114	329.9	206.8	18.9	33.8
1.5	12	29764	315.0	131.0	19.1	33.3
2	13	37169	335.3	178.2	29.1	44.4
2	Fracture					

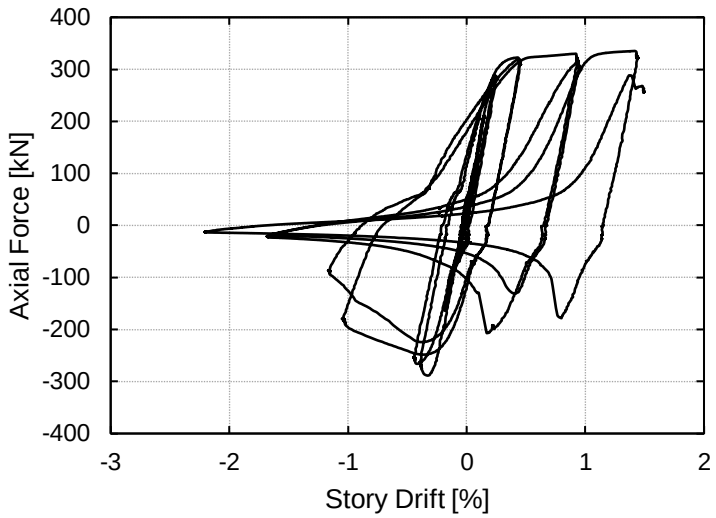

Figure B-9 Brace E11443 hysteretic response (D/t = 41.7; λ = 86.0)

Table B-10 Experimental results for brace F1143 (D/t = 40.5; λ = 86.1)

Drift (%)	Cycle	Cumulative dissipated energy (kN-mm)	Max. tensile force (kN)	Max. compressive force (kN)	Max. deformation (mm)	Min. deformation (mm)
0.1	1	12.0	30.3	20.7	1.0	1.4
0.1	2	20.8	29.8	21.2	0.9	0.7
0.25	3	99.4	59.4	61.2	1.5	2.6
0.25	4	173	57.6	60.7	1.6	2.6
0.5	5	289	172.6	182.4	2.3	5.8
0.5	6	396	175.0	180.3	2.2	5.8
0.75	7	2861	295.8	258.1	4.5	12.8
0.75	8	5316	297.5	240.8	4.2	13.6
1	9	11588	328.3	232.4	8.6	21.5
1	10	15462	318.1	132.2	8.8	19.3
1.5	11	23146	331.3	124.8	18.9	29.7
1.5	12	28533	273.5	83.1	19.6	30.3
2	13	37446	336.2	113.2	29.2	40.5
2	14	44337	275.8	76.5	29.9	42.8
3	15	57069	348.8	110.5	49.1	62.7
3	16	63856	316.6	92.4	49.2	63.2
4	17			Fracture		

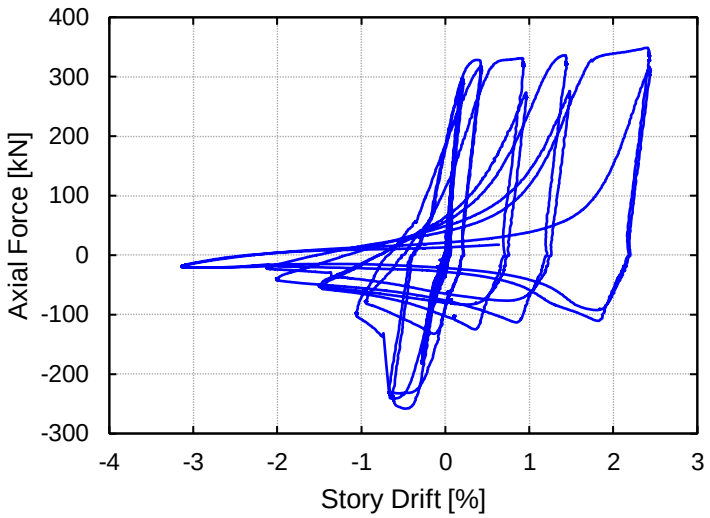

Figure B-10 Brace F11443 hysteretic response (D/t = 40.5; λ = 86.1)

Table B-11 Experimental results for brace E1273 (D/t = 44.0; λ = 77.3)

Drift (%)	Cycle	Cumulative dissipated energy (kN-mm)	Max. tensile force (kN)	Max. compressive force (kN)	Max. deformation (mm)	Min. deformation (mm)
0.1	1	9	33.8	23.4	1.0	0.8
0.1	2	17	32.8	23.7	0.9	0.9
0.25	3	77	75.8	72.5	1.8	2.3
0.25	4	130	74.5	72.9	1.7	2.2
0.5	5	242	213.2	178.0	3.3	4.5
0.5	6	370	214.4	174.1	3.3	4.2
0.75	7	932	341.4	325.0	5.3	7.1
0.75	8	1413	342.3	323.3	4.7	7.3
1	9	9332	410.1	350.6	8.6	21.3
1	10	14437	399.1	230.2	8.8	21.6
1.5	11	23017	413.7	206.7	18.8	32.2
1.5	12	28164	385.2	166.4	19.2	32.7
2	13	Fracture				

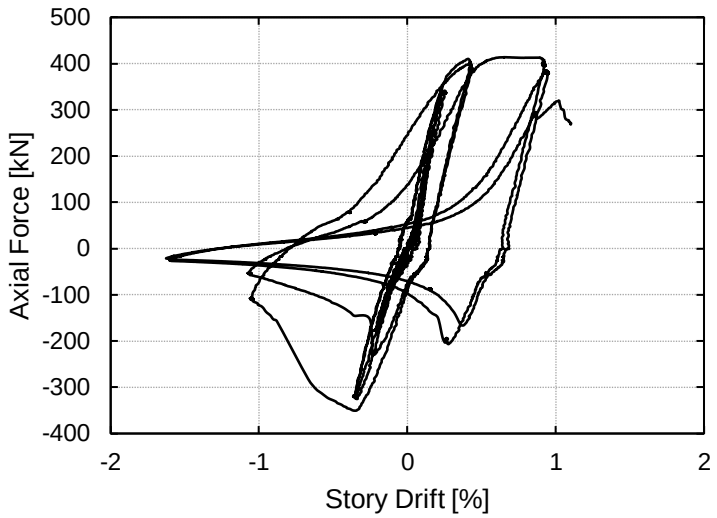

Figure B-11 Brace E1273 hysteretic response (D/t = 44.0; λ = 77.3)

Table B-12 Experimental results for brace F1273 (D/t = 44.4; λ = 77.4)

Drift (%)	Cycle	Cumulative dissipated energy (kN-mm)	Max. tensile force (kN)	Max. compressive force (kN)	Max. deformation (mm)	Min. deformation (mm)
0.1	1	7	25.8	24.9	0.8	0.5
0.1	2	16	25.1	25.0	1.0	0.6
0.25	3	89	59.2	73.9	1.6	2.4
0.25	4	154	55.3	77.0	1.2	2.7
0.5	5	269	171.5	204.5	2.3	5.3
0.5	6	369	172.8	204.0	2.3	5.2
0.75	7	1354	316.2	335.4	4.0	8.9
0.75	8	2117	328.3	328.5	3.5	9.1
1	9	10298	404.2	335.3	7.4	21.9
1	10	17542	401.1	264.3	7.4	24.1
1.5	11	27815	411.3	255.3	17.3	34.1
1.5	12	Fracture				

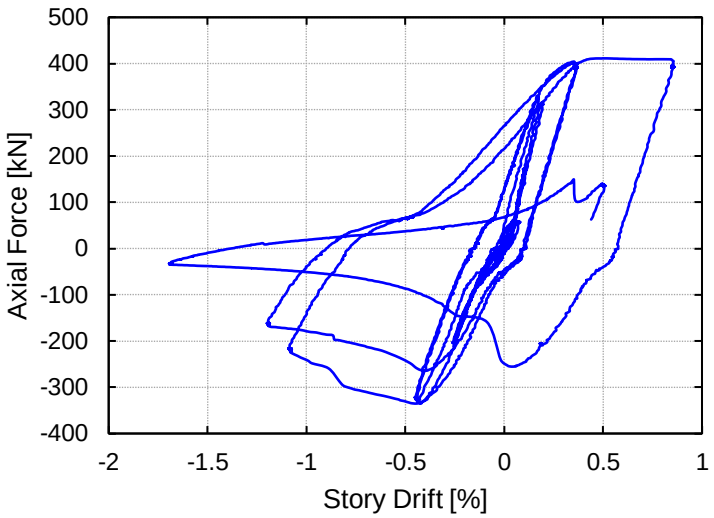

Figure B-12 Brace F1273 hysteretic response (D/t = 44.4; λ = 77.4)

Appendix C

Table C-1 Abaqus crushable foam volumetric hardening material model input (unconfined foam model)

Yield Stress (MPa)	Uniaxial Plastic Strain (mm/mm)	Yield Stress (MPa)	Uniaxial Plastic Strain (mm/mm)
2.519	0.000	5.043	1.065
3.040	0.800	5.107	1.068
3.103	0.815	5.185	1.073
3.174	0.834	5.255	1.078
3.177	0.834	5.315	1.080
3.312	0.865	5.394	1.084
3.380	0.879	5.449	1.088
3.448	0.890	5.522	1.091
3.525	0.902	5.585	1.096
3.587	0.913	5.661	1.099
3.658	0.924	5.724	1.101
3.740	0.934	5.793	1.104
3.795	0.942	5.862	1.107
3.862	0.950	5.934	1.110
3.935	0.960	6.001	1.112
4.000	0.969	6.079	1.116
4.081	0.979	6.140	1.119
4.140	0.987	6.220	1.120
4.208	0.993	6.276	1.123
4.279	1.001	6.351	1.125
4.350	1.007	6.421	1.125
4.425	1.015	6.485	1.127
4.482	1.021	6.570	1.129
4.554	1.025	6.624	1.131
4.632	1.032	6.690	1.134
4.697	1.039	6.764	1.134
4.765	1.043	6.832	1.136
4.838	1.050	6.910	1.137
4.903	1.054	6.971	1.138
4.970	1.058		

A summary of the confined and unconfined foam test results is provided in Table C-2. The crush stress is taken as the stress corresponding to 15% strain, as the plateau region of the compressive response is well defined by this point in the response. The densification modulus is defined as the slope of the stress-strain response following the plateau region. For specimens fabricated from nominal tube diameters of 101, 114, and 127 mm, the average increase in Young's modulus between the unconfined and confined specimens is 4.3, 15.3, and 25.7%, respectively. Similarly, it is shown that the densification modulus for specimens fabricated from nominal tube diameters of 101, 114 and 127 mm increased by 65.9, 77.6, and 58.0%, respectively, when comparing the unconfined and confined specimens. The large difference in densification modulus is likely attributed to the restraint provided by the steel tube for the confined specimens as the foam begins to undergo large transverse deformation. Ultimately, the restraint provided by the steel tube allows the confined specimens to achieve maximum forces much higher than that of the unconfined specimens with ratios of maximum force reaching 2.1, 2.5 and 1.9 for the specimens extracted from tube diameters of 101, 114, and 127 mm, respectively.

Table C-2 Summary of confined and unconfined foam test results

Diameter: 101 mm

	Unconfined				Confined			
	Young's Modulus (MPa)	Densification Modulus (MPa)	Crush Stress (MPa)	Max. Force (kN)	Young's Modulus (MPa)	Densification Modulus (MPa)	Crush Stress (MPa)	Max. Force (kN)
1	165.2	74.4	5.6	135.4	166.1	205.7	5.9	286.8
2	158.8	69.0	5.5	136.0	159.5	125.7	5.9	297.8
3	160.8	114.5	5.4	135.1	180.2	96.4	6.6	281.0
Average	161.6	86.0	5.5	135.5	168.6	142.6	6.1	288.5
St. Dev.	2.7	20.3	0.1	0.4	8.6	46.2	0.3	7.0

Diameter: 114 mm

	Unconfined				Confined			
	Young's Modulus (MPa)	Densification Modulus (MPa)	Crush Stress (MPa)	Max. Force (kN)	Young's Modulus (MPa)	Densification Modulus (MPa)	Crush Stress (MPa)	Max. Force (kN)
1	162.0	138.6	5.5	185.4	171.9	166.5	7.3	481.2
2	147.6	81.9	5.4	185.2	177.5	167.6	7.5	434.3
3	135.2	103.4	5.1	194.2	163.5	241.3	7.0	494.5
Average	148.3	108.0	5.3	188.3	171.0	191.8	7.3	470.0
St. Dev.	11.0	23.4	0.2	4.2	5.8	35.0	0.2	25.8

Diameter: 127 mm

	Unconfined				Confined			
	Young's Modulus (MPa)	Densification Modulus (MPa)	Crush Stress (MPa)	Max. Force (kN)	Young's Modulus (MPa)	Densification Modulus (MPa)	Crush Stress (MPa)	Max. Force (kN)
1	166.2	148.9	5.9	301.8	214.5	155.5	7.8	556.7
2	172.0	95.0	5.8	301.9	187.4	192.0	7.4	558.2
3	156.8	170.3	5.8	304.0	220.4	306.8	8.4	612.3
Average	165.0	138.1	5.8	302.6	207.4	218.1	7.9	575.7
St. Dev.	6.3	31.7	0.1	1.0	14.4	64.5	0.4	25.9

Table C-3 Abaqus crushable foam material model inputs based on the confined foam tests

Young's Modulus (MPa)	k	k_t	v
166.1	1	0.1	0.2

Table C-4 Abaqus crushable foam volumetric hardening material model input (confined foam model)

Yield Stress (MPa)	Uniaxial Plastic Strain (mm/mm)
4.120	0.000
4.455	0.093
4.760	0.133
5.163	0.174
5.468	0.218
5.757	0.260
6.145	0.309
6.346	0.359
6.754	0.410
7.191	0.466
8.178	0.521
9.412	0.582
10.725	0.648
12.644	0.718
14.730	0.792
18.344	0.874
22.434	0.962
28.960	1.060
39.022	1.166
53.999	1.289
67.296	1.375

Table C-5 Parametric study section properties

$D \times t$ (mm × mm)	D/t	λ	Brace Length (mm)
HSS 152.4 × 4.8	34.5	41	1575
HSS 152.4 × 4.8	34.5	50	2075
HSS 152.4 × 4.8	34.5	60	2575
HSS 152.4 × 4.8	34.5	69	3075
HSS 152.4 × 4.8	34.5	79	3575
HSS 152.4 × 4.8	34.5	88	4075
HSS 127 × 4.8	28.7	49	1575
HSS 127 × 4.8	28.7	61	2075
HSS 127 × 4.8	28.7	72	2575
HSS 127 × 4.8	28.7	84	3075
HSS 127 × 4.8	28.7	95	3575
HSS 152.4 × 7.1	23.1	41	1575
HSS 152.4 × 7.1	23.1	51	2075
HSS 152.4 × 7.1	23.1	61	2575
HSS 152.4 × 7.1	23.1	70	3075
HSS 152.4 × 7.1	23.1	80	3575
HSS 152.4 × 7.1	23.1	90	4075
HSS 152.4 × 6.4	25.8	60	2575
HSS 152.4 × 6.4	25.8	89	4075
HSS 190.5 × 4.8	43.1	70	4075
HSS 177.8 × 7.9	24.1	69	3575
HSS 177.8 × 9.5	20.1	69	3575
HSS 219.1 × 8.2	28.8	68	4575
HSS 190.5 × 6.4	32.2	71	4075
HSS 244.5 × 7.9	33.1	61	4575
HSS 244.5 × 6.4	41.3	61	4575
HSS 177.8 × 6.4	30.0	60	3075
HSS 190.5 × 6.4	32.2	79	4575
HSS 190.5 × 9.5	21.5	80	4575

Appendix D

Table D-1 Weld material isotropic hardening inputs

Plastic Strain (mm/mm)	Yield Stress (MPa)	Plastic Strain (mm/mm)	Yield Stress (MPa)
0.0000	569.59	0.0444	637.66
0.0011	572.02	0.0458	640.57
0.0022	575.43	0.0472	643.36
0.0034	578.52	0.0487	645.78
0.0048	581.33	0.0500	646.84
0.0067	583.34	0.0514	650.38
0.0091	583.99	0.0529	653.37
0.0115	584.90	0.0546	655.90
0.0140	587.11	0.0563	658.77
0.0165	589.76	0.0581	661.74
0.0191	592.16	0.0600	664.52
0.0216	594.33	0.0620	667.06
0.0240	596.51	0.0640	670.01
0.0262	598.33	0.0661	672.80
0.0281	600.80	0.0682	675.34
0.0300	603.34	0.0704	678.15
0.0316	605.15	0.0727	680.99
0.0329	606.35	0.0751	683.57
0.0337	605.80	0.0776	686.24
0.0342	608.61	0.0800	688.56
0.0348	612.26	0.0825	690.86
0.0355	615.54	0.0850	693.21
0.0363	618.67	0.0876	695.34
0.0372	621.48	0.0903	697.51
0.0382	623.93		
0.0393	626.61		
0.0405	629.72		
0.0418	632.49		
0.0431	635.03		

Table D-2 RHS corner material isotropic hardening inputs

Plastic Strain (mm/mm)	Yield Stress (MPa)
0.0000	519.26
0.0010	544.23
0.0022	560.26
0.0035	570.44
0.0049	578.22
0.0063	581.75
0.0078	585.64
0.0093	587.97
0.0109	590.26
0.0124	591.50
0.0141	592.95
0.0157	594.03

Table D-3 RHS flat material isotropic hardening inputs

Plastic Strain (mm/mm)	Yield Stress (MPa)	Plastic Strain (mm/mm)	Yield Stress (MPa)
0.0000	426.01	0.0711	520.22
0.0021	427.64	0.0754	522.81
0.0062	443.15	0.0796	524.44
0.0101	453.65	0.0840	526.61
0.0139	464.64	0.0882	529.73
0.0177	473.60	0.0925	531.19
0.0216	480.16	0.0968	533.33
0.0255	487.06	0.1011	535.33
0.0294	492.38	0.1054	538.27
0.0334	495.74	0.1097	539.24
0.0374	499.55	0.1139	542.09
0.0415	503.61		
0.0457	505.25		
0.0499	508.67		
0.0540	510.95		
0.0583	512.50		
0.0625	516.31		
0.0668	518.24		

Table D-4 A36 plate material isotropic hardening inputs

Plastic Strain (mm/mm)	Yield Stress (MPa)
0.0000	298.35
0.0115	337.61
0.0193	358.67
0.0270	376.42
0.0344	391.49
0.0419	403.67
0.0494	413.78
0.0561	421.85
0.0619	427.69
0.0665	431.56
0.0698	433.81
0.0721	435.21
0.0736	435.50
0.0747	436.02
0.0756	436.65
0.0765	437.38
0.0772	437.49
0.0779	437.99
0.0785	438.37
0.0790	438.68
0.0795	439.06
0.0800	439.18
0.0804	439.54
0.0809	439.66
0.0813	440.40
0.0817	440.57
0.0822	440.78
0.0826	441.19
0.0830	441.90

References

Abramowicz, W. (2003). Thin-walled structures as impact energy absorbers. Thin-Walled Structures, 41(2), 91-107.

AISC. (2005). Seismic Provisions for Structural Steel Buildings. Chicago, IL: American Institute of Steel Construction.

AISC. (2010). Specification for Structural Steel Buildings (ANSI/AISC 360-10). American Institute of Steel Construction, Chicago-Illinois.

AISC. (2016a). Seismic Provisions for Structural Steel Buildings. Chicago, IL: American Institute of Steel Construction.

AISC. (2016b). Specification for Structural Steel Buildings (ANSI/AISC 360-16). American Institute of Steel Construction, Chicago-Illinois.

AISC. (2017). Steel Construction Manual (Fifteenth Edition). Chicago, IL: American Institute of Steel Construction.

ASTM. (2016). ASTM E8/E8M-16a: Standard Test Methods for Tension Testing of Metallic Materials. West Conshohocken, PA, USA: ASTM International.

Bezerra, U. T., Alves, S., Barbosa, N. P., & Torres, S. M. (2016). Hourglass-shaped specimen: compressive strength of concrete and mortar (numerical and experimental analyses). Revista Ibracon de Estruturas e materiais, 9(4), 510-524.

Chan, T., & Gardner, L. (2008). Compressive resistance of hot-rolled elliptical hollow sections. Engineering Structures, 30(2), 522-532.

Chang, K.-C., & Lee, G. C. (1987). Strain rate effect on structural steel under cyclic loading. Journal of engineering mechanics, 113(9), 1292-1301.

Chen, B., & Liu, J. (2004). Properties of lightweight expanded polystyrene concrete reinforced with steel fiber. Cement and Concrete Research, 34(7), 1259-1263.

Clark, P. W., Frank, K., Krawinkler, H., & Shaw, R. (2002). Protocol for Fabrication, Inspection, Testing and Documentation of Beam-colum Connection Tests and Other Experimental Specimens: SAC Joint Venture.

Constantinou, M., & Symans, M. (1993). Seismic response of structures with supplemental damping. The Structural Design of Tall Buildings, 2(2), 77-92.

D'Mello, R. J., & Waas, A. M. (2013). Inplane crush response and energy absorption of circular cell honeycomb filled with elastomer. Composite Structures, 106, 491-501.

Davalos, J. F., Qiao, P., Xu, X. F., Robinson, J., & Barth, K. E. (2001). Modeling and characterization of fiber-reinforced plastic honeycomb sandwich panels for highway bridge applications. Composite structures, 52(3-4), 441-452.

Davies, G., & Packer, J. A. (1982). Predicting the strength of branch plate-RHS connections for punching shear. Canadian Journal of Civil Engineering, 9(3), 458-467.

Davies, G., Wardenier, J., & Stolle, P. (1981). The effective width of branch crosswalls for RR cross joints in tension. Delft University of Technology, Delft, Stevin Report, (6-81), 6.

D'Mello, R. J., Guntupalli, S., Hansen, L. R., & Waas, A. M. (2012). Dynamic axial crush response of circular cell honeycombs. Proceedings of the royal society a: mathematical, physical and engineering sciences, 468(2146), 2981-3005.

Elchalakani, M., Zhao, X.-L., & Grzebieta, R. (2003). Tests of cold-formed circular tubular braces under cyclic axial loading. Journal of Structural Engineering, 129(4), 507-514.

European Committee for Standardization (EC3). (2005). Eurocode 3: Design of steel structures—Part 1.1: General rules and rules for buildings.

Fadden, M., & McCormick, J. (2014). Finite element model of the cyclic bending behavior of hollow structural sections. Journal of Constructional Steel Research, 94, 64-75.

Fell, B., Kanvinde, A., Deierlein, G., & Myers, A. (2009). Experimental investigation of inelastic cyclic buckling and fracture of steel braces. Journal of Structural Engineering, 135(1), 19-32.

Fisco, N., & Adeli, H. (2011). Smart structures: part II—hybrid control systems and control strategies. Scientia Iranica, 18(3), 285-295.

Fu, H., Erki, M., & Seckin, M. (1991). Review of effects of loading rate on concrete in compression. Journal of structural engineering, 117(12), 3645-3659.

Gibson, L. J. (1981). The elastic and plastic behaviour of cellular materials. University of Cambridge,

Goggins, J. M., Broderick, B. M., & Elghazouli, A. Y. (2006). Experimental Behaviour of Hollow and Filled RHS Bracing Members Under Earthquake Loading. In Composite Construction in Steel and Concrete V (pp. 698-707).

Goggins, J., Broderick, B. M., Elghazouli, A., & Lucas, A. (2006). Behaviour of tubular steel members under cyclic axial loading. Journal of Constructional Steel Research, 62(1), 121-131.

Goggins, J., Broderick, B., Elghazouli, A., & Lucas, A. (2005). Experimental cyclic response of cold-formed hollow steel bracing members. Engineering Structures, 27(7), 977-989.

Haddad, M., & Shrive, N. (2019). Investigating the inelastic cyclic behaviour of large-size steel wide-flange section braces. Construction and Building Materials, 199, 92-105.

Haddad, M., Brown, T., & Shrive, N. (2010). Experimental cyclic loading of concentric HSS braces. Canadian Journal of Civil Engineering, 38(1), 110-123.

Haddad, M., Brown, T., & Shrive, N. (2011). Finite element modeling of concentric HSS braces under cyclic loading. Canadian Journal of Civil Engineering, 38(5), 493-505.

Han, S.-W., Kim, W. T., & Foutch, D. A. (2007). Seismic behavior of HSS bracing members according to width–thickness ratio under symmetric cyclic loading. Journal of Structural Engineering, 133(2), 264-273.

Hines, E. M., Appel, M. E., & Cheever, P. J. (2009). Collapse performance of low-ductility chevron braced steel frames in moderate seismic regions. Engineering journal, 46(3), 149.

Hooputra, H., Gese, H., Dell, H., & Werner, H. (2004). A comprehensive failure model for crashworthiness simulation of aluminium extrusions. International Journal of Crashworthiness, 9(5), 449-464.

Ikeda, Y. (2009). Active and semi-active vibration control of buildings in Japan—Practical applications and verification. Structural Control and Health Monitoring: The Official Journal of the International Association for Structural Control and Monitoring and of the European Association for the Control of Structures, 16(7-8), 703-723.

Imani, R., Mosqueda, G., & Bruneau, M. (2015). Finite element simulation of concrete-filled double-skin tube columns subjected to postearthquake fires. Journal of Structural Engineering, 141(12), 04015055.

Jain, A. K., Hanson, R., & Goel, S. (1980). Hysteretic cycles of axially loaded steel members. Journal of the Structural Division, 106(8), 1777-1795.

Jung, W.-Y., & Aref, A. J. (2003). A combined honeycomb and solid viscoelastic material for structural damping applications. Mechanics of Materials, 35(8), 831-844.

Kareem, A., Kijewski, T., & Tamura, Y. (1999). Mitigation of motions of tall buildings with specific examples of recent applications. Wind and structures, 2(3), 201-251.

Kumar, P. A., Sahoo, D. R., & Kumar, N. (2015). Limiting values of slenderness ratio for circular braces of concentrically braced frames. Journal of Constructional Steel Research, 115, 223-235.

Kurobane, Y., Packer, J., Wardenier, J., & Yeomans, N. (2004). Design guide for structural hollow section column connections. CIDECT Design Guide No. 9. Köln: TÜV-Verlag.

Lai, J.-W., Chen, C.-H., & Mahin, S. A. (2010). Experimental and analytical performance of concentrically braced steel frames. Paper presented at the Structures Congress 2010.

Lampinen, B., & Jeryan, R. (1982). Effectiveness of polyurethane foam in energy absorbing structures (0148-7191). Retrieved from

Lapczyk, I., & Hurtado, J. A. (2007). Progressive damage modeling in fiber-reinforced materials. Composites Part A: Applied Science and Manufacturing, 38(11), 2333-2341.

Lehman, D. E., Roeder, C. W., Herman, D., Johnson, S., & Kotulka, B. (2008). Improved seismic performance of gusset plate connections. Journal of Structural Engineering, 134(6), 890-901.

Lemaitre, J., & Chaboche, J. Mechanics of solid materials. 1990. Cambridge University Press.-1000-500 0, 500, 1000.

Li, Q., Magkiriadis, I., & Harrigan, J. J. (2006). Compressive strain at the onset of densification of cellular solids. Journal of cellular plastics, 42(5), 371-392.

Lin, T.-C., Chen, T.-J., & Huang, J.-S. (2012). In-plane elastic constants and strengths of circular cell honeycombs. Composites science and technology, 72(12), 1380-1386.

Linul, E., Marsavina, L., Voiconi, T., & Sadowski, T. (2013). Study of factors influencing the mechanical properties of polyurethane foams under dynamic compression. Paper presented at the Journal of Physics: Conference Series.

Liu, Q., Mo, Z., Wu, Y., Ma, J., Tsui, G. C. P., & Hui, D. (2016). Crush response of CFRP square tube filled with aluminum honeycomb. Composites Part B: Engineering, 98, 406-414.

Liu, Z., & Goel, S. C. (1988). Cyclic load behavior of concrete-filled tubular braces. Journal of Structural Engineering, 114(7), 1488-1506.

Liu, Z., & Goel, S. C. (1988). Cyclic load behavior of concrete-filled tubular braces. Journal of Structural Engineering, 114(7), 1488-1506.

Lu, L. H. (1997). The static strength of I-beam to rectangular hollow section column connections: TU Delft, Delft University of Technology.

Lu, L., De Winkel, G., Yu, Y., & Wardenier, J. (1994). Deformation limit for the ultimate strength of hollow section joints. Paper presented at the Proc. Sixth International Symposium on Tubular Structures.

Marikunte, S., Aldea, C., & Shah, S. P. (1997). Durability of glass fiber reinforced cement composites:: Effect of silica fume and metakaolin. Advanced Cement Based Materials, 5(3-4), 100-108.

McFarland, R. (1963). Hexagonal cell structures under post-buckling axial load. AIAA journal, 1(6), 1380-1385.

Meguid, S., Attia, M., & Monfort, A. (2004). On the crush behaviour of ultralight foam-filled structures. Materials & design, 25(3), 183-189.

Mirfendereski, L., Salimi, M., & Ziaei-Rad, S. (2008). Parametric study and numerical analysis of empty and foam-filled thin-walled tubes under static and dynamic loadings. International Journal of Mechanical Sciences, 50(6), 1042-1057.

Moon, J., Lehman, D. E., Roeder, C. W., & Lee, H.-E. (2013). Strength of circular concrete-filled tubes with and without internal reinforcement under combined loading. Journal of Structural Engineering, 139(12), 04013012.

Mozafari, H., Molatefi, H., Crupi, V., Epasto, G., & Guglielmino, E. (2015). In plane compressive response and crushing of foam filled aluminum honeycombs. Journal of Composite Materials, 49(26), 3215-3228.

Mulliken, A., & Boyce, M. (2006). Polycarbonate and a polycarbonate-POSS nanocomposite at high rates of deformation.

Nip, A. K., Gardner, L., & Elghazouli, A. Y. (2013). Ultimate behaviour of steel braces under cyclic loading. Proceedings of the Institution of Civil Engineers-Structures and Buildings, 166(5), 219-234.

Nip, K., Gardner, L., & Elghazouli, A. (2010). Cyclic testing and numerical modelling of carbon steel and stainless steel tubular bracing members. Engineering Structures, 32(2), 424-441.

Olabi, A.-G., Morris, E., & Hashmi, M. (2007). Metallic tube type energy absorbers: a synopsis. Thin-walled structures, 45(7-8), 706-726.

Olurin, O., Fleck, N. A., & Ashby, M. F. (2000). Deformation and fracture of aluminium foams. Materials Science and Engineering: A, 291(1-2), 136-146.

O'Shea, M. D., & Bridge, R. Q. (1997). Local buckling of thin-walled circular steel sections with or without internal restraint. Journal of Constructional Steel Research, 41(2-3), 137-157.

Packer, J. A. (1993). Overview of current international design guidance on hollow structural section connections. Paper presented at the The Third International Offshore and Polar Engineering Conference.

Packer, J. A., Wardenier, J., Zhao, X.-L., van der Vegte, A., & Kurobane, Y. (2009). Design Guide for Rectangular Hollow Section (RHS) Joints Under Predominantly Static Loading (2nd ed.). Geneva, Switzerland.

Packer, J., Chiew, S., Tremblay, R., & Martinez-Saucedo, G. (2010a). Effect of material properties on hollow section performance. Proceedings of the Institution of Civil Engineers-Structures and Buildings, 163(6), 375-390.

Packer, J., Sherman, D., & Lecce, M. (2010b). Steel design guide 24. Hollow structural section connections.

Packer, J., Wardenier, J., Kurobane, Y., Dutta, D., & Yeomans, N. (1992). Design guide for rectangular hollow section (RHS) joints under predominantly static loading-CIDECT. TíV-Verlag GmbH, Köln, Germany.

Papka, S. D., & Kyriakides, S. (1994). In-plane compressive response and crushing of honeycomb. Journal of the Mechanics and Physics of Solids, 42(10), 1499-1532.

Papka, S. D., & Kyriakides, S. (1998). In-plane crushing of a polycarbonate honeycomb. International Journal of Solids and Structures, 35(3-4), 239-267.

Paz, J., Díaz, J., Romera, L., & Costas, M. (2014). Crushing analysis and multi-objective crashworthiness optimization of GFRP honeycomb-filled energy absorption devices. Finite Elements in Analysis and Design, 91, 30-39.

Popov, E. P., & Black, R. G. (1981). Steel struts under severe cyclic loadings. Journal of the Structural Division, 107(9), 1857-1881.

Popov, E. P., Mahin, S. A., & Zayas, V. (1979). Cyclic inelastic buckling of thin tubular columns. Journal of the Structural Division, 105(11), 2261-2277.

Qi, C., Yang, S., & Dong, F. (2012). Crushing analysis and multiobjective crashworthiness optimization of tapered square tubes under oblique impact loading. Thin-Walled Structures, 59, 103-119.

Reid, S., Reddy, T., & Gray, M. (1986). Static and dynamic axial crushing of foam-filled sheet metal tubes. International Journal of Mechanical Sciences, 28(5), 295-322.

Remennikov, A. M., & Walpole, W. R. (1998). A note on compression strength reduction factor for a buckled strut in seismic-resisting braced system. Engineering Structures, 20(8), 779-782.

Roeder, C. W., Lumpkin, E. J., & Lehman, D. E. (2011). A balanced design procedure for special concentrically braced frame connections. Journal of Constructional Steel Research, 67(11), 1760-1772.

Rolloos, A. (1969). The effective weld length of beam to column connections without stiffening plates. IIW Document XV-276-69.

Santosa, S., & Wierzbicki, T. (1998). Crash behavior of box columns filled with aluminum honeycomb or foam. Computers & Structures, 68(4), 343-367.

Sheehan, T. (2013). Cyclic Behaviour of Hollow and Concrete-Filled Circular Hollow Section Braces. University of Warwick.

Sheehan, T., & Chan, T.-M. (2014). Cyclic response of hollow and concrete-filled circular hollow section braces. Proceedings of the Institution of Civil Engineers-Structures and Buildings, 167(3), 140-152.

Simpson, B. G., & Mahin, S. A. (2018). Experimental and numerical investigation of strongback braced frame system to mitigate weak story behavior. Journal of Structural Engineering, 144(2), 04017211.

Simulia (2017). Abaqus/CAE. Dassault Systemes Simulia Corporation. Johnston, RI, USA.

Smith, B., Szyniszewski, S., Hajjar, J., Schafer, B., & Arwade, S. (2012). Steel foam for structures: A review of applications, manufacturing and material properties. Journal of Constructional Steel Research, 71, 1-10.

Song, C. Y., Teng, J. G., & Rotter, J. M. (2004). Imperfection sensitivity of thin elastic cylindrical shells subject to partial axial compression. International journal of solids and structures, 41(24-25), 7155-7180.

Structural & Fiberglass Materials - Carbon-Core Corporation. (2020). Retrieved from http://www.carbon-core.com/

Symans, M., Charney, F., Whittaker, A., Constantinou, M., Kircher, C., Johnson, M., & McNamara, R. (2008). Energy dissipation systems for seismic applications: current practice and recent developments. Journal of structural engineering, 134(1), 3-21.

Szyniszewski, S., Smith, B., Hajjar, J., Arwade, S., & Schafer, B. (2012). Local buckling strength of steel foam sandwich panels. Thin-Walled Structures, 59, 11-19.

Tarlochan, F., Samer, F., Hamouda, A., Ramesh, S., & Khalid, K. (2013). Design of thin wall structures for energy absorption applications: enhancement of crashworthiness due to axial and oblique impact forces. Thin-Walled Structures, 71, 7-17.

Tremblay, R. (2002). Inelastic seismic response of steel bracing members. Journal of Constructional Steel Research, 58(5-8), 665-701.

Tremblay, R., Archambault, M.-H., & Filiatrault, A. (2003). Seismic response of concentrically braced steel frames made with rectangular hollow bracing members. Journal of Structural Engineering, 129(12), 1626-1636.

Tsivilis, S., Tsantilas, J., Kakali, G., Chaniotakis, E., & Sakellariou, A. (2003). The permeability of Portland limestone cement concrete. Cement and concrete research, 33(9), 1465-1471.

Tu, Y., & Wang, G. (2010). Damping parameter identification and study of metal foam filled steel tube. Journal of Materials in Civil Engineering, 22(4), 397-402.

U.S. Composites, Inc. (2020). Retrieved from uscomposites.com.

Vendra, L. J., & Rabiei, A. (2007). A study on aluminum–steel composite metal foam processed by casting. Materials Science and Engineering: A, 465(1-2), 59-67.

Wardenier, J., Davies, G., & Stolle, P. (1981). The effective width of branch plate to RHS chord connections in cross joints. Delft University of Technology, Delft, Stevin Report (6-81), 6.

Wardenier, J., Kurobane, Y., Packer, J. A., Van der Vegte, G., & Zhao, X. (2008). Design guide 1 for circular hollow section (CHS) joint under predominantly static loading, 2nd. CIDECT, Construction with hollow steel sections.

Wei, D. (2017). Enhancement of Steel Moment Connections Through Non-Traditional Sections and Materials. (Doctoral dissertation). University of Michigan.

Wierzbicki, T. (1983). Crushing analysis of metal honeycombs. International Journal of Impact Engineering, 1(2), 157-174.

Wu, E., & Jiang, W.-S. (1997). Axial crush of metallic honeycombs. International Journal of Impact Engineering, 19(5-6), 439-456.

Zhang, J., & Ashby, M. (1992). The out-of-plane properties of honeycombs. International journal of mechanical sciences, 34(6), 475-489.

Zhao, X.-L., Grzebieta, R., & Lee, C. (2002). Void-filled cold-formed rectangular hollow section braces subjected to large deformation cyclic axial loading. Journal of Structural Engineering, 128(6), 746-753.

Zi, G., Kim, B. M., Hwang, Y. K., & Lee, Y. H. (2008). An experimental study on static behavior of a GFRP bridge deck filled with a polyurethane foam. Composite structures, 82(2), 257-268.